

Improvements of CMOS Hall Microsystems and Application for Absolute Angular Position Measurements

Michel Demierre

Thesis Supervisor: Prof. Radivoje S. Popovic

IMM – Institute of Microelectronics and Microsystems

LMIS - Microsystems Laboratory

September 2003

Contents

1	Introduction	5
1.1	Preliminary analysis of the microsystem.....	7
1.2	Motivations	8
1.3	Thesis organization.....	9
2	Basics and state of the art	11
2.1	Hall sensor: basics characteristics	11
2.1.1	Hall voltage and sensitivities.....	11
2.1.2	Thermal drift	17
2.1.3	Piezo-resistance and piezo-Hall Effects.....	20
2.1.4	Reduction of the offset from electronics	22
2.1.5	Spinning Current	25
2.2	Calibration of Hall sensors	28
2.3	CMOS vertical Hall sensors	31
2.3.1	4-Contacts DNTUB vertical Hall sensors	32
2.3.2	Coupling of 4-Contacts DNTUB vertical Hall sensors	33
2.3.3	6-Contacts DNTUB vertical Hall sensors	33
2.4	Absolute contactless angular sensors	34
2.4.1	Hall sensors at the magnet periphery	35
2.4.2	2-D Vertical Hall sensor.....	36
2.4.3	Magnetotransistors	37
2.4.4	Integrated Magneto Concentrators Disk	38
2.4.5	Magnetoresistive sensors.....	39
2.4.6	Angle extraction	40
2.5	Conclusion	41
2.6	References	42
3	Calibration Coils and Synergies with the Hall Microsystem	49
3.1	Figure of Merit.....	50
3.2	Coils for Hall plates and vertical Hall sensors	51
3.3	Stress Influence.....	53
3.4	Models	53
3.4.1	Integrated FlatCoils for Hall Plates.....	53
3.4.2	Integrated Flat Coils for vertical Hall sensors.....	59

3.5	Technology limitations.....	63
3.6	Coil optimization.....	64
3.6.1	Hall plate.....	64
3.6.2	Vertical Hall sensor.....	67
3.7	Final layout.....	71
3.7.1	Miniaturized Hall plate.....	71
3.7.2	Vertical Hall sensors.....	71
3.8	Measurements.....	72
3.9	CMOS technologies trends applied to coils.....	73
3.10	Array of sensors and coils.....	74
3.11	Integrated magnetoconcentrators.....	75
3.12	Separation of the external and the calibration field.....	75
3.12.1	Frequency multiplexing.....	76
3.12.2	Spatial multiplexing.....	76
3.12.3	Shielding with integrated magnetoconcentrators.....	77
3.13	Parasitic coupling between the coil and the sensor.....	78
3.13.1	Reduction of the parasitic coupling.....	79
3.14	Self-Calibration.....	81
3.14.1	Twin Hall Microsystem.....	81
3.14.2	Results.....	83
3.15	Geometrical reference.....	85
3.16	Conclusions.....	87
3.17	References.....	88
4	Miniaturized Hall plates.....	91
4.1	Layout.....	92
4.1.1	Lateral diffusion.....	92
4.2	Measurements.....	95
4.2.1	Input resistance.....	95
4.2.2	Sensitivity.....	96
4.3	Sensor optimization.....	98
4.3.1	Length of arms.....	98
4.3.2	Non-uniform implantation width.....	100
4.4	Offset and residual offset.....	102
4.5	Model.....	105
4.5.1	Lateral diffusion.....	105
4.5.2	Junction field effect.....	106
4.5.3	Current related sensitivity.....	108
4.6	Integrated magnetoconcentrators.....	109

4.7	Conclusion	110
4.8	References	111
5	Spinning Current.....	113
5.1	Electronic part.....	114
5.2	Modulation using a switch box.....	115
5.3	Amplification.....	117
5.4	Peak-to-Peak detector and Buffer.....	120
5.4.1	Correlated double sampling difference amplifier.....	121
5.4.2	Track-and-Hold	123
5.4.3	Buffer	126
5.4.4	Residual offset from peak to peak detector and Buffer.....	126
5.5	Microsystem residual offset	127
5.6	Noise	129
5.6.1	Hall sensor	130
5.6.2	Modulator	130
5.6.3	Preamplifier.....	130
5.6.4	Correlated double sampling	130
5.6.5	Microsystem Noise.....	131
5.7	Feedback Spinning Current	132
5.7.1	Principle	133
5.7.2	Modifications	135
5.7.3	Simulations.....	135
5.7.4	Electronics dynamic behavior	137
5.7.5	Measurements.....	139
5.8	4-Phases Spinning Current	141
5.9	2D-Spinning Current	145
5.10	Conclusion.....	146
5.11	References	148
6	Angular position sensors.....	151
6.1	Hall Sensors related non-linearities.....	152
6.1.1	Offset.....	153
6.1.2	Sensitivity Mismatch.....	155
6.1.3	Non-orthogonality	156
6.1.4	Magnetic sensor non-linearity.....	158
6.2	Other sources of non-linearities.....	159
6.2.1	Mechanical alignment	159
6.2.2	Ferromagnetic materials.....	161
6.3	Statistical approach of the non-linearities	162

6.4	Angular noise.....	164
6.5	Vertical Hall Sensors 2-D microsystem	164
6.5.1	Principle	164
6.5.2	Magnetic Measurements	166
6.5.3	Angular measurements	168
6.5.4	Discussion	170
6.6	2-D microsystem with integrated flux concentrators	171
6.6.1	Principle	171
6.6.2	Material related non-linearity.....	174
6.6.3	Misalignment related non-linearity	176
6.6.4	Measurements.....	178
6.6.5	Discussion	183
6.7	Comparison between the two sensing elements	184
6.8	Conclusion	185
6.9	References	186
7	Conclusion and Outlook	189
7.1	A toolbox for Hall microsystems	189
7.2	Angular position sensors	190
7.3	Outlook.....	193

Abstract

The compatibility of some Hall sensors with CMOS electronics allows the co-integration of sensors and electronics on the same chip to obtain a low cost microsystem. In addition to a careful sensor design, the relationships between the system components, i.e. sensors and electronics, allow us to improve substantially the behavior of the microsystem. The first objective of this thesis is to create a toolbox to construct very accurate CMOS Hall microsystems; each so-called tool solves a limitation of Hall sensors. We also built for angular measurements a 2-dimensional Hall microsystem, i.e. a microsystem with two orthogonal axes of sensitivity. This microsystem is based on vertical Hall sensors placed orthogonally.

CMOS Hall sensors suffer from several non-idealities, such as low sensitivity, sensitivity drift, offset and non-linearities. What's more, a 2-dimensional sensor suffers from sensitivity mismatch between the X- and Y-sensors and non-orthogonality between the measurement axes. Sensitivity drift and offset are the most challenging problems for which new tools are necessary.

The first tool is calibration coils for the self-calibration of Hall microsystems. These coils are in-situ using the metallization layers of the technology. We obtain a coil efficiency of 290mT/A and 230mT/A for respectively miniaturized Hall plates and miniaturized CMOS vertical Hall sensors. Note that miniaturized sensors are obligatory for efficient coils. Using external laboratory voltage and current references, we obtain an outstanding thermal drift of less than 30ppm/°C. We also propose a calibration scheme, called geometrical reference, which is independent of the electric references; the sensitivity is in that case a function of only the sensor and the coil geometry.

The second tool is an efficient reduction of the Hall sensor offset using the spinning current technique. We analyze the sources of residual offset of our microsystem to find the major sources of residual offset: the electronic circuit and the sensor itself. We develop a feedback scheme for the spinning current method to reduce drastically the residual offset by one order of magnitude to a 1.2mV standard deviation from the output. Miniaturized sensors are degenerated, because they suffer from non-linearities; that's why a four phases spinning current is required. We also multiplex the electronics for the X and Y axis of the angular sensor in order to guarantee the matching of the amplification chain and to reduce the electronics surface.

Our main industrial challenge, based on accurate Hall microsystems, is an absolute 360° angular position sensor without any dead angles reaching a 0.3% (1.1°) and 0.1% (0.36°) accuracy respectively without and with calibrations. The measurement principle, we choose at the beginning of this work, consists in measuring the magnetic field from a permanent magnet placed in front of the sensor on the rotating shaft. The magnet generates a rotating magnetic field at the surface of the CMOS chip. Measuring this field along two orthogonal axes allow us to calculate the angle over 360° with and without calibration using the arctangent function. This principle is very robust in respect to mechanical tolerances, to the variations of the sensor sensitivity and to the strength of the permanent magnet.

We develop for the first time a CMOS angular sensor based on vertical Hall sensors. We reach an outstanding accuracy of 0.5° (1.4‰) with only an easy offset compensation. In this thesis work, the sources of non-linearities are also studied and explained, allowing their calibration. With additional sensitivity mismatch and non-orthogonality compensations, an accuracy of 0.17° (0.5‰) is obtained. These results are compared with those of a sensor using an integrated ferromagnetic disk and Hall plates. With an offset compensation, the accuracy is degraded to 2° (5.6‰) due to the tolerances during the post processing. However an accuracy of 0.4° (1.1‰) can be obtained with an additional calibration of the gain mismatch. This sensor is better adapted to low field measurements. The full range is limited by the saturation of the ferromagnetic elements and the field is amplified by the concentrators. The sensor based on vertical Hall sensors, is better adapted to high precision, especially without complex calibrations, with a larger magnetic field. Measurements demonstrate that coils, our first tool, is useless for angular measurement because the ratio of the X and Y signals is calculated, getting ride of the drifts if they are matched. The accurate matching of these drifts is typically less than 10ppm/ $^\circ\text{C}$ even when low cost plastic packaging is used. The low offset microsystem, our second tool, is required to reach high accuracy and low thermal drift without calibration.

Version abrégée

La compatibilité de certains capteurs à effet Hall avec l'électronique CMOS permet la co-intégration des capteurs et de l'électronique sur la même puce électronique pour obtenir un microsysteme bon marché. En plus du design soigné des capteurs, les relations entre les composants du système, c'est-à-dire les capteurs et l'électronique, nous permettent d'améliorer sensiblement le comportement du microsysteme. Le premier objectif de cette thèse est de créer une boîte à outils pour construire des microsystemes CMOS à effet Hall précis ; chaque outil permettant de résoudre une limitation des capteurs. Nous avons aussi construit, spécifiquement pour la mesure angulaire, un microsysteme à 2 dimensions mesurant le champ magnétique selon deux axes orthogonaux. Ce microsysteme est basé sur des capteurs Hall verticaux placés orthogonalement.

Les capteurs Hall souffrent de plusieurs imperfections telles qu'une faible sensibilité, une dérive de cette même sensibilité, un offset ou encore des non-linéarités. De plus, un capteur à 2 dimensions subit en plus les imperfections liées au non-appareillement de la sensibilité entre les deux axes et aussi à une non-orthogonalité entre les axes de mesure. La dérive en sensibilité et l'offset des capteurs sont les problèmes pour lesquels nous avons développé de nouveaux outils.

Le premier outil consiste en des bobines permettant la calibration de microsystemes à effet Hall. Elles sont réalisées en utilisant les couches métalliques disponibles avec le procédé CMOS. Nous obtenons une efficacité de 290mT/A et 230mT/A respectivement pour des capteurs Hall usuels et verticaux. Ces bobines permettent une calibration précise du microsysteme. En utilisant des instruments de laboratoire comme référence de courant et de tension, nous obtenons une précision remarquable de 30ppm/°C. Nous proposons un nouveau schéma, appelé référence géométrique, qui est indépendant de ces références électriques. La sensibilité est alors seulement fonction de la géométrie de la bobine et du capteur.

Le deuxième outil consiste en une électronique à "spinning current" permettant une forte réduction de l'offset du capteur à effet Hall. En analysant les sources d'offset d'un premier microsysteme, nous avons constaté que l'offset provenait à la fois de l'électronique et du capteur à effet Hall. Nous avons développé une électronique utilisant une contre-réaction afin de réduire d'un ordre de grandeur, à 1,2mV d'écart type, la partie électronique de l'offset. Les capteurs miniaturisés

que nous utilisons sont « dégénérés » car ils sont fortement non-linéaires. Par conséquent, une électronique de type “spinning current” à 4 phases est requise. Nous avons aussi multiplexé les deux axes X et Y du capteur avec la même électronique pour garantir un appareillement de la chaîne d’amplification et aussi pour réduire la surface de l’électronique.

Notre principal challenge industriel, basé sur des microsystemes à effet Hall précis, est un capteur de position angulaire absolu sur 360° sans angle mort. La précision désirée pour cette application est de 0.3% (1.1°) et 0.1% (0.36°) respectivement sans et avec calibration. Le principe de mesure, choisi au début de cette thèse, consiste à mesurer le champ magnétique produit par un aimant permanent fixé sur l’axe dont la position doit être mesurée. Le microsysteme placé en face de l’aimant, mesure ce champ magnétique sur deux axes orthogonaux, permettant ainsi de calculer la position angulaire sur 360° en utilisant la fonction arctangeante. Ce principe de mesure est très robuste aux tolérances mécaniques, ainsi qu’à la sensibilité absolue des capteurs et à l’intensité du champ magnétique de l’aimant.

Nous avons développé pour la première fois un microsysteme angulaire CMOS basé sur des capteurs Hall verticaux. Une précision exceptionnelle de 0.5° (1.4‰) a été atteinte en n’effectuant que la calibration de l’offset. Grâce à cette thèse, les sources de non-linéarité ont été trouvées et décrites, permettant ainsi leur calibration. Grâce à une calibration de l’écart de sensibilité entre les axes et de la non-orthogonalité, une précision de 0.17° (0.5‰) est obtenue. Ces résultats ont été comparés à des capteurs basés sur un disque ferromagnétique et des capteurs à effet Hall. Avec une calibration de l’offset, la précision est seulement de 2° (5.6‰) à cause des tolérances mécaniques du procédé de déposition de ces disques. Cependant, la précision est fortement améliorée jusqu’à 0.4° (1.1‰) avec une calibration de l’écart de gain entre les axes. Ce capteur est plutôt adapté aux faibles champs magnétiques, car la gamme de champs magnétiques est limitée par la saturation du matériau ferromagnétique. De plus, le disque joue le rôle de concentrateur magnétique, augmentant ainsi la sensibilité du microsysteme. Le capteur utilisant des capteurs Hall verticaux permet d’obtenir une précision supérieure, particulièrement en évitant des calibrations. Il est aussi mieux adapté aux champs magnétiques plutôt forts. Des mesures ont démontré que les bobines de calibrations, notre premier outil, sont inutiles pour les capteurs angulaires. L’extraction de l’angle utilise le rapport des signaux provenant des axes X et Y. De ce fait, seul le mauvais appareillement des deux axes provoque des erreurs de la mesure angulaire. L’appareillement de la dérive thermique est typiquement meilleur que $10\text{ppm}/^\circ\text{C}$, même avec une encapsulation plastique bon marché. Notre deuxième outil, un microsysteme à faible offset, est par contre requis pour obtenir une grande précision et une faible dérive thermique.

1 Introduction

Due to the large market demand, a considerable effort has been made to develop position sensors for linear and rotational displacements. Position sensors can be found in the majority of systems containing moving parts. They are based on various principles, including mechanical, resistive, optical, capacitive, inductive, and magnetic. However only a few of them offer a high accuracy, low cost, small volume, high reliability in harsh environments and a contactless measurement. An efficient solution is the combination of Hall sensors and a permanent magnet fixed on the moving part of the system.

Certain specific Hall sensors have the huge advantage of being compatible with CMOS technologies, allowing the co-integration with complex electronic interfaces, including analog to digital converters, microcontrollers or a calibration table. Furthermore, a single CMOS chip easily makes redundant measurements, because of its small size and low price. Unfortunately Hall sensors suffer from several non-idealities, such as low sensitivity, sensitivity drift, offset and non-linearities. To obtain a high accuracy, we first have to find the way to increase substantially the accuracy. For this reason, we develop tools to build an efficient Hall microsystem. These tools are based on the relationships between the different microsystem parts and especially synergetic relationships.

Position sensors based on the Hall effect are widely used in industrial, domestic and automotive appliances. For instance, one tenth of Hall sensors are found inside modern cars, either to verify that the doors are closed or to measure the position of the engine or cam shaft. For the next generation of vehicles, position sensors are also needed to measure the position of the throttle or for the electronic steering wheel, i.e. a steering without a direct mechanical connection. These new applications require absolute position sensing with an accuracy often better than 1%. The absolute value is not a function of the previous state of the system; even if a power failure occurs the new measurement is exact. This is in contrast to the case of incremental sensors.

Up until now, only few solutions have been considered as candidates for applications of absolute angular position sensing. This thesis focuses firstly on the development, design, fabrication and characterization of accurate Hall single chip microsystems. Based on this work, a contactless angular position sensor using the Hall effect is developed. An angular position sensor transforms the angular position of a rotating shaft into electrical signals suitable to transmit this information about the angle. Our microsystem is based on the measurement of

the two orthogonal components of the magnetic field, B_X and B_Y , from a diametrically magnetized permanent magnet which is fixed on the rotating shaft (Fig. 1.1). This Hall sensor with two orthogonal axes of sensitivity is called a 2-axis or a 2-dimensionnal Hall sensor. These two output signals are proportional to the cosine and the sine of the angle of rotation. The angle is extracted by using the arctangent function of the ratio of these two signals. It allows a measurement without dead angles (area where the measurement is impossible) and without discontinuities over 360° .

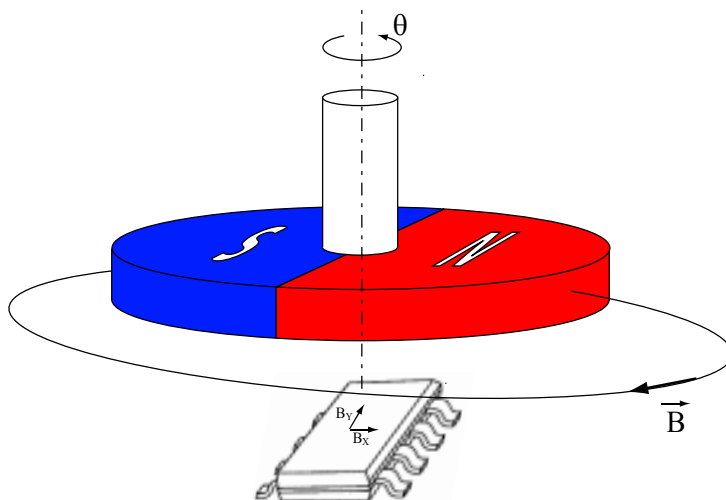


Fig. 1.1 Principle of angular measurement with a rotating permanent magnet. The 2D Hall microsystem measures the projection of the magnetic field \vec{B} from the magnet on the two orthogonal axes X and Y to obtain the sine and cosine of the rotation angle. The angle is calculated from these two values without dead angles and without discontinuities over 360° .

A 2-dimensional Hall sensor is also the basis for other types of position sensors. For instance a contactless joystick is the combination of this sensor with an tilting magnet (Fig. 1.2). A permanent magnet is placed with its magnetization parallel to the “stick” which is held by the user. The microsystem measures the field in the plane perpendicular to the stick. The Hall signals are the sine of the two tilt angles. For small angles, the sensor’s response is approximately linear with the angular displacement. Using contactless measurement, instead of the classical two potentiometers structures, allows the simplification of the mechanical part, for instance using flexible articulations.

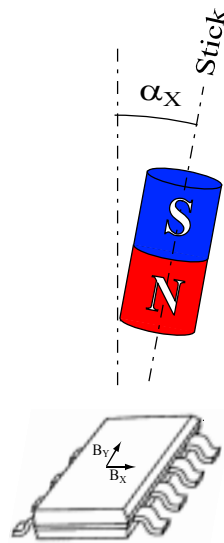


Fig. 1.2 Joystick based on a 2-dimensionnal Hall sensor. When the magnetization is perpendicular to the sensor plane, the sensor outputs are nil. For small inclinations α_X and α_Y , the output signals vary linearly with the angles.

1.1 Preliminary analysis of the microsystem

The magnetic field from a small rare earth permanent magnet used for angular measurements ($\text{Ø}6\text{mm}$) is typically 100mT at a distance of 1mm from its surface; about 2000 times the earth's magnetic field.

Hall sensors in silicon are unfortunately not ideal. For angular measurements, they suffer mainly from offset, low sensitivity, white and $1/f$ noise and sensitivity drift.

The offset of a CMOS Hall plate, i.e. the unbalancing of the sensor, is as large as 10mT (just over 1mV with 1mA biasing) when using silicon sensors. This offset, of more than 10% of the external field, is of course incompatible with high accuracy measurements. Consequently a specific interface for offset reduction, called the spinning current electronics, is required.

The sensitivity is about 100mV/T for a biasing current of 1mA . The amplitude of the magnetic signal, when the magnet is rotating, is only $\pm 10\text{mV}$. This signal

has to be amplified by a factor of 200 to work closer to the full scale of the 5V supply voltage of the electronics.

The output resistance of the sensor is about $5\text{k}\Omega$. Even if the 100mV/T sensitivity is poor, the equivalent magnetic white noise from the sensor is only $10\mu\text{T}$ for a 10KHz bandwidth; this corresponds to a good noise to signal ratio of 0.1% . Note that the preamplifier has to be carefully designed so as not to greatly increase the white noise. Hall sensors also suffer from $1/f$ noise. This noise induces fluctuations in the sensor signal which substantially decreases the low frequency accuracy of the angular sensor. Fortunately this noise will be greatly suppressed with the spinning current method used for offset reduction.

Hall sensors also suffer from sensitivity drifts. The thermal drift is about $0.1\%/^{\circ}\text{C}$. A long-term drift, which mainly depend on the thermo-mechanical stresses, is induced by packaging. This drift is a major limitation of Hall sensors made of silicon. For instance a thermal shock creates sensitivity variations as great as several percent.

Usual Hall sensors, also called Hall plates, measure the magnetic field perpendicular to the chip surface. Unfortunately, it is not possible to combine several of these sensors to measure the magnetic field in two orthogonal directions. A specific sensor, called vertical Hall sensor, measures the field parallel to the chip surface. Two sensors, placed orthogonally to each other, measure the two components of the in-plane magnetic field to obtain a 2-dimensionnal sensor. A second way to obtain sensitivity to the magnetic field parallel to the chip's surface is to combine Hall plates with a post-processing of the integrated magneto-concentrators, because these magneto-concentrators are able to change the direction of the magnetic field.

With a fully integrated microsystem, the orthogonality of the X- and Y- axes is determined by the excellent accuracy of the alignment process. Furthermore, the matching of the properties of the two axes is superior to that of a two chip system.

1.2 Motivations

The aim of this doctoral work is to develop a toolbox for accurate CMOS microsystems based on the Hall effect. The so-called tools are based on the relationships between the microsystem parts. Secondly the tools are applied to an absolute angular position sensor. The industrial challenge is to break, at room temperature, the 1% and 3% accuracy barrier respectively with and without calibration with a thermal drift of less than $50\text{ppm}/^{\circ}\text{C}$. This complex system

requires a multidisciplinary approach to understand the relationships between the mechanics, the magnetic circuit, the Hall sensors, the front-end electronics and the signal processing.

The first object is to develop a precise, 1-dimensionnal CMOS Hall sensor. The main limitations of silicon Hall sensors in this application being the sensitivity drift, we first have to deal with the in-situ self-calibration of Hall microsystems and especially on how to calibrate the sensor with an efficient integrated coil to generate a magnetic field for the calibration. We investigate how to obtain an ultra-low sensitivity drift of less than 50ppm/°C with an integrated Hall microsystem. A second major limitation of Hall sensors is the offset. We examine the offset sources of the microsystem from a systemic point of view. Solutions have been found to deal with both the electronics and sensor offset.

Secondly, two dimensional Hall sensors are studied. A major industrial challenge is to develop an angular sensor with an accuracy greater than 1° (<3‰) without calibration. Until now, no solutions have reached this high level of accuracy. A second challenge is to find the sources of errors to bridge the gap of 1‰ accuracy with their calibration.

In order to achieve these goals, we have developed a tool box to build both a one- and 2-dimensional Hall sensor for angular measurement; each chapter of this thesis is devoted to the analysis of a so-called tool with the name corresponding to the title of the chapter.

1.3 Thesis organization

In chapter 2, we summarize the current knowledge about Hall sensors. The Hall element is analyzed, including its imperfections, such as the thermal behavior and the offset. The state of the art offset reduction techniques for the electronics and the sensor are also described. Finally, we present the main principles of contactless angular measurement using a rotating permanent magnet. For each solution, we identify their advantages and limitations. Based on this chapter, we try in this thesis to fill in the gaps of the existing solutions. We identify two solutions based on recently developed CMOS vertical Hall sensors or Hall plates combined with a ferromagnetic disk. These solutions are analyzed and compared in the next chapters.

The chapter 3 deals with the in-situ calibration of Hall sensors. Two types of coils, using the metal layers of the CMOS process, are developed to generate a magnetic field perpendicular and parallel to the chip surface for, respectively, Hall plates and vertical Hall sensors. Using these coils, a self-calibrated

microsystem is developed. In order to increase the efficiency of the coils, the chapter 3 demonstrates that the sensor has to be dramatically miniaturized. This is the topic of the next chapter.

The chapter 4 is devoted to the miniaturization of a Hall plate. The consequences and the limitations of the miniaturization are described in detail by measurements, simulations of the CMOS process and a simplified model. The CMOS vertical Hall sensor, which is intrinsically miniaturized because of the small implantation depth, is not studied in this chapter.

In the chapter 5, the spinning current techniques are studied from the systemic point of view. The sources of residual offset are identified, allowing us to substantially decrease the residual offset from the microsystem using a better system approach.

The chapter 6 is devoted to angular sensors. We analyze angular sensors using two working principles: CMOS vertical Hall sensors and Hall plates with a ferromagnetic disk to deflect the magnetic field. The sources of inaccuracy are studied with care for both principles. Finally the two solutions are compared both theoretically, experimentally and from an industrial point of view.

The conclusions and the outlook of this thesis are given in the last chapter.

2 Basics and state of the art

This chapter first introduces the Hall sensor theory, including the effects of stresses from the packaging on the Hall sensor. The offset voltage is coming from the front-end electronics and the offset; the state of the art of both offset reduction is described. It is followed by the calibration of Hall sensors, including integrated calibration coils. A CMOS vertical Hall sensor we developed at the same time as this thesis is also presented.

The end of this chapter deals with absolute contactless angular sensors. It focuses on the solutions using a magnetic principle, i.e. a rotating permanent magnet. The state of the art is given with a particular care to demonstrate the limits of each solution. All the solutions we present generate a sine and cosine signals. The methods to extract the angle from these two values are given.

This chapter presents the elements of a complex microsystem. We take a special care to establish the relationships between each component, in order to improve the global system performances [Popovic97].

2.1 Hall sensor: basics characteristics

2.1.1 Hall voltage and sensitivities

The Hall effect, discovered in 1879 by E. H. Hall [Hall79], is a physical effect arising when a magnetic field is applied on a an electrical current flowing in a conductor or a semiconductor. Hall sensors consist of a thin plate of thickness t (Fig. 2.1). The magnetic field B , orthogonal to the sensor plane causes the Hall effect. Two contacts are used to bias the sensor with a current I . Two additional contacts are required to measure the Hall voltage V_H .

The Hall voltage V_H is equal to:

$$V_H = \frac{G}{t} \frac{r_H}{qN} IB \quad (2.1)$$

The Hall voltage depends on parameters which describe the geometry (G and t) and the material (N and r_H) of the sensor. The geometrical factor G represents the efficiency of the sensor geometry. With an optimal geometry, i.e. a very long

rectangular Hall device, the geometrical factor is 1. N is the density of charge carriers. The Hall factor r_H depends on the influence from the scattering and the material anisotropy; it is about 1.2 for a CMOS NWell at room temperature and in a low magnetic field. The elementary charge is q .

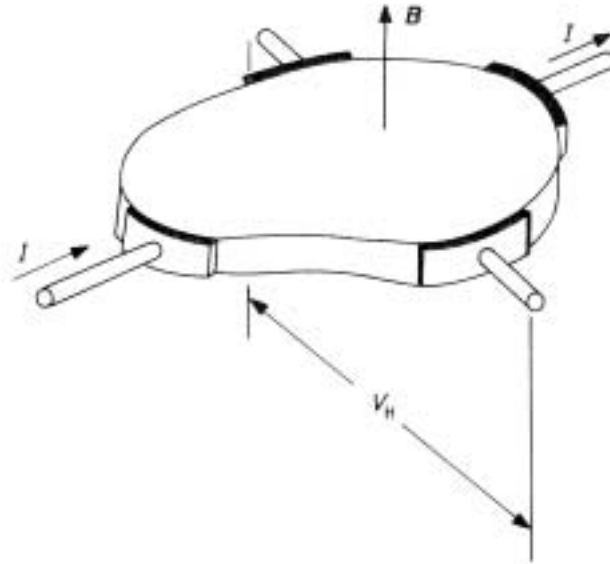


Fig. 2.1 The Hall sensor is a thin conductor or semiconductor with 4 electrical contacts. When a current flows through the plate, a voltage V_H , called the Hall voltage, proportional to the magnetic field B (orthogonal to the sensor) appears (reprinted from [Popovic91]).

The current related sensitivity S_I is defined as:

$$V_H = S_I IB \quad \text{with} \quad S_I = \frac{G}{t} \frac{r_H}{qN} \cong \frac{1}{t} \frac{1}{qN} \quad (2.2)$$

The square resistance R_{\square} , also called the sheet resistivity, which is the resistance of a square surface of the sensor material, is always found in the design parameters of CMOS technologies. R_{\square} is equal to:

$$R_{\square} = \frac{1}{q\mu N t} \quad (2.3)$$

with μ being the mobility. The mobility determines how strongly the motion of a charge carrier is influenced by an electrical field. It depends on the material and

on the doping concentration (Fig. 2.2). Note also that the mobility of the electrons is about triple that of holes.

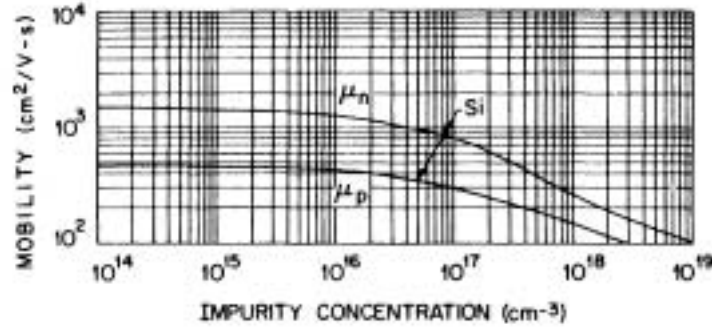


Fig. 2.2 Mobility of silicon per doping concentration at 300°K (reprinted from [Sze85])

The current related sensitivity is, with μ_H the Hall mobility:

$$S_I = G\mu_H R_{\square} \quad \text{with} \quad \mu_H = r_H \mu \quad (2.4)$$

The voltage related sensitivity is defined, with R_{IN} the input resistance of the sensor and N_{\square} its size stated in number of squares, as:

$$V_H = S_V V B \quad \text{with} \quad S_V = \frac{S_I}{R_{IN}} = \mu_H \frac{G}{N_{\square}} \quad (2.5)$$

This equation shows the importance of a high mobility for the efficiency of Hall devices when the biasing voltage is limited.

The sensitivity can also be expressed in terms of the power dissipated inside the sensor. It is useful when the power dissipation, i.e. the temperature increase, is the limit for the biasing. It is called the power related sensitivity S_p :

$$V_H = S_p \sqrt{UI} B \quad \text{with} \quad S_p = \sqrt{S_I S_V} = G\mu_H \sqrt{\frac{R_{\square}}{N_{\square}}} = \frac{G}{\sqrt{t} N_{\square}} r_H \sqrt{\frac{\mu}{qN}} \quad (2.6)$$

The Hall sensor can be modeled by a resistive bridge (Fig. 2.3). The offset, defined as a parasitic voltage in the absence of a magnetic field, comes from a ΔR mismatch of these resistances. Its sources are the tolerances during the processes (mask, etching and alignment), the non-uniformity of the doping and the piezoresistive effect.

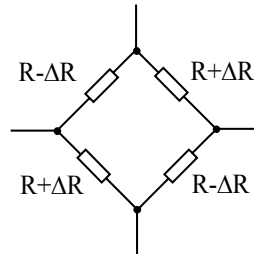


Fig. 2.3 Simplified model of a Hall plate sensor : a 4 resistances bridge (Wheatstone bridge). A mismatch ΔR of the bridge resistances is the origin of the offset.

For the voltage biasing, the offset is:

$$V_{OFF} = \frac{\Delta R}{R} V \quad (2.7)$$

Note that the offset can be compensated by subtracting from the Hall voltage a fraction of the biasing voltage obtained by a voltage divider [Blanch97].

For the current biasing, the offset is:

$$V_{OFF} = \frac{\Delta R}{R} \frac{1}{q\mu N} \frac{N_{\square} I}{t} \quad (2.8)$$

The magnetic offset equivalent B_{OFF} , which is the corresponding magnetic field to the offset voltage, is:

$$B_{OFF} = \frac{V_{OFF}}{S_I I} = \frac{\Delta R}{R} \frac{1}{\mu_H} \frac{1}{G} N_{\square} \quad (2.9)$$

The equivalent magnetic offset is independent of the biasing: the same result is obtained for both the voltage and the current biasing, even if the offset voltage is different. To give a rough estimate, for an NWell sensor ($N=4*10^{16}\text{cm}^{-3}$ and $\mu_H=1200\text{cm}^2/\text{Vs}$) with $N_{\square}=1$, $G=0.8$ and $\Delta R/R=1\%$, the equivalent magnetic offset B_{OFF} is 10mT.

Rectangular sensor

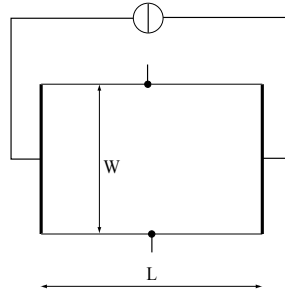


Fig. 2.4 Rectangular Hall sensor with point sense contacts. L and W are respectively the length and the width of the sensor.

The input resistance R_{IN} of a rectangular Hall plate (Fig. 2.4) of a length L and width W is:

$$R_{IN} = \frac{L}{W} R_{\square} \quad (2.10)$$

To reduce R_{IN} and increase the voltage related sensitivity, the ratio L/W should be reduced. For a short rectangular Hall plate ($L/W \ll 1$) with point sense contacts, the geometrical factor G is [Lippman58]:

$$G = 0.742 \frac{L}{W} \left[1 + \frac{\theta_H^2}{6} \left(3.625 - 3.257 \frac{L}{W} \right) \right] \quad (2.11)$$

θ_H is the Hall angle, which is equal to:

$$\theta_H = \tan^{-1}(\mu_H B) \quad (2.12)$$

For a low magnetic field, when $\theta_H \cong 0$, the previous equation is simplified to:

$$G = 0.742 \frac{L}{W} \quad (2.13)$$

From (2.4), (2.10) and (2.13) we calculate that the voltage related sensitivity is:

$$S_V = G \frac{W}{L} \mu_H \cong 0.742 \mu_H \quad (2.14)$$

With a low doping of N-type silicon, with $\mu_H=1700\text{cm}^2/\text{Vs}$, the maximal voltage related sensitivity is 12.6%/T. For a CMOS NWell, with a doping level of $4 \cdot 10^{16}\text{cm}^{-3}$, μ_H is decreased to $1200\text{cm}^2/\text{Vs}$. The voltage related sensitivity is reduced to 8.9%/T.

Cross like Hall sensor

To be compatible with the spinning current techniques (see §2.1.5), the sensor must be invariant with the biasing rotations. A cross (Fig. 2.5) is chosen for the 2- and 4-phases spinning current method because of a good geometrical factor and its immunity to alignment tolerances from the process [Randjel00]. L corresponds to the length of the cross arm and W to the width.

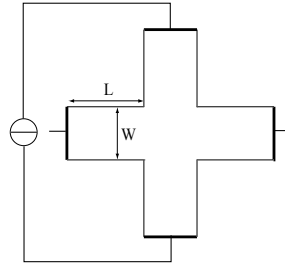


Fig. 2.5 Cross like Hall sensor with L the length of the arms and W the width. Its symmetry allows to permutate the biasing and sensing contacts.

For a cross like Hall sensor, the geometrical factor is, with an accuracy better than 0.5% for $\frac{W}{2L} \leq 0.39$ [Versnel81]:

$$G = 1 - 5.0267 \frac{\theta_H}{\tan(\theta_H)} e^{-\frac{\pi W + 2L}{2W}} \quad (2.15)$$

With a low magnetic field, the following simplified result is preferred:

$$G = 1 - 1.045 e^{-\frac{\pi L}{W}} \quad (2.16)$$

The input resistance of a cross is the sum of the resistances of the central block and the two arms. The central square is reduced to 2/3 of a square because of the two arms for sensing placed in parallel. The number of squares is approximately:

$$N_{\square} \cong 2 \frac{L}{W} + \frac{2}{3} \quad (2.17)$$

From previous results, we can write that the voltage related efficiency is:

$$S_V = \frac{S_I}{R_{\square} N_{\square}} \cong \frac{G}{2 \frac{L}{W} + \frac{2}{3}} r_H \mu \quad (2.18)$$

For the NWell, with a doping level of $4 \cdot 10^{16} \text{cm}^{-3}$ and using the optimal cross geometry ($W/L=2.55$), the voltage related sensitivity is $5.75\%/T$ (Fig. 2.6). It is 35% lower than the sensitivity of a rectangular sensor.

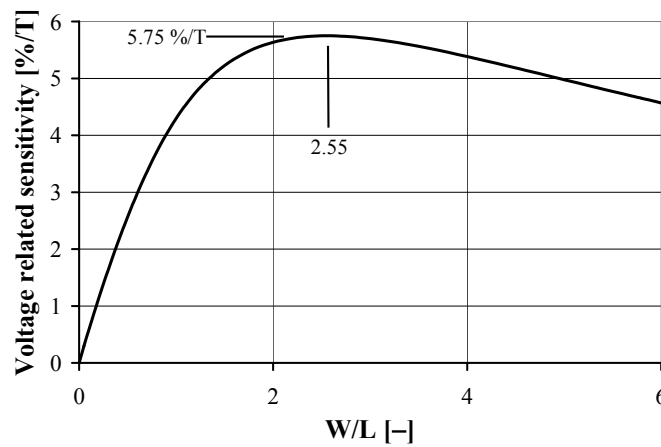


Fig. 2.6 Voltage related efficiency per width over length ratio of the sensor's arms for the NWell with $\mu_H=1200 \text{cm}^2/\text{Vs}$.

2.1.2 Thermal drift

The thermal drift can affect both the sensitivities, the offset and the input resistance of the Hall sensor.

Firstly we analyze the temperature behavior of the current related sensitivity. The temperature coefficient α_{r_H} of the Hall factor r_H (Fig. 2.7) ranges between 0 and $500 \text{ppm}/^\circ\text{C}$ for the $4 \times 10^{16} \text{cm}^{-3}$ NWell [Dragan00] in the industrial temperature range. With a lower doping level, α_{r_H} is almost independent of the concentration of the impurities and the temperature; and is worth approximately $700 \text{ppm}/^\circ\text{C}$ [Dragan00].

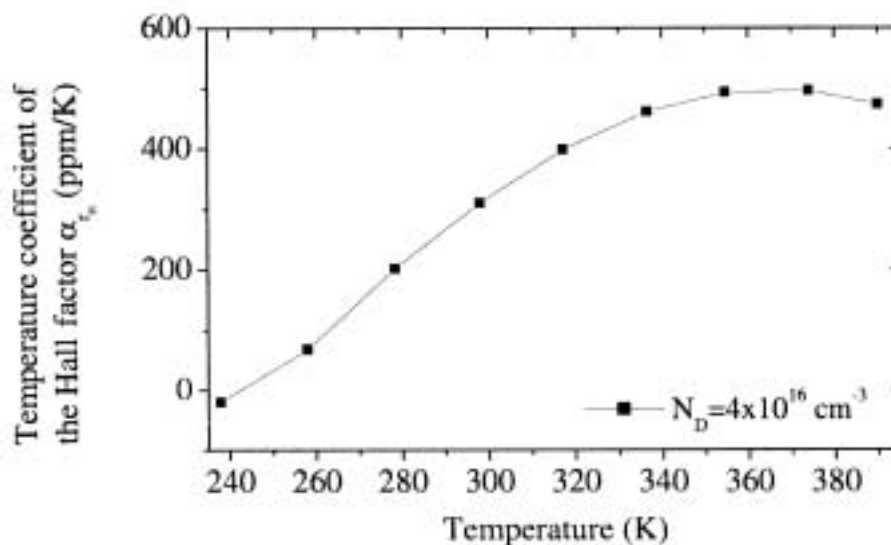


Fig. 2.7 Measured temperature dependency of the Hall factor in silicon for a $4 \times 10^{16} \text{ cm}^{-3}$ NWell (from [Dragan00]).

The electron concentration remains the same over a wide temperature range when all the impurities are ionized (Fig. 2.8). The carrier density N is, in this case, equal to the concentration of impurities; this region is called extrinsic. At low temperatures, some carriers are “frozen” due to the thermal energy being too low for complete ionization. The carrier density N becomes lower than the concentration of impurities: this is called the freeze-out effect. At high temperatures, the intrinsic concentration n_i becomes larger than the concentration of impurities: the carrier density therefore increases.

CMOS microsystems are used in the extrinsic region reaching to the beginning of the freeze-out effect of the N- and P-Well. Electronics do not work properly when the intrinsic region is reached, especially when a lowly doped high resistive polysilicon is used. The electron concentration in n-type silicon varies of about 1% in the temperature range from -40°C to 125°C for donor concentration from 10^{14} to 10^{16} cm^{-3} [Popovic91]. The drift of the NWell electron density ($N=4 \times 10^{16} \text{ cm}^{-3}$) varies from $400 \text{ ppm}/^\circ\text{K}$ at -25°C to $50 \text{ ppm}/^\circ\text{K}$ at 120°C [Manic00].

The thermal expansion of silicon is only $2.6 \text{ ppm}/^\circ\text{K}$. That’s why the geometrical factor G and the sensor width t are considered constant.

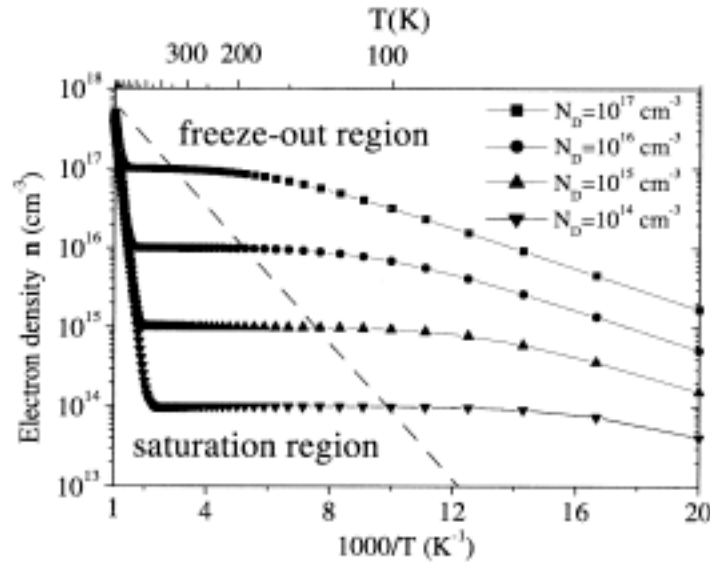


Fig. 2.8 Electron density versus temperature. CMOS Hall sensors, are used at the saturation (extrinsic region) and at the beginning of the freeze-out (reprinted from [Manic00]).

The thermal drift of the current related sensitivity α_{S_I} is (Fig. 2.11):

$$\alpha_{S_I} = \frac{1}{S_I} \frac{dS_I}{dT} = \alpha_{r_H} - \alpha_N \quad (2.19)$$

Due to the combination of the freeze-out effect and the temperature dependency of the Hall factor, the sensitivity drift is in the range of $\pm 500 \text{ ppm}/^\circ\text{K}$ throughout the industrial temperature range. α_{S_I} is zero near the room temperature.

Sources of current, used to bias the sensor, also have their own drift of about $500 \text{ ppm}/^\circ\text{K}$. This drift is added to the drift of the current related efficiency, resulting in a sensitivity drift up to $1\% / ^\circ\text{K}$.

The drift of the voltage related sensitivity α_{S_V} is an order of magnitude larger due to the significant drift of the mobility α_μ (Fig. 2.9):

$$\alpha_{S_V} = \frac{1}{S_V} \frac{dS_V}{dT} = \alpha_{r_H} - \alpha_\mu \cong -1\% / ^\circ\text{K} \quad (2.20)$$

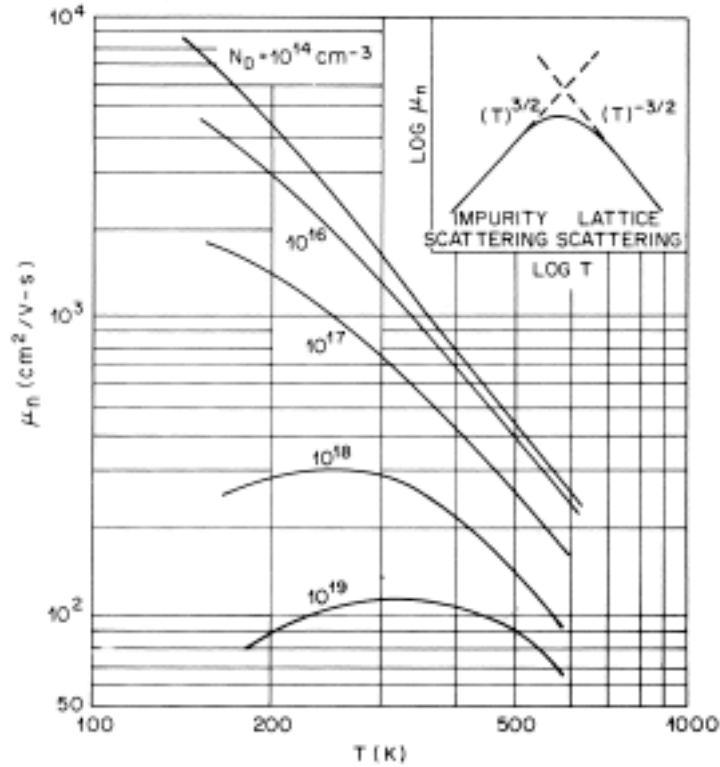


Fig. 2.9 Mobility of N-doped silicon versus temperature (reprinted from [Sze85]). It is about $-1\%/^{\circ}\text{K}$ for low N- doped silicon at 300°K .

The square resistance thermal drift is also greatly from the drift of the mobility:

$$\alpha_{R_{\square}} = \frac{1}{R_{\square}} \frac{dR_{\square}}{dT} = -\alpha_N - \alpha_{\mu} \cong 1\%/^{\circ}\text{K} \quad (2.21)$$

From Equ. (2.9), the thermal coefficient of the magnetic equivalent offset is $1\%/^{\circ}\text{K}$ at 300°K (Fig. 2.9) for both voltage and current biasing, if the relative resistances mismatch $\Delta R/R$ is a constant. The offset voltage stays constant for constant voltage biasing. For current biasing, its drift is about $1\%/^{\circ}\text{K}$ at 300°K .

2.1.3 Piezo-resistance and piezo-Hall Effects

A packaged sensor is a complex combination of different materials. The different thermal expansion coefficients induce thermo-mechanical stresses. Because of the conjunction of stresses and piezo effects, fluctuations of the sensor behavior appear (Fig. 2.10). Plastic and viscoelastic deformations induce a drift and, more importantly, a long term drift. This drift is unpredictable and depends on the history of the microsystem. Consequently the main source of instabilities is the packaging, especially in the case of low cost plastic encapsulation.

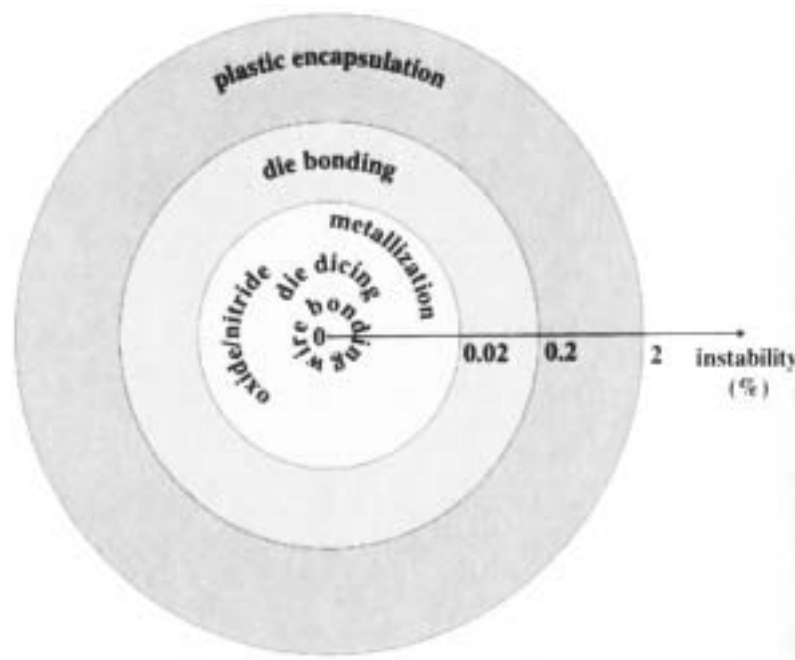


Fig. 2.10 Instabilities due to stresses (piezo-Hall and piezo-resistance) for various sources from the IC processing and packaging (reprinted from [Manic00]). Low-cost plastic encapsulation is the main source of instabilities.

Two physical stress-related effects deteriorate the Hall sensor performances: the piezo-resistance effect which modifies the material resistivity and the piezo-Hall effects which is related to variations in sensitivity.

The piezo-resistance effects provoke relative variations $\Delta R/R$ of the bridge resistances (Fig. 2.3). This unbalances the sensor resulting in an offset as demonstrated in Equ. (2.9). Using the spinning current technique (§2.1.5), the combination of stresses, piezo-resistance and junction field effects (§4.5.2) are also a source of residual offset (§4.4), even if the offset from piezo-resistance effect is cancelled.

The variation of the current related sensitivity due to stresses is called the piezo-Hall effect. The origin of this effect is similar to that of a piezo-resistance. The dominant stress components are the normal stresses σ_{XX} and σ_{YY} in the plane parallel to the chip surface [Manic01]. The relative variation of the current related sensitivity is:

$$\frac{\Delta S_I}{S_I} = P_{12}(\sigma_{XX} + \sigma_{YY}) \quad (2.22)$$

P_{12} is one of the piezo-Hall coefficients estimated at $40 \times 10^{-11} \text{Pa}^{-1}$ for the NWell ($4 \times 10^{16} \text{cm}^{-3}$).

The piezo-Hall effects drastically modify the behavior of the encapsulated sensors (Fig. 2.11), especially when low-cost plastic packaging is used. Thermo-mechanical stresses are non-deterministic and depend on the sensor history. Calibration is unfortunately poorly efficient at correcting this type of drifts. What's more sensitivity variations of up to 2% are measured with thermal shocks [Manic00].

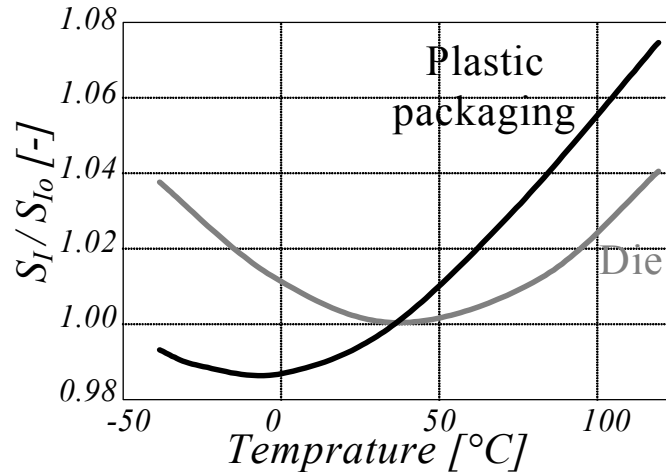


Fig. 2.11 Thermal drift of the current related sensitivity of an NWell sensor for a die and inside a plastic package. The combinations of piezo-hall effect and thermo-mechanical stresses substantially modify the sensor behavior (from [Manic00]).

2.1.4 Reduction of the offset from electronics

The signal from the sensor has to be amplified. Unfortunately, CMOS amplifiers suffer from offset and $1/f$ noise. For instance, the offset of a CMOS operational amplifier is as great as 2mV. With a Hall sensor with $S_I=80\text{V/AT}$ and $I=1\text{mA}$, the magnetic equivalent offset is 25mT. It is several orders of magnitude larger than the intrinsic sensor offset after the spinning current techniques (see §2.1.5).

The techniques, used to reduce the offset and $1/f$ noise from the electronics, can be divided in three groups: chopper, auto-zero techniques and correlated double sampling.

Chopper Technique

The basic principle of the chopper technique is to modulate the signal before the offset and $1/f$ noise source and to then demodulate it after amplification. We call residual offset the offset which appears after the demodulation.

The origin of this offset is no more the initial offsets of the amplifiers, which are modulated at the chopping frequency. Spikes during commutations are the main source of residual offset [Enz87]. To achieve a low, 500nV residual offset, a low frequency modulation is required in order to limit the effect of the transients [Menolfi99]. The decrease in the switching frequency is limited by the double of the $1/f$ corner frequency.

A technique to further reduce the switching frequency is to use the Nested-chopper technique (Fig. 2.12). The first modulation removes the $1/f$ noise, while the second modulation removes the residual offset due to the spikes. A 100nV residual offset is obtained by [Bakker00] using an ultra low 16 Hz chopping frequency in order to reduce the residual offset from spikes. The cost of this principle is a smaller clock frequency ($V_{CHOPLOW}$), thus reducing the microsystem bandwidth.

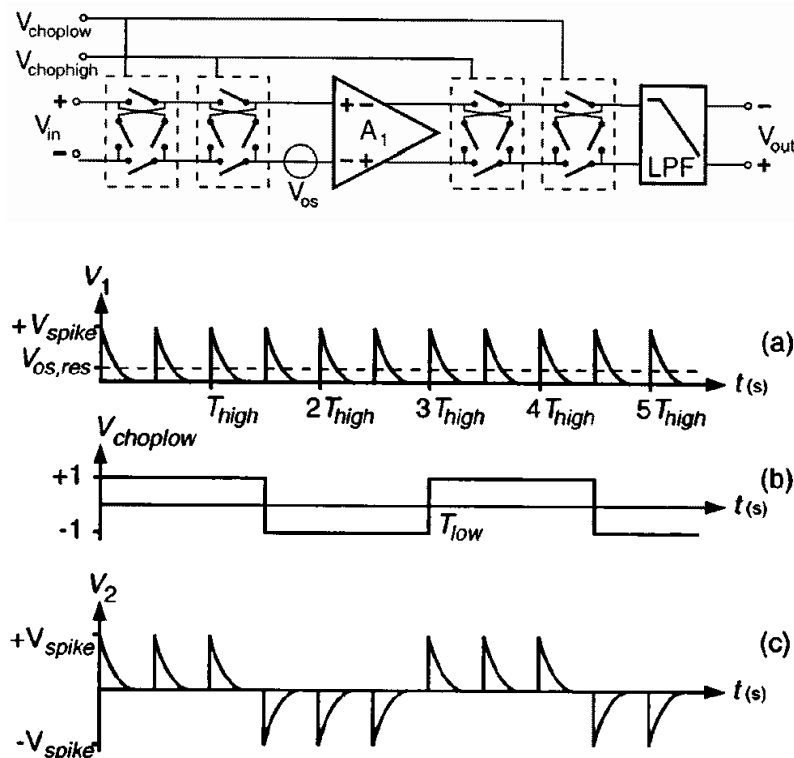


Fig. 2.12 The Nested chopper amplifier, with two fit into each other choppers, substantially reduces the residual offset from spikes (reprinted from [Bakker00]).

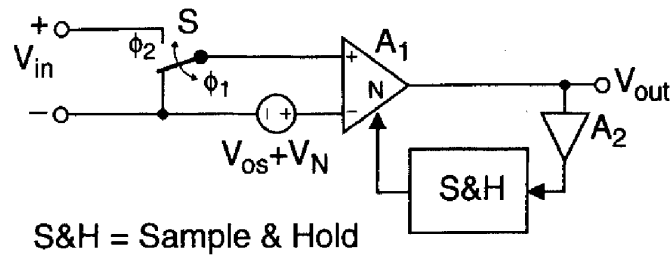
The limitation of this technique is the low pass filtering required for attenuating the residual square wave ripple created by the initial offset: it requires a large silicon surface and reduces ones more the bandwidth. As this system is placed after the demodulation, its own offset is a residual offset. One way to avoid these problems is to use a Track-and-Hold demodulator [Bilotti99], but this causes also a residual offset due to the charge injection inside the switch capacitors circuits.

Auto-zeroing and correlated double sampling

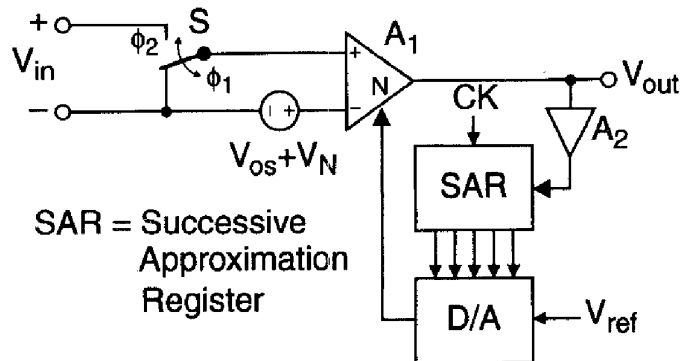
Auto-zeroing (AZ) is also used to reduce the electronics offset. This technique is composed by two phases: calibration and evaluation. During calibration, the input of the electronics is short circuited to measure its offset. The offset is stored in a capacitor with a sample and hold or a digital register (Fig. 2.13). During the evaluation, the memorized offset is subtracted from the signal. Auto-zeroing is incompatible with continuous-time applications, because the output is not valid during the auto-zeroing phase. The time sharing (ping-pong) technique can be used to obtain a continuous time operation [Randjel00]: the front-end of the electronics is duplicated – one part operates when the other is under calibration. When the offset is sampled, the white noise is increased substantially due to undersampling.

The correlated double sampling (CDS) technique can be defined as an auto-zeroing operation followed by a sample and hold. It is widely used in sampled-data systems. The effect of CDS on the amplifier offset and noise is very similar to that of AZ.

These techniques suppress the offset from electronics, but they are unfortunately unable to suppress the intrinsic sensor offset. The next section presents a chopping method which includes the sensor. This technique is called the spinning current method.



(a)



(b)

Fig. 2.13 Principle of auto-zero amplifiers, with (a) analog and (b) digital holding of the offset (reprinted from [Enz96]).

2.1.5 Spinning Current

A major drawback of Hall sensors is their high offset voltage of several tenths of militesla. Ideally, to suppress this sensor offset, the magnetic field has to be chopped. An implementation is presented in [Chiesi97] with a saturable magnetic shield. Unfortunately, this principle is not applicable with CMOS technology. Note that the principle of chopping is also used for fluxgate sensors [Chiesi99].

The spinning current is an active implementation of the orthogonal coupling [Maupin80] of Hall sensors (Fig. 2.14). The output and supply terminals of each Hall cell are periodically interchanged so that the Hall voltage polarity is changed in each state, while the offset voltage appears as a DC at the output terminal [Munter90]. A demodulator is consequently necessary to extract the Hall voltage after amplification. Note that it is also possible to modulate the offset, while the Hall voltage stays constant. Using this principle, the low frequency noise and the offset of the preamplifier are summed with the Hall voltage; thus the Hall signal. However the $1/f$ noise and the offset of the sensor are replaced by those of the preamplifier.

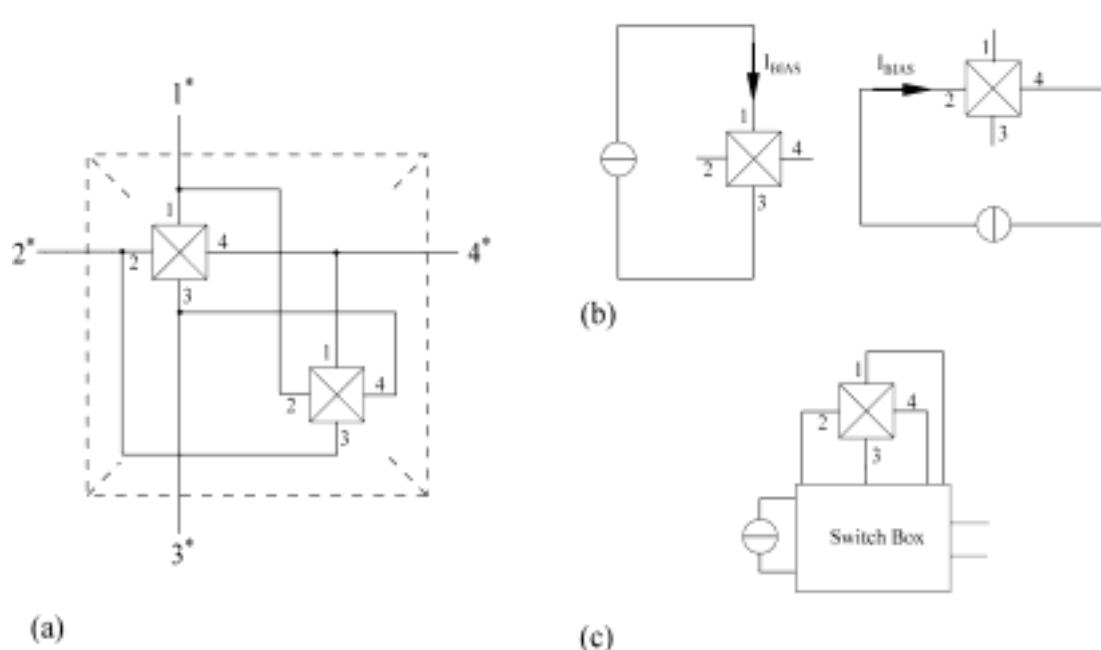


Fig. 2.14 (a) Orthogonal coupling of two Hall sensors. (b) The biasing and sensing are permuted using the symmetry of the Hall sensor. (c) The spinning current method: the biasing and sensing contacts are switched periodically in order to modulate either the Hall voltage or the offset.

The modulation is no longer obtained before, but within the sensor. However the main part of the offset and $1/f$ noise is suppressed. Compared to the orthogonal coupling, the spinning current has the advantage of guaranteeing the matching of the parameters such as stress, because the same sensor is used for all the phases. In other words, the sensors used with orthogonal coupling are not completely identical, resulting in an offset related to the mismatch of their parameters.

We called 2-phases (twofold orthogonal switching), 4-phases (fourfold orthogonal switching) and 8-phases spinning current depending on the number of directions of biasing. A simple 2-phases spinning current, where the current flows in two orthogonal directions, suppresses the linear offset component in the current I biasing from the stresses and junction field effect [Ruther02a]. The piezoresistive effect due to mechanical stress is suppressed. 4-phases spinning current, also called orthogonal switching, suppresses also the quadratic terms of the residual offset in biasing [Ruther02a]. The thermoelectric offset from fixed bias current, such as power dissipation inside electronics, is also completely compensated [Ruther02b]. A few $100\mu\text{T}$ residual offset is obtained. Both the junction field effect and piezoresistive effect are greatly suppressed. The residual offset can be reduced further by increasing the number of biasing

directions. A specific 8 contacts Hall sensor is required for the 8-phases spinning current method (Fig. 2.15). The residual offset is as low as $5\mu\text{T}$ [Bakker99].

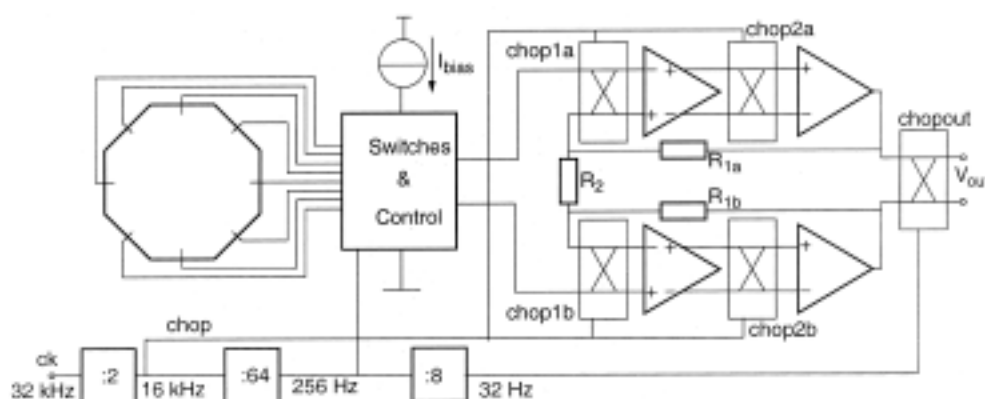


Fig. 2.15 Combination of 8 phases spinning current and nested chopper amplifier. The residual offset is as low as $5\mu\text{T}$ (reprinted from [Bakker99]).

An array of four 4-contacts sensors [Hohe99], with two sensors aligned with the wafer edge and two at an angle of 45° in order to artificially generate the 8 phases (Fig. 2.16), reaches $15\mu\text{T}$.

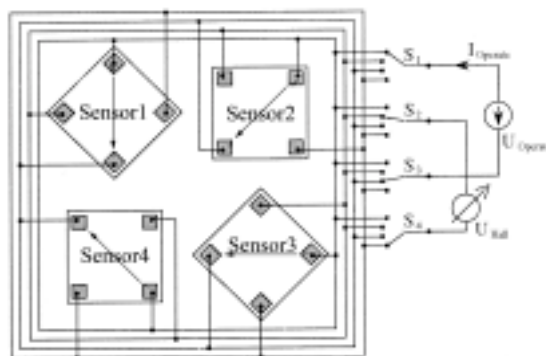


Fig. 2.16 Sensor array with current orientation at 45° to artificially create the 8-phases spinning current (reprinted from [Hohe99]).

The biasing continuously rotates inside the sensor using the continuous spinning current and a 4-contacts Hall sensor [Steiner98b]. To do that, the two axes are simultaneously biased with a sine and a cosine. The residual offset is inferior to $10\mu\text{T}$.

2.2 Calibration of Hall sensors

The Hall devices response is very linear up to 1T [Schott99]. Its response is defined by the slope (sensitivity), the offset and their respective drifts. For a calibration at one temperature, two measurements, at different magnetic fields, are necessary for the calibration of the sensitivity and the offset. The sensitivity can also be determined using variations of the calibration field to measure the slope, while the offset is for instance measured by shielding the sensor from the external field.

The calibration coefficients to compensate the microsystem are often digitally programmed on the chip [MLX90215] (Fig. 2.17) using a ROM (PROM) and extracted through binary-weighted capacitors [Malco99], current sources or resistors. On-chip zener-zapping circuits are often used as PROM to store the calibration words.

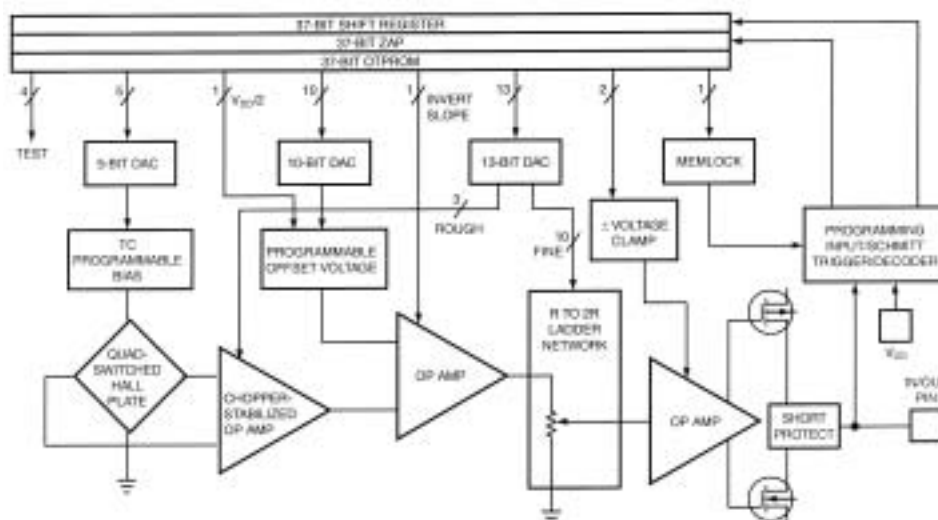


Fig. 2.17 CMOS processing provides calibration and programmability of the MLX90215 Hall sensor from Melexis® (reprinted from [Travis98]).

Unfortunately this technique is unable to compensate totally the drift from non deterministic sources, such as encapsulation stresses (§2.1.3). One way to cope with this limitation is to perform a self-calibration by adding a coil to generate a magnetic reference signal in order to measure the microsystem sensitivity. For a flat circular coil, the reference magnetic field is proportional to the current over the diameter ratio. In the case of silicon, which is the substrate of CMOS chips, its thermal expansion is only 3ppm/°C, more than 100 times smaller than the sensitivity drift of Hall sensors. Moreover if the gauge factors, i.e. the influence of relative deformations, are compared, we also found that coils are more than

100 times more robust to deformation and especially deformation induced by stresses.

Unfortunately, it is not possible to determine the offset with a calibration coil, given that it is not possible to distinguish between the offset and an external signal. Therefore the offset has to be reduced as much as possible using for instance the spinning current technique.

Note that this coil can also be used for the microsystem self-test or for production purposes [Trontelj01].

Integrated coils

The idea of auto-calibrating Hall sensors sensitivity using an on-chip integrated coil (Fig. 2.18) was first published in 1996 [Simon96]. The combination of an integrated coil and a magnetic sensor was patented in 1994 [Trontelj94]. The coil is drawn directly with the metallic layer of the process, without additional post-processing steps. Two principles to measure the sensitivity are proposed. The first one measures the output of the sensor with two calibration fields, i.e. to bias the currents. The sensitivity is calculated from these two values. The second one is to modulate the calibration current of the coil. The sensitivity is calculated using a synchronous detection. In both cases, the output of the system is adjusted according to the measured sensitivity. A thermal drift of less than 100ppm/°C is obtained [Simon96]; this produces an improvement factor greater than 18. However the proposed principle uses a driftless current source, which is not integrated.

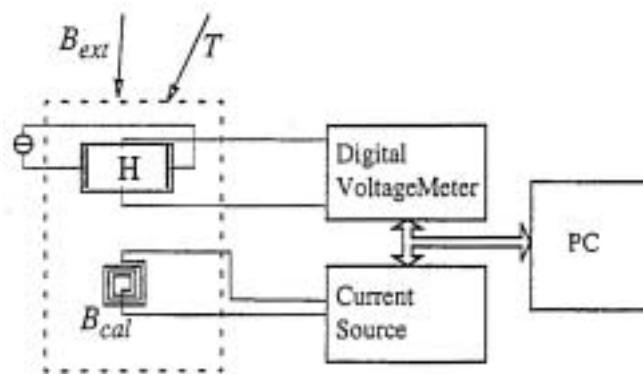


Fig. 2.18 First experimental set-up for self-calibration using an on-chip integrated coil (reprinted from [Simon96]).

The size of the Hall sensor used for the previous result is $100 \times 200 \mu\text{m}^2$ [Simon96]. The efficiency of the coil, i.e. the magnetic field over the current ratio, of 30mT/A is poor due to its large internal diameter; a magnetic field of up to 0.3mT is obtained without heating up the device [Bellekom95]. Recently the

efficiency of the coil has been increased by a factor of 5 using a miniaturized Hall sensor and a coil with only 3 turns [Trontelj99]. Miniaturization of the coil and consequently the sensor is an elegant way, used in the §3, to drastically increase the coil performances.

A circuit to compensate the magnetic field sensor without calculating the Hall voltage has been patented [Petr88] (Fig. 2.19). A coil generates a modulated reference magnetic field. The sensitivity is extracted with a correlator, such as a synchronous detector. This sensitivity is subtracted from a reference voltage, i.e. a reference sensitivity, thus generating an error voltage used as the input of a regulator. Because of its proportionality with the Hall signal, the output of the regulator is connected to the sensor biasing for the feedback loop. The output of the Hall sensor after amplification is the system output.

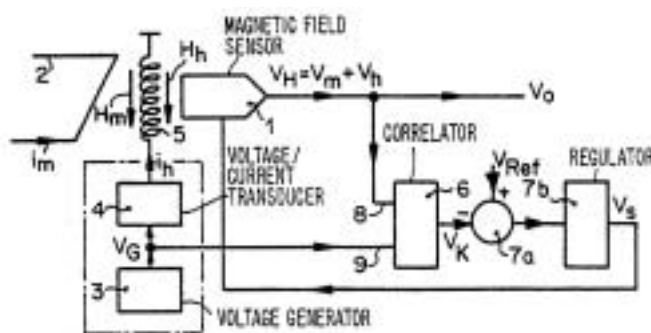


Fig. 2.19 Self-calibration without any correction of the magnetic field sensor output. The feedback of a regulator is directly connected to the sensor biasing (reprinted from [Petr88]).

The coil can also be used as a magnetic feedback [Barjen95]. The field of the coil is subtracted from the unknown external field in order to maintain the sensor output field at zero. The output of the system with the feedback is proportional to the current through the coil. The full scale of the system is limited by the maximum field generated by the coil.

To generate the calibration field, the coil is connected to a reference current source. The drift of the magnetic field is proportional to the drift of this source. Using CMOS electronics, the accuracy of this reference is limited to about 500ppm/°C; this being much larger than the drift of less than 100ppm/°C presented above. It is almost impossible to obtain a current source with such ultra-low drifts. The company Schneider Electric Industry took out a patent [Hazard99] on removing the influence of electronic references. Their invention consists in a digital sensitivity-meter. The same voltage is used as a reference for the digital to analog converter and for current source of the calibration coil.

Their system gives the sensor's sensitivity digitally to calibrate the system using a digital compensation of the magnetic. The drawback of the proposed method is that the system needs an ultra low drift resistor which cannot be integrated using standard CMOS technologies.

Coils are also co-integrated with several types of magneto-resistive (MR) sensors (Fig. 2.20). They are used to calibrate the sensor, for a feedback configuration or to compensate the parasitic magnetic "offset" fields from magnetized materials. The ratio of the magnetic field over the current is 10mT/A ; allowing a magnetic field of $10\mu\text{T}$ with a current of 1mA . Note that the higher detectivity of MR sensors makes the calibration easier with integrated coils compared to that with Hall sensors. An integrated coil is used for the pre-magnetization of some MR sensors (see §2.4.5). A $2\mu\text{s}$ magnetic pulse is generated by a current of several amps. A field higher than $50\mu\text{T}$ is produced at the chip's surface [Honeywella]; a ratio of magnetic field over current of about 20mT/A is poor.

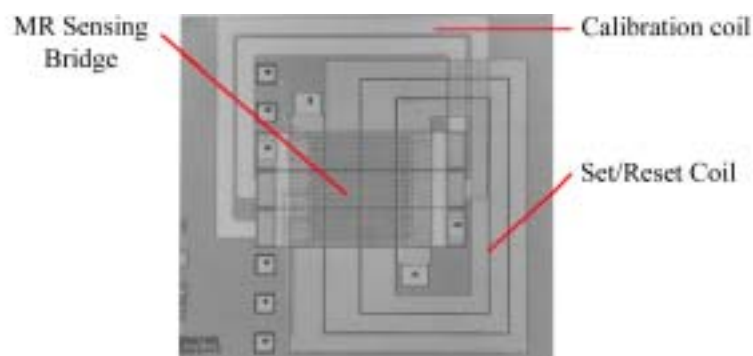


Fig. 2.20 Honeywell[®] Magneto-resistive sensor including a calibration coil and a set/reset coil for flipping (from [Honeywellb]).

Note that integrated coils are proposed, so as to generate pulsed magnetic fields of several Tesla [Mackay00]. The magnetostatic energy stored in a coil is proportional to its volume. Due to the small diameter of integrated coils, the energy is drastically reduced. The coil, composed of a single loop, produces a field of 50T , with a current of 3500A .

2.3 CMOS vertical Hall sensors

A specific technology for vertical Hall sensors exists [Popovic84]. Unfortunately this technology is not CMOS compatible; the co-integration with electronics is impossible. This is the reason why vertical Hall sensors compatible with CMOS

electronics are developed by many companies and research groups. It was proposed to isolate the sensor with a sophisticated pre-processing of deep trench-etching [Steiner98a] or a post-processing [Paranjape92].

Isolating the sensor with the standard NWell of CMOS process limits the current distribution to the surface because of the small depth of the well ($4\mu\text{m}$ for AMS0.8 μm CXQ). This increases the offset and reduces the current related sensitivity. We recently developed vertical Hall sensors using the deep DNTUB diffusion of high-voltage CMOS technologies [Schurig02], because of the larger $7\mu\text{m}$ depth of this well. These sensors are used in the chapter 6 for angular measurements.

This sensor is compatible with integrated coil for calibration. A specific coil design is required to produce a field collinear with the sensitivity direction, i.e. parallel to the chip surface. Note that CMOS vertical Hall sensors are intrinsically miniaturized because of the limited junction depth of the CMOS process, resulting in efficient calibration coils.

2.3.1 4-Contacts DNTUB vertical Hall sensors

To be compatible with the spinning current techniques, a sensor with 4 contacts (Fig. 2.16) is developed to obtain a higher symmetry. Because of the limited junction depth of the 4-contacts sensors, their resistive bridges are not balanced as shown on the next figure; this results initially in a high offset of several Tesla (!), which is one order of magnitude larger than the magnetic field we use for the angular sensor. Even if this high initial offset (asymmetry) is theoretically suppressed by the spinning current method (0), it degrades its efficiency.

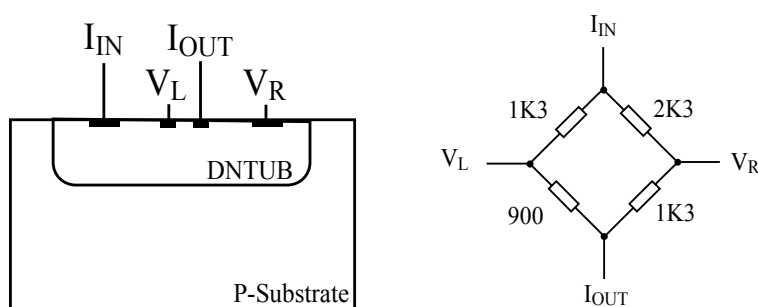


Fig. 2.21 Cross-section of the DNTUB 4-contacts vertical Hall sensors and its equivalent resistance bridge. A large offset of several Tesla is induced by the limited junction depth.

What's more the initial offset limits the gain of the first stage preamplifier, because of its saturation. Furthermore variations of the common mode, when the biasing direction is changed using the spinning current method, generates a

parasitic signal because of the limited common mode rejection of amplifiers. This parasitic signal is seen as a residual offset, i.e. a modulated signal at the output of the preamplifier.

2.3.2 Coupling of 4-Contacts DNTUB vertical Hall sensors

We propose the orthogonal coupling of two 4-contacts vertical Hall sensors [Schurig02] to suppress the correlated offset (Fig. 2.22). The equivalent sensor is balanced, even if the common mode is not at the same voltage during biasing and if the measurement contacts are switched, i.e. using the spinning current method (see §2.1.4). However, an asymmetry is still observed because of the junction field effect. This asymmetry is a source of residual offset.

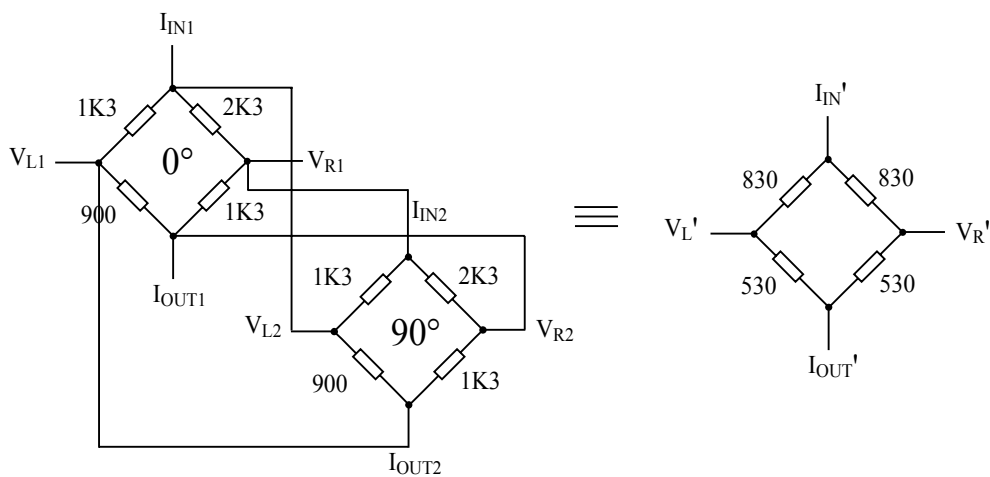


Fig. 2.22 Orthogonal coupling of 4-contacts sensor is used to cancel the unbalancing of the sensor. Note that a common mode variation is still present.

2.3.3 6-Contacts DNTUB vertical Hall sensors

Another way to reduce the sensor asymmetry is to add two lateral contacts (Fig. 2.23) which are short-circuited to reduce the resistance between external contacts [Schurig02]. This reduces the resistance between the outer contacts I_{IN} and V_R in order to balance the bridge.

Note that a couple of 6-contacts vertical Hall sensors is an efficient way to obtain a low initial offset.

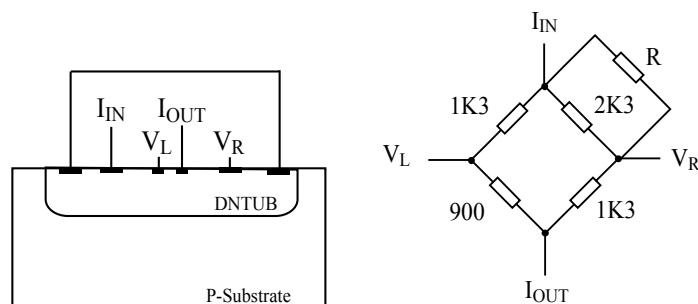


Fig. 2.23 6-Contacts vertical Hall sensors and its equivalent resistor bridge. The two short-circuited contacts are equivalent to an added resistor in parallel with the larger resistance between I_{IN} and V_R .

2.4 Absolute contactless angular sensors

Nowadays, resistive potentiometers, with a high accuracy, a low-cost and sometimes multi-turns, are the most used absolute angular sensor. They have a limited lifetime because of wear. For instance, small displacements around the same position, called dither, locally degrade quickly the resistive material. They also suffer from noise due to contact fluctuations during movements. Contactless sensors do not suffer from wear and have a long lifetime. However contactless sensors are more complex and their accuracy is often poor.

Contactless angular sensors are based on capacitive, inductive, optical and magnetic principles. Magnetic sensors are often preferred because of their robustness, insensitivity to dirt and the low price. We now concentrate on magnetic contactless sensors with an absolute 360° measurement.

Magnetic angular sensors are based on the principle of a rotating permanent magnet. They are well adapted for harsh environments. They are also of small size, low cost and accurate. Most absolute magnetic angular sensors have sine and cosine outputs. The angle is extracted using the arctangent function without dead angles over 360° . The measured angle depends on the ratio of the two signals. Consequently it is insensitive to the sensitivity drift. We present below the main principles.

2.4.1 Hall sensors at the magnet periphery

Four Hall plates are placed on the periphery of the permanent magnet, two for each orthogonal direction (Fig. 2.24). They measure the vertical component of the magnetic field. This sensor has the advantage of the compatibility with CMOS technologies, because of standard Hall plates.

The alignment tolerances robustness of this sensor is poor. With accurate positioning (100 μ m misalignment for the sensor and the magnet and a 1.5° tilt), the accuracy is only 1% with a \varnothing 1.7mm permanent magnet [Metz97].

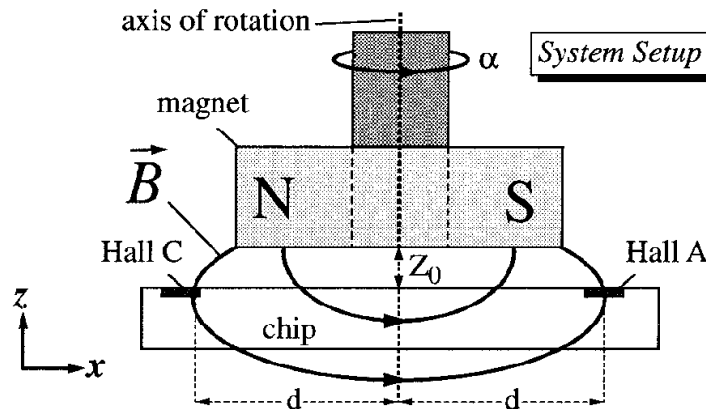


Fig. 2.24 Cross-section of the angular sensor. The chip measures the vertical magnetic field produced by a rotating permanent magnet. The sensor is based on standard Hall plates, compatible with CMOS technologies (reprinted from [Metz97]).

The same principle can be extended for an array of Hall plates placed around a circle [Trontelj01]. The outputs of the sensors are connected to two adders, to obtain the sine (2.23) and the cosine (2.24) of the rotation angle α :

$$\sin(\alpha) = \sum_{i=1}^n Sa_i + \sum_{i=1}^n Sb_i - \sum_{i=1}^n Sc_i - \sum_{i=1}^n Sd_i \quad (2.23)$$

$$\cos(\alpha) = -\sum_{i=1}^n Sa_i + \sum_{i=1}^n Sb_i + \sum_{i=1}^n Sc_i - \sum_{i=1}^n Sd_i \quad (2.24)$$

Using this principle, an angular sensor of the company TWK [RXW22] can obtain an excellent accuracy of $\pm 0.7^\circ$ (2‰) and one from Austria Microsystems [AS5020E] has a resolution of 6 bits (5.6°).

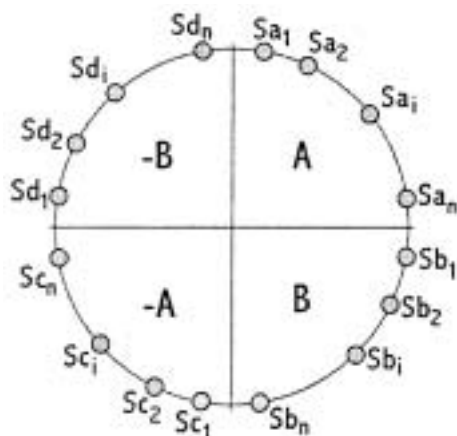


Fig. 2.25 Array of Hall plates positioned around a circle, the center of which is the axis of the rotating magnet (reprinted from [Trontelj01]).

2.4.2 2-D Vertical Hall sensor

Vertical Hall sensors measure the magnetic field parallel to the chip's surface. The orthogonal combination of two sensors with a common central contact [Burger01] measures the two components of the magnetic field in the sensor plane (Fig. 2.26). The drawbacks of this sensing element are the incompatibility with CMOS technology and the obligation to use a specific technology. Therefore the co-integration with a spinning current electronics is impossible. What's more this sensor is incompatible with the spinning current method in order to automatically compensate the offset.

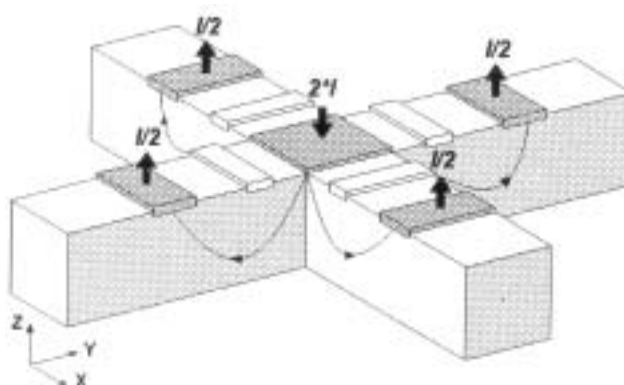


Fig. 2.26 2-Dimensionnall vertical Hall sensor with a central common electrode (reprinted from [Burger01]).

A product based on this sensor is now commercialized by the company Novotechnik [VertX]. It reaches an accuracy of $\pm 0.35^\circ$ (1‰) with a temperature coefficient of less than 50ppm/°C. To reach this high accuracy, only the device offset is calibrated during the production using a digital memory for the storing.

A new sensor, similar to this one, based on two CMOS vertical Hall sensors (§2.3) and a spinning current electronics are studied in detail in the chapter 6.

2.4.3 Magnetotransistors

Double-collector lateral pnp magnetotransistors are sensitive to the magnetic field parallel to the chip surface. The orthogonal combination of two of them, like a cross, measures the 2 components of the planar magnetic field (Fig. 2.27). The original offset can reach as high as 200mT; it is more than two orders of magnitude larger than the Hall plates offset with spinning current electronics. After its calibration, the angular non-linearity is below 0.3% (1°), because of gain-mismatch between axes, as shown in §6.

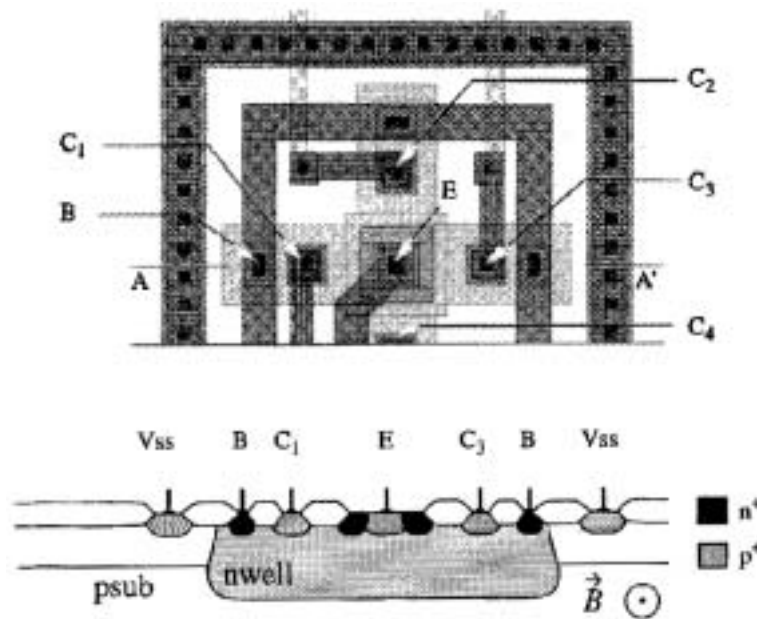


Fig. 2.27 Combination of two double-collector lateral pnp Magnetotransistors to measure the components of the in plane magnetic field (reprinted from [Häberli96]).

2.4.4 Integrated Magneto Concentrators Disk

Integrated Magneto Concentrators (IMC) are made of soft amorphous ferromagnetic metals with a high permeability (more than 10^4), a low coercive field (less than 1mA/cm) and a saturation field greater than 0.5T. They are used as a passive magnetic amplifier because they “suck up” the magnetic field [Blanch00] [Drljaca02]. IMCs also convert an external magnetic field parallel with the chip’s surface into a field perpendicular to the surface [Randjel02]. This field is measured by a conventional Hall plate.

Recently, an angular sensor consisting of a ferromagnetic disk and Hall plates placed at its periphery (Fig. 2.28) was invented [Popovic01]. To obtain a sine and a cosine output, it is composed of 4 sensors placed at right angles. Two of them are placed at the opposite sides of the ferromagnetic disk to obtain a push-pull measurement and to cancel an homogeneous external field.

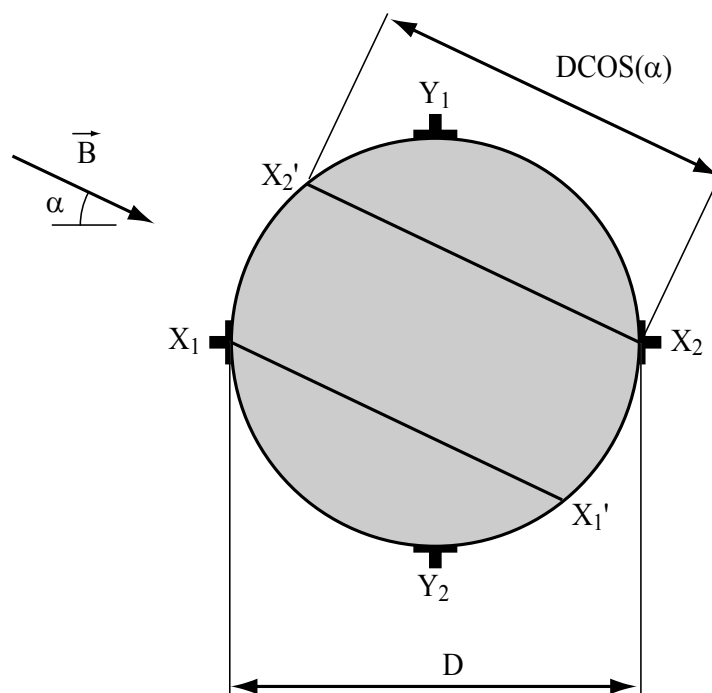


Fig. 2.28 With an angle α between the magnetic field and the sensor, the effective length of the concentrator D is reduced to an effective length of $D \cdot \text{COS}(\alpha)$. Consequently the Hall voltages are proportional with $\text{COS}(\alpha)$ and $\text{SIN}(\alpha)$ on the X- and Y- axes (adapted from [Popovic01]).

The integrated magneto concentrator disk amplifies the magnetic field, depending on its diameter. The range of the magnetic field is limited by the saturation of the disk which introduces non-linearities. Consequently, this sensor

is more adapted to a low magnetic field. Its accuracy is studied in detail in the chapter 6.

2.4.5 Magnetoresistive sensors

William Thompson first observed the magnetoresistive effect in ferromagnetic materials in 1856. In an anisotropic magnetoresistive (AMR) sensor, the resistance of a thin nickel-iron film is modified by the magnetization direction in the sensor plane; the resistance changes by 2-3%. AMR sensors can be bulk manufactured on silicon wafer.

With R_{\parallel} the resistance when the current is parallel to the magnetization and R_{\perp} when it is orthogonal. The angular response of a magnetoresistance is:

$$R(\theta) = R_{\parallel} - (R_{\parallel} - R_{\perp}) \sin^2 \theta = \frac{1}{2}(R_{\parallel} + R_{\perp}) - \frac{1}{2}(R_{\parallel} - R_{\perp}) \cos(2\theta) \quad (2.25)$$

with θ the angle between the current and the magnetization.

With high level magnetic fields (>50mT), the internal magnetization vector directly follows the external magnetic field vector [KMZ41]. In much lower fields, such as the earth magnetic field, the pre-magnetization H_0 is taken away from the equilibrium position with the external field perpendicular to H_0 . When the field is removed, the magnetization comes back to the pre-magnetized privileged direction, because of the shape anisotropy of the sensor [KMZ52].

The quadratic response determines the period of the angular measurement of 180° . Some tricks, such as barber pole [KMZ52] or pre-magnetization with a permanent magnet, permit a linearization of the response of the AMR sensor. Therefore a 360° measurement becomes conceivable. Also, additional “polarity” detectors, such as low cost Hall sensors, are used to detect the quadrant in order to remove the 180° ambiguity [Honeywell]. A small auxiliary field, generated by planar coils, is also proposed by the company Bosch (AMR360) to get rid of the ambiguity about the angle [Tretler01].

Typically, 4 MR sensors are connected in a Wheatstone bridge. They suffer from offset, like Hall sensors, but the higher sensitivity reduces the residual magnetic equivalent offset to $200\mu\text{T}$ for a low magnetic field sensor [Honeywellc]. The flipping technique [Platil02] is used to modulate the magnetic the signal, in the same manner as that of the spinning current technique (§2.1.5). The principle is to rotate the magnetization with an integrated coil in order to change the sign of the MR signal without modifying the offset. The residual offset is reduced to less than $1\mu\text{T}$. Current pulses of several amps are required. This is incompatible with many applications, like measuring a field higher than $40\mu\text{T}$ [Honeywella].

MR sensors are also usable working in a state of saturation [KMZ41], when the external field is high enough to rotate the magnetization. This is the case for contactless potentiometer working with a rotating magnetic field of about 100mT. The angular offset is, in this case, less than 1° , independently of the magnetic field amplitude. Note that the flipping is not utilizable in this case. The offset calibration is not easy, because it is only possible using a rotating external magnetic field, due to the saturation of the ferromagnetic material.

Giant magneto-resistive sensors are composed of a sandwich of ferromagnetic and non-magnetic layers thinner than the free path of electrons in the material (10nm) [Lenssen00]. The changes in resistance, more than one order of magnitude larger than AMR, are as high as 70%. The anisotropy in the magnetic field measurement (directivity) uses the demagnetizing property of narrow stripes: a magnetic field applied perpendicular to the stripe is cancelled by the demagnetizing field. Stability and hysteresis are now the weak spots of GMR. Nevertheless GMR angular sensors are under development for automotive applications. The expected advantages are a larger working distance, 360° measurements and economic system solutions due to the higher signal output [Treatler01].

More recently Colossal magnetoresistance (CMR) materials have been studied. The resistance change is as high as 10^3 to $10^8\%$. These CMR sensors are still a long way from commercial applications [Caruso98].

2.4.6 Angle extraction

The calculation of the arctangent of this signal's ratio is required from the sine and the cosine. This trigonometric calculation can, for instance, be made digitally using the so-called CORDIC algorithm [Volder59] on a microcontroller [Vern97] or an ASIC [UZZ9001]. This iterative algorithm, invented in 1959 by J.E. Volter, replaces multiplications or complex functions by additions and shifts in registers, i.e. multiplication by 2^N , with N an integer. The CORDIC algorithm allows the implementation of the angular sensor self-test, because it also calculates the amplitude of the magnetic field [Dietmayer00]. An ADC is required to convert the analog signals of the sensor to the digital world.

Several other numerical methods exist to iteratively calculate the arctangent. They require more complicated operations than the CORDIC algorithm and are ill adapted for low cost microcontrollers and the integration inside ASICs.

The trigonometric relation (2.26), already used with inductive resolvers, is another way to indirectly extract the angle α from the sine a and the cosine b . It can be implemented with a sine table in the ROM [Kayal97] and an iterative method or with analog electronics [Demierre98].

$$a \sin(\theta) + b \cos(\theta) = \sqrt{a^2 + b^2} \sin(\theta + \alpha) \text{ with } \alpha = \tan^{-1}\left(\frac{a}{b}\right) \quad (2.26)$$

A novel approach uses the inherent features of an incremental ADC which calculates the ratio of an input and a reference [Häberli96]. With the X-signal as input and the Y-signal as reference, the tangent of the angle is calculated. A ROM is used for the linearization.

It is also possible to extract the angle using approximate functions [Maenaka90] which can be implemented with analog electronics:

$$\alpha \cong \frac{1.57a}{0.63b + \sqrt{0.88a^2 + b^2}} \quad \text{or} \quad \alpha \cong \frac{\left(\frac{a}{b}\right)^{1.2125}}{1 + \left(\frac{a}{b}\right)^{1.2125}} \quad (2.27)$$

Analog electronics are only recommended when a low accuracy, low power or high speed angle extraction are used.

2.5 Conclusion

Only a few solutions for 360° contactless absolute angle measurement based on a rotating permanent magnet exists. They use Hall sensors, magnetotransistors and magnetoresistive sensors. Their precision is good enough for low accuracy 1% angle measurement, but we found that the most of them are unable to bridge the gap of 1‰ accuracy requested for new applications. Moreover an accuracy of 3‰ is not achievable without a sensor calibration.

An angular sensor based on standard Hall plates placed on the periphery of the permanent magnet. The sensor is compatible with CMOS electronics, allowing the co-integration with the front-end electronics and the signal processing. This type of angular sensor is sensitive to the mechanical tolerances between the magnet and the sensor. However a commercial product from the company TWK reaches an excellent accuracy of ±0.7° (2‰). This accuracy is closed to our objective of 1‰.

Vertical Hall sensors based on a specific technology reach the 1‰ accuracy with only offset compensation. Unfortunately, this sensor is not compatible with the CMOS electronics. Moreover it is not compatible with the spinning current techniques to reduce its offset: a calibration of offset is necessary to go beyond a 1% accuracy with a 200mT magnet. Even so it is an excellent angular sensor,

especially when the external field is large. A vertical Hall sensors compatible with the CMOS technology is studied within this thesis.

Angular sensors using an integrated magneto concentrator's disk amplifies the external field and the field is limited by the saturation of the ferromagnetic material. Consequently they are more adapted for low field. This sensor is also studied within this thesis.

Magnetotransistors sensitive to the magnetic field parallel to the chip surface do not fulfill our objective of 1‰ and 3‰ accuracy respectively with and without calibration, because they suffer from a too large initial offset and a gain-mismatch between axes which have to be calibrated.

Magnetoresistives sensors are usable both for high and low field measurement. Using the flipping techniques, the offset of anisotropic magnetoresistive (AMR) sensor is only in the order of $1\mu\text{T}$. For larger magnetic field, the accuracy is limited without calibration to 1° , independently to the external field, because of offset. Note that this offset can be calibrated, but a rotating magnetic field is necessary during the measurement. The angular range of AMR sensor is only 180° . However some tricks allow 360° measurements. Giant magnetoresistive (GMR) and eventually colossal magnetoresistive (CMR) sensors have a higher sensitivity and a 360° range. They are surely the future of magnetoresistives sensor and good candidates for the 1‰ accuracy over 360° .

2.6 References

- [AS5020E] AustriaMicrosystems, 6-Bit Absolute Angular Position Encoder, Datasheet AS5020-E, 2002.
- [Bakker99] A. Bakker, A.A. Bellekom, S. Middelhoek and J.H. Huijsing, Low-Offset Low-Noise 3.5mW CMOS Spinning-Current Hall Effect Sensor with Integrated Chopper Amplifier, 13th European Conference on Solid-State Transducers, 28C2, pp. 1045-1048, 1999.
- [Barjen95] U. Barjenbruch, Kompensationsverfahren für Magnetfeldsensoren, German patent DE 4334708 A1, 1995.
- [Bellekom95] S. Bellekom, P. De Vries and P. Simon, Smart Silicon Hall Devices, Sensors and their Applications VII, Proceedings of the Seventh Conference on Sensors and their Applications, pp. 98-103, 1995.

-
- [Blanch97] H. Blanchard, C. de Raad Iseli and R.S. Popovic, Compensation of the temperature dependant offset drift of a Hall sensor, Vol. A60, pp.10-13, 1997.
- [Blanch00] H. Blanchard, F. De Montmollin, J. Hubin and R. S. Popovic, Highly sensitive Hall sensor in CMOS technology, Sensors and Actuators A, Volo. 82, Issues 1-3, pp. 144-148, 2000.
- [Burger01] F. Burger, High Precision Miniaturized Magnetic Angular Encoder, Ph.D. Thesis, (EPFL No 2269), Hartung-Gorre (Konstanz, Germany), ISBN : 3-89649-629-8, 2001.
- [Caruso98] M.J. Caruso and C.H. Smith, A new Perspective on Magnetic Filed Sensing, Honeywell, 1998.
- [Chiesi97] L. Chiesi, K. Haroud, J.A. Flanagan and R.S. Popovic, Chopping of a Weak Magnetic Field by a Saturable Magnetic Shield, Sensors and Actuators, Vol. A60, pp.5-9, 1997.
- [Chiesi99] L. Chiesi, Planar 2D Fluxgate Mangetometer for CMOS Electrnic Compass, Ph.D. Thesis, (EPFL No 2016), Hartung-Gorre (Konstanz, Germany), ISBN : 3-89649-478-3, 1999
- [Demierre98] M. Demierre, Dispositif de réglage de précision sans contact, Travail de diplôme, EPFL, DMT-IMS, 1998.
- [Dietmayer01] K.C.J. Dietmayer, Integrated Online Diagnosis for AMR-Based Angular Measurement Systems, Sensors and Actuators, A91, pp, 12-15, 2001.
- [Drljaca02] P.NM. Drljaca, F. Vincent, P.-A. Besse, R.S. Popovic, Design if Planar Magnetic Concentrators for High Sensitivity Hall Devices, Sensors and Actuators A, pp.10-14, 2002.
- [Enz87] C. Enz, E.A. Vittoz, F. Krummenacher, A CMOS Chopper Amplifier, IEEE Journal of Solid-State Circuits, Vol. SC-22. No. 3, pp. 335-342, 1987. [Hall79]E.H. Hall, On a new action of magnetism on a permanent electric current, American Journal of Mathematics, Vol. 2, pp.287-292, 1879.
- [Häberli96] A. Häberli, M. Schneider, P. Malcovati, R. Castagneti, F. Maloberti, H. Baltes, Two dimensional Magnetic Microsensor with On-Chip Signal Processing for Contactless Angle Measurement, IEEE Journal of Solid-State Circuits, Vol. 31 (12), pp.1902-1907, 1996.

- [Hazard99] P. Hazard and A. Boulahtit, Dispositif de mesure de la sensibilité d'un capteur de champ magnétique à effet Hall, Schneider Electric Industries SA, demande de brevet français FR 9909380, 1999.
- [Hohe99] H.-P. Hohe, N. Weber and D. Seitzer, Sensor Topology for Offset Reduction in Hall-Effect Devices, Eurosensors XIII, pp. 605-608, 1999.
- [Honeywella] Honeywell, Set/Reset Function for Magnetic Sensors, application note AN213, Honeywell.
- [Honeywellb] Honeywell, Magnetic Sensor Products, 2002.
- [Honeywellc] Honeywell, Handling sensor bridge offset, Application note AN212.
- [Honeywelld] Honeywell, Application of Magnetic Position Sensors, Application note AN211, 2002.
- [Kayal97] M-Kayal and M. Declercq, Mixed-Mode ASIC for Absolute Angle Measurement, European Microelectronic Application Conference (EMAC'97), Barcelone, Spain, pp.45-47, 1997.
- [KMZ41] Philips Semiconductors, KMZ41 Magnetic Field Sensor, Datasheet KMZ41, 2000.
- [KMZ52] Philips Semiconductors, Electronic Compass Design using KMZ51 and KMZ52, Application note AN00022.
- [Lenssen00] K.-M.H. Lenssen, D.J. Adelerhof, H.J. Gassen, A.E.T. Kuiper, G.H.J. Somers and J.B.A.D. van Zon, Robust giant magnetoresistance sensors, Sensors and Actuators 85, pp. 1-8, 2000.
- [Lippman58] H.J. Lippmann, F. Kuhrt, Der Geometrieinfluss auf den Hallcontacts, Solide-State Electron., Vol. 52, pp. 63-68, 1958.
- [Mackay00] K. Mackay, M. Bonfirm, D. Givord and A. Fontaine, 50T pulsed magnetic fields in microcoils, Journal of applied physics, Vol. 87(4), pp. 1996-2002, 2000.
- [Maenaka90] K. Maenaka, M. Tsukahara et T. Nakamura, « Monolithic Silicon Magnetic Compass », Sensors and Actuators, A21-A23, pp. 747-750, 1990.

-
- [Maupin80] J.T. Maupin and M.L. Geske, The Hall effect in silicon circuits, The Hall effect and its applications, ed: C.L. Chien and C.R. Westgate, New York London Plenum Press, pp 421-445, 1980.
- [MLX90215] Melexis, MLX90215 Precision Programmable Linear Hall Effect Sensor, Datasheet Melexis, 2002.
- [Munter90] P.-J.-A- Munter, A low-offset spinning-current Hall plate, Sensors and Actuators, A21-A23, pp. 743-746, 1990.
- [Paranjape92] M. Paranjape, L. Ristic, Micromachined vertical Hall magnetic field sensor in standard complementary metal oxide semiconductor technology, Applied Physics Letters, Vol. 60(25), pp. 3188-3190, 1992.
- [Petr88] Jan Petr, Compensating circuit for a magnetic field sensor, United States Patent, US 4752733, 1988.
- [Platil02] A. Platil, M. Vopalensky, P. Ripka, P. Kaspar and H. Hauser, Improvement of AMR Magnetometer Precision, Eurosensors XVI, Prague, Czech Republic, pp. 339-340, 2002.
- [Popovic84] R.S. Popovic, The Vertical Hall-Effect Device, IEEE Electron Dev. Lett., EDL-5(9),1984, pp. 357-358.
- [Popovic91] R.S. Popovic, Hall Effect Devices, Adam Hiliger, B.E. Jones (Ed.), New York, ISBN 0-7503-0096-5, 1991.
- [Popovic97] R.S. Popovic and J.A. Flanagan, Sensor Microsystems, Microelectron. Reliab., Vol. 37, No. 9, pp. 1401-1409, 1997.
- [Popovic01] R.S. Popovic, P. Drljaca and C. Schott, A new CMOS Hall Angular Position Sensor, Technisches Messen 68(6), pp.286-291, 2001.
- [Ruther02a] P. Ruther, U. Schiller, W. Buesser, R. Janke and O. Paul, Thermomagnetic Residual Offset in Integrated Hall Plates, to be published in Proc. IEEE Sensors conference, USA, 2002.
- [Ruther02b] P. Ruther, U. Schiller, W. Buesser, R. Janke and O. Paul, Influence of the Junction Field Effect on the Offset Voltage of Integrated Hall-Plates, European Conference on Solid-State Transducers, Prague, pp. 709-710, 2002.
- [RXW22] TWK, Electro-magnetic Absolute and Incremental Encoders RXW 22 series, Datasheet TWK, 2003.
-

- [Randjel00] Z.Randjelovic, Low-Power High Sensitivity Integrated Hall Magnetic Sensor Microsystems, Ph.D. Thesis, (EPFL No 2198), Hartung-Gorre (Konstanz, Germany), ISBN : 3-89649-617-4, 2000.
- [Schott99] C. Schott, Accurate Magnetic Field Transducers based on Silicon Hall sensor, Ph. D. Thesis (EPFL No 1985), Hartung-Gorre (Konstanz, Germany), ISBN : 3-89649-477-5, 1999.
- [Schurig02] E. Schurig, M. Demierre, C. Schott and R. S. Popovic, "A vertical Hall device in CMOS high-voltage technology", Sensors and Actuators, Vol. A97, pp. 47-53, 2002.
- [Steiner98a] R. Steiner and F. Kroener, In-plane sensitive Vertical Hall Trench-Hall device, International Electron Devices Meeting, pp. 479-482, 1992.
- [Steiner98b] R. Steiner, Ch. Mayer, A. Häberli, F.P. Steiner, H. Baltes, Offset reduction in Hall devices by continuous spinning current method, Sensors and Actuators A, 66, pp. 167-172, 1998.
- [Sze85] S.M. Sze, Semiconductor Devices, John Wiley & Sons, ISBN : 0-471-87424-8, 1985.
- [Travis98] B. Travis, Hall-effect Sensor ICs sport magnetic personalities, EDN-Europe, Cahners Publishing, pp. 81-92, 1998.
- [Treutler01] C.P.O. Treutler, Magnetic sensors for automotive applications, Sensors and Actuators, A91, pp. 2-6, 1991.
- [Trontelj94] J. Trontelj, R. Opara, A. Pletersek, Integrierte Schaltung mit einem Magnetfeldsensor, European Patent Office, 0 655 628 A2, 1994.
- [Trontelj99] J. Trontelj, Optimization of Integrated Magnetic Sensor by Mixed Signal Processing, Instrumentation and Measurement Technology Conf., pp. 299-302, 1999.
- [Trontelj01] J. Trontelj Jr., Functionality Test for Magnetic Angular Positioning Integrated Circuit, Informacije MIDEM 31, Ljubljana, pp.287-289, 2001.
- [UZZ9001] Philips Semiconductors, UZZ9001, Sensor Conditioning Electronics, product specification, 2000.
- [Versnel81] W. Versnel, Analysis of symmetrical Hall plates with finite contacts, Journal of applied Physics, Vol. 52, pp.4659-4666, 1981.

- [Vern97] Jean-Louis Vern, *Algorithmes et Développements pour le 8051*, International Thomson Publishing, France, ISBN 2-84180-136-5, pp. 152-157, 1997.
- [VertX] Novotechnik, *Contactless Angle Sensors Measuring absolute up to 360° Series VX*, Datasheet.
- [Volder59] J. E. Volder, *The CORDIC Trigonometric Computing Technique*, IRE Transactions on Electronic Computers, vol. EC-8, no. 3, 1959, 330-334.

3 Calibration Coils and Synergies with the Hall Microsystem

Magnetic sensitivity of Hall elements (2.1.1) depends on stress, temperature, aging and thermal shocks (2.1.3) [Dragan00]. These effects, particularly serious in plastic-encapsulated sensors, can hardly, or even not at all, be compensated with complex electronics and lookup tables (§2.2) [Melexis01].

One promising way to avoid this limitation is to use a stable magnetic actuator to generate an in situ reference magnetic field [Simon95]. This reference, which is a coil built directly with the metallic layers of the CMOS process, is the basic element for the self-calibration of magnetic microsystems [Popovic96]. The stability of the coil is guaranteed by the geometric stability of the coil substrate (§2.2), i.e. the silicon. For instance its thermal expansion of only 3ppm/°C. We demonstrate in this chapter that the thermal drift induced by thermo-mechanical stresses of a coil is about 100 times smaller than the one of a Hall sensor by comparing the gauge factor of a Hall sensor with the one of a coil.

When a coil, which generates a field perpendicular to the chip surface, is added around a Hall plate of usual size, the ratio between the magnetic field and the current consumption, i.e. the efficiency of the coil, is poor (§2.2). Previous published values are 30mT/A for standard plate [Simon95] and 150mT/A for a miniaturized Hall plate [Trontelj99]. This limits its range of applications, especially for low power microsystems. The magnetic field at the center of a current loop is reverse-proportional to its diameter. This is the reason why, the coil and consequently the sensor have to be scaled down to increase the coil efficiency. The goal is to reduce the supply current of the coil to a few milliamps for a calibration field of about 1mT. A coil which generates a field parallel to the chip surface to be compatible with vertical Hall sensors is also studied in details within this chapter.

A twin Hall spinning current microsystem [Frounch01], which contains two sensing parts, will also be studied in this chapter. The first microsystem measures, as usual, the external field, whereas the second performs the calibration by measuring the field generated by the integrated coil. The additional sensor works as a so-called sensitivity meter. A feedback loop using the sensor biasing maintains a constant sensitivity and external field measurement sensitivity by modifying the biasing [Petr88].

The accuracy of the magnetic actuator depends only on the current flow through the coil and on the geometry. Current sources with only a few ppm/°C of thermal drift are not realizable with CMOS circuits, where the voltage drift and current references are respectively 50ppm/°C and 500ppm/°C. Specific electronic systems [Hazard99] have been proposed to obtain a system independent of electronic references with the cost of a low drift resistor and an analog to digital converter. We propose a new principle where only the geometry of the coil defines the stability of the magnetic reference. Geometry changes are very low compared to sensor's parameters, because of the 3ppm/°C expansion coefficient of silicon, which leads to a similar drift for the induced magnetic field.

One main limitation when performing self-calibration is how to distinguish between the calibration field and an external field [Simon95]. Our goal is to obtain a sensor with two outputs: one for the external field measurement and the other one for calibration. These two signals have to be decoupled, i.e. the calibration signal is independent to the field to measure. Several ways are explored in order to separate the calibration magnetic field.

3.1 Figure of Merit

The figure of Merit of the coil, which measures its performances, directly depends on the intended application. We found several main figures of Merit for a coil inside a microsystem.

The first one is the magnetic field: a higher intensity magnetic field increases the signal to noise ratio at the output of the microsystem. The magnetic field is proportional to flow of the current through the coil. As a result, the coil is designed to support the highest current [Mackay00]. Our goal is to reach a continuous field of about 1mT, but with a limited current of only a few mA. This is the reason why another figure of merit is required for our microsystem.

A particularly important parameter for a microsystem is current consumption. Indeed current consumption is really the main parameter in a microsystem. It is why we choose the ratio of the magnetic field over the current consumption to be the main figure of merit. We will define this as the current related efficiency of a coil.

A third essential parameter is the voltage limitation of the CMOS electronic (5V for a 0.8μm technology). The figure of merit is in this case the ratio between the magnetic field and the supply voltage. This is called the voltage related efficiency, equal to the quotient of the current related efficiency over the resistance of the coil.

In most cases, the resistivity of the coil and the current are small enough so as the maximum allowed voltage with CMOS electronics is not reached. In this case, the current mostly limits the magnetic field; it is why the current related efficiency is used to determine the figure of merit. In the following sections, we have often abusively called the efficiency, the current related efficiency.

Microsystems generally use linear circuits for the biasing. For this reason, the total power dissipation inside the microsystem is the product of the CMOS supply voltage and the current consumption. Therefore optimizing the power consumption is equivalent to optimizing the current consumption. Secondly, the chip temperature increase is small because of the low power dissipated by the coil. That is why the power related efficiency has, in this case, no sense.

3.2 Coils for Hall plates and vertical Hall sensors

The coils are obtained using the metallic layers of the CMOS process; the plane of the coil is parallel to the chip surface. The sensitivity direction of Hall plates is orthogonal to the chip surface, whereas it is parallel in the case of vertical Hall sensors (§2.3) [Popovic84]. Two types of coils are respectively required to create a field perpendicular and parallel to the chip surface (Fig. 3.1).

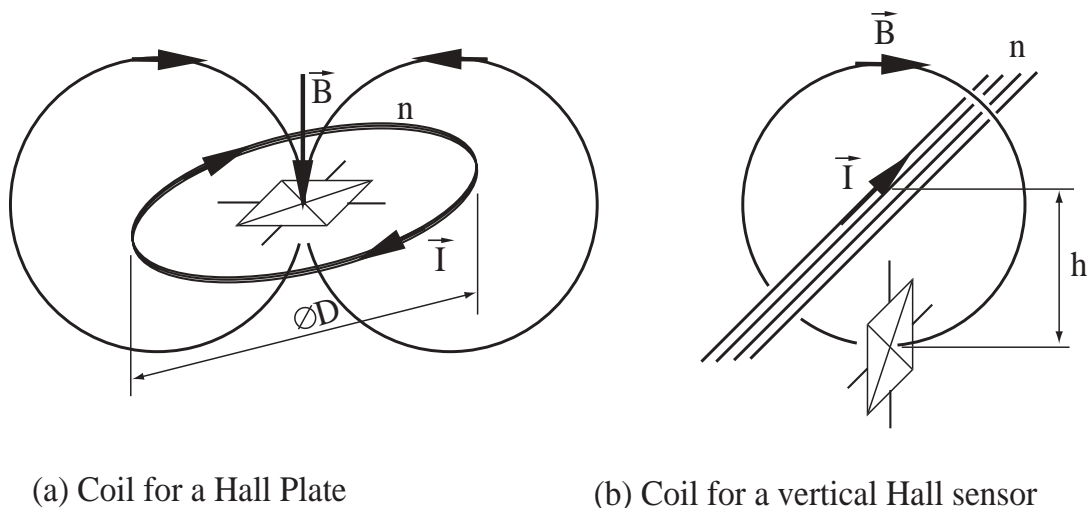


Fig. 3.1 Calibration coils for a Hall plate (a) and a vertical Hall sensors (b). In the case of the Hall plate, we use the field perpendicular to the coil plane, while in the case of the vertical Hall sensors we use the field parallel. n wires are biased with a current I .

For Hall plates, the best way to produce the required field is to use a flat circular coil surrounding the sensor (Fig. 3.1). With a first approximation, the coil efficiency (the ratio B over I) is, with D the diameter of the loop, n the number of turns and μ the permeability:

$$\frac{B}{I} \cong \frac{\mu \cdot n}{D} \quad (3.1)$$

This equation clearly shows the intuitive design rules necessary to increase the coil efficiency: increasing the number of turns and decreasing the coil diameter D .

Using the CMOS process, the sensor is not placed in the same plane as the coil, but at a distance Z_0 below in the NWell (Fig. 3.2). The effect of this vertical distance, modeled in the §3.4.1, decreases the efficiency of the coil, especially for small ratio of coil size (radius for circular coil or half length L for square coils) over the distance Z_0 , i.e. $L/Z_0 < 5$.

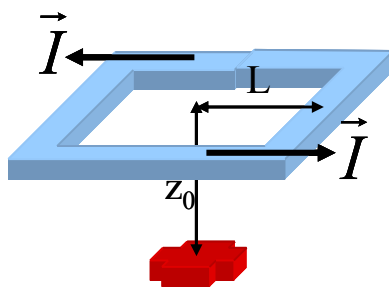


Fig. 3.2 The vertical distance Z_0 between the Hall sensor and the coil noticeably reduces efficiency when $L/Z_0 < 5$.

In the case of vertical Hall sensors, the field is the horizontal component of an array of n wires placed above the sensor (Fig. 3.1). If they are in the same plane as the sensor, the efficiency is equal, with h the distance between the sensor and the wires, to:

$$\frac{B}{I} \cong \frac{\mu n}{2\pi h} \quad (3.2)$$

To increase the coil efficiency, the distance h between the sensor and the wires has to be minimized. This distance is mostly fixed by the process. Consequently the design rule of increasing coil efficiency is achieved by adding turns to the coil.

3.3 Stress Influence

The effects of mechanical stresses on the Hall sensor sensitivity and on the coil can be compared using the gauge factor. The gauge factor describes the effect of the relative deformations ε . The magnetic field B at the center of the coil is inversely proportional to the diameter of a flat circular coil (Hall plate) and also inversely proportional to the distance between the coil and the sensor (vertical Hall sensors). It is also proportional to its supply current I . For a relative isotropic deformation ε , we obtain from (3.1), with the coil and the sensor in the same plane, the following relative variations of B :

$$\frac{\Delta B}{B} = \frac{\Delta I}{I} - \varepsilon \quad (3.3)$$

The Piezohall coefficient P_{12} leads to a relative sensitivity variation as high as $40 \times 10^{-11} \text{Pa}^{-1}$ [Dragan00], when a stress is applied along an X or Y direction of the chip plane with a 170GPa Young modulus E for silicon. The following variation of the current related sensitivity is calculated [Dragan00]:

$$\frac{\Delta S_I}{S_I} \cong 2P_{12}\sigma = 2P_{12}E\varepsilon = 136\varepsilon \quad (3.4)$$

These simple evaluations of the gauge factor demonstrate that stresses and deformations have about 100 times fewer influences on the coil than on the Hall sensor. As a result, the thermal drift of the coil field is only a few ppm/°C if the coil current is constant.

3.4 Models

3.4.1 Integrated FlatCoils for Hall Plates

As we will demonstrate later, high-efficiency coils can only be obtained if the vertical distance Z between the coil and the Hall sensor is small [Trontelj94]. Fig. 3.3 shows the rapid decrease of the magnetic field with the vertical distance Z_0 .

If this distance is equal to the coil's half-length, the field is only 40% that of the field at the center of the same coil. The distance between coil and sensor is principally defined by the thickness of the oxide and the depth of the sensor. It is typically one micrometer between the sensor and the upper layer of metal and also between each following metallic layer in CMOS technology. When using an

external coil, this distance will typically be an order of magnitude higher. Thus, using integrated coils is the only way to obtain a high figure of merit.

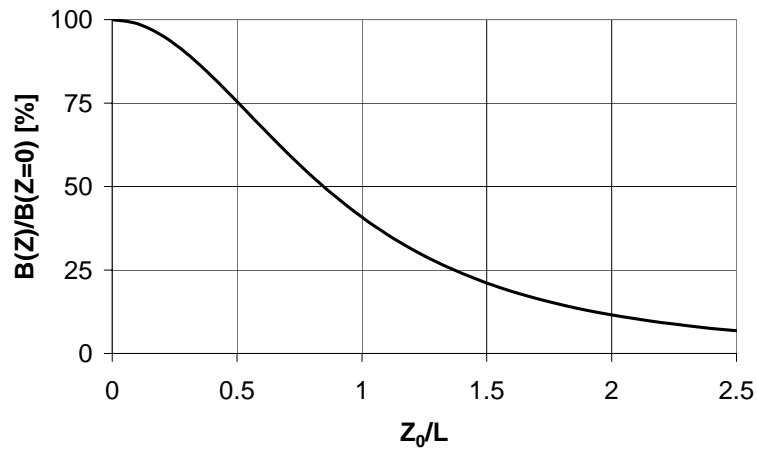


Fig. 3.3 Decrease of the magnetic field at the center of the coil with the distance Z_0 . When the distance is equal to the half-length of the coil, the field is only 40% that of the field at the center of the coil, as calculated at the §3.4.1.

To increase the magnetic field of the coil, the Equ. (3.1) demonstrates that the internal diameter of the coil has to be decreased, but also the number of turns (external diameter). The number of turns is increased by reducing the pitch and the width of the metallic lines. These geometrical parameters are favorable to the high resolution of CMOS technologies.

We calculate the magnetic field in the coil's center along the $(0,0,z)$ -axis. For the analytical calculation, we approximate the current distribution by introducing a mean linear current density J defined by the current I in one turn and the pitch P of the coil (Fig. 3.4).

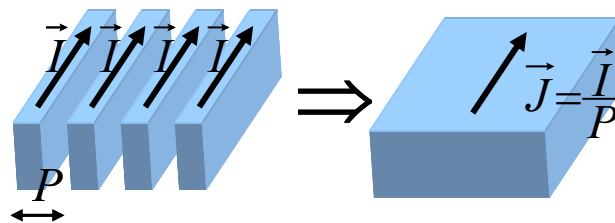


Fig. 3.4 Approximation of the coil turns by an average linear current density J .

The linear current density is consequently equal to:

$$J = \frac{I}{P} \quad (3.5)$$

We consider a square ring of current with a length $2L$ and a width dL (Fig. 3.5). The metallic layer's thickness is neglected.

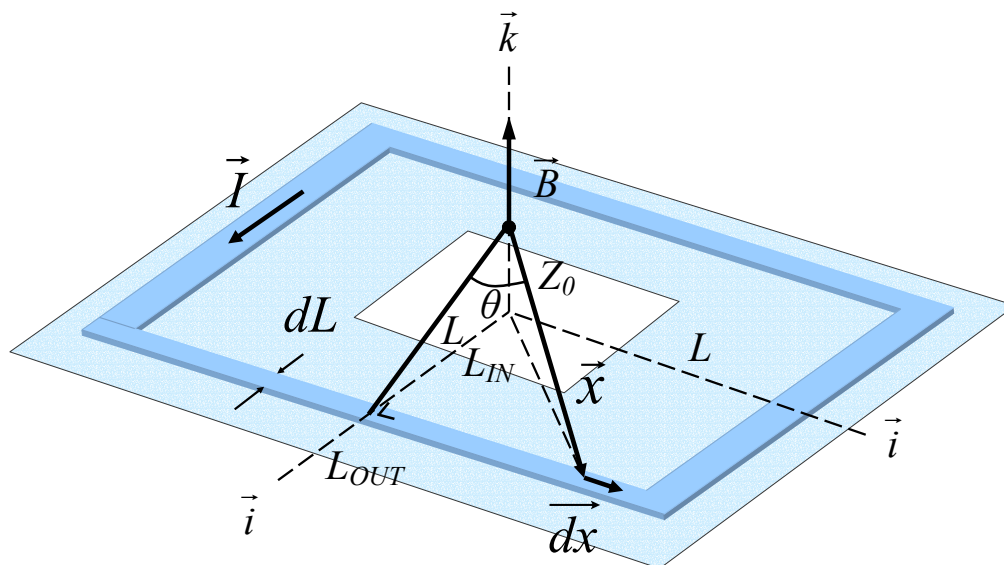


Fig. 3.5 Schematic of a coil for the calibration of a Hall plate. The central part of the coil is used to place the sensor.

The Biot-Savart Law gives us the contribution of an element \overline{dx} to the field \overline{B} .

$$d^2 \overline{B} = \frac{\mu}{4\pi} \cdot \frac{I}{P} \cdot dL \cdot \frac{\overline{x} \times \overline{dx}}{|\overline{x}|^3} \quad (3.6)$$

Only the magnetic field normal to the chip in the direction \vec{k} is measured by the Hall sensor.

$$d^2 B_k = \frac{\mu}{4\pi} \cdot \frac{I}{P} \cdot dL \cdot \vec{k} \cdot \frac{\overline{x} \times \overline{dx}}{|\overline{x}|^3} \quad (3.7)$$

with:

$$\vec{k} \cdot \vec{x} \times \overline{dx} = \begin{pmatrix} 0 \\ 0 \\ 1 \end{pmatrix} \cdot \begin{pmatrix} dx \\ 0 \\ 0 \end{pmatrix} \times \begin{pmatrix} x \\ L \\ z_0 \end{pmatrix} = dx \cdot L \quad (3.8)$$

$$|\vec{x}| = \sqrt{x^2 + L^2 + z_0^2} = \frac{\sqrt{L^2 + z_0^2}}{\cos(\theta)} \quad (3.9)$$

We integrate this relation along \overline{dx} over one turn to obtain the contribution of the ring:

$$\frac{dB_k}{dL}(L) = 2 \cdot \frac{\mu}{4\pi} \cdot \frac{I}{P} \int \frac{\vec{j} \cdot \vec{x} \times \overline{dx}}{|\vec{x}|^3} = \frac{\mu}{2\pi} \cdot \frac{I \cdot L}{P} \int_0^L \frac{\cos^3(\theta) \cdot dx}{(L^2 + z_0^2) \sqrt{L^2 + z_0^2}} \quad (3.10)$$

With:

$$x = \sqrt{L^2 + z_0^2} \tan(\theta) \quad (3.11)$$

$$dx = \frac{\sqrt{L^2 + z_0^2}}{\cos^2(\theta)} d\theta \quad (3.12)$$

We find:

$$\frac{dB_k}{dL}(L) = \frac{\mu}{2\pi} \cdot \frac{I}{P} \cdot \frac{z_0 \cdot L}{L^2 + z_0^2} \int \cos(\theta) \cdot d\theta \quad (3.13)$$

And finally with:

$$\int \cos(\theta) \cdot d\theta = \sin(\theta) = \frac{x}{\sqrt{x^2 + y^2 + z_0^2}} \quad (3.14)$$

We obtain the derivate of the magnetic field:

$$\frac{dB_k}{dL}(L) = \frac{\mu}{2\pi} \cdot \frac{I}{P} \cdot \frac{z_0 \cdot L}{L^2 + z_0^2} \frac{x}{\sqrt{L^2 + z_0^2}} \Bigg|_0^L = \frac{\mu}{2\pi} \cdot \frac{I}{P} \cdot \frac{z_0}{L^2 + z_0^2} \cdot \frac{L^2}{\sqrt{2L^2 + z_0^2}} \quad (3.15)$$

At $z_0=0$, in the same plane as the coil, the field contribution is inversely proportional to L .

For the Hall sensor position z_0 , given by the thickness of the oxide, the ring of maximum efficiency is determined by:

$$\frac{d^2 B}{dL^2}(L_0, z_0) = 0 \quad \Leftrightarrow \quad \rho_0 = \frac{L_0}{z_0} = \sqrt{\frac{1 + \sqrt{5}}{2}} = 1.272 \quad (3.16)$$

We introduce the normalized variables ρ and \bar{B} defined as:

$$\rho = \frac{L}{z_0} \quad \text{and} \quad B = \left(\frac{\sqrt{2}\mu}{\pi} \cdot \frac{I}{P} \cdot \frac{1}{\rho_0} \right) \cdot \bar{B} \quad (3.17)$$

With this normalization the ring of maximal efficiency produces in its center ($z=0$) the field $d\bar{B} = d\rho$.

Equ. (3.15) becomes (Fig. 3.6):

$$\frac{d\bar{B}}{d\rho}(\rho) = \sqrt{2}\rho_0 \cdot \frac{\rho^2}{(1 + \rho^2)\sqrt{1 + 2\rho^2}} \quad (3.18)$$

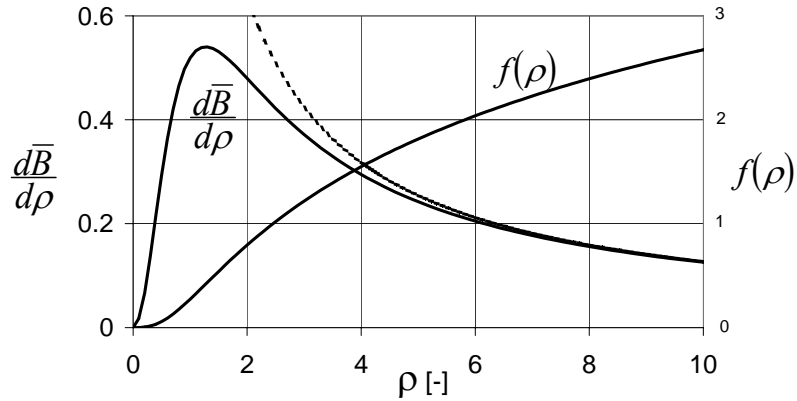


Fig. 3.6 Normalized magnetic field and its derivate. The maximum efficiency is found for $r=1.272$ where the field reaches a value equal to 54% of the field at the center of the coil ($z=0$). The dashed line shows the effect obtained if the distance between the coil and the sensor is neglected. The total magnetic field is calculated from $f(r)$ using Equ. 6.

The total field is expressed, with L_{OUT} (ρ_{OUT}) and L_{IN} (ρ_{IN}) the external and internal size of the coil, as:

$$\bar{B}(z_0) = f(\rho_{OUT}) - f(\rho_{IN}) \quad (3.19)$$

With:

$$f(\rho) = \rho_0 \cdot \left[\ln\left(\sqrt{2\rho^2 + 1} + \sqrt{2}\rho\right) + \frac{1}{\sqrt{2}} \ln\left(\frac{\sqrt{2\rho^2 + 1} - \rho}{\sqrt{2\rho^2 + 1} + \rho}\right) \right] \quad (3.20)$$

If $\rho_{IN} \gg 1$, we obtain from Equ. (3.19) and (3.20) the simplified results represented in dashed line in the Fig. 3.6:

$$\frac{d\bar{B}}{d\rho}(\rho) = \rho_0 \cdot \frac{1}{\rho} \quad (3.21)$$

$$\bar{B}(z_0) = \rho_0 \cdot \ln\left(\frac{\rho_{OUT}}{\rho_{IN}}\right) \quad (3.22)$$

Current related efficiency

From the coil model (3.19), the current related efficiency of the coil E_I is easily extracted:

$$E_I = \frac{B}{I} = \frac{\sqrt{2}\mu}{\pi} \cdot \frac{1}{P} \cdot \frac{f(\rho_{OUT}) - f(\rho_{IN})}{\rho_0} \quad (3.23)$$

If $\rho_{IN} \gg 1$, the following simplified result can be found from (3.22):

$$E_I = \frac{\sqrt{2}\mu}{\pi \cdot \rho_0} \cdot \frac{1}{P} \cdot \ln\left(\frac{\rho_{OUT}}{\rho_{IN}}\right) = \frac{\sqrt{2}\mu}{\pi \cdot \rho_0} \cdot \frac{1}{P} \cdot \ln\left(\frac{L_{OUT}}{L_{IN}}\right) \quad (3.24)$$

Voltage related efficiency

The voltage related efficiency E_U is the ratio between the magnetic field and the supply voltage:

$$E_U = \frac{B}{U} = \frac{B}{I} \cdot \frac{I}{U} = \frac{E_I}{R} \quad (3.25)$$

With R the resistance of the coil.

The n number of turns in a coil, with an internal half length of L_{IN} and external of L_{OUT} is, for a pitch P :

$$n = \frac{L_{OUT} - L_{IN}}{P} \quad (3.26)$$

The number of squares for the turn i is, with e the width of the metallic lines:

$$N_i = 8 \frac{(L_{IN} + i \cdot e)}{P} \quad (3.27)$$

From a previous equation, the total number of squares N is, for the full n turns of the coil:

$$N = 8 \cdot \frac{L_{IN} \cdot n}{e} + 4 \cdot \frac{P \cdot n \cdot (n-1)}{e} \quad (3.28)$$

The resistance of the coil is:

$$R = R_{\square} \cdot N \quad (3.29)$$

with R_{\square} the sheet resistance of the metallic layer in Ω/\square . Consequently, the voltage related efficiency is:

$$E_U = \frac{e \cdot P}{4R_{\square} (L_{OUT} - L_{IN})(L_{OUT} - L_{IN} - P)} E_I \quad (3.30)$$

3.4.2 Integrated Flat Coils for vertical Hall sensors

For the analytical calculation, we approximate like before the current in the coil plane $\vec{i} \vec{j}$ by introducing a mean linear current density J (Fig. 3.7) defined by the current I of one stripe over the coil pitch P ratio.

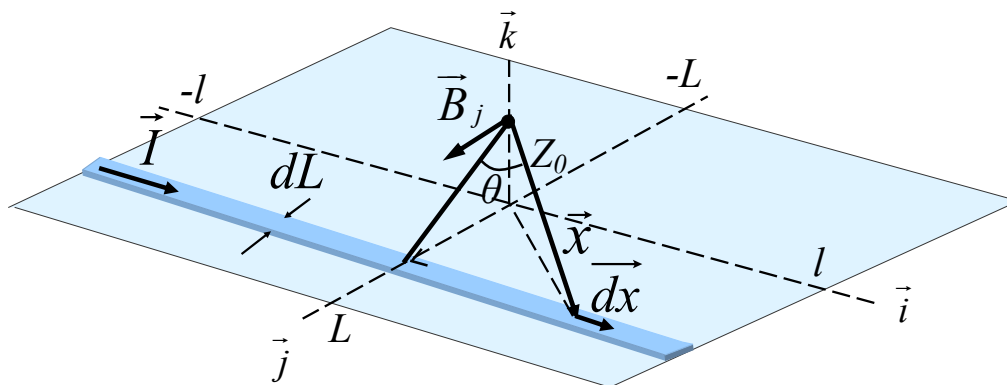


Fig. 3.7 Coil for vertical Hall sensors with current lines parallel to the \vec{i} axis. The field measured is parallel to the \vec{j} axis.

We consider an infinite line of current with the width dL (Fig. 1). The metallic layer thickness is neglected. The Biot-Savart Law gives us the contribution of an

element to the field parallel to the coil plane and also perpendicular to the vertical Hall sensor.

$$d^2\vec{B} = \frac{\mu}{4\pi} \cdot \frac{I}{P} \cdot dL \cdot \frac{\vec{x} \times \overline{dx}}{|\vec{x}|^3} \quad (3.31)$$

Only the field parallel to the chip in the direction \vec{j} is measured by the sensor.

$$d^2B_j = \frac{\mu}{4\pi} \cdot \frac{I}{P} \cdot dL \cdot \vec{j} \cdot \frac{\vec{x} \times \overline{dx}}{|\vec{x}|^3} \quad (3.32)$$

We integrate this relation along \overline{dx} over one line of length $2l$ to get the contribution of each elementary stripe.

$$\frac{dB_j}{dy}(y) = 2 \cdot \frac{\mu}{4\pi} \cdot \frac{I}{P} \int \frac{\vec{j} \cdot \vec{x} \times \overline{dx}}{|\vec{x}|^3} \quad (3.33)$$

With :

$$\vec{j} \cdot \vec{x} \times \overline{dx} = \begin{pmatrix} 0 \\ 1 \\ 0 \end{pmatrix} \cdot \begin{pmatrix} dx \\ 0 \\ 0 \end{pmatrix} \times \begin{pmatrix} x \\ y \\ z_0 \end{pmatrix} = dx \cdot z_0 \quad (3.34)$$

$$|\vec{x}| = \sqrt{x^2 + y^2 + z_0^2} = \frac{\sqrt{y^2 + z_0^2}}{\cos(\theta)} \quad (3.35)$$

The Equ. (3.33) becomes:

$$\frac{dB_j}{dy}(y) = \frac{\mu}{2\pi} \cdot \frac{I}{P} \int_0^L \frac{\cos^3(\theta) \cdot dx}{(y^2 + z_0^2) \sqrt{y^2 + z_0^2}} \quad (3.36)$$

With :

$$x = \sqrt{y^2 + z_0^2} \tan(\theta) \quad \text{and} \quad dx = \frac{\sqrt{y^2 + z_0^2}}{\cos^2(\theta)} d\theta \quad (3.37) \quad (3.38)$$

$$\frac{dB_j}{dy}(y) = \frac{\mu}{2\pi} \cdot \frac{I}{P} \cdot \frac{z_0}{y^2 + z_0^2} \int \cos(\theta) \cdot d\theta \quad (3.39)$$

with :

$$\int \cos(\theta) \cdot d\theta = \sin(\theta) = \frac{x}{\sqrt{x^2 + y^2 + z_0^2}} \quad (3.40)$$

The Equ. (3.39) becomes:

$$\frac{dB_j}{dy}(y) = \frac{\mu}{2\pi} \cdot \frac{I}{P} \cdot \frac{z_0}{y^2 + z_0^2} \frac{x}{\sqrt{y^2 + z_0^2}} \Big|_0^l = \frac{\mu}{2\pi} \cdot \frac{I}{P} \cdot \frac{z_0}{y^2 + z_0^2} \cdot \frac{l}{\sqrt{l^2 + y^2 + z_0^2}} \quad (3.41)$$

This equation can be integrated from $-L$ to L .

$$B_j = 2 \cdot \frac{\mu}{2\pi} \cdot \frac{I \cdot z_0 \cdot l}{P} \int_0^L \frac{dy}{(y^2 + z_0^2) \sqrt{l^2 + y^2 + z_0^2}} \quad (3.42)$$

And finally we found the magnetic field B_j :

$$B_j = \frac{\mu}{\pi} \cdot \frac{I}{P} \tan^{-1} \left(\frac{l \cdot L}{z_0 \sqrt{L^2 + l^2 + z_0^2}} \right) \quad (3.43)$$

Current related efficiency

From Equ. (3.43), we found that the current related efficiency is (Fig. 3.8):

$$E_l = \frac{B}{I} = \frac{\mu}{\pi \cdot P} \tan^{-1} \left(\frac{l \cdot L}{z_0 \sqrt{L^2 + l^2 + z_0^2}} \right) \quad (3.44)$$

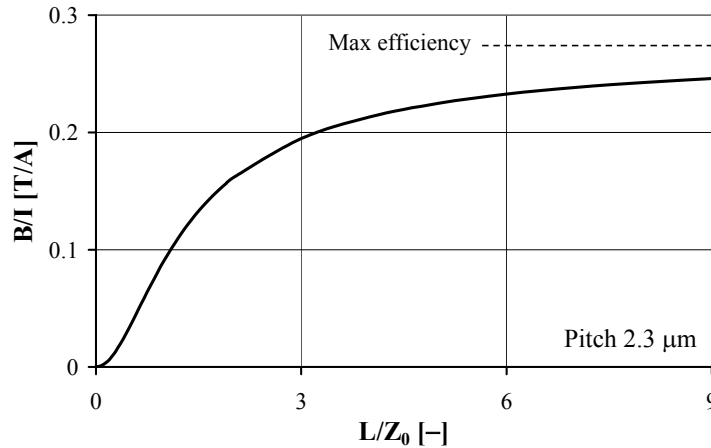


Fig. 3.8 Current related efficiency for a square coil ($l=L$) and a pitch of $2.3\mu\text{m}$. The efficiency reaches 90% of the maximum theoretical efficiency (3.45) where L/Z_0 is equal to 9.

For an infinite plate, i.e. where the vertical distance Z_0 is negligible compared to the coil dimensions l and L , the field, with the minimal $2.3\mu\text{m}$ pitch of METAL2, is equal to:

$$E_{I.MAX} = \frac{B_{max}}{I} = \lim_{\frac{l}{z_0}, \frac{L}{z_0} \rightarrow \infty} \left[\frac{\mu \cdot 1}{\pi \cdot P} \tan^{-1} \left(\frac{\frac{l \cdot L}{z_0 \cdot z_0}}{\sqrt{\left(\frac{L}{z_0}\right)^2 + \left(\frac{l}{z_0}\right)^2 + 1}} \right) \right] = \frac{\mu \cdot 1}{2 \cdot P} = 0.27 \text{ T/A} \quad (3.45)$$

This maximal field is shown in the Fig. 3.8. The field is already 90% of the maximum field when the L over Z_0 ratio ($l=L$) is equal to 10.

Voltage related efficiency

The number of squares of the active area of the coil is, with P the pitch and e the width of the metal lines:

$$N = \frac{l \cdot L}{P \cdot e} \quad (3.46)$$

There is also the parasitic resistance of the return lines (Fig. 3.9) to close the conductive loop. The number of squares is consequently multiplied by a factor g depending of the geometry of the whole coil. This parameter is between 2 and 4; 2 if the lateral lines are neglected and the width of the metallic lines are constant and 4 if the coil is symmetric (square).

We found that the voltage related efficiency is, with R_{\square} the sheet resistance:

$$E_V = \frac{E_I}{R} = \frac{\mu \cdot e}{\pi \cdot R_{\square} \cdot g \cdot L \cdot l} \tan^{-1} \left(\frac{l \cdot L}{z_0 \sqrt{L^2 + l^2 + z_0^2}} \right) \quad (3.47)$$

3.5 Technology limitations

The coils are drawn using the metallic interconnection layers. Using the metal layers of the CMOS technology is a very favorable process, because we benefit directly from the high resolution, small distance from the sensor and a good alignment of the CMOS technology.

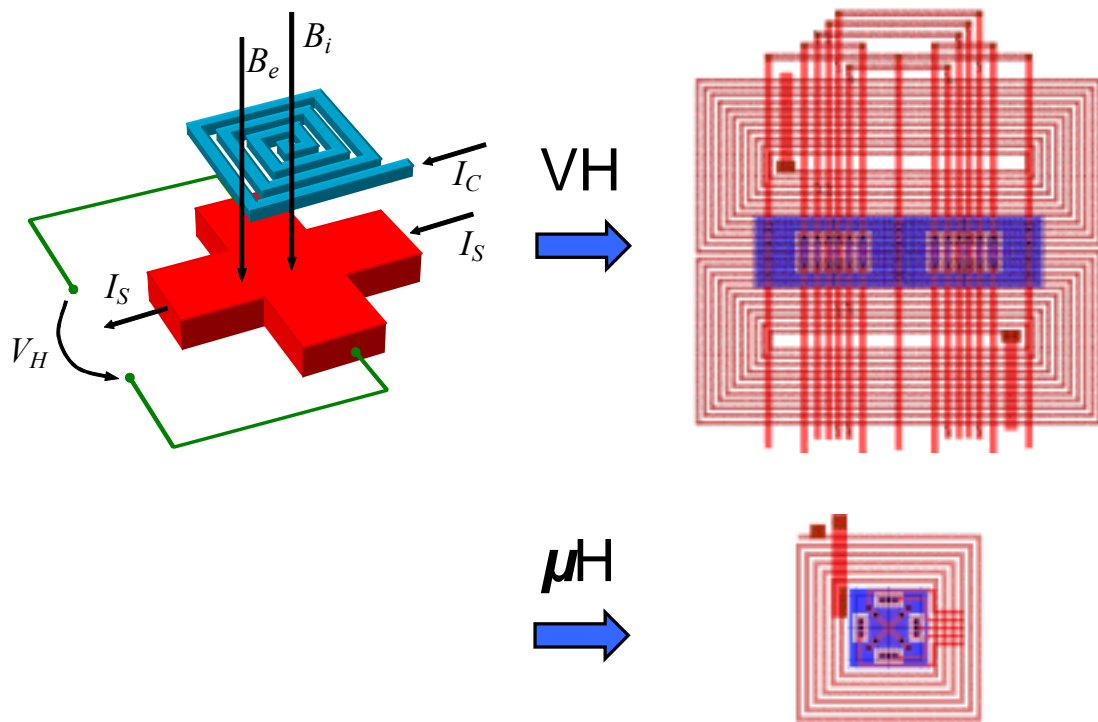


Fig. 3.9 Layout of the coils with vertical Hall sensors (VH) and miniaturized Hall plates (μH) using AMS $0.8\mu\text{m}$ CXQ and CXZ. This technology contains two metallic layers. The METAL1 layer is mainly used for sensor connections and the METAL2 layer for the coil. These two coils have roughly the same efficiency (ratio of B over I).

For these designs, we use the AMS $0.8\mu\text{m}$ CXQ (Hall plate) and CXZ (deep NWell for vertical Hall sensors) technologies. Two metallic layers METAL1 and METAL2 are available in this technology: the first is used for the sensor connections and the second for the coil (Fig. 3.9).

The maximum possible permanent current is limited by the electromigration (process parameters). METAL2 layer allows current density of up to $3\text{mA}/\mu\text{m}$ and METAL1 of only $0.9\text{mA}/\mu\text{m}$. In some other cases, pulses of current can be used; the maximum current is roughly multiplied by a factor 10 depending on

the type of pulses. For the next analysis we use the values given for a permanent current, i.e. a permanent calibration.

The minimum width and spacing, determined by design rules, is respectively $1.1\mu\text{m}$ and $1\mu\text{m}$ for METAL1 and $1.2\mu\text{m}$ and $1.1\mu\text{m}$ for METAL2. The minimum pitches of $2.1\mu\text{m}$ and $2.3\mu\text{m}$ are roughly the same. The sheet resistances of metallic layers are $100\text{ m}\Omega/\square$ for METAL1 and $60\text{m}\Omega/\square$ for METAL2; METAL2 is favorable for the voltage related efficiency.

The electrical parameters are in the majority favorable to the METAL2 coil because of higher current density and lower resistivity. However METAL1 is closer to the sensor than METAL2. We can evaluate from process parameters that the vertical distance between coil and sensor is 60% larger for METAL2 with Hall plates and 50% larger with vertical Hall sensors. This is of course in favor of the METAL1 layer.

If METAL1 is used for the coils, the connection of the sensor requires vias and contacts. This forbids the use of METAL1 in the proximity of the sensor due to design rules: this area is a dead surface for the coil. The total surface of the via, including metallization of minimum VIA, is as large as $4\mu\text{m}^2$.

3.6 Coil optimization

As previously explained in §3.1, there are several figures of merit: the maximum magnetic field, the current related efficiency and the voltage related efficiency. The maximum field is limited by the polarization current and the maximum polarization voltage.

The voltage is limited to 4V by the saturation of the 5V integrated electronics (1V of margin for the current source). As explained in §3.9, an array of 4 coils putted in series is used to increase the signal-to-noise ratio. Consequently, only a quarter of this voltage is available for each coil in series: the maximum polarization voltage is consequently fixed to 1V.

3.6.1 Hall plate

The distance between the sensor and the coil is fixed by the sum of the oxide layers and the depth of the sensor inside the silicon. The depth of the sensor NWell is $4\mu\text{m}$ (AMS $0.8\mu\text{m}$ CXQ). We can approximate its center of measurement as half of the junction depth. The distance between the coil and the silicon is determined by the oxide and aluminum width: $0.7\mu\text{m}$ and $2.3\mu\text{m}$

respectively for METAL1 and METAL2. Consequently, the typical total distance Z_0 is worth $2.7\mu\text{m}$ for METAL1 and $4.3\mu\text{m}$ for METAL2.

The Fig. 3.10 presents the magnetic field for the optimized coil as a function of the polarization current for a 1V biasing. The size L of the coil is optimized with respect to the process parameters (maximum current density) and to the design rules (the minimum width and spacing of the metal layer). For low current, the parameter to calculate the metal width is the minimum metal width of the technology and for large current it is the maximum allowed current density.

This graph demonstrates that the METAL2 layer is much better than that of METAL1 when the current is higher than 1.5mA. For lower current there is no significant difference between the two metal layers.

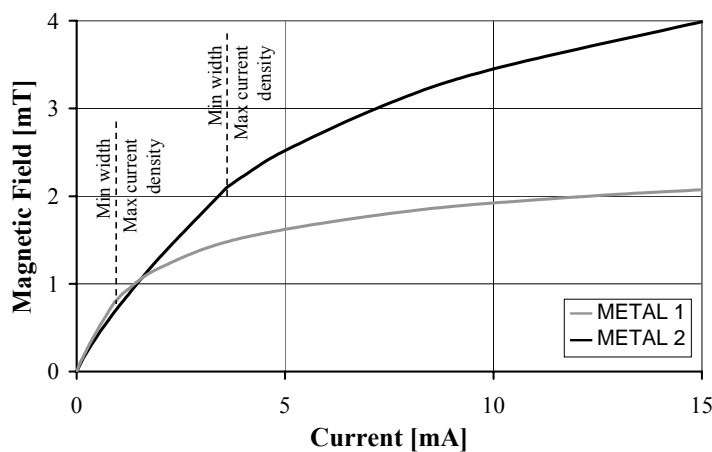


Fig. 3.10 Magnetic field for the optimized coil for each current using typical process parameters and design rules of the CMOS process. For a current higher than 1.5mA METAL2 is much better. Note that a discontinuity appears when the minimum allowed width of the metal is reached, i.e. the width of the turns is no more proportional to the current. For low current, the parameter is the minimum width and for large current it is the maximum current density.

The current related efficiency is also a function of the biasing (Fig. 3.11). The greater the polarization current, the less resistive the coil will be. Consequently the coil has fewer turns and is less efficient. This is the reason why the efficiency is reduced for larger currents. The discontinuity is also due to the variations of the parameters for the optimization. It depends if the width of the lines is determined by process parameters or design rules.

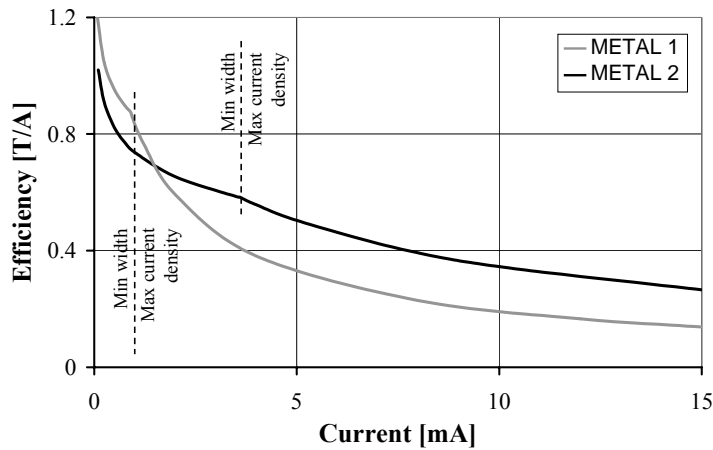


Fig. 3.11 The maximum current related efficiency of a coil is a function of the polarization current. For both of the layers, the current related efficiency decreases when the current is increased. A discontinuity is visible because of the optimization criterion: minimum allowed metal width or maximum current density.

From the two previous figures, we understand that more current leads to greater magnetic fields and less current related efficiency. There is a compromise depending on the application because there are no optimum values.

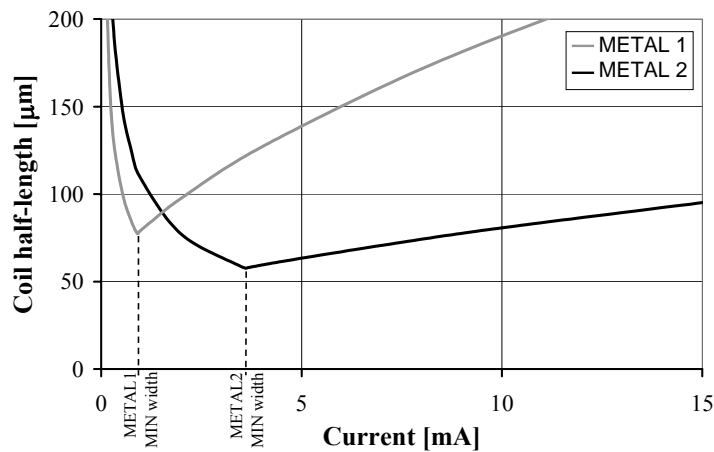


Fig. 3.12 Magnetic field for an optimized coil using typical process parameters and design rules of the CMOS process. For a current higher than 1.5mA the METAL2 is much better.

For a design, the size of the coil is another key parameter. The Fig. 3.12 shows the influence of the biasing current to the size of the coil. The size is minimal when the current density is maximal and when the width of the metal is minimal,

i.e. we use the accuracy of the process and "saturate" the aluminum. From these two values, it was found that the optimum current is 1mA ($0.9 \cdot 1.1$) for METAL1 and 3.6mA ($3 \cdot 1.2$) for METAL2.

For the coil, a current consumption of up to 5mA is reasonable, if it is compared to the biasing current of the sensors. We choose a METAL2 layer because of a much higher magnetic field, smaller coils and relatively good coil efficiency. Furthermore, it is easier to design sensor connections with METAL1 and to keep METAL2 for the coil. Consequently, the coil nominal current is 3.6mA.

We now analyze the behavior of the coil with the optimized metal layer and biasing current with the variations of its size. The magnetic field increases with the size up to 2mT, before the 1V voltage limitation (Fig. 3.13). For larger coils, the magnetic field decreases, because of the coil resistance.

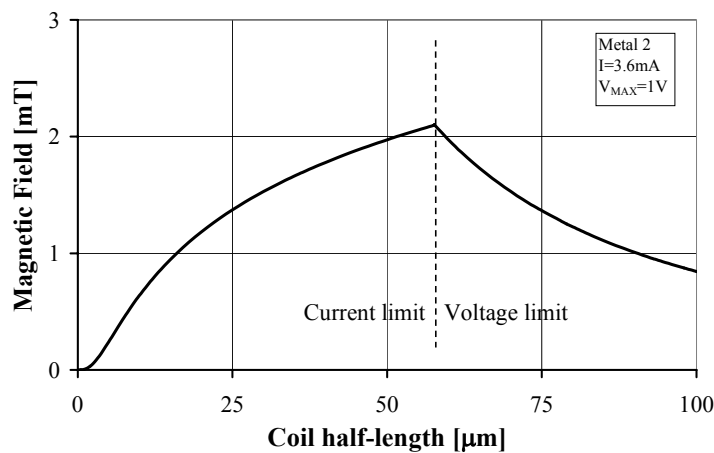


Fig. 3.13 Magnetic field for a METAL2 coil with 3.6mA of biasing current and a 1V compliance. The maximum magnetic field, when the voltage reaches 1V for 3.6mA, is 2.1mT for a coil half-length of $60\mu\text{m}$.

3.6.2 Vertical Hall sensor

We analyze a coil with an equal length l and width L (As calculated in §3.4.2, the equations are symmetric in l and L). The parameter g , depending on the geometry of the coil, is worth 3 with our designs.

The distance between the sensor and the coil is fixed by the sum of the oxide layers and the depth of the sensor inside the silicon. The depth of the sensor's Deep NWell is $7\mu\text{m}$. It is difficult to evaluate where the "center of gravity" of the sensor is; both the sensitivity and the magnetic field are functions of the depth Z_0 . We approximate that the average value is at $1/3$ of the sensor's depth

($2.3\mu\text{m}$). The $2.3\mu\text{m}$ distance between the coil and the silicon is determined by the oxide and aluminum width. Consequently, we evaluate that the total distance Z_0 is $3\mu\text{m}$ using METAL1 and $4.6\mu\text{m}$ using METAL2.

The Fig. 3.14 describes the variations of the magnetic field with a biasing current for the optimized coil and for each current. It demonstrates that the METAL2 layer generates more magnetic field than METAL1 when the polarization current is higher than 1.1mA . The current density is limited to $0.9\text{mA}/\mu\text{m}$ for METAL1 while it is $3.6\text{mA}/\mu\text{m}$ for METAL2; the pitch is 4 times larger for the METAL1 layer when minimum widths are overtaken. Consequently the magnetic field is roughly 4 times smaller using METAL1 when a current higher than 4mA is used.

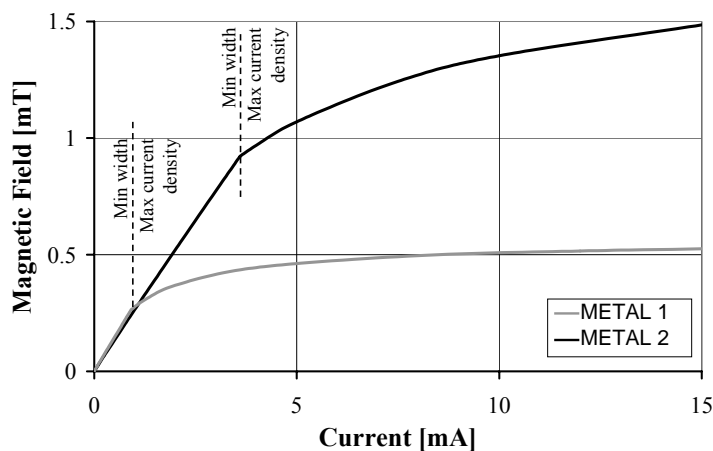


Fig. 3.14 Magnetic field for an optimized coil (its size is a function of the current) using typical process parameters and design rules of the CMOS process. For currents higher than 1.5mA the METAL2 is much better. Note that a discontinuity appears when the minimum allowed metal width is reached.

The second main parameter is the current related efficiency (Fig. 3.15). The current related efficiency is roughly constant when the pitch of the coil is the minimum allowed by the technology. When the current is too high, i.e. the maximum current density is reached, the width of metal lines has to be increased. For this reason, the efficiency decreases rapidly.

From the analysis of the current related efficiency and the magnetic field, it is clear that METAL2 offers better performances with currents greater than 1mA. To obtain a reasonable current related efficiency, it is better to use coils with a minimal metal width (1.2 μm with METAL2).

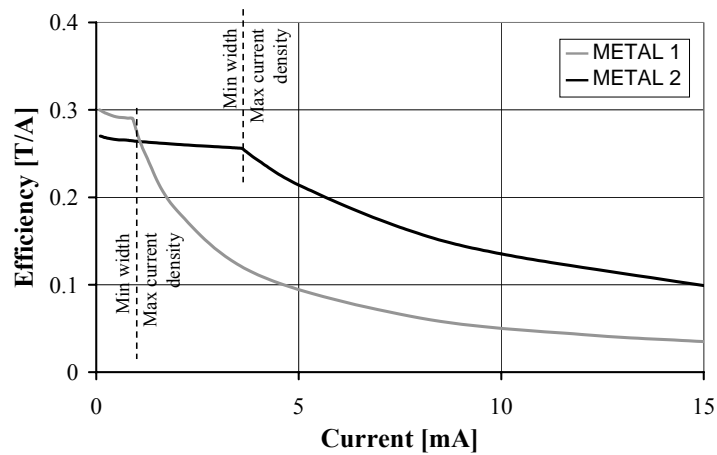


Fig. 3.15 The current related efficiency of the coil is a function of the polarization current. For both layers, the current related efficiency decreases when the current is increased. A discontinuity is visible because of the minimum allowed metal width.

We found that the coils are smallest when the width of metal lines is minimal (design rules) and the current density maximal (process parameters) (Fig. 3.16). The optimum currents are consequently 1mA (0.9mA/ μm *1.1 μm) for the METAL1 layer and 3.6mA (3mA/ μm *1.2 μm) for the METAL2 layer.

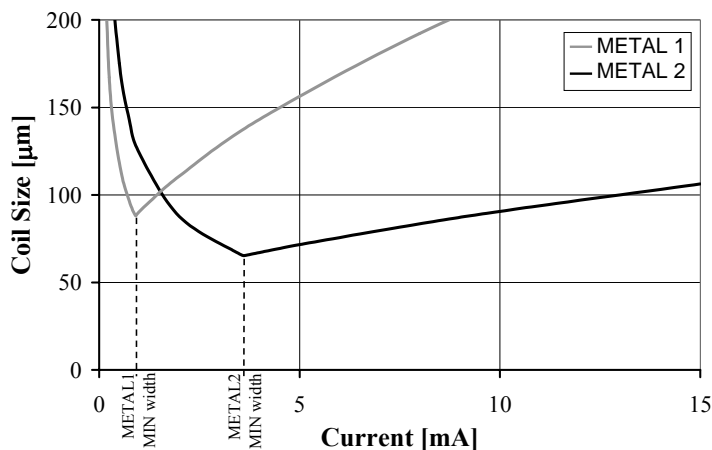


Fig. 3.16 Magnetic field for an optimized coil using typical process parameters and design rules of the CMOS process. For currents greater than 1.5mA METAL2 is much better. Note that a discontinuity appears when the minimum allowed metal width is reached.

Previous analyses clearly demonstrate that METAL2 is the best layer when the polarization current is several mA. The Fig. 3.17 presents the magnetic field for variations of the coil size for the chosen 3.6mA biasing. A magnetic field close to 1mT is produced with an optimum coil. A coil of half the optimum size still produces a field greater than 90% the maximum field.

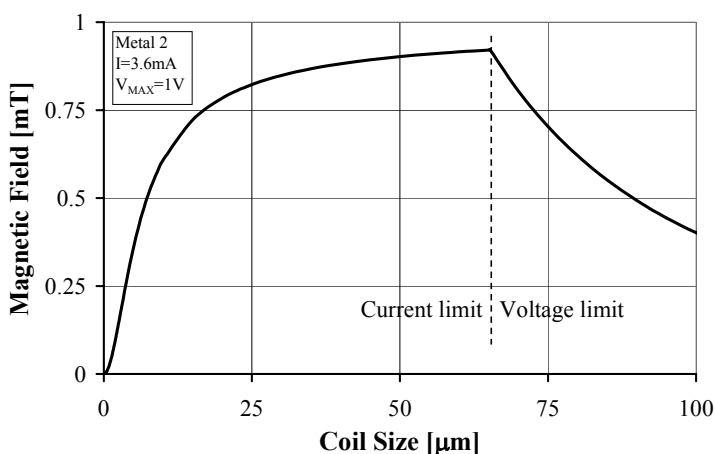


Fig. 3.17 Magnetic field for a METAL2 coil with 3.6mA of biasing current and a 1V compliance. The maximum field, when the voltage reaches 1V for 3.6mA, is 0.9mT.

3.7 Final layout

3.7.1 Miniaturized Hall plate

Our coil, with a minimum width and pitch, has 24 turns, corresponding to the optimization detailed in §3.4.1. Its half length L is $66\mu\text{m}$ ($\rho_{OUT}=15$). We calculate the efficiency, without a hole to place the sensor ($\rho_{IN}=0$), as being:

$$\frac{B}{I} \cong 620 \text{ mT/A} \quad (3.48)$$

The internal part of the coil is removed in order to place the sensor (§3.2). The required half length is at least $50\mu\text{m}$ ($\rho_{IN}=5.7$) when typical Hall plates ($100\mu\text{m}$) are used. We found a coil efficiency of merely:

$$\frac{B}{I} < 70 \text{ mT/A} \quad (3.49)$$

At least 85% of the efficiency is lost due to the sensor size (!). This is incompatible with a low power microsystem. Therefore miniaturized Hall sensors are developed in the §4. The required half length to place this sensor is only $11.9\mu\text{m}$ ($\rho_{IN}=2.7$). This value is close to the maximum efficiency of the loops, with $\rho=1.272$. We calculate a new coil efficiency of:

$$\frac{B}{I} \cong 400 \text{ mT/A} \quad (3.50)$$

When the internal loops are removed and replaced by the miniaturized Hall sensor, the loss of efficiency is less than 35% of the total magnetic efficiency.

A permanent magnetic field of 1.4mT is produced by this coil with the 3.6mA maximum allowed permanent current due to electromigration.

3.7.2 Vertical Hall sensors

There is no need for a hole in the coil to connect the sensor using a METAL2 layer and vertical Hall sensors. The optimum coil measures $65 \times 65 \mu\text{m}^2$ with the minimum pitch allowed in this technology. Because of the limited surface for a sensing part, we choose a width L and length l equal to $25 \mu\text{m}$ and $40 \mu\text{m}$ respectively. The Fig. 3.17 demonstrates that the efficiency reduction is small.

We calculate from (3.44) that the coil efficiency is:

$$\frac{B}{I} \cong 240 \text{mT/A} \quad (3.51)$$

The maximum permanent current, respecting the electromigration rules, is 3.6mA. The magnetic field which is created is 0.85mT.

Our coil efficiency is 85% of the theoretical maximum field from an infinite METAL2 coil.

3.8 Measurements

For the miniaturized Hall plate (μH), the coil input resistance is 240Ω . With the nominal current of 3.6mA, the voltage is 0.86V; 15% lower than the 1V calculated voltage drop. A magnetic efficiency of 390mT/A (Fig. 3.18) is obtained, which results in a permanent field of 1.4mT with the 3.6mA nominal current.

For the vertical Hall sensors (VH), we measure a magnetic efficiency of 230mT/A (Fig. 3.18). This corresponds to a permanent magnetic field slightly smaller than 1mT.

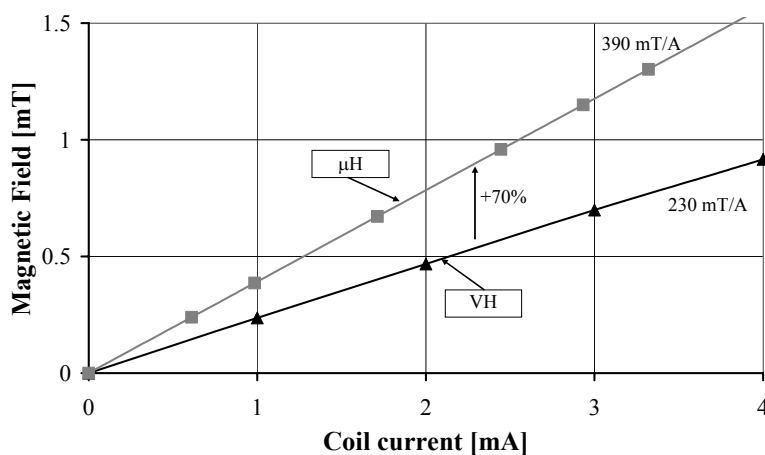


Fig. 3.18 Measurements of the magnetic field. Two coils are developed for Hall plates (μH) and vertical Hall sensors (VH) using AMS $0.8\mu\text{m}$ CXQ and CXZ.

The models of μH sensors provides magnetic fields of 390mT/A and 240mT/A for, respectively, miniaturized Hall plates and vertical Hall sensors. These values correspond well with the measurements. As theoretically predicted, the efficiency of the coil is 70% greater using Hall plates than vertical Hall sensors.

Thanks to high magnetic efficiency, the current required to polarize the coil is low. As a result, the power dissipated by the coil at maximum permanent current is less than 5mW, resulting in a small temperature increase of the chip.

3.9 CMOS technologies trends applied to coils

The trend of CMOS technologies is towards size reduction, including the layer of metallization. The minimum width and the spacing are proportional to the scaling factor s , with the resistivity and current density remaining constant. The supply voltage is also proportional to s in order to maintain a constant electrical field [Frank01]. The table bellow summarizes the performances of the coils extracted from the model of coils for vertical Hall sensors (§3.4.2).

<i>Oxide and metal thickness [m]</i>	1	s
<i>CMOS max voltage [V]</i>	s	s
<i>Current density [A/m]</i>	1	s
<i>Metal resistivity [Ω/\square]</i>	1	$1/s$
<i>Coil surface [m²]</i>	s^2	s^2
<i>Coil resistance [Ω]</i>	1	$1/s$
<i>Nominal current of the coil [A]</i>	s	s^2
<i>Current related efficiency [T/A]</i>	$1/s$	$1/s^2$
<i>Voltage related efficiency [T/V]</i>	$1/s$	$1/s$
<i>Magnetic field [T]</i>	1	1

Table 1. Evolution of coil for vertical Hall sensors performances with the size reduction of CMOS technologies. Two hypotheses for scaling rules are proposed: constant thickness of field oxide and having the metal and the thickness proportional to the scaling factor. Voltage and current related efficiency are in both cases increased by the scaling factor s , while the magnetic field remains constant.

The current related coil efficiency will be increased proportionally to the increase of the scaling factor s . The nominal current of the coil will decrease.

Consequently, the maximum field will stay constant, but with a much lower current consumption. Note that the coil resistance stays constant, because of both maximum voltage and nominal current being proportional to the scaling factor s .

3.10 Array of sensors and coils

The signal to noise ratio of the sensor is doubled when using an array of four sensors and summing the sensors output voltages (see §5.6.1) [Frounch01]. The first internal turns of a coil generate the main contribution to the magnetic field (Fig. 3.6). With an array of sensors, the center part, which is more efficient and has a low resistivity (§3.4.1), can be connected several times in series (Fig. 3.20) to obtain the same resistance as that of single coil.

By summing the Hall voltages, the magnetic signal from the coil is roughly multiplied by the number of sensors in the array and the noise is increased by its square root. Therefore it is more efficient to have an array of smaller coils than only one big one. In order to keep the resistance of the coil, which is limited by the supply voltage and current, constant, the number of turns on each sensor has to be decreased. Therefore, there is an optimal number of sensors in an array. We found that 4 coils and sensors is the solution closest to the best signal to noise ratio.

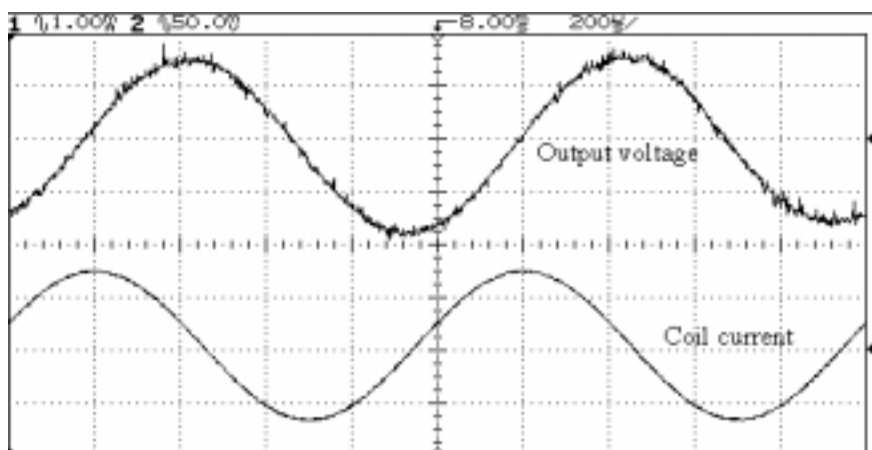


Fig. 3.19 Output signal of a microsystem [Frounch01] using an array of Hall sensors and a spinning current amplification (BW of 1.7 KHz). The integrated coil is supplied with a sine signal of only 1mA RMS and a frequency of 1KHz. The phase shift is due to the filtering.

We achieved a magnetic efficiency of the array of 1570mT/A. It should be compared to previously published values which are about one order of magnitude smaller. For a bandwidth of 1Hz, which is enough for calibration, it results a SNR of 66dB with a coil current of 3.6mA_{RMS} (Fig. 3.19).

3.11 Integrated magnetoconcentrators

A post processing method [Popovic01] to glue at the wafer level a ferromagnetic layer on the chip's surface [Drljaca02] has been developed in our institute. This patented method is used to amplify the magnetic field and to change its direction. The normal use of these magnetoconcentrators is to “suck” the external magnetic field, increasing therein the sensitivity of the microsystem, but the material saturation limits the range of magnetic fields [Drljaca02b].

Furthermore, by putting this ferromagnetic layer on one side of the coil at the chip's surface, it is theoretically possible to double its efficiency, because the reluctance of the magnetic circuit is divided by two. Due to the distance between the coil and the ferromagnetic layer, mainly the oxide isolation and nitride passivation thickness, the coil efficiency is only increased by 40% using this ferromagnetic layer. Experimentally, for the first time we reach an efficiency of 2000mT/A with the 4 coils array.

3.12 Separation of the external and the calibration field

The measured magnetic field is the sum of the unknown external field and the calibration field. One important problem when performing self-calibration is in how to distinguish between the calibration field and an external field [Simon95], due to the perturbations caused by the external magnetic field to the calibration.

One solution is to remove the external field during calibration. This is only possible for some applications, such as a current sensor where the current in the sensor can be suppressed using switches. In the case of angular sensors, where the field is generated by a rotating permanent magnet, this is not feasible.

Our goal is to obtain a sensing part with two outputs (one for the external field measurement and the other one for calibration) without crosstalk. To do that, we explore several methods.

3.12.1 Frequency multiplexing

The first method is to modulate the coil current in order to place the calibration signal outside the bandwidth of the unknown field. The calibration signal is extracted after amplification using synchronous detection. Ideally, the calibration frequency is much greater or smaller than that of the external field. Due to capacitive coupling (see §3.13) between the coil and the sensor [Trontelj94], the coil current frequency is restricted. In our system, we choose 1KHz.

3.12.2 Spatial multiplexing

We introduce a spatial coding of these two fields. This novel solution consists in generating a field with the coil in the opposite directions to each of the pairs of the sensor array (Fig. 3.20), while the external field remains in the same

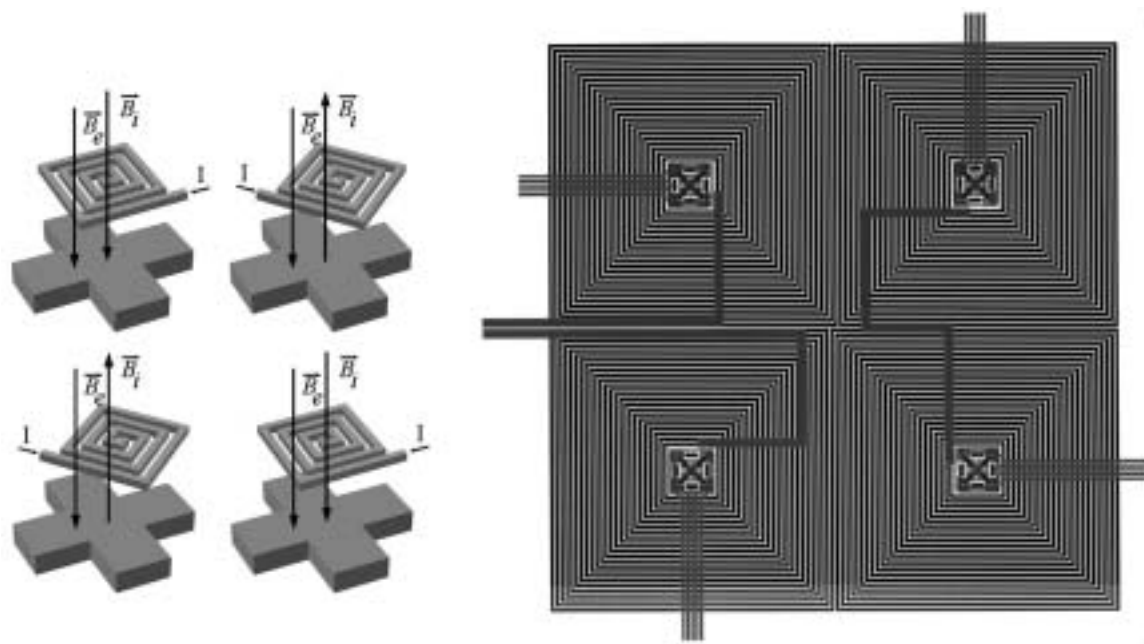


Fig. 3.20 Principle and layout of one sensing part for spatial filtering of the coil's internal and the external signal. 4 coils are put in series around the four Hall sensors. They generate a magnetic field in the opposite direction to one pair of sensors. Modifying the sensors connections, it is possible to sum the signal to measure the external homogenous magnetic field or to subtract the signals in order to measure the coil signal.

direction. To obtain the external field, the Hall voltages are summed and calibrated with the Hall voltages from each pair of sensors and subtracted. For

this purpose, the switch box connections used for spinning current have to be changed using other analog switches but using the same electronic blocks. This technique is based on the matching between four sensors' sensitivity to cancel the external field. We reach with this method a rejection factor of the external field as high as 400.

3.12.3 Shielding with integrated magnetoconcentrators

A final method used to separate the calibration field from the external signal is to shield the sensitivity-meter (Fig. 3.21). Covering the sensitivity-meter with a ferromagnetic layer, it will no more be sensitive to the external field parallel to the chip, as long as it is not saturated. This technique is both useable for Hall plates and vertical Hall sensors.

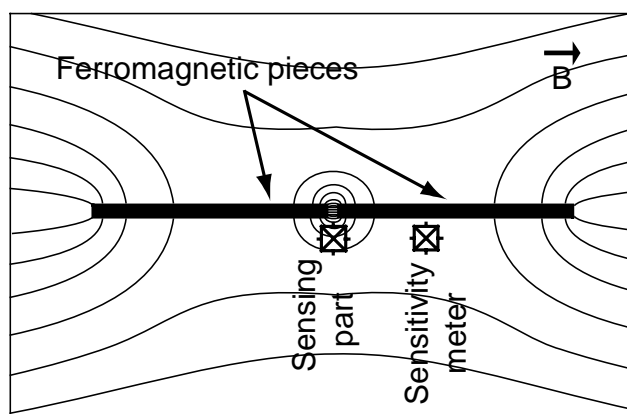


Fig. 3.21 Simulation of a magnetic field parallel to the chip surface with two magnetoconcentrators. Using these ferromagnetic pieces, it is possible to shield the sensitivity-meter and to concentrate the magnetic flux on the sensor. Note that the sensitivity of the system is increased and the coil efficiency of the sensitivity-meter coil is also increased by 40%.

3.13 Parasitic coupling between the coil and the sensor

Ideally, there is only a magnetic coupling between the coil and the sensor. The capacitive coupling between the coil and the sensor is the main parasitic effect [Trontelj94] [Demierre02]. It limits the modulation frequency of the current through the coil. The main contribution comes from direct capacitive coupling from the coil to the sensor and its connections (Fig. 3.22). The coupling through the substrate modifies only the frequency response higher than 50KHz. If this effect is negligible, the cross-signal increases with a slope of 20dB/decade (Fig. 3.23).

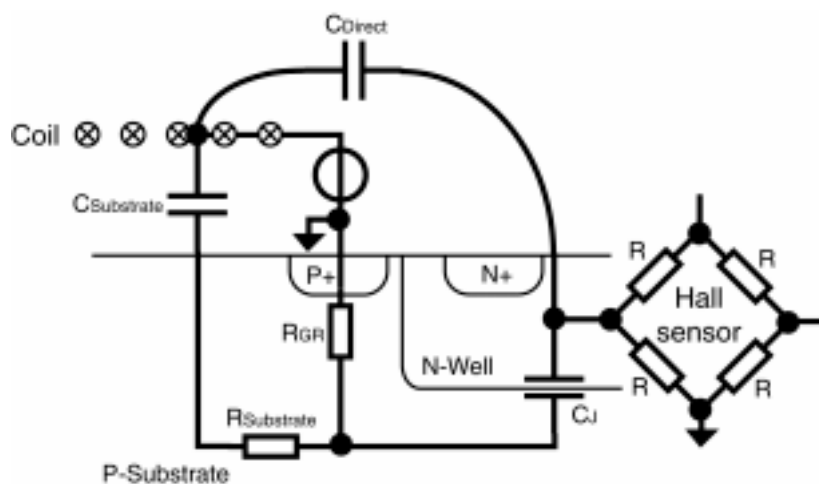


Fig. 3.22 *Electrical model of the coupling between the coil and the sensor. $R_{Substrate}$ is the substrate resistance, R_{GR} is the resistance of the guard ring which surrounds the sensor and C_J the junction capacitance. The main capacitor for parasitic coupling is C_{Direct} which represents the direct coupling without going through the substrate.*

Capacitive coupling causes a common mode and a differential signal at the output of the sensor. The contribution of the common mode is much higher than the differential element, but it is strongly reduced with the common mode rejection of the differential preamplifier. The differential signal is related to asymmetries between the coil and the sensor including its connections. We propose several methods to reduce these two perturbations. By using synchronous detection, we separate the Hall and the parasitic voltages, because the phase shift between the Hall signal and the parasitic signal is 90 degrees.

3.13.1 Reduction of the parasitic coupling

The design of the coils and the sensors permits us to reduce the coupling using several rules. The first rule is to make the sensors, its connections and the coils symmetric in order to reduce the differential signal. The second rule is to connect the coils in such a way as to generate capacitive signals which are subtracted by an array of sensors/coils, whereas the Hall voltages are summed. The next rule is to connect the inner part of the coil, which is close to the sensor, to a constant voltage (Fig. 3.23); the parasitic coupling is divided by a factor $3\frac{1}{2}$. This demonstrates that the inner loops of the coil have more influence. The last rule is to shield the active area of the sensor with a conductive layer connected to a constant voltage (Fig. 3.23), i.e. using the METAL1 layer which is between sensor and METAL2 layer; this only reduces the coupling by a factor 2, because the active area of the sensor and its connections are not shielded.

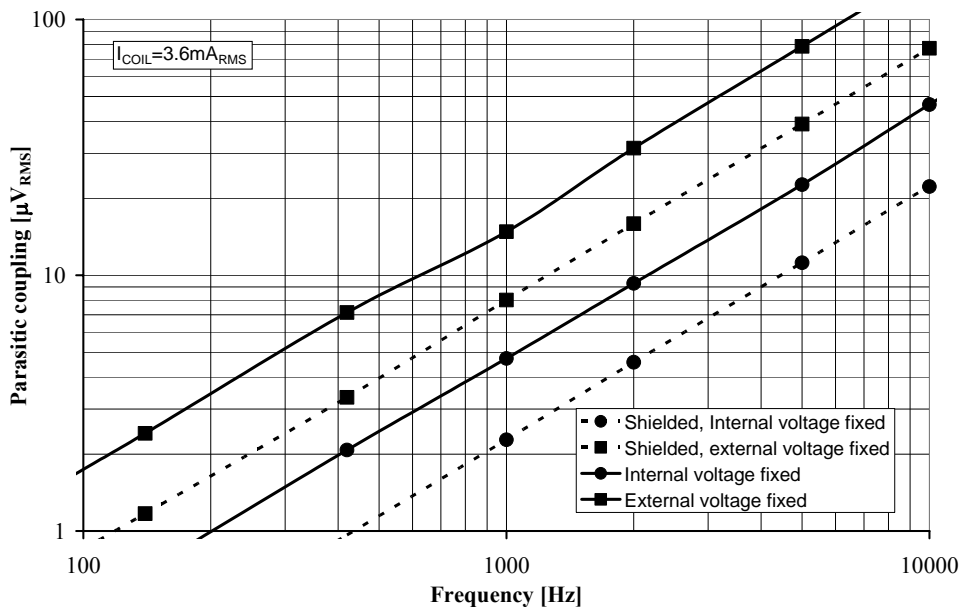


Fig. 3.23 Measurements of the capacitive coupling between the coil and the sensor. Comparison with (plain lines) and without (dashed lines) shielding and with external or internal part of the coil to a fixed voltage. These two methods both reduce the coupling by a factor 7.

Spinning current also reduces this parasitic signal, similarly to the $1/f$ noise elimination. Without the spinning, the parasitic capacitive signal $P(t)$ is a sine with an amplitude P_0 and a frequency F_C at the output of the amplifier.

$$P(t) = P_0 \sin(2\pi F_C t) \quad (3.52)$$

During the first spinning phase A, with a period T_S .

$$V_A = V_{HALL} + P(nT_s) \quad (3.53)$$

During the phase B, $T_S/2$ later:

$$V_B = -V_{HALL} + P\left[T_s \left(n + \frac{1}{2}\right)\right] \quad (3.54)$$

At the output of the demodulator, the signal V_{OUT} is:

$$\begin{aligned} V_{OUT} = V_A - V_B &= 2 \cdot V_{HALL} + P(nT_s) - P\left[T_s \left(n + \frac{1}{2}\right)\right] \\ &\cong 2 \cdot V_{HALL} - \frac{T_s}{2} P'(nT_s) = 2 \cdot V_{HALL} - \pi F_C T_s P_0 \cos(2\pi n F_C T_s) \end{aligned} \quad (3.55)$$

If we compare the parasitic signal amplitude with and without spinning with a frequency F_S , an attenuation of a factor A_C is found:

$$A_C = \frac{2 F_S}{\pi F_C} \quad (3.56)$$

As expected, the measurements confirm a huge attenuation when a spinning current of several 100KHz is employed.

3.14 Self-Calibration

3.14.1 Twin Hall Microsystem

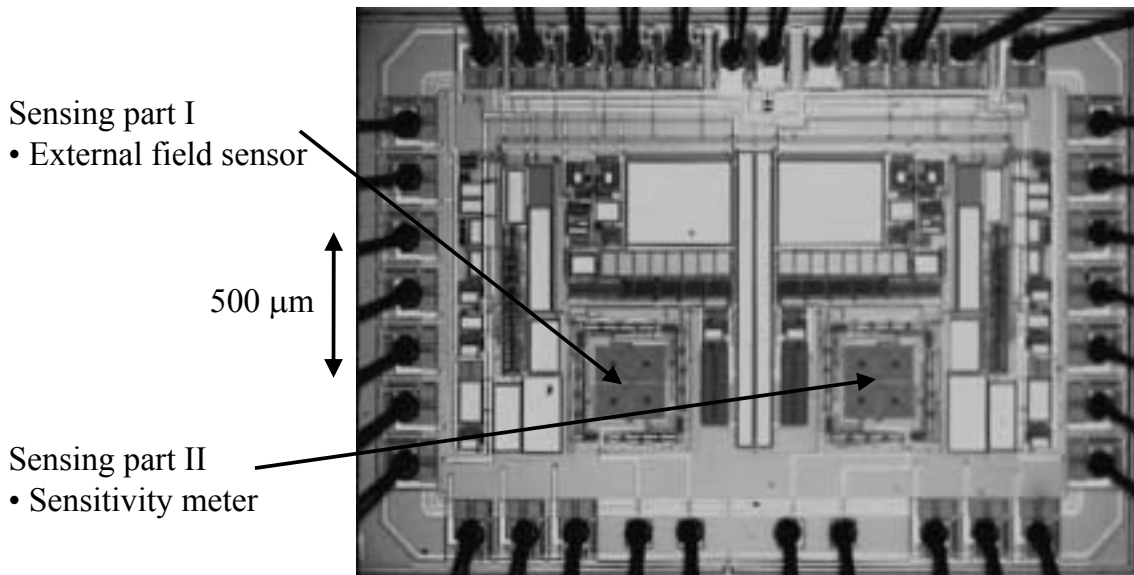


Fig. 3.24 Picture of the twin microsystem. This system contains two identical sensing parts. The first one is used to measure the external, unknown field, whereas the second measures the reference magnetic field produced by an integrated coil. This microsystem contains twice electronics for the spinning current.

Based on the idea of the integrated calibration coil, we developed a twin Hall microsystem using spinning current technique [Frounch01]. This microsystem contains two sensing parts (Fig. 3.24): the first of them is used for measuring the external field, the other for calibrating the microsystem (see §2.2) [Petr88]. The two sensing parts are close to each other, this ensures a good matching of their characteristics; we assume that the drifts of both sensors are equal. One sensor is used as a so called sensitivity-meter. This Hall sensor measures the stable reference magnetic field coming from the integrated coil described before.

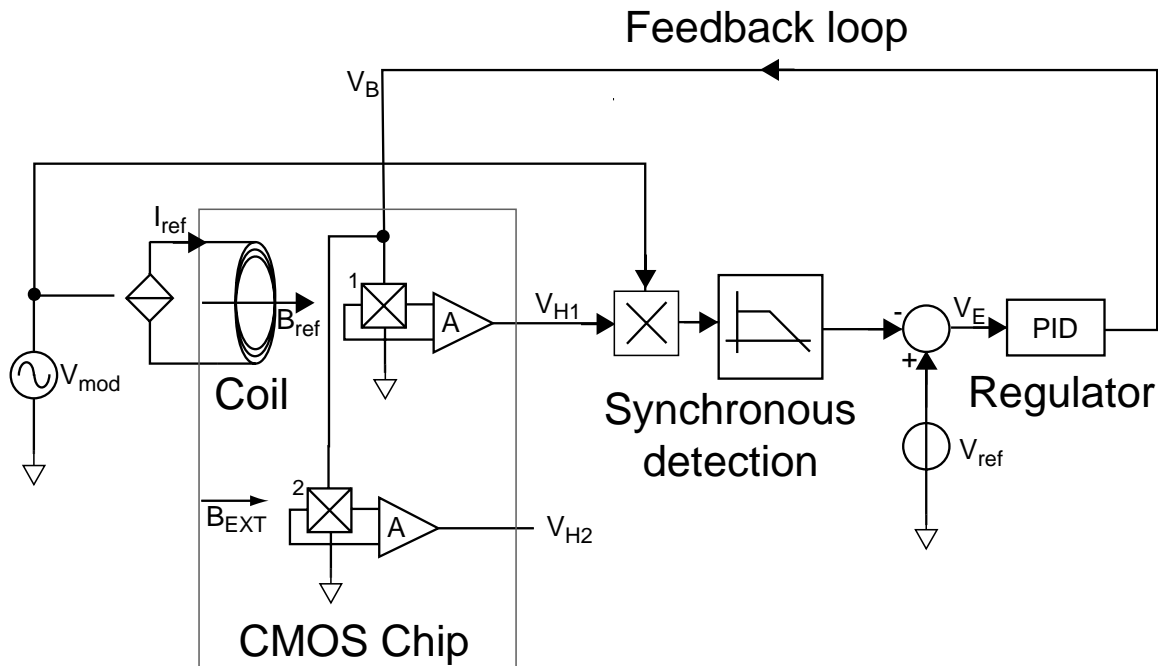


Fig. 3.25 Simplified bloc diagram of the self calibration system. One sensor is used to measure the internal field coming from the integrated coil B_{REF} ; this part is called the sensitivity meter. The second sensor measures the external field B_{EXT} . The output of the PID regulator directly controls the biasing voltage V_B of both Hall sensors.

The output V_{H2} of the sensitivity-meter (Fig. 3.25) is the product of the reference magnetic field B_{ref} , the voltage related sensitivity S_{V2} , the biasing voltage V_B and the preamplifier gain A_2 . The signal to noise ratio at the output of this amplifier is very poor due to the high sensor and electronic thermal noise. For this reason, the bandwidth of the sensitivity-meter is strongly limited by an external cutoff frequency low pass filter of 0.5Hz. This value is much higher than the usual sensitivity fluctuations for most applications; the thermal time constant is less than 1Hz. After filtering, it results in an SNR of about 70dB. To avoid residual offset and 1/f noise after the spinning current block, an AC coil with a current at a frequency of 1KHz is used.

This filtered output signal is subtracted from the reference sensitivity voltage V_{ref} to obtain the voltage error V_e . By adapting the biased voltage V_B , the Proportional Integrator Derivator (PID) regulator maintains the error voltage V_e at zero:

$$V_e = V_{ref} - V_{H2} = V_{ref} - S_{V2} V_B B_{ref} A_2 = 0 \quad (3.57)$$

The reference magnetic field B_{ref} is proportional to the coil current I_{ref} and the constant Γ dependant only on the geometry of the coil:

$$B_{ref} = \Gamma I_{ref} \quad (3.58)$$

Since the regulated bias voltage V_B is common to both sensors, the output voltage V_{H1} of the first sensor, which measures the output field, is equal to:

$$V_{H1} = S_{V1} V_B B_{EXT} A_1 \quad (3.59)$$

Here S_{V1} is the voltage related sensitivity, A_1 the gain of the preamplifier and B_{EXT} the external field to be measured. Due to matching, the ratios A_1/A_2 and S_{V1}/S_{V2} are roughly equal to one. From previous equations, we find that the sensitivity S of the microsystem using self-calibration is given by:

$$S = \frac{V_{H1}}{B_{EXT}} = \frac{1}{\Gamma} \frac{V_{ref}}{I_{ref}} \equiv \frac{1}{\Gamma} R \quad (3.60)$$

With R an equivalent resistor equal to the ratio V_{ref}/I_{ref} .

In this way, we replace the semiconductor parameters of the sensor by the coil parameters, which have a negligible drift. The parameter R is equivalent to a resistor which transforms voltage reference to current.

A driftless resistor can be used instead of two reference sources; this idea is equivalent to canceling the current drift in Equ. (3.58). The company Schneider Electric Industry took out a patent [Hazard99] with a similar idea of removing the influence of electronic references, but only for digital electronics. Their invention is to develop a digital sensitivity-meter which is insensitive to electrical references. The same voltage is used as reference for a digital to analog converter and for the calibration of the current source. Their system directly gives a digital signal of the sensor sensitivity to calibrate the system using a digital compensation of the magnetic sensor instead of an analog one in our case. The drawback of the proposed method is that the system needs a driftless resistor which cannot be integrated using standard CMOS technologies.

3.14.2 Results

In order to test this principle, we integrated the two sensors, the two preamplifiers and the calibration coil on a CMOS chip (Fig. 3.25). Using external current and voltage references and a regulator, the sensitivities of the 6 samples of the microsystem are measured from -20°C to 100°C with sensors

glued to a plastic substrate. We obtained an average drift of less than 30ppm/°C (Fig. 3.26). The drift coming from thermo-mechanical stresses induced by packaging, as high as 750ppm/°C [Dragan00], is reduced by a factor 25 using the proposed calibration technique.

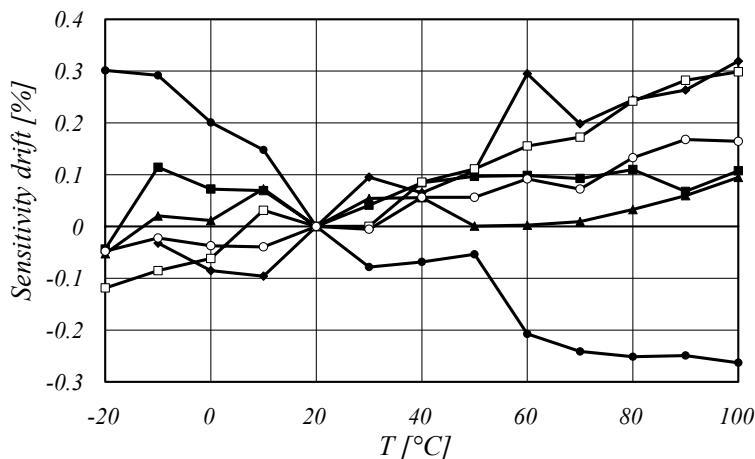


Fig. 3.26 Sensitivity thermal drift for 6 chips glued on a plastic substrate. A drift of only between 10 and 30ppm/°C is obtained.

The results (Fig. 3.26) clearly demonstrate that the residual drift varies from chip to chip. Mismatches between components on the same chip, including the sensors, are the sources of the residual drift. This is the main limitation of the present twin sensor microsystem. Note that the distance between the sensing part is not minimal with this first design and they are not at the center of the chip, where the stresses are homogeneous [Dragan00]; better results are expected with a new design.

We estimate the reference magnetic field drift due to geometry variations to be about 5ppm/°C. With discrete components and laboratory instruments, the accuracy of the regulator is below 5ppm/°C and the drifts of the references are negligible.

Stresses applied to the sensor will also induce piezoresistive effects. They unbalance the resistor bridge of the sensor and consequently create an offset voltage. In Fig. 3.27, the offset temperature drift using the spinning current method is measured. The calibration principle with the self-calibration coil is unfortunately unable to compensate offset and therefore offset drift. This drift in our microsystem is as high as $1 \div 2 \mu\text{T}/^\circ\text{C}$. The only way to resolve this problem is to reduce residual offset of the spinning current method.

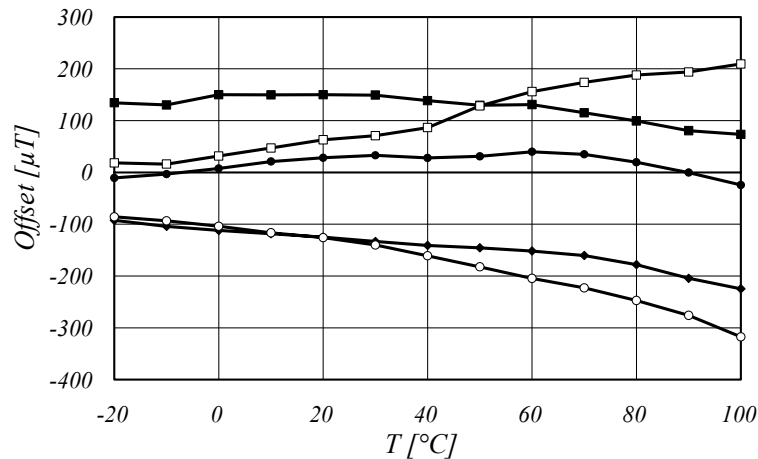


Fig. 3.27 Offset thermal drift for a sample of 5 chips glued on a plastic substrate. Offset variations cannot be removed with our calibration method. It is typically $1\div 2 \mu T/^{\circ}C$. For most DC applications this effect is clearly the limiting factor.

3.15 Geometrical reference

Using CMOS electronics, it is almost impossible to develop a current source with such ultra-low drifts of less than $5 \text{ ppm}/^{\circ}C$. We propose two schemes to solve this problem in such a way that the complete system can be fully integrated.

As shown in Equ. (3.60), the two references have to be replaced by a single one, using a resistor R to generate the current reference for the coil and the voltage reference for the regulator. To avoid resistor drift it is impossible to use standard CMOS resistors. Consequently an external (discrete) high accuracy resistor is required.

To avoid the use of an external resistor R , we propose to replace the voltage sensitivity reference by a current reference (Fig. 3.28). Of course, it is impossible to subtract voltages and currents. This is the reason why the amplifiers have to be transconductance amplifiers, which means they provide a current output.

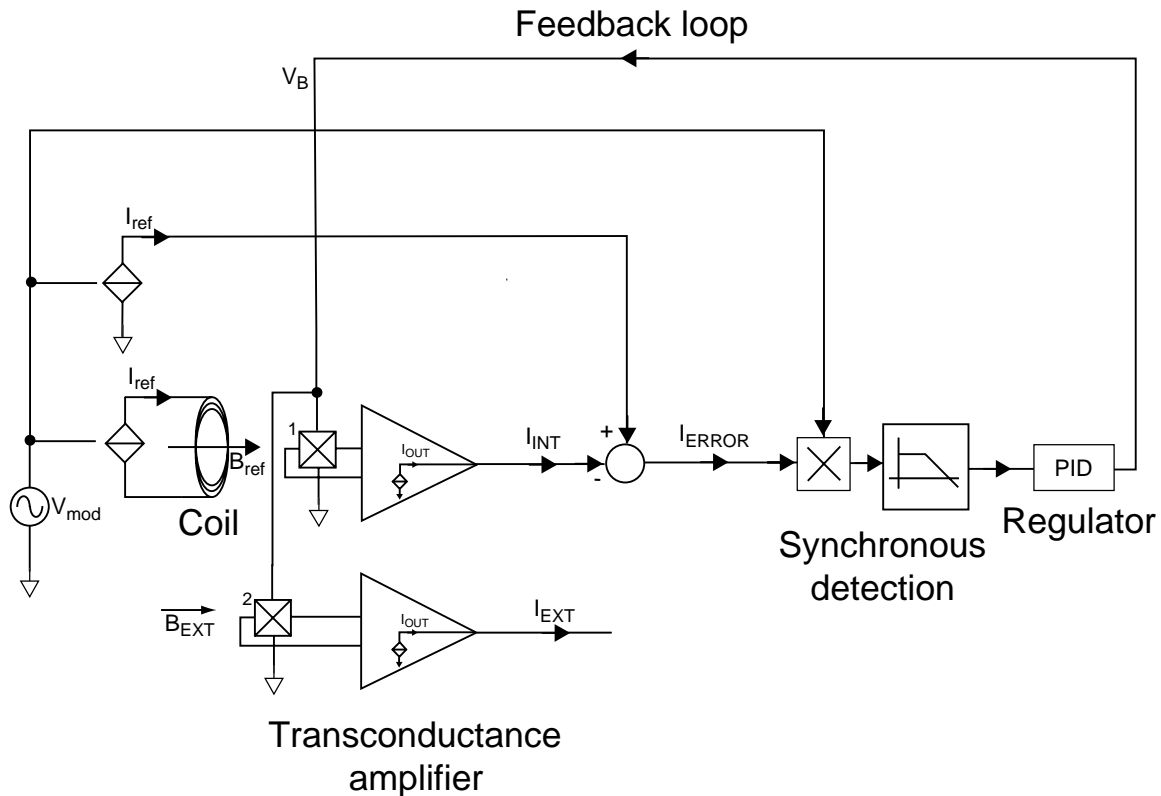


Fig. 3.28 Bloc diagram of the fully integrated self calibration system which is not sensitive to voltage or current reference drifts. A single AC source is used to modulate both coil current and reference current sources. Transconductance amplifiers are necessary in order to make the current outputs (I_{INT} and I_{EXT}) compatible with our sensitivity current reference. The internal current I_{INT} is subtracted from the modulated reference current to obtain the sensitivity error. When the sensitivity is compensated, this current is equal to zero. The output of the microsystem is a current output I_{EXT} , because the amplifier is the same as for calibration.

Using transconductance amplifiers, the voltage of both Hall sensors are converted to current outputs to be compatible with the sensitivity reference I_{REF} . The internal current I_{INT} , which measures the calibration field, is subtracted from

the reference current; the sensitivity error I_{ERROR} is therefore obtained. This value is used as input of a regulator which controls the polarization voltage (or the current) of both internal and external sensors to maintain the sensitivity constant. Consequently, the sensitivities of both internal and external sensors are equal.

Using this technique, the sensitivity only depends on the Γ parameter describing the coil geometry (3.61); the sensitivity is no longer related to the properties of the semiconductor.

$$S = \frac{1}{\Gamma} \quad (3.61)$$

As a result, the microsystem output I_{EXT} is a current output; an external driftless resistor is only required if a voltage output is needed for the application.

3.16 Conclusions

Two types of coils are studied; one for Hall plates and the second for vertical Hall sensors. We propose for each coil an analytical model (§3.4.1 and §3.4.2). Comparisons with measurements match well the model, with respectively a 2.5% and a 19% deviation (§3.8). Based on this model, we optimize the coils in order to obtain a compromise between magnetic field, current related efficiency and coil size.

For Hall plates, we demonstrate the advantages of scaling down the coil size and consequently the sensor size; using small coils with miniaturized sensors, their performances are increased by a factor 6. We also found the limitation of the scaling down due to the vertical distance between the coil and the sensor. This distance is determined by the CMOS process. A current related efficiency of 390mT/A is obtained, which compare well with the other published values of 30mT/A [Simon95] and 150mT/A [Trontelj94].

We demonstrate the advantages of the arrays of coils and sensors (§3.10). With an array of 4 coils, an efficiency of 1568mT/A is obtained. This is then increased to 2000mT/A by adding a ferromagnetic layer (integrated magneto-concentrators) on the surface of the chip in order to reduce the reluctance of the magnetic circuit.

For vertical Hall sensors, the developed coil produces 85% of the maximum theoretical field. We measure a current related efficiency of 285mT/A. The coil produces a field of up to 1mT with only a 3.6mA current. This field is large enough for the calibration.

The coils are optimized using as parameter the maximum current density of the conductive layer. This current density allows the permanent use of the coil without degradation of the conductive stripes because of electromigration. For some applications, where the temperature variations are slow, the calibration is requested only periodically. The current density can be increased substantially when the duty cycle is small. It results a larger magnetic field with a specific coil.

We apply several methods in §3.12 to separate the calibration field from the external unknown magnetic field. An AC magnetic field and a synchronous demodulation are able, in the frequency domain, to separate the calibration signal from the bandwidth of the field to be measured. We separate the calibration signal spatially by generating the calibration field using an array of coils which generates a field in opposite directions. Ferromagnetic integrated layers are used to shield the calibration sensor from the external field. This technique also increases the calibration coil efficiency to 40%.

We also developed a self-calibrated Hall microsystem (§3.14.1). It is based on a twin Hall microsystem. The first one continuously measures the external field, while the second performs the calibration; we have called it a sensitivity-meter. The sensitivity-meter produces an SNR of 70 dB for a bandwidth of 1Hz with only a 3.6mA coil polarization. We reach a thermal drift as low as $10\div 30\text{ppm}/^\circ\text{C}$, even if the position of the Hall sensors are not optimal (near by and at the center of the chip). Note that this method not only greatly reduces thermal drift, but also any types of drifts, including long term fluctuations.

We have also proposed a way to obtain a magnetic measurement which is not dependant on voltage and current references. We call it a geometrical reference (§3.15), because only the geometry of the coil determines the sensitivity of the system. The only way to obtain this type of reference is to use a microsystem with a current output. An external precision resistor is only required if a voltage output is needed for the application.

In the case of coils for Hall plates, a miniaturized sensor is required. The next chapter studies the miniaturization of the Hall sensor and its consequences.

3.17 References

- [Demierre02] M. Demierre, S. Pesenti, J. Frounchi, P.-A. Besse and R. S. Popovic, Reference magnetic actuator for self-calibration of a very small Hall sensor array, *Sensors & Actuators A: Physical*, 97, pp. 39-46, 2002.

-
- [Dragan00] Dragan Manic, *Drift in Silicon Integrated Sensors and Circuit due to Thermo-Mechanical Stresses*, ed. Hartung-Gorre Verlag, Konstanz, 2000.
- [Drljaca02] P. M. Drljaca, P. Kejik, F. Vincent, D. Piguet, F. Gueissaz, R. S. Popovic, *Single Core Fully Integrated CMOS Micro-fluxgate Magnetometer*, proceedings of the XVI Eurosensors Conference, Prague, 2002.
- [Drljaca02b] P. M. Drljaca, F. Vincent, P.-A. Besse and R. S. Popovic, *Design of planar magnetic concentrators for high sensitivity Hall devices*, *Sensors & Actuators A: Physical*, Vol 97, pp. 10-14, 2002.
- [Frounch01] J. Frounchi, M. Demierre, Z. Randjelovic, and R. Popovic, *Integrated Hall Sensor Array Microsystem*, ISSCC2001 Conference, San Francisco, pp. 248-249, 2001.
- [Hazard99] P. Hazard and A. Boulahtit, *Dispositif de mesure de la sensibilité d'un capteur de champ magnétique à effet Hall*, Schneider Electric Industries SA, demande de brevet français FR 9909380, 1999.
- [Mackay00] K. Mackay, M. Bonfim, D. Givord and A. Fontaine, *50T Pulsed Magnetic Fields in Microcoils*, *Journal of Applied Physics*, Vol.87 (4), 2000.
- [Melexis01] MLX90215 – Precision Programmable Linear Hall Effect Sensor, Datasheet Melexis, 2001.
- [Petr88] J. Petr, H. Lienhard, *Compensating circuit for a magnetic field sensor*, US Patent 4752733, 1988.
- [Popovic84] R.S. Popovic, *The Vertical Hall-Effect Device*, *IEEE Electron Dev. Lett.*, EDL-5(9), pp. 357-358, 1984.
- [Popovic96] R.S. Popovic, J.A. Flanagan, P.A. Besse, *The future of magnetic sensors*, *Sensors and Actuators A56*, pp. 39-55, 1996.
- [Popovic01] R.S. Popovic, P.M. Drljaca, C. Schott, R. Racz, *Integrated Hall Sensor / Flux Concentrator Microsystems*, Invited Lecture, 37th International Conference On Microelectronics, Devices And Materials, MIDEM 01, Bohinj, Slovenia, October 2001.
- [Simon95] P.L.C. Simon, P.H.S. de Vries, S. Middelhoek, *Autocalibration of silicon Hall devices*, *Transducers 95*, 291-A12, pp. 237-240, 1995

[Trontelj99] Janez Trontelj, Optimization of Integrated Magnetic Sensor by Mixed Signal Processing, Instrumentation and Measurement Technology Conf., pp. 299-302, 1999.

[Trontelj94] Janez Trontelj, Lojze Trontelj, Roman Opara, Anton Pletersek, CMOS Integrated Magnetic Field Source Used as a Reference in Magnetic Field Sensors, Instrumentation and Measurement Technology Conf., 1994 461-463.

4 Miniaturized Hall plates

When a coil is placed around a usual sized Hall plate, the coil efficiency, i.e. the ratio of the magnetic field over the current consumption, is poor (§3.7.1) [Demierre02]; about 85% of the magnetic field is lost when the internal turns of the coil are removed to place the sensor. This considerably limits the applications of coils, especially for low power microsystems. This is the reason why the coil and consequently the sensor placed at the center of the coil have to be scaled down. Moreover, the spatial resolution is enhanced. The scaling down of the Hall sensor and its consequences are the topic of this chapter.

What are the limits of the CMOS Hall sensor miniaturization? By a first approximation, the characteristics of Hall sensors (current and voltage related sensitivity, and resistance) are independent of the size of the sensors (§2.1). However the lateral diffusion during the diffusion during the process and the junction field effect limit the miniaturization.

In this chapter, we developed a miniaturized Hall plate with an implantation window of 2.4 μm . This sensor, a miniaturized Hall plates, is optimized taking also into account the lateral diffusion and the junction field effect. We also developed a simplified model to qualitatively understand the consequences of the size reduction on the sensor behavior. We assume that we remain in a linear drift of carriers, without velocity saturation. The advantages of miniaturized sensors with integrated magnetoconcentrators [Drljaca01] are also studied.

CMOS Vertical Hall sensors using a high-voltage technology (see §2.2.1) are intrinsically miniaturized because of the limited depth of implantation CMOS Wells [Schurig02]. They suffer from the same non-linear behavior because of a large junction field effect. Even if the first generation of these sensors was designed myself, they were afterwards optimized by a colleague for its own thesis. This sensor is naturally not presented within this chapter, but the main characteristics are presented in the §2.2.1.

4.1 Layout

To be compatible with the spinning current techniques (§2.1.5), the sensor has to be symmetrical with the rotations of the biasing. A cross (§2.1.1) is chosen for the 2- and 4-phases spinning current method because of a relatively good geometrical factor G (0.8 with the arms length equal to their width) and its immunity to alignment tolerances of the process [Randjel00].

The active area of the sensor using AMS 0.8 μm CXQ is the NWell of PMOS transistors. It has a 4 μm t_{NW} depth and a $2 \cdot 10^{16} \text{cm}^{-3}$ $N_{D,NW}$ doping level. It is buried using the P+ implantation ($N_{A,P+} = 2 \cdot 10^{16} \text{cm}^{-3}$) used for drain and source of PMOS transistors. This implantation has a 0.5 μm t_{P+} depth. Buried sensors are less sensitive to surface effects and trapped charges in the oxide layer. These charges induce image charges in the active layer; they are sources of 1/f noise and instabilities of the sensitivity [Randjel00]. Moreover, this P+ implant makes the sensor thinner achieving therefore a higher current related sensitivity. Ohmic contacts with the NWell are obtained using the N+ implantation below the contacts.

4.1.1 Lateral diffusion

The NWell of AMS 0.8 μm CXQ is obtained through a diffusion with a depth of 4 μm . This diffusion is not only vertical, but also lateral, diffusing beyond the edge of the mask [Sze85]. With a 4 μm depth of the Nwell, the lateral diffusion length, which is about 80% of the depth of diffusion, extends over more than 3 μm (Fig. 4.1). The laterally diffused part of the well has a lower doping level than the centrally diffused part. Miniaturized sensors have a width of implantation of only several micrometers; it is the same order of magnitude as

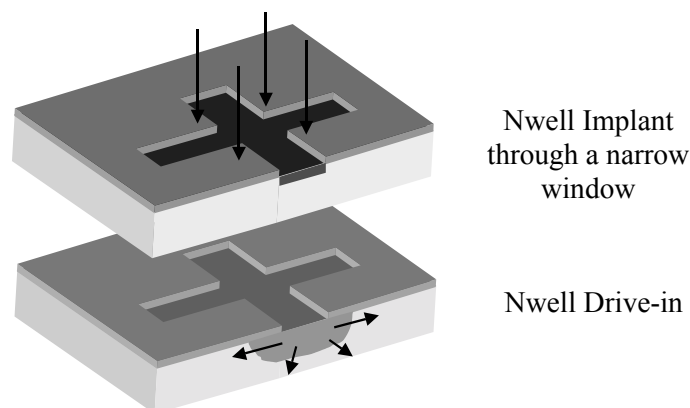


Fig. 4.1 The doping level of small Hall devices is decreased by lateral diffusion during Drive-in. This will directly increase the current related sensitivity.

the length of diffusion. Consequently this lateral diffusion occurs inside the whole NWell; its doping level is lower than the value of the process parameters.

The doping level of modern CMOS technologies is too high for Hall devices to obtain a reasonable current related sensitivity of more than 100V/AT (see §2.1). We have therefore used the lateral diffusion to voluntarily reduce the doping [Randjel99] [Patent]. Simulation from the software ISE-TCAD of the AMS 0.8 μ m CXQ CMOS process confirms the rapid decrease of the doping level with the reduction of the implantation width; this is due to the lateral diffusion (Fig. 4.2).

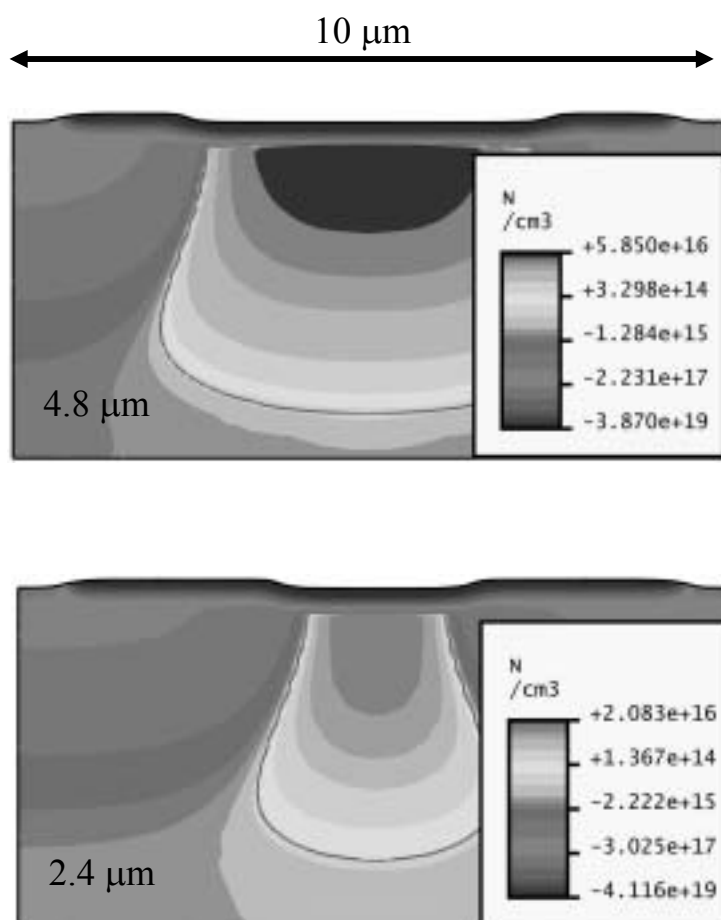


Fig. 4.2 2-D Process simulation of the sensor using Genesis. In this technology, the lateral diffusion is limited by a self aligned P-well which gives this typical pear shape. P+ implant is used to bury the sensor.

This technology implants a PWell complementary to the NWell. This implantation also has a lateral diffusion which goes against the lateral diffusion

of the NWell. It is similar to an increase of the substrate doping level in the area of lateral diffusion. As a result a “pear shape” is observed because of the smaller depth of implantation of the PWell.

The doping level depends on the width of implantation. We compared the simulation to the doping level extracted from the measurements of the current related sensitivity. The current related sensitivity is inversely proportional to this doping, if we assume that the geometrical factor, the sensor depth and the Hall factor are constant. We measure a current-related sensitivity of about 180 V/AT for a 2.4 μm implantation, which is almost twice that found in Hall sensors of conventional size made with the same technology. The good correlation between the process simulation and the sensitivity measurements (Fig. 4.3) allows us to use simulations to optimize the sensor geometry (§4.3).

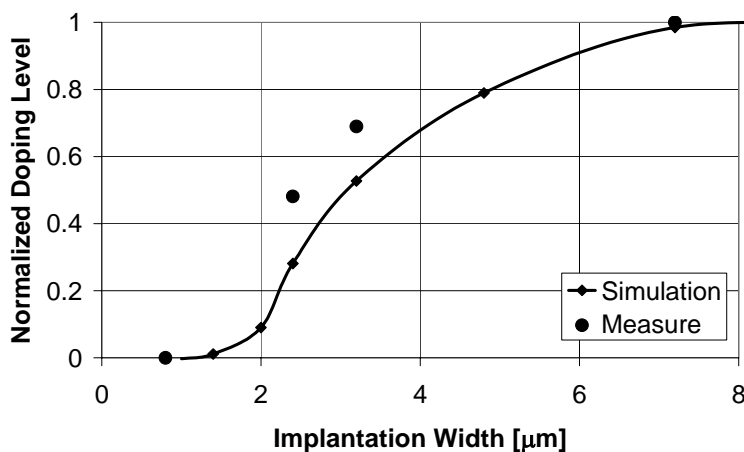


Fig. 4.3 Process simulation of the doping level with the scaled down sensor. It is compared to the inverse of the measured current related sensitivity. The results are normalized to a large sensor; the normalization corresponds to $7.3 \cdot 10^{16} \text{ cm}^{-3}$ for the simulation and to a sensor with a sensitivity of 89V/AT for the measurements. We assume that the depth of diffusion t_{NW} remains constant to extract the doping level from sensitivity measurements.

A miniaturized sensor with a mask width for the NWell of only 2.4 μm (Fig. 4.4) is chosen for the next part of this chapter; this value is more than 20 times smaller than that of common Hall devices in this technology. While designing this sensor, the design rules for the NWell were not completely respected. However, they are defined for transistors and some are not directly related to the limitations of the fabrication process.

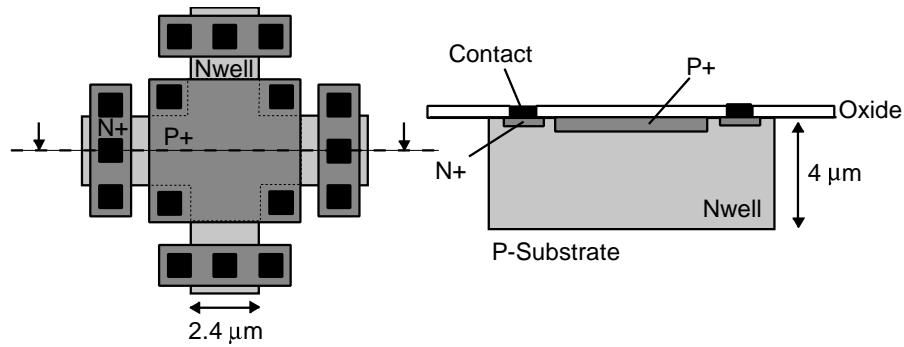


Fig. 4.4 Miniaturized Hall sensor with a $2.4\mu\text{m}$ implantation width. This width, inferior to the $4\mu\text{m}$ diffusion length, is more than 20 times smaller than common Hall devices

4.2 Measurements

4.2.1 Input resistance

The NWell resistance per square R_{\square} is a constant, even if there is lateral diffusion when the substrate is not doped. We can calculate from §2.1 that R_{\square} is equal to:

$$R_{\square} = \frac{1}{q \cdot \mu \cdot D_{NW}} \quad (4.1)$$

With D_{NW} the implanted dose, q the electron charge and μ the mobility.

The measurements (Fig. 4.5) show on the contrary that the square resistance increases with the reduction of the implantation width. This is due to the junction field effect (see the model at the §4.3) and also to the complementary highly doped PWell which pinch the NWell for small implantation. Junction field effect is also the source of the non-linear behavior with input voltage. It strongly appears when the implantation width is smaller than half the depth of implantation ($<2\mu\text{m}$).

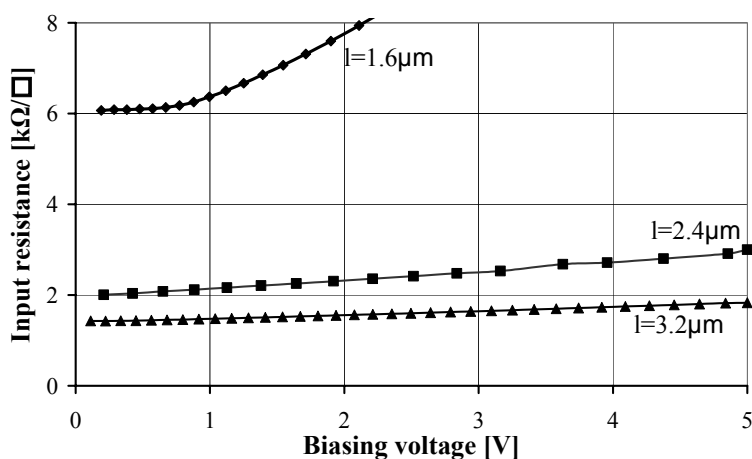


Fig. 4.5 Measurements of the resistance per square vs. variations of the input voltage for several implantation widths. The substrate and the bottom sensor contact are short-circuited. For implantation width smaller than the depth of diffusion, the lateral diffusion decreases the doping level, which increases the resistance. The junction field effects substantially modify the resistance; when it is dominant (top curve), it is demonstrated by a strong non-linear behavior.

4.2.2 Sensitivity

The current related sensitivity is inversely proportional to the doping level (§2.1). When the design rules for NWell are respected, i.e. a negligible lateral diffusion, the sensitivity is constant and is fixed by the process parameters of the process. However when the implantation width is the same order of magnitude as the diffusion depth, it decreases due to lateral diffusion. Consequently, with a small implantation width, the current related efficiency is increased (Fig. 4.6).

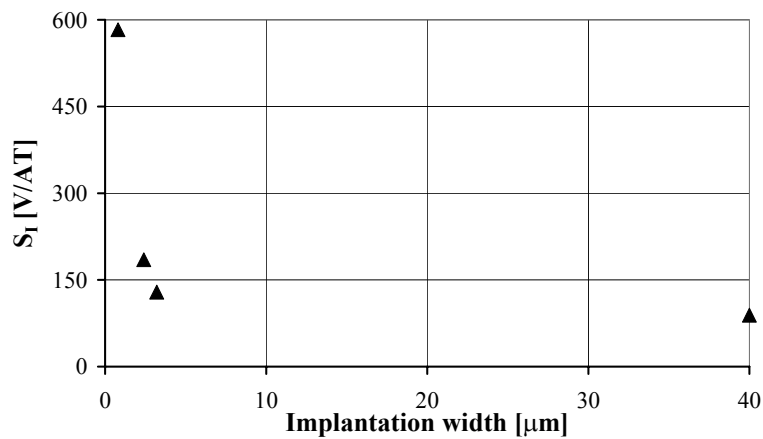


Fig. 4.6 Measurements of the current related sensitivity for several implantation widths. The current related sensitivity stays constant when the implantation width is much greater than the diffusion length.

The higher input impedance of the sensor restricts the biasing current. However an array of sensors can be used to increase the total biasing current and thus the signal to noise ratio.

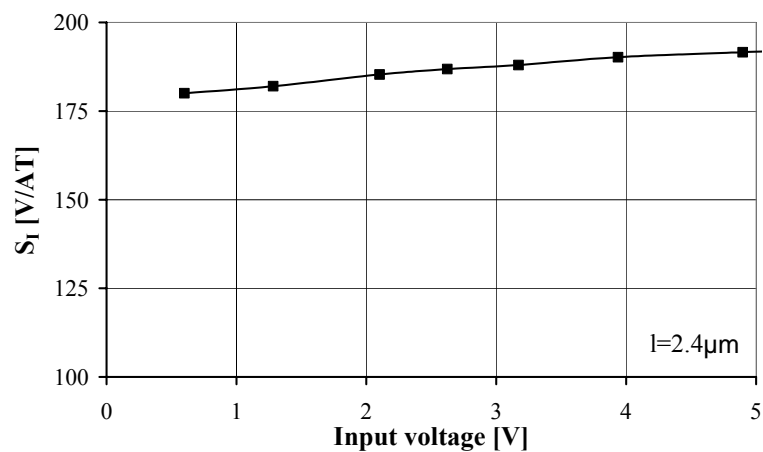


Fig. 4.7 Measurement of the variations of the current related sensitivity with the biasing voltage. Due to junction field effect and with the increase of the biasing, the thickness of the active area is reduced. Consequently the current related efficiency is also increased. The substrate and the bottom sensor contact are short-circuited for this measurement.

The current related sensitivity is also inversely proportional to the sensor thickness. As it is reduced by the junction field effect, the current related sensitivity is increased with the sensor input voltage (Fig. 4.8).

4.3 Sensor optimization

4.3.1 Length of arms

The current and the voltage related sensitivity depend on the geometry of the sensor. The geometry of the cross is determined by the length L and the width W of the arms (Fig. 2.5). The current related sensitivity S_I (see §2.1.1) is proportional to the geometrical factor (Fig. 4.8):

$$S_I \propto G \quad (4.2)$$

The voltage related sensitivity S_V (see §2.1.1) is the ratio of the current related sensitivity over the input resistance R_{IN} . The input resistance is calculated based on the number of squares: the central part of the sensor is approximately 2/3 of a square. Each branch is equal to L/W squares. We found that the voltage related efficiency is (Fig. 4.8):

$$S_V \propto \frac{G}{2\frac{L}{W} + \frac{2}{3}} \quad (4.3)$$

With a non-linear resistor, because of the junction field effect, the resistance of the arm connected to the higher potential increases rapidly with the applied voltage. It is equivalent to an increase of the resistivity of the arm connected to the biasing voltage; less supply voltage remains for the active sensor part. Consequently the voltage related efficiency is strongly degraded by this additional parasitic resistance.

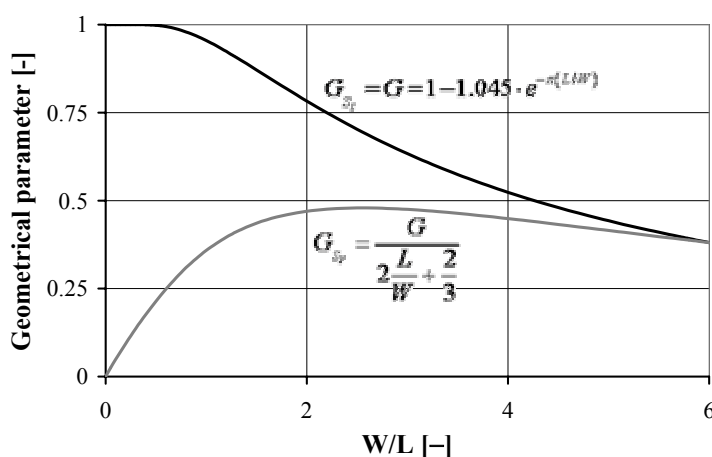


Fig. 4.8 The current and the voltage related sensitivity of a Hall plate with a cross shape are functions of the sensor geometry: the ratio between the arm width W and its length L .

The resistance of the arm connected to the biasing is increased by a parameter k_{JFE} depending on the influence of the junction field effect on the arm (Fig. 4.9):

$$S_V \propto \frac{G}{\frac{L}{W}(2 + k_{JFE}) + \frac{2}{3}} \quad (4.4)$$

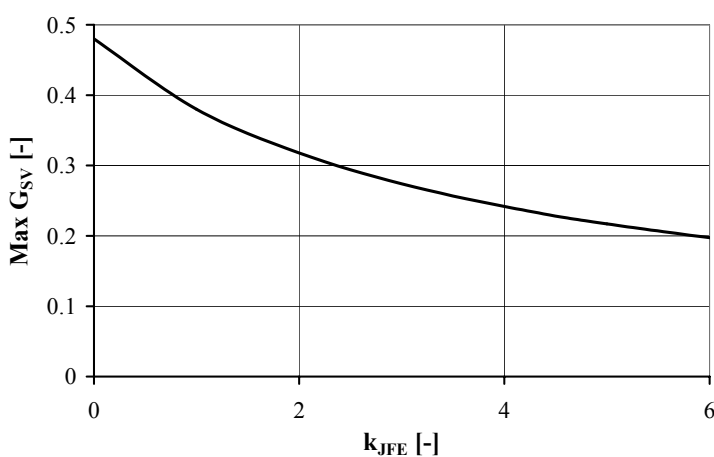


Fig. 4.9 Influence of the junction field effect on the geometrical parameter of the voltage related sensitivity. The parameter k_{JFE} represents the equivalent increase in arm length with the junction field effect.

To limit this effect, the length of the arms have to be reduced in comparison to usual optimal sensors (with negligible non-linear effects) in order to optimize

the voltage related efficiency without reducing the current related efficiency too much.

However, reducing the arm length deteriorates the geometrical factor G . Fortunately the resulting decrease of the current related sensitivity is small. The input resistance, on the other hand, is reduced noticeably. Since the voltage related sensitivity is proportional to the ratio of geometrical factor over the input resistance, the voltage related sensitivity is increased (Fig. 4.10). Moreover, when the input resistance is decreased and if the biasing current remains constant, the voltage difference between the sensor and the substrate is also decreased. This also reduces the junction field effect. Note that because of the junction field effect, the behavior of the sensor varies according to the connection to the ground or to V_{DD} .

Measurements (Fig. 4.10) confirm that the voltage related efficiency is strongly increased, especially for high biasing voltage, when the arms are shortened, whereas the variations of the current related efficiency are small. A voltage related efficiency of 2.5 %/T is obtained for low voltage biasing, but this is only 40% of the maximal theoretical value for a cross inside an NWell (Fig. 2.6).

4.3.2 Non-uniform implantation width

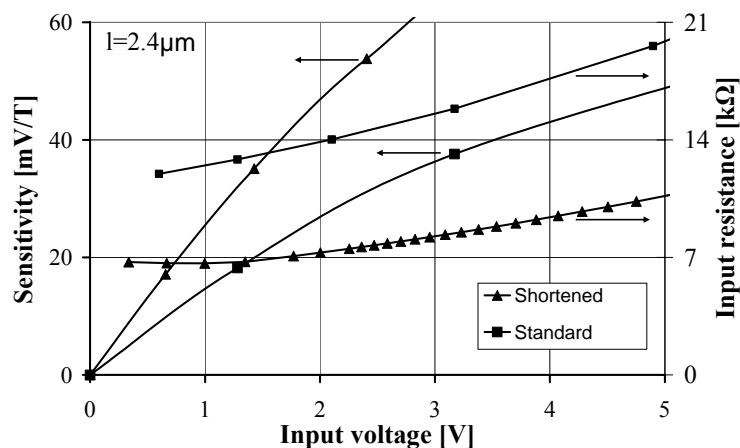


Fig. 4.10 Measurement of the arm length reduction on the sensitivity and on the input resistance. Due to non-linear properties of resistors, the sensitivity falls when arm length is optimized with usual geometrical rules. The substrate and the bottom sensor contact are short-circuited for this measurement.

Using a cross, the doping level is higher at its intersection, because the implantation width is of roughly a factor $\sqrt{2}$ larger in the orthogonal direction (Fig. 4.11). A lower doping level at the arms of the sensor substantially increases

the input resistance for a given current related efficiency; this is not favorable for the voltage related efficiency. Consequently, we increase the width of implantation in the arms in order to increase the doping level, the width and consequently decrease the resistance. A more uniform doping level of the sensor is obtained and the shape is closer to the usual cross.

The layout is drawn with a bias of $+0.6\mu\text{m}$, i.e. the mask is shrunk compared with the implantation mask. Consequently, small variations on the layout induce huge modifications of the implantation mask. A small notch on the layout decreases the width of implantation by about 40% in comparison to the width of the arm (Fig. 4.11). After diffusion, the active area is increased, which results in a cross with a more uniform doping level. The geometry (length and width) is close to the optimal for power related efficiency, i.e. good current and voltage related efficiency (see §2.1.1).

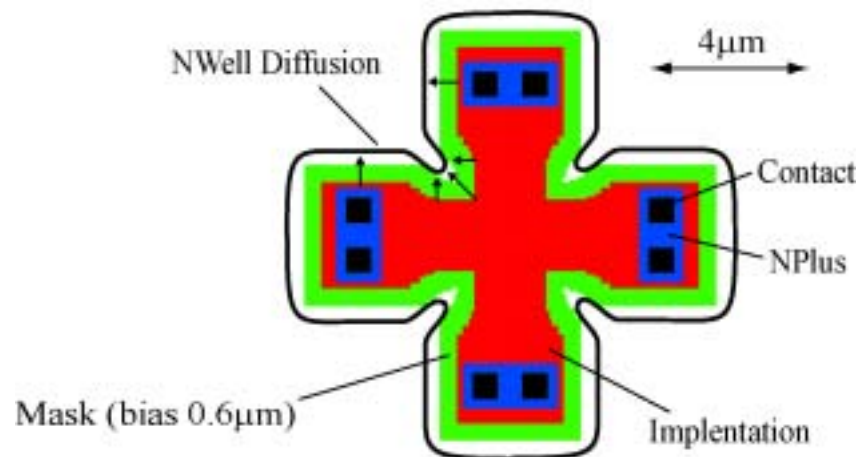


Fig. 4.11 The layout is drawn with a bias of $+0.6\mu\text{m}$ compared to the implantation mask. A small notch on the mask decreases the doping inside the center of the cross. After diffusion, the implantation area is increased, which results in a cross with a homogenous doping level.

The measurements confirm that the input resistance is reduced (Fig. 4.12) and the voltage related sensitivity is also strongly increased. The current related efficiency is almost constant, because the geometrical factor stays almost constant. We obtain a voltage related sensitivity of more than $4.5\%/T$ at low voltage biasing. It is 78% of the theoretical value (Fig. 2.6). For a 5V biasing, the voltage related efficiency drops to only 3.1%.

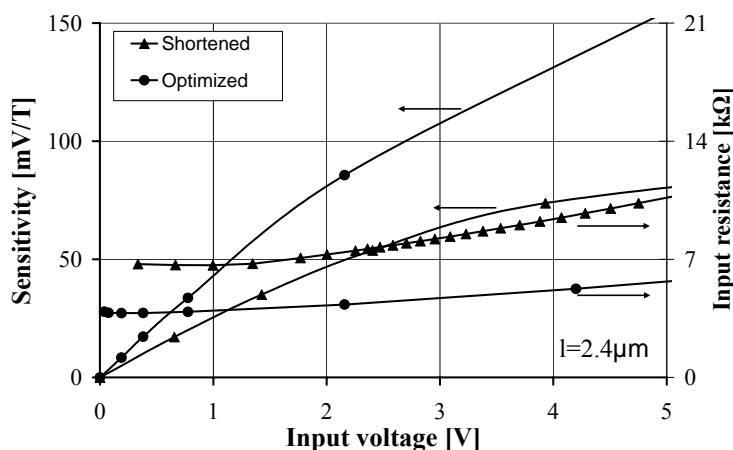


Fig. 4.12 Measurements of the fully optimized sensor. By increasing the doping in the sensor arms, the input resistance is reduced, while the current related sensitivity remains almost constant. Consequently, the voltage related sensitivity is increased by a factor 3 compared to the first sensor generation.

The distance between the two lateral metallurgical junctions of this miniaturized sensor is about $3.5\mu\text{m}$. The depletion width is $0.5\mu\text{m}$ on each side for a small biasing voltage. Consequently, the spatial resolution of the sensor in the sensor plane is only $2.5\mu\text{m}$ for a $4\mu\text{m}$ depth.

4.4 Offset and residual offset

The offset of Hall sensors, described in §2.1, is caused by asymmetry in the equivalent resistor bridge (Fig. 2.3). The tolerances during the fabrication process (masks, etching, implantations and diffusions) are slightly more important with small sensors: they cause a higher offset. Offset of usual sized Hall sensors is typically less than 0.1% of the supply voltage, whereas it is roughly one order of magnitude larger with a $2.4\mu\text{m}$ implantation mask.

CMOS sensors allow us to add electronic circuits around the sensor. Using the spinning current method described in §2.1.5, this initial offset from the geometry is cancelled [Ruther02a]. However a residual offset is still present. The sources of this residual offset, related to the non-linear behavior of the sensor and the equivalent bridge of resistances, are well understood [Ruther02a] [Steiner99]. The previous model demonstrates that small sensors are more subject to junction field effect. As a result, a higher residual offset after the spinning current method

is expected. Miniaturization increases both the offset and the residual offset after the spinning current method.

The combination of stresses and the junction field effect is a major source of residual offset (§2.1.5). Using 2-phases spinning current, i.e. the current flow in two orthogonal directions, the sensor biasing quadratic term of the residual offset is not cancelled [Ruther02]. An offset voltage from the electronic $V_{O,E}$, which is not a function of the biasing, is added. Measurements of the Fig. 4.13 confirm these two hypotheses.

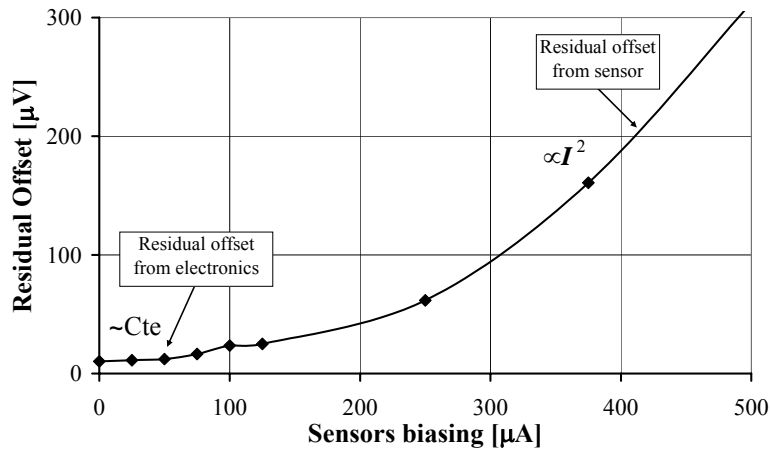


Fig. 4.13 The residual offset after the 2-phases spinning current method comes from the electronics and the sensor. The electronic part is roughly independent of the sensor biasing, whereas the Hall part is a quadratic function of the biasing current.

The residual offset is, by a first approximation, a quadratic function of the current using 2-phases spinning current [Ruther02]. Consequently, we found that the combination with the residual offset from electronics $V_{OFF,E}$ is:

$$V_{ROF} = V_{OFF,E} + K_{ROF} I^2 \quad (4.5)$$

with K_{ROF} a parameter describing the quadratic increase of the residual offset from the sensor with the biasing current.

From the voltage offset V_{ROF} , we can obtain the magnetic equivalent residual offset B_{ROF} :

$$B_{ROF} = \frac{V_{ROF}}{S_I \cdot I} \quad (4.6)$$

With S_I the current related sensitivity and I the biasing current.

With a low biasing, the magnetic residual offset equivalent is inversely proportional to the current, because of a constant offset voltage and a negligible residual offset from the sensor (Fig. 4.14). With a high biasing, when the offset from the electronics is negligible, the residual offset comes from the sensor and it increases linearly with the current.

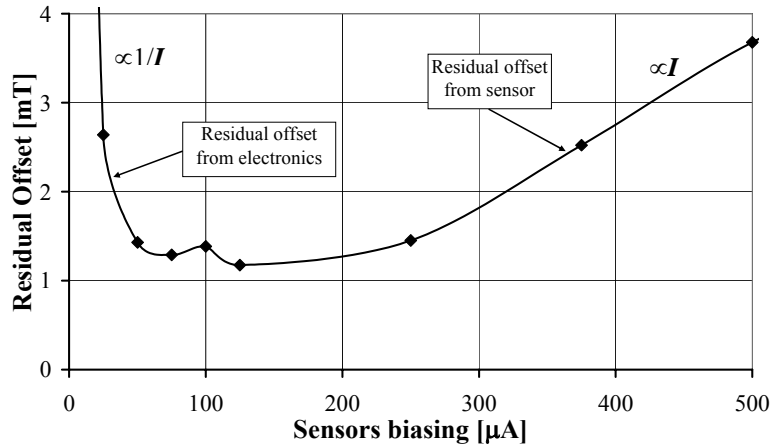


Fig. 4.14 Magnetic equivalent residual offset. When the sensor offset is the dominant factor, the magnetic equivalent residual offset is proportional to the biasing current. When the residual offset from the electronics is the dominant factor, i.e. at low biasing, the magnetic residual offset is reverse proportional to the biasing current. Consequently there is an optimum for the biasing

Consequently there is an optimum current $I_{OPTIMUM}$ to obtain the lowest residual offset:

$$I_{OPTIMUM} = \sqrt{\frac{V_{OFF,E}}{K_{ROF}}} \quad (4.7)$$

It jointly depends on the electronics and on the sensor's performances. The lower the residual offset from electronics, the lower the optimal sensor biasing current will be.

4.5 Model

4.5.1 Lateral diffusion

From the implantation depth of NWell and its average doping $N_{D,NW}$, we can calculate the implantation dose D_{NW} using the depth of implantation t_{NW} :

$$D_{NW} = (N_{A,SUB} + N_{D,NW})t_{NW} \quad (4.8)$$

This dose is implanted through a stripe of width l . With a small stripe, i.e. small sensors, the lateral diffusion stretches the implantation laterally to obtain an equivalent implantation of length l^* . A half ellipse is obtained with a S^* surface:

$$S^* = \frac{\pi}{4} l^* \cdot t_{NW} \quad (4.9)$$

The lateral diffusion length is proportional to the depth of implantation, with a factor of proportionality k . This k factor is, for a low doped substrate, about 80% of the implantation depth [Sze85]. We calculate the equivalent length after diffusion:

$$l^* = l + 2k \cdot t_{NW}$$

The obtained NWell doping level $N_{D,NW}^*$ after implantation through the stripe l and diffusion inside the surface S^* is equal to:

$$N_{D,NW}^* = \frac{D_{NW}}{S^*} l - N_{A,SUB} = \frac{4}{\pi} \cdot \frac{l}{l^*} (N_{A,SUB} + N_{D,NW}) - N_{A,SUB} \quad (4.10)$$

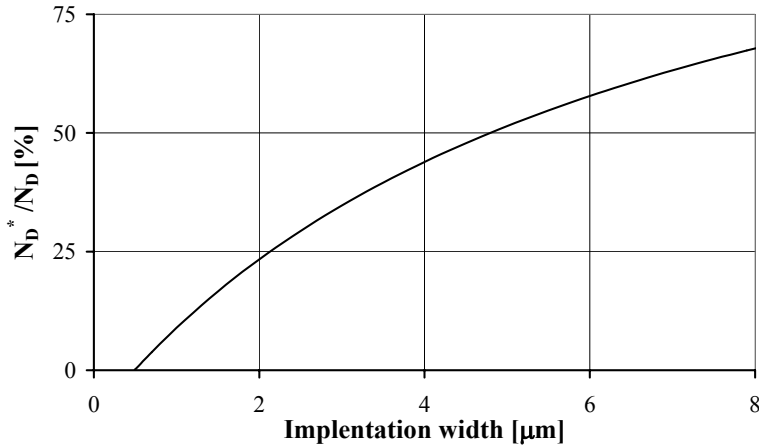


Fig. 4.15 The doping level for a narrow slot of an NWell diffusion (AMS0.8μm CXQ) is lower with a small implantation width because of lateral diffusion.

4.5.2 Junction field effect

Junction field effect (JFE) reduces the surface of the sensor's cross section (Fig. 4.16).

The NWell is surrounded by the P substrate and by the P+ on top. With the

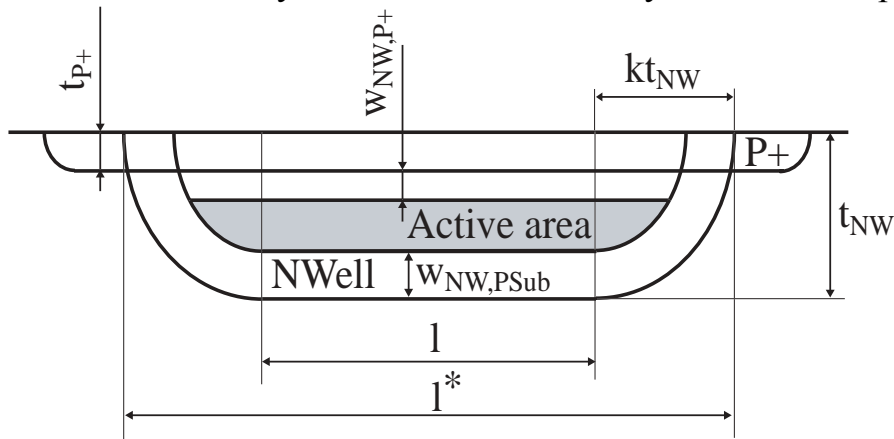


Fig. 4.16 Cross-section of the Hall sensor. The active area is decreased because of the NWell depletion layer.

approximation of an abrupt junction, the length of depletion inside the NWell is:

$$w_{NW,P} = \sqrt{\frac{2\epsilon_S}{q} \frac{N_A}{(N_A + N_{D,NW}^*) N_{D,NW}^*}} (V_{bi} + V) \quad \text{and} \quad V_{bi} = \frac{kT}{q} \ln \frac{N_A N_{D,NW}^*}{n_i^2} \quad (4.11)$$

With V_{bi} the built in voltage, V the indirect junction polarization, q the electron charge, ϵ_S the silicon permittivity, k the Boltzman constant, n_i the intrinsic doping level and T the temperature.

The active area surface S_{JFE}^* with JFE is:

$$S_{JFE}^* = \frac{\pi}{4} (t_{NW} - t_{P+} - w_{NW,PSub} - w_{NW,P+}) (l + 2kt_{NW} - 2w_{NW,PSub}) \quad (4.12)$$

From previous equations, we can now calculate that the resistance per square R_{\square} :

$$R_{\square} = \frac{\rho \cdot l}{S_{JFE}^*} \quad (4.13)$$

and

$$\rho = \frac{1}{q \cdot \mu \cdot N_{D,NW}^*} \quad (4.14)$$

where ρ is the resistivity of the NWell and μ the mobility.

This model (Fig. 4.17) proves that small sensors are more easily subject to JFE: resulting in less linear resistors. According to the publications [Ruther02] and [Steiner99], they consequently have a higher residual offset after the spinning current method. The behavior corresponds to the measurements (Fig. 4.5), despite the complementary PWELL of the AMS 0.8 μ m CXQ CMOS process is not modeled (Fig. 4.2); the JFE is underestimated, because of the lateral diffusion of the PWELL inside the sensor which reduces the doping level of the sensor's active area.

4.5.3 Current related sensitivity

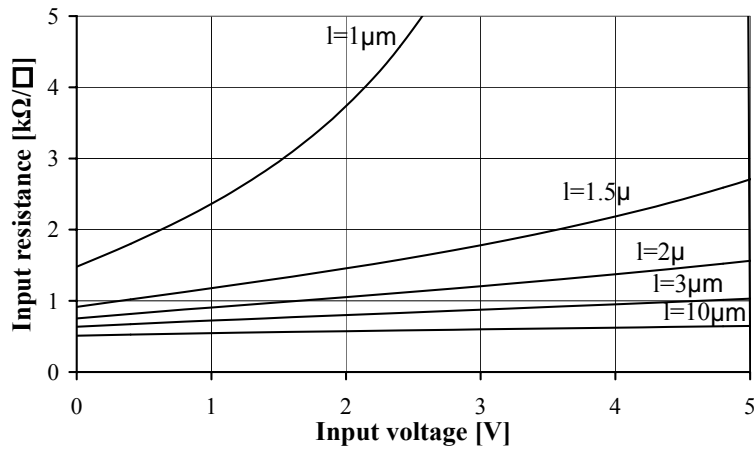


Fig. 4.17 The resistance per square for a narrow slot of NWell is increased because of lateral diffusion. The junction field effects are greatly increased with the size diminution. This behavior is the same as that found in the measurements.

The current related sensitivity S_I is equal to:

$$S_I = \frac{G}{r_H \cdot q N_{D,NW}^*} \frac{1}{(t_{NW} - t_{P+} - w_{NW,Sub} - w_{NW,P+})} \quad (4.15)$$

with $G \cong 0.8$ the geometrical factor and $r_H \cong 1.2$ the Hall factor.

The current related sensitivity is greatly increased with a reduction in size. Because of the variation of the depletion length, the efficiency is also a function of the common mode voltage. The measurements correspond well with the model (Fig. 4.18).

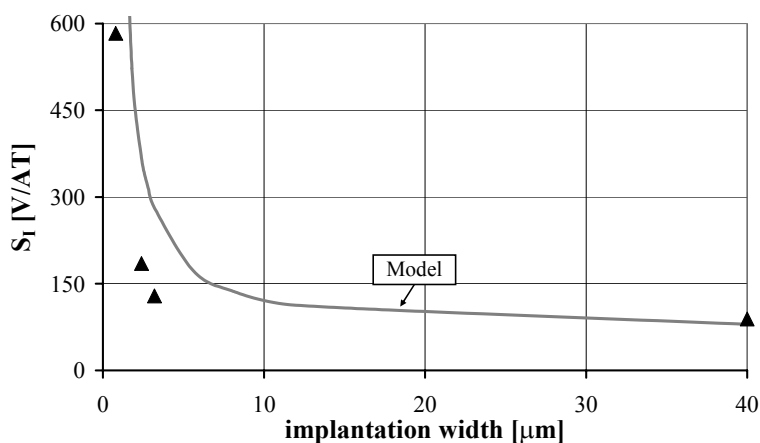


Fig. 4.18 Comparisons between the measurements and the model for the current related sensitivity with a low biasing, i.e. small input voltage. A good matching is observed.

4.6 Integrated magnetoconcentrators

The normal usage of integrated magnetoconcentrators (IMC) is to “suck” the external magnetic field, increasing the sensitivity of the microsystem [Drljaca01]. To obtain highly sensitive sensors, two concentrators, separated with a micrometric gap of typically $30\mu\text{m}$, are placed on the chip surface (Fig. 4.19). At the corner of the concentrators, a fringing is produced in the Z direction, when an external magnetic field parallel to the chip surface is applied; this vertical field can be measured by Hall plates. The magnetic gain, i.e. the vertical over the external field ratio, is typically increased up to a value of 10 with typical sized concentrators and usual sensors.

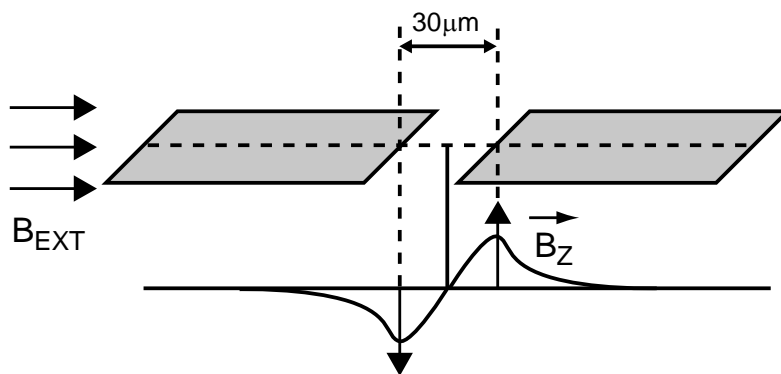


Fig. 4.19: Fringing field B_Z below two magnetoconcentrators.

Magnetic simulations show that the width of the fringing field peak is less than $20\mu\text{m}$ for the chosen geometry [Popovic01]. With miniaturized sensors with a $5\mu\text{m}$ active area, the peak of the magnetic field is less averaged and as a result the efficiency is increased by 70% compared to usual $50\mu\text{m}$ sensors (Fig. 4.20). The improvement in performance is limited by the $6\mu\text{m}$ distance between the sensor and the magneto-concentrator. The averaging is insignificant because of the sensor's spatial resolution, which is roughly equal to the distance between the IMC and the sensor. The alignment of the concentrator with the sensor is a limitation of the technology; a resolution and an alignment precision of less than $5\mu\text{m}$ are obtained. It results a variation of the magneto-concentrator gain of less than 5%.

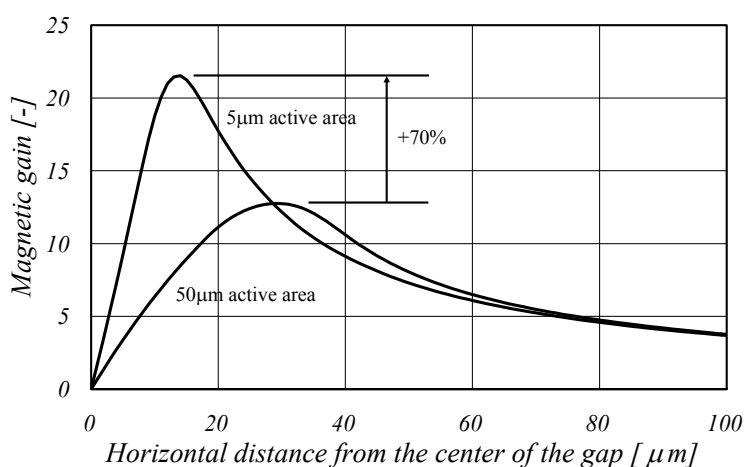


Fig. 4.20: Simulation of the magnetic gain for a small $5\mu\text{m}$ and a typical $50\mu\text{m}$ size of the sensor's active area with a gap of $30\mu\text{m}$ between concentrators. Usual sensors average out the peak of the fringing field. Using small sensors the sensitivity is increased by 70% for a vertical distance between the concentrator's surface and the sensor of $6\mu\text{m}$.

4.7 Conclusion

We have developed a miniaturized Hall sensor compatible with the calibration coils presented in the previous chapter. The sensor has a cross shape to be compatible with the spinning current method. It has an implantation width of only $2.4\mu\text{m}$ for a $4\mu\text{m}$ NWell depth. The optimized sensor has a $4.5\%/T$ voltage related efficiency with a low voltage biasing (§4.3.2). This is 78% of the theoretical value (Fig. 2.6). When the sensor is biased with a 5V signal, the voltage related efficiency falls to 3.1% because of the junction field effect.

The spatial resolution of this sensor in the sensor plane is about $2.5\mu\text{m}$; this makes it useful for a high resolution mapping and imaging of a magnetic field. An emerging application is the detection of a single magnetic microbead, a few micrometers in diameter [Besse02]. We also demonstrate that $5\mu\text{m}$ miniaturized sensors are 70% more efficient than usual $50\mu\text{m}$ sensors when they are combined with magnetoconcentrators (§4.6).

Although the current related sensitivity of miniaturized Hall sensor is increased because of the reduction of the doping level by the lateral diffusion, they are more subject to the junction field effect, resulting in a lower voltage related efficiency and a larger residual offset (§4.4). This offset voltage is in first approximation proportional with the square of the biasing current. When a residual offset from the electronics is also present, we found that there is an optimum biasing current needed for the sensor in order to minimize the magnetic equivalent residual offset. It depends both on the properties of the electronics and the sensor: the lower the electronic offset, the lower the optimal biasing and the residual offset will be. A further step is to test 4-phases spinning current (§2.1.5) electronics in order to reject the quadratic function of the biasing. The spinning current is precisely the topic of the next chapter.

4.8 References

- [Besse02] P.-A. Besse, G. Boero, M. Demierre, V. Pott, R. S. Popovic, Detection of a single magnetic microbead using a miniaturized silicon Hall sensor, *Applied Physics Letters*, Vol. 80, No. 22, pp. 4199-4201, June 2002.
- [Demierre02] M. Demierre, S. Pesenti, J. Frounchi, P.-A. Besse and R. S. Popovic, Reference magnetic actuator for self-calibration of a very small Hall sensor array, *Sensors & Actuators A*, Vol 97, pp. 39-46, 2002.
- [Drljaca01] P. M. Drljaca, V. Schlageter, F. Vincent, R. S. Popovic, High Sensitivity Hall Magnetic Sensors Using Planar Micro and Macro Flux Concentrators, *TRANSDUCERS'01, Eurosensors XV*, Munich, Germany, 2001.
- [Frounch01] J. Frounchi, M. Demierre, Z. Randjelovic and R. Popovic, Integrated Hall Sensor Array Microsystem, *ISSCC2001 Conference*, San Francisco, pp. 248-249, 2001.

- [Patent] Verfahren zur Herstellung von Hallelementen, EP 1 045 461 A2, Europäische Patentanmeldung.
- [Popovic96] R. S. Popovic, J. A. Flanagan, and P. A. Besse, The future of magnetic sensors, *Sensor and Actuators A*, vol. 56, no 1-2, pp. 39-55, 1996.
- [Popovic01] R.S. Popovic, C. Schott, P.M. Drljaca and R. Racz, A new CMOS Hall angular position sensor, *Technisches Messen*, Vol. 6, pp. 286-291, 2001.
- [Randjel99] Z. Randjelovic, R.S. Popovic, J. Petr and F. Riedl, Low-Power High Sensitive CMOS Magnetic Field Hall Sensor, *Proc. Of Eurosensors XIII*, 15B3, The Hague, The Netherlands, pp. 601-604, 1999.
- [Randjel00] Z. Randjelovic, Low-Power High Sensitivity Integrated Hall Magnetic Sensor Microsystems, Ph.D. Thesis, (EPFL No 2198), Hartung-Gorre (Konstanz, Germany), ISBN : 3-89649-617-4, 2000.
- [Randjel02] Z. Randjelovic, M. Kayal, R.S. Popovic and H. Blanchard, Highly Sensitive Hall Magnetic Sensor Microsystem in CMOS Technology, *IEEE Journal of Solid-State Circuits*, Vol. 37, pp. 151-159, 2002.
- [Ruther02] P. Ruther, U. Schiller, W. Buesser, R. Janke and O. Paul, Influence of the Junction Field Effect on the Offset Voltage of Integrated Hall-Plates, *European Conference on Solid-State Transducers*, Prague, pp. 709-710, 2002.
- [Schurig02] E. Schurig, M. Demierre, C. Schott and R. S. Popovic, "A vertical Hall device in CMOS high-voltage technology", *Sensors and Actuators A*, Vol. 97, pp. 47-53, 2002
- [Steiner99] R. Steiner, C. Maier, M. Mayer, S. Bellekom and H. Baltes, Influence of Mechanical Stress on the Offset Voltage of Hall Devices Operated with Spinning Current Method, *Journal of Microelectromechanical Systems*, Vol. 8, No. 4, pp. 466-471, 1999.
- [Sze85] S.M. Sze, *Semiconductor Devices*, John Wiley & Sons, ISBN : 0-471-87424-8, 1985.

5 Spinning Current

Hall sensors are widely used for measurements of low magnetic fields in the range of 1-100mT [Popovic96]. The offset voltage is the most obvious effect with Hall sensors when they measure DC magnetic fields. It is mostly caused by mask misalignments, the piezoresistive effect and doping non-homogeneities. The offset and its temperature drift limit the accuracy and reproducibility of magnetic Hall sensors [Daniil82]. The dynamic offset cancellation technique, also called the spinning current method, proposed in [Munter90] can be used to reduce the offset voltage and the low frequency 1/f noise of a Hall sensor (see §2.1.4). Employing this modulation technique the initial offset of several tenths of a mT is reduced to a few hundred μT of residual offset for a large output bandwidth [Bilotti97] [Frounch01]. The residual offset can reach less than $10\mu\text{T}$ with ultra low spinning frequency and 8 contacts Hall sensors [Bakker99] or with continuous spinning current [Steiner98].

There are two main sources of residual offset (see §4.4). The first one is intrinsic to the Hall sensor itself. The second one comes from the electronic circuit nonidealities. In this chapter, we concentrate on the point of view of the electronic circuits; we focus on the sources of residual offset related to the electronics. For each block of the electronics, the sources of residual offset are described and solutions to reduce them are explained.

2-phases spinning current, i.e. the current flows in two orthogonal sensor directions, is not efficient enough with CMOS compatible vertical Hall sensors, especially when the sensors are coupled (see §2.3.2). A 4-phases spinning current (§2.1.5), i.e. the current flows in the four orthogonal directions, is developed and tested to decrease their residual offset.

A new configuration to reduce electronics residual offset is realized. It uses a better systemic approach, i.e. the microsystem performances are increased without significant modifications of the electronics block.

Noise, analyzed within the next sections, is another figure of merit of Hall microsystems. The baseband noise of a Hall microsystem is decomposed into white and 1/f noise. One goal of the spinning current electronics is to suppress 1/f noise without increasing the white noise level. The 1/f noise of the sensors and amplifiers is outside the signal bandwidth after demodulation. Consequently, it is possible to suppress it by filtering or by correlated double sampling.

5.1 Electronic part

The microsystem is based on a spinning current technique (§2.1.5). An analog signal for the microsystem is preferred and a bandwidth of several KHz is required for most of the angular measurements (typically up to 200'000 RPM). These reasons will orientate our choice of architecture [Frouch01].

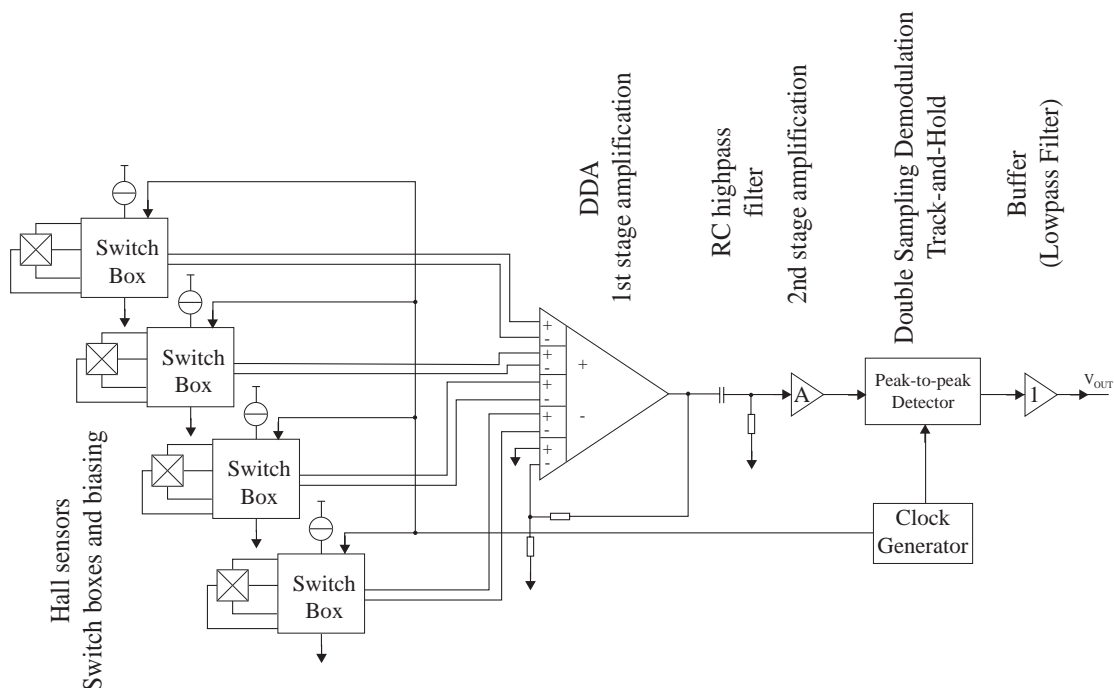


Fig. 5.1 Microsystem block diagram. 4 Hall sensors are connected to switch boxes. The amplification and the summation of the Hall signals are done by a DDA. It is followed by a RC High pass filter and a second amplification stage. The signal is extracted with a peak-to-peak detector. In front of the output pad a buffer and a low-pass filter can be added.

The block diagram of a microsystem is shown in Fig. 5.1. It consists of a Hall plates array with its corresponding switching networks (switch box). It separates the Hall useful signals from the parasitic offset and $1/f$ noise by modulation. A Differential Difference Amplifier (DDA) is used for the first stage of amplification and to totalize the signals from several sensors. Its gain is limited by the electronic saturation because of both offset from sensors and from the amplifier itself. After this first amplification, a high-pass filter removes the unwanted DC component before the next stage of amplification. The output signal of the amplification chain is then demodulated. A switched-capacitor peak-to-peak detector is used for the demodulation. It is composed of a synchronous correlated double sampling difference amplifier followed by a

sample and hold circuit. A buffer and eventually a low-pass filter are connected before the pad. The clocks for the switch capacitors circuits and the switches are generated on the chip, along with a voltage reference circuitry and several current sources for the Hall cells biasing.

5.2 Modulation using a switch box

The switch box permutes the contacts of the Hall sensor with the current source and the preamplifier (Fig. 5.2). It contains eight analog switches to turn the current in two orthogonal directions (2-phases spinning current). Two types of switches are used. The first ones control the sensor biasing; they are called current switches. Their parasitic resistors are generally about 1/10 of the sensor resistance in order to achieve a negligible voltage drop. The second ones, called voltage switches, switch the amplifier to the sensor outputs. Even if no current flows through them, their resistance has to be small, because they are sources of Johnson white noise.

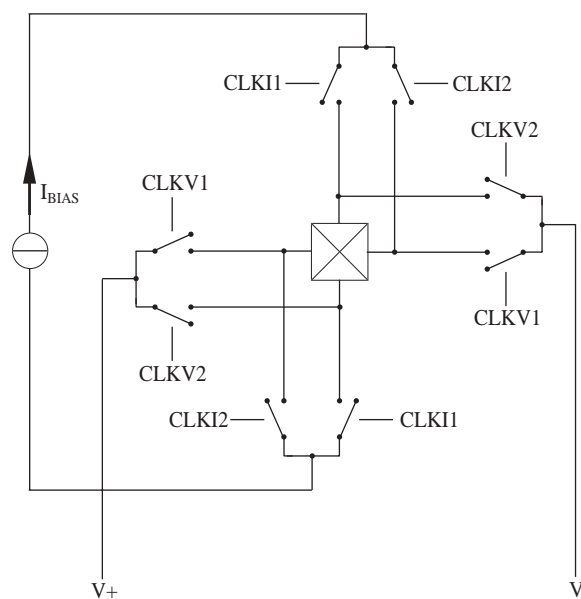


Fig. 5.2 The switch box is composed of current and voltage switches, respectively connected to current clock CLKI and voltage clock CLKV. This figure is for a 2-phases spinning, where the current flows in two orthogonal directions for two phases.

Ideally, the output signal of the modulator is a square wave with an amplitude equal to twice the Hall voltage. Unfortunately, parasitic spikes appear during commutations (see §2.1.5). Spikes are caused by the switch boxes nonidealities,

i.e. charge injection, clock feed-through and parasitic capacitors, but also by the parasitic capacitors of the Hall sensor itself. During the previous phase, the output contacts of the sensor are connected to the biasing voltage V_{Bias} and the ground. After commutation, they become the sensor output with a common mode voltage $V_{Bias}/2$. The voltage has to swing between these values during the transients provoking spikes. The RC time constant of this transient is determined by the sensor resistance and parasitic capacitances.

When odd harmonics of spikes are demodulated, a DC signal is generated; a residual offset appears. Since the RC time constant of spikes τ is small compared to the spinning $1/2f_M$, the residual offset V_{ROF} is, without filtering before demodulation [Enz87]:

$$V_{ROF} \cong 2\tau f_M V_{Spike} \quad (5.1)$$

One way to drastically reduce the residual offset from spikes is to limit the bandwidth before demodulation to double the spinning frequency [Enz87] to filter the higher harmonics of the spikes and leads to a residual offset equals to:

$$V_{ROF} \cong (2\tau f_M)^2 V_{Spike} \quad (5.2)$$

A second way to reduce these transients is to stop the processing of the signal when the spikes become intrusive (guard band); the clock generator produces different kinds of signals for current, voltage and signal processing switches. A track-and-hold demodulator can hold the signal during the transients [Bilotti99], where the spikes are presents or the input of the preamplifier can be short circuited during spikes [Port01].

Note that the microsystem does not use demodulation, but recovers the signal using a correlated double sampling technique (see §5.4.1). If the samples are taken at the center of each half-period with a negligible sampling time, we find that the residual offset from spikes referenced at its input is:

$$V_{ROF} \cong V_{Spike} e^{-\frac{1}{4\tau f_M}} \quad (5.3)$$

To avoid residual offset from spikes, the correlated double sampling is used instead of demodulation (Fig. 5.3), when $\tau f_M \ll 0.1$.

The best way to increase spike rejection is to reduce the time constant τ of the spikes. For this, parasitic capacitors have to be decreased. One way is to reduce the surface of the switches. This leads to a trade-off with the switches resistance (their thermal noise and the sensor biasing current). Note that miniaturized sensors surface (see §4) is much smaller than ones of the switches, as a result

their NWell/P-Substrate parasitic capacitance is also much smaller. Decreasing the modulation frequency also reduces the effects of spikes, but at the same time will reduce the microsystem's bandwidth.

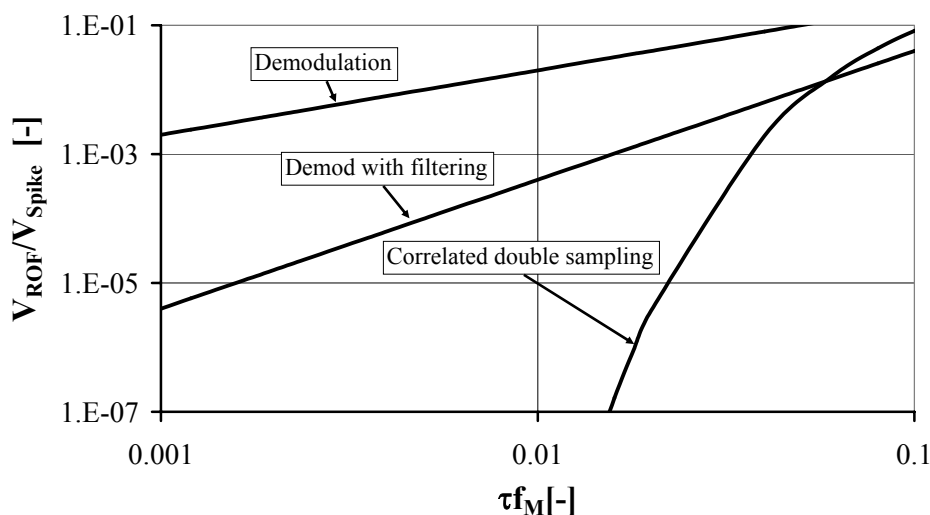


Fig. 5.3 Residual offset from spikes for different types of detection: demodulation, demodulation after filtering at double the modulation frequency and correlated double sampling. τ is the time constant of spikes and f_M the frequency of modulation.

Measurements show that the residual offset is not dependant on the spinning frequency up to spinning frequencies of 400KHz, in contradiction with the previous equations (5.1) (5.2) (5.3). Consequently the residual offset due to spikes is not a major source of residual offset. Other sources, which are not frequency dependant, provokes this offset.

Analog switches are unfortunately not ideal. They suffer from current leakage, on-resistance and parasitic capacitance. Mismatches of this parameter provoke residual offset. Spice Simulations of these non-idealities shows that their contributions are less than $1\mu\text{T}$ [Endo02].

5.3 Amplification

The Hall voltages are small (about $100\mu\text{V}$ for a field of 1mT) and therefore they have to be amplified to measure magnetic fields in the 100mT range. Using spinning current, the Hall signals are modulated. Therefore the amplification has

to be performed in the AC domain. The amplifier is made up of two amplifier stages separated by a high-pass filter to remove the low frequency component (sensors and 1st preamplifier stage offsets and 1/f noise).

For the first amplification stage, we used a DDA [Säckin87]. It is connected as a floating input amplifier. The gain is fixed by a voltage divider connected to a "zero" reference $V_{DD}/2$ provided by a ratiometric voltage divider. This architecture requires a low number of components compared to the usual instrumentation amplifier (3 operational amplifiers and several matched resistors). In addition, several inputs can be easily added to connect several Hall sensors (Fig. 5.4); it requires only 3 additional transistors for each additional input. An array of Hall sensors is employed to increase the signal-to-noise ratio and to reduce the initial offset voltage [Trontelj99].

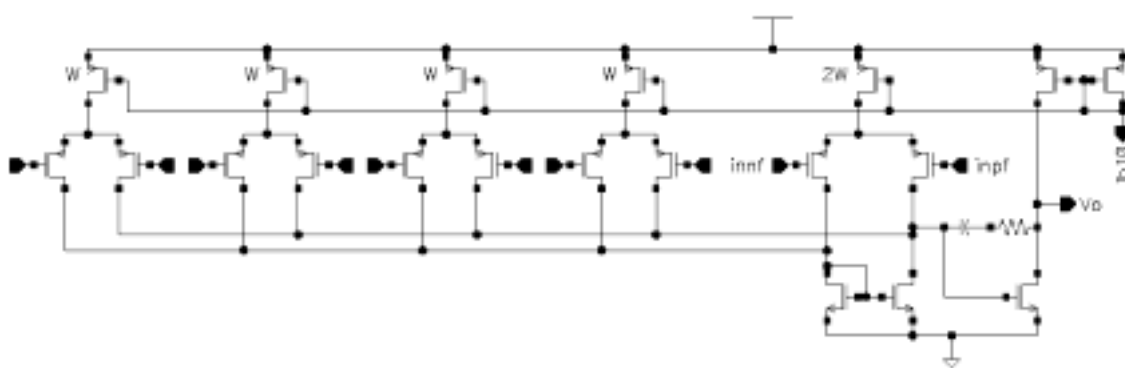


Fig. 5.4 A five input pair preamplifier [Frounch01]. Four differential inputs are used for the sensor connections and one for the feedback to fix the DDA gain.

DDA is an efficient way to suppress the common mode. However, its performance deteriorates when two inputs are not at the same common mode level. This effect is a major source of residual offset of the whole system with degenerated sensors.

With the CMOS vertical Hall sensors couples (see §2.3.2), the common mode varies for the different phases of the spinning current method. As the behavior of the DDA is not ideal in case of common mode, a parasitic square wave appears at the output of the DDA with the spinning current. This signal is unfortunately similar to a Hall signal and it is seen as a residual offset. Spice simulations with a DDA gain of 52 show that the equivalent residual offset at the input of the DDA is equal to 0.038‰ of the common mode variation (Fig. 5.5). With a sensor sensitivity of 60 mV/T and a common mode variation of 70mV (2V biasing), the residual offset is as high as 45μT with a 60mV/T sensor sensitivity.

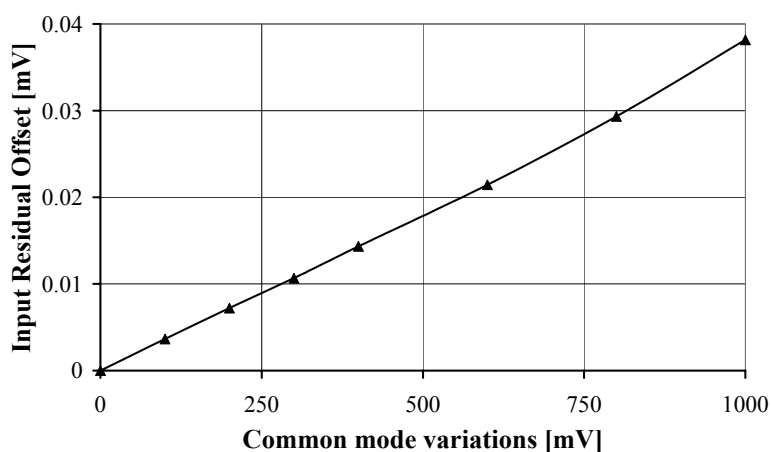


Fig. 5.5 Spice simulations of the residual offset zeroed to the input of the DDA when the common mode at the sensor output varies.

A single CMOS vertical Hall sensor suffers from a large initial offset that reaches 30mV with a 2V biasing (see §2.3.1). As it is correlated, two sensors with opposite spinning phases are connected to the input of the DDA in order to cancel it. Unfortunately, it doubles the previous common mode effects (0.076%). The residual offset is equal to 40 μ T with a 60mV/T sensor sensitivity. This residual offset do not depend on the spinning frequency.

Several solutions are known to decrease the residual offset coming from common mode. The first one is to use cascode current sources inside the DDA [Säckin87] or to decrease the DDA gain. Another method is to force the sensor common mode to remain at the same voltage using an adapted biasing scheme with an additional operational amplifier and a feedback loop on the sensor biasing (Fig. 5.6) [Matsui81]. The DDA can eventually be replaced by an instrumentation amplifier which is more robust to common mode variations. Note that decreasing the biasing voltage does not improve the magnetic equivalent residual offset because both the sensitivity and the residual offset are proportional to the biasing.

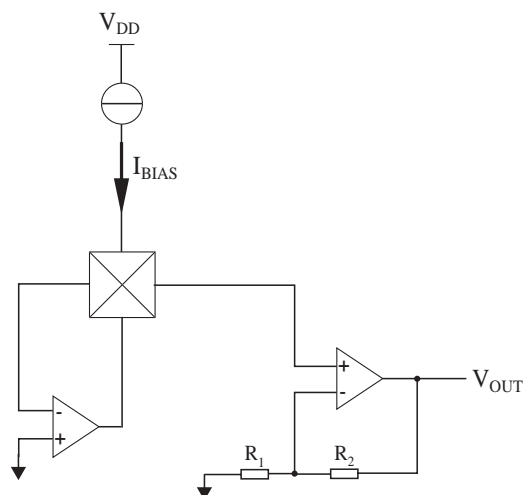


Fig. 5.6 Sensor biasing to define a virtual reference at one of the sensor outputs in order to maintain common mode voltage near the reference voltage [Matsui81]. This technique can also simplify the amplification by removing differential signals.

A decoupling capacitor between two stages was used to avoid saturation of the next preamplifier (RC high-pass filter). This parasitic DC component comes from the offsets of sensors and 1st stage amplifier. Its cutoff frequency is ideally higher than the $1/f$ noise corner frequency. The second stage consists of an operational amplifier connected as a non-inverting amplifier.

The residual offset caused by the preamplification and the filtering is negligible if their behavior is linear. However the spinning frequency is limited by the bandwidth and the slew rate of the amplifiers to guarantee stable signals at the end of each phase. A residual offset, which is dependant on the spinning frequency, appears if this is not guaranteed.

5.4 Peak-to-Peak detector and Buffer

The Hall voltage, which is modulated by the spinning current method, is extracted by shifting its spectrum back to the baseband. The circuit is based on the correlated double sampling technique (CDS) [Enz96] in which the voltage is sampled in the first clock phase and subtracted from the voltage sampled in the second phase. The $1/f$ noise of the electronics and from the sensor is consequently cancelled by subtraction [Kansy80]. As demonstrated in §5.2, the CDS greatly reduces the residual offset from spikes for high frequency of

modulation. Another limitation of demodulation is the low-pass filtering required for attenuating the square ripple due to the offset. The CDS does not provoke ripple at the modulation frequency and its harmonics, because of the subtraction instead of the modulation. However a ripple at even harmonics of the modulation frequency comes from interlaced sampling [Bilotti99].

The Peak-to-Peak detector is split into a CDS difference amplifier and a track-and-hold (or a sample-and-hold with its output always valid). Since the output voltage is valid only in the second phase of the CDS part, a track-and-hold circuitry is necessary to keep the output voltage level constant over the whole clock period. It allows continuous-time operation of the peak to peak detector by holding the results during the evaluation period.

5.4.1 Correlated double sampling difference amplifier

The correlated double sampling difference amplifier used in our system subtracts the Hall voltage between the two spinning phases (Fig. 5.7), i.e. to obtain twice the Hall voltage. The transfer function of this stage has zeroes at the multiple of the clock frequency so that the clock frequency must be much higher than the maximum magnetic field frequency of interest.

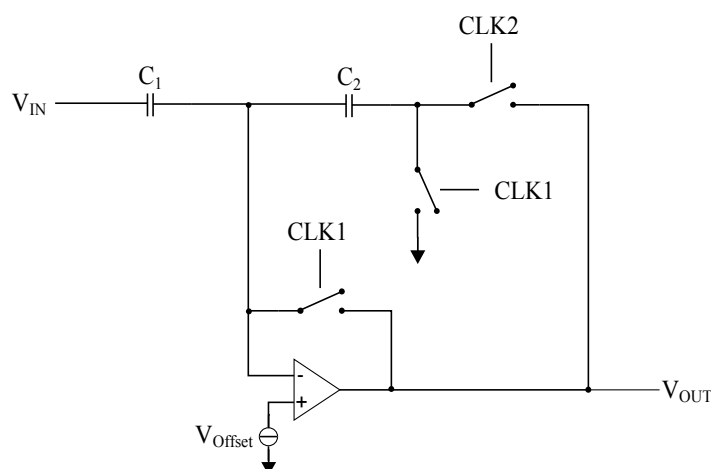


Fig. 5.7 The P2P detector is based on a switch capacitors circuit. It is controlled by two clocks CLK1 and CLK2 in order to sample the signal in the first and second period of spinning. To reduce charge injection, 12 pF capacitors are used for C_1 and C_2 . During 1st phase, the offset of the OA is sampled in the C_2 capacitor to perform auto-zero.

During first phase, the capacitor C_1 is connected between the input $V_{IN,1}$ during first phase and V_{offset} of the OA to obtain a charge $Q_{1,1}$. C_2 is connected between V_{offset} and the reference voltage to store the OA offset with a charge of $Q_{2,1}$.

$$\frac{Q_{1,1}}{C_1} = V_{IN1} - V_{offset} \quad (5.4)$$

$$\frac{Q_{2,1}}{C_2} = V_{offset} \quad (5.5)$$

During the second phase, with the switches set in other positions, one terminal of C_1 is connected to the new input value $V_{IN,2}$ and the other one is connected to V_{offset} . The charge Q_1 in this capacitor $Q_{1,2}$ is now:

$$\frac{Q_{1,2}}{C_1} = V_{IN2} - V_{offset} \quad (5.6)$$

The charges of C_1 go through C_2 :

$$Q_{2,2} = (Q_{1,1} - Q_{1,2}) + Q_{2,1} = C_1 (V_{IN1} - V_{IN2}) + C_2 \cdot V_{offset} \quad (5.7)$$

And finally:

$$V_{OUT} = V_{offset} - \frac{Q_{2,2}}{C_2} = V_{offset} - \frac{1}{C_2} \left[(V_{IN1} - V_{IN2}) + C_2 \cdot V_{offset} \right] = \frac{C_1}{C_2} (V_{IN2} - V_{IN1}) \quad (5.8)$$

With C_1 equal to C_2 :

$$V_{OUT} = V_{IN2} - V_{IN1} \quad (5.9)$$

How shows the Equ. (5.9), this circuit is insensitive to the OA offset. During the first phase, its output is equal to V_{offset} , while it becomes V_{OUT} during the second phase. The OA has to follow these voltage swings.

A small "deglitching" 1pF capacitor is always added between input and output to hold the output voltage during transient (negative feedback).

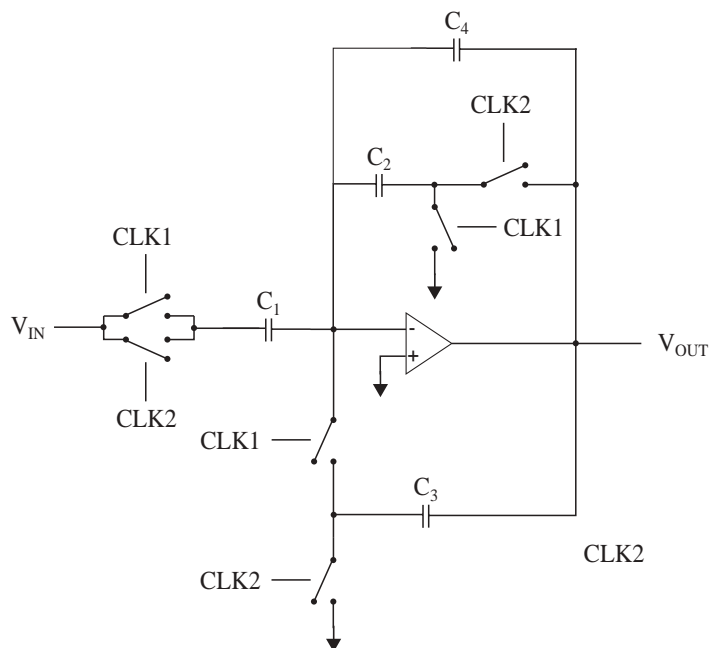


Fig. 5.8 The enhanced switch capacitors synchronous differential amplifier with limited output voltage swing. It requires twice the number of capacitors and switches.

To increase the frequency response, a more elaborated circuit is also used in order to limit the voltage swing at the output of the operational amplifier between the two phases (Fig. 5.8). This demodulator is only profitable without a multiplexing of signals at its input (see §5.9). For instance with a 2-D microsystem, the output voltage swings between the X- and Y-axes.

5.4.2 Track-and-Hold

As the output of the correlated double sampling difference amplifier is only valid during the second phase, a Track-and-Hold, i.e. a sample-and-hold whose output is always valid, is required (Fig. 5.9). It is based on a sampling circuit and a holding capacitor [Razavi01].

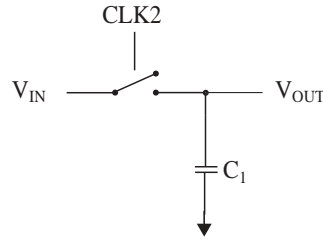


Fig. 5.9 Basic track-and-hold circuit. It maintains a valid output during the evaluation phase of the correlated double sampling difference amplifier.

In order to add a first order SC low-pass filter, a more elaborate circuit is used (Fig. 5.10). This circuit inverts the signal and always maintains a valid output.

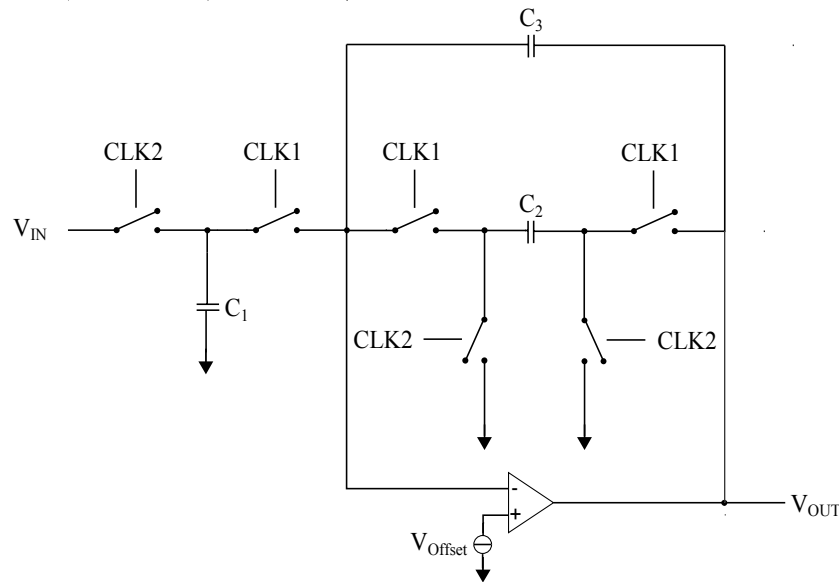


Fig. 5.10 Switch capacitors 1st order low pass filter used as a sample-and-hold. The C3 capacitor stores the result during the first phase of evaluation ($C_3 > C_2$). C_1 and C_2 are equal for a unitary gain.

We calculate that the output voltage is equal to:

$$V_{OUT,N} = \frac{C_3}{C_3 + C_2} V_{OUT,N-1} - \frac{C_1}{C_3 + C_2} V_{IN,N-1} + \left(\frac{C_1 + C_2}{C_3 + C_2} \right) V_{offset} \quad (5.10)$$

With $C_1 = C_2$, we find:

$$V_{OUT,N} = \frac{C_3}{C_3 + C_2} V_{OUT,N-1} - \frac{C_2}{C_3 + C_2} V_{IN,N-1} + 2 \left(\frac{C_2}{C_3 + C_2} \right) V_{offset} \quad (5.11)$$

If the transients are ended, i.e. the input stays constant between $V_{OUT,N-1}$ and $V_{OUT,N}$:

$$V_{OUT,N} = -V_{IN} + 2V_{offset} \quad (5.12)$$

To evaluate the frequency response, we employ the z transform of (5.11) is used:

$$V_{OUT}(z) = \frac{C_3}{C_3 + C_2} z^{-1} V_{OUT}(z) - \frac{C_2}{C_3 + C_2} z^{-1} V_{IN}(z) \quad (5.13)$$

$$G(z) = \frac{V_{OUT}(z)}{V_{IN}(z)} = \frac{C_2}{C_3 - (C_3 + C_2)z} \quad (5.14)$$

The transfer function is obtained by replacing z by $e^{j\omega T}$:

$$G(\omega) = \frac{V_{OUT}(\omega)}{V_{IN}(\omega)} = \frac{C_2}{C_3 - (C_3 + C_2)e^{j\omega T}} \quad (5.15)$$

If the sampling frequency is much higher than the signal frequency:

$$e^{j\omega T} \cong 1 + j\omega T \quad (5.16)$$

$$G(\omega) \cong -\frac{1}{1 + \frac{C_3 + C_2}{C_2} j\omega T} \quad (5.17)$$

This is equivalent to a low pass filter (Fig. 5.11) with the following cutoff frequency:

$$f_c = \frac{1}{2\pi T} \frac{C_2}{C_2 + C_3} \quad (5.18)$$

The switch/capacitor combination is roughly equivalent to a resistor. The equivalent RC schematic is described in Fig. 5.11.

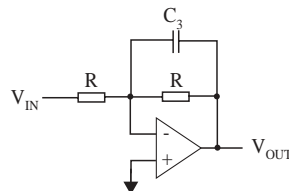


Fig. 5.11: RC equivalent circuit of the switch capacitor SH with low pass filter.

The equivalent R^* resistor and the cut off frequency are, with f the clock frequency:

$$R^* = \frac{1}{f \cdot C_2} \quad (5.19)$$

$$f_c = \frac{1}{2\pi} \frac{1}{R^* \cdot C_3} = \frac{f}{2\pi} \frac{C_2}{C_3} \quad (5.20)$$

5.4.3 Buffer

A buffer is placed at the output of the microsystem. Its main non-ideality is the OA offset, which has a standard deviation of approximately 1mV in this technology. As it appears after demodulation, the buffer offset is seen as a residual offset. Consequently, the standard deviation of the magnetic equivalent residual offset is equal to 250 μ T with a microsystem sensitivity of 4V/T.

5.4.4 Residual offset from peak to peak detector and Buffer

The peak-to-peak detector and the buffer do not cancel the OA offset; the double of the OA offset comes from the sample-and-hold. Consequently, there is a factor of $\sqrt{5}$ of the typical OA standard deviation of offset at the microsystem output. This residual offset do not depend on the spinning frequency.

The main part of the offset is produced by the imperfections of SC circuits (not ideal switches) [Enz86]. The factors affecting the residual offset are mainly the charge injection and clock feed-through. To evaluate the offset from SC circuits, residual offset is measured with microsystems where the inputs are connected to the reference signal. Only the nonidealities of SC circuits and buffers are present if the hypothesis of negligible transients is considered. We measure a 15mV standard deviation of the residual offset at the output of the microsystem. This residual offset does not depend on the spinning frequency, because the quantity of parasitic charges at each period is not changed.

Several other strategies can also be used to reduce the residual offset: increasing the capacitors (for a given quantity of charges, the voltage drop is smaller), decreasing the switches surface (the number of parasitic charges is decreased), adding dummy switches to absorb the charge injection and clock feed-through, and using differential structures. Note that increasing the value of the capacitor and decreasing the switch surface (consequently increasing the parasitic resistance) are the opposite of a high spinning frequency.

5.5 Microsystem residual offset

Sources of residual offset, presented in previous sections, are present before and after the amplification. For sources of residual offset appearing after the amplification the voltage is divided by the electronic gain when it is reported to the input. Therefore it is essential to know the gain G of the electronics to evaluate the magnetic equivalent residual offset. The microsystem is characterized by the Hall sensors' current related sensitivity S_I , the biasing current I and the number of sensors N . The choice of the electronic gain G is directly related to the saturation of the electronics. We introduce the saturation field B_{SAT} , defined as the field where the electronics saturate. It is assumed that the electronics saturate when the output signal is equal to $V_{DD}/2$:

$$B_{SAT} = \frac{1}{G \cdot N \cdot S_I \cdot I} \frac{V_{DD}}{2} \quad (5.21)$$

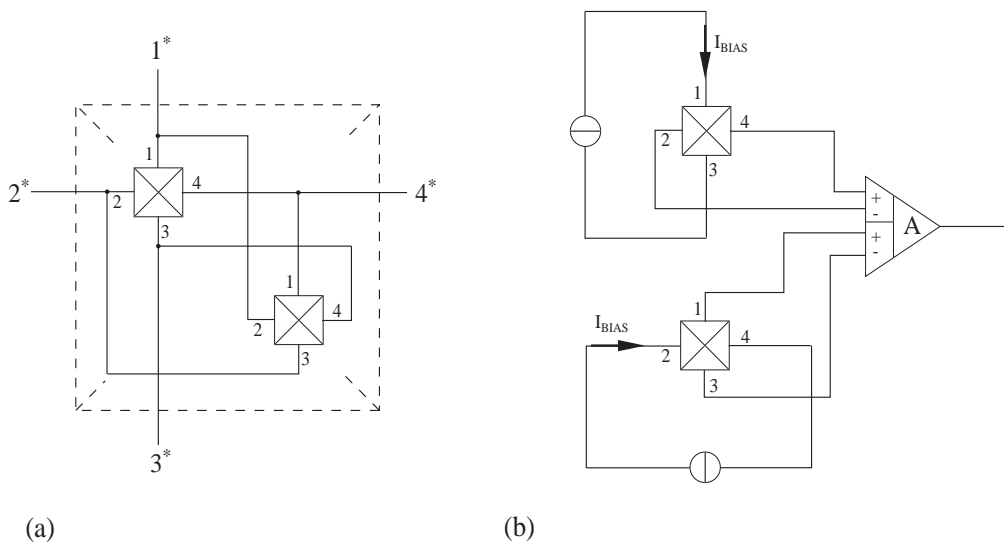


Fig. 5.12: Offset reduction is achieved by the orthogonal coupling of Hall sensors [Maupin80]. The coupling is done by the connection of the sensor itself (a) or by summing the signals with the preamplifier (b). This approach can be extended to the 4 directions of biasing with 4 sensors.

The sensor itself is a source of residual offset. If an array of Hall sensors is used, the residual offsets are totalized inside the DDA. Let's assume that they are not correlated. The standard deviation of the offset voltage is increased by a factor

\sqrt{N} , while the sensitivity is increased by N . Note that a good system design with an array of sensors will suppress the correlated residual offset between sensors. The principle is to place sensors in pairs with opposite spinning phases [Randjel00]; the mutual compensation of a sensor couple biased orthogonally tends to cancel out their asymmetry (Fig. 5.12) [Maupin80].

As explained in §5.3, the DDA creates a residual offset due to the initial offset being seen as a common mode difference between DDA inputs $V_{\Delta CM}$ proportional to the biasing current I_{BIAS} :

$$V_{\Delta CM} = A_{\Delta CM} I_{BIAS} \quad (5.22)$$

This effect is present on each input. Consequently, the equivalent magnetic residual offset B_{ROFF} is equal to its division by the sensitivity. This term is often negligible compared to the Hall sensor residual offset $B_{SENS,ROFF}$. With an ideal sensor, i.e. a symmetric sensor, $A_{\Delta CM}$ is null, but variations of the process result in a deviation of this parameter. It is supposed to be strongly correlated between each sensor of a same chip.

Based on previous explanations, the magnetic equivalent residual offset is, when spikes are negligible:

$$B_{ROFF} = \frac{1}{N} \sum B_{SENS,ROFF} + \frac{1}{N \cdot S_I} G_{\Delta CM} \cdot \sum A_{\Delta CM} + B_{SAT} \cdot \frac{2}{V_{DD}} \cdot V_{SC,ROFF} \quad (5.23)$$

Its standard deviation is:

$$\sigma(B_{ROFF}) = \sqrt{\frac{1}{N} \sigma^2(B_{SENS,ROFF}) + \left(\frac{G_{\Delta CM}}{S_I} \cdot \sigma(A_{\Delta CM}) \right)^2 + \left(B_{SAT} \cdot \frac{2}{V_{DD}} \cdot \sigma(V_{SC,ROFF}) \right)^2} \quad (5.24)$$

The previous equations (5.23) (5.24) shows several ways to reduce the residual offset of a spinning current microsystem. The first one, to decrease the sensor residual offset is to use an array of N sensors. The disadvantage is a larger chip surface and a higher current consumption for sensors biasing. The second one, to decrease the residual offset from the electronics, is to decrease the full scale B_{SAT} of the chip (i.e. increasing the electronic gain). Note also that decreasing the chip supply voltage increases the residual offset from the electronic circuits. The performances of three microsystems are summarized in the Table 1. The importance of both electronics and Hall sensor residual offset is shown. A good correlation between measured and calculated residual offset is observed.

	<i>VH μSI</i>	<i>VH μSII</i>	<i>VH μSIII</i>
S_I : <i>Sensor sensitivity</i>	<i>180V/AT</i>	<i>180V/AT</i>	<i>180V/AT</i>
N : <i>Number of sensors</i>	<i>2</i>	<i>2</i>	<i>2</i>
$B_{S,ROFF}$: <i>Sensor Residual offset</i>	<i>330μT</i>	<i>1.2mT</i>	<i>330μT</i>
V_{DD} : <i>Supply voltage</i>	<i>5V</i>	<i>5V</i>	<i>5V</i>
$A_{\Delta CM}$: <i>Common mode swing</i>	<i>90V/A</i>	<i>90V/A</i>	<i>90V/A</i>
$G_{\Delta CM}$: <i>DDA ΔCMR</i>	<i>0.076‰</i>	<i>0.076‰</i>	<i>0.076‰</i>
$V_{SC,ROFF}$: <i>Electronic Residual offset</i>	<i>15mV</i>	<i>1.2mV</i>	<i>1.2mV</i>
B_{SAT} : <i>μSystem saturation field</i>	<i>680mT</i>	<i>830mT</i>	<i>830mT</i>
<i>Calculated residual offset</i>	<i>4mT</i>	<i>950μT</i>	<i>500μT</i>
<i>Measured residual offset</i>	<i>4mT</i>	<i>1mT</i>	<i>450μT</i>

Table 1. Residual offset for 3 microsystems based on CMOS vertical Hall sensors [Schurig02]. The first, which measures magnetic fields up to 680mT, uses 4-phases spinning current. The residual offset, mainly coming from the electronic circuits after amplification, is due to the small gain. The second microsystem is a 2-phases spinning current with an improved spinning current electronics block. In this case the sensor is the main residual offset source. The third microsystem is the combination of both enhancements: 4-phases spinning current and low residual offset electronics.

5.6 Noise

Ideally, the microsystem using the spinning current method will completely suppress the 1/f noise without introducing white noise. Measurements confirm that the 1/f disappears (Fig. 5.13), but unfortunately the white noise is increased. The white and 1/f noise are analyzed below for each part of the circuit.

5.6.1 Hall sensor

The sensor output resistance R_{HALL} is the intrinsic source of Johnson noise. If an array of N sensors is implemented to sum each Hall voltage, the thermal white noise is increased by \sqrt{N} . Note that the SNR is also increased by the same factor because the sensitivity is increased by N . $1/f$ noise is present at the sensor output (Fig. 5.13) [Hooge94]. One goal of the spinning current method is to separate the signal from the $1/f$ noise in order to suppress this noise.

5.6.2 Modulator

A major source of white noise is the parasitic serial resistance of the voltage switches R_{ON} provoking Johnson noise. The size of the switches is a compromise between the parasitic effects of the switches (charge injection, clock feed-through and parasitic capacitance), the white noise and eventually the chip surface. A good compromise for low noise applications is that the two switches noise PSD equals one of the sensor ($2R_{ON}=R_{HALL}$). This increases the RMS noise only by a factor $\sqrt{2}$.

Modulation bring back the higher frequency of $1/f$ in the baseband [Enz96]. The effect in this case is insignificant because of the much higher spinning frequency than the $1/f$ noise corner frequency.

5.6.3 Preamplifier

The amplifiers, mainly the DDA, are also a source of voltage white noise (Johnson and Shot noise). The simulated equivalent input noise of the first preamplifier (DDA) is $24\text{nV}/\sqrt{\text{Hz}}$ and is equivalent to the noise of a $35\text{k}\Omega$ resistor at room temperature. The $1/f$ noise of the preamplifiers is separated from the signal because of the Hall voltage modulation, if its corner frequency is lower than the spinning frequency.

5.6.4 Correlated double sampling

The capacitor switch technique increases white noise during sampling [Furrer01] [Fischer82]. This is due to undersampling at a frequency f_s of the input white noise bandwidth B . The PSD is increased by a factor $G_{N,US}$:

$$G_{N,US} = \frac{S_N^*}{S_N} = \frac{2B}{f_s} \quad (5.25)$$

Where S_N and S_N^* are the PSD noise before and after the sampling.

The bandwidth of the preamplifier is reduced to limit the thermal noise spectrum before reaching the switched-capacitor circuitry. However, this reduction is limited to avoid attenuation due to settling time (10% attenuation when the bandwidth is twice the sampling frequency). $G_{N,US}$ is typically between 6 and 9, i.e. the voltage noise is multiply by a factor about 2.5-3.

The sampled noise, provoked by the parasitic channel resistance of the switch is negligible with sampling capacitors of several pF [Vittoz85].

The 1/f noise of the SH and the output buffer is not cancelled by the modulation, because it appears after the P2P detector. It is a major source of 1/f noise at the output of the microsystem. Fortunately it is not observable at the output of the microsystem (Fig. 5.13), because of the high amplification of white noise sources in the preamplifier.

5.6.5 Microsystem Noise

In one of the microsystems, an array of four Hall plates and complete readout electronics are implemented in a standard 0.8 μ m CMOS technology. It contains miniaturized 2.4 μ m Hall sensors (see §4). The sensor output resistance R_{HALL} is 18k Ω . Its sensitivity S_{HALL} is 36mV/T at 200 μ A biasing.

The switch R_{ON} resistance is 12k Ω . It results in a noise of 20nV/ \sqrt Hz at each input of the DDA. The array of 4 sensors multiplies by 4 the sensitivity, but also the noise PSD. The DDA, which is the other main source of noise from amplifiers, has a 24nV/ \sqrt Hz white noise V_{DDA} . The undersampling increases the PSD by a factor $G_{N,US}$ of about 7. The equivalent magnetic noise b_{NOISE} is consequently equal to:

$$b_{NOISE} = \frac{1}{NS_{HALL}} \sqrt{G_{N,US} \left[4kTN (R_{HALL} + 2R_{ON}) + v_{DDA}^2 \right]} \quad (5.26)$$

The 0.8 μ T/ \sqrt Hz noise calculated from Equ. (5.26) correlates well with the 0.9 μ T/ \sqrt Hz white measured of the Fig. 5.13.

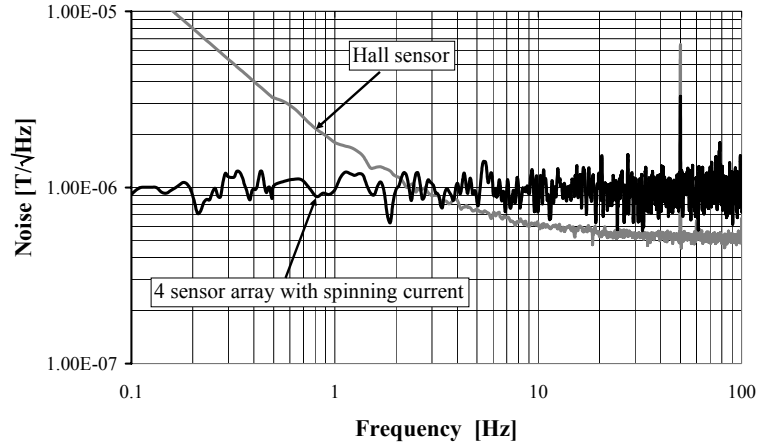


Fig. 5.13: Comparison of the equivalent magnetic noise between a sensor and the spinning current microsystem with 4 sensors. The $1/f$ noise is lost in the thermal noise at frequencies down to 0.1Hz.

5.7 Feedback Spinning Current

The residual offset from the electronics is composed of two parts. The first component $V_{O,S}$, which appears before the amplification, is mainly from the sensor itself. The sensor magnetic residual offset equivalent is not dependant on the electronic gain, but only on the sensor sensitivity S . The second component $V_{O,E}$ appears after the amplifier by gain A (Fig. 5.14). It originates essentially from the switched capacitor nonidealities of the peak-to-peak detector. As demonstrated previously, it is the main residual offset source provoked by the electronic circuits. The magnetic equivalent residual offset B_{OFF} is thus equal to:

$$B_{OFF} = \frac{1}{A \cdot S} (A \cdot V_{O,S} + V_{O,E}) = \frac{1}{S} \left(V_{O,S} + \frac{V_{O,E}}{A} \right) \quad (5.27)$$

The magnetic equivalent residual offset is inversely proportional to the electronic gain: the higher the gain, the lower the magnetic residual offset equivalent.

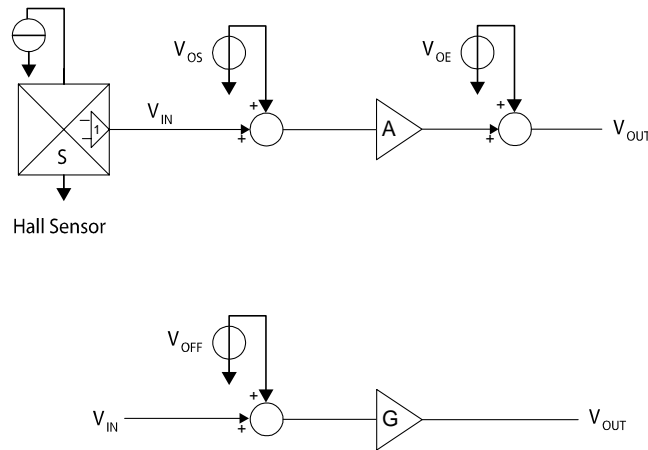


Fig. 5.14 Simplified schematic of the electronics. Two residual offset sources are present. The first one, mainly from the sensor, appears before the amplification. The second one, which is mainly from the peak to peak detector, is after the amplifier. These two sources can be replaced by an offset source referenced at the input and an amplifier with the same gain.

Unfortunately, the electronics saturation point, which limits the full scale FS of the microsystem to half the supply voltage V_{DD} , limits also the electronics gain: this gain cannot be increased for a given saturation magnetic field B_{SAT} .

$$FS = \pm \frac{V_{DD}}{2} = \pm A \cdot S \cdot B_{SAT} \quad (5.28)$$

Based on this concept of increasing the gain, we propose an innovative and systematic approach to greatly reduce the offset source, i.e. with limited modifications to the electronics.

5.7.1 Principle

The principle is based on a FB loop (Fig. 5.15). It is well known that FB cannot reduce the offset, if the offset arises before the FB loop. In this new architecture, the source of offset is inside the loop and after the gain A_{FB} .

With the FB topology, this final electronic gain G is mostly inversely proportional to the FB gain B (5.29) and it is virtually independent of the direct gain A_{FB} .

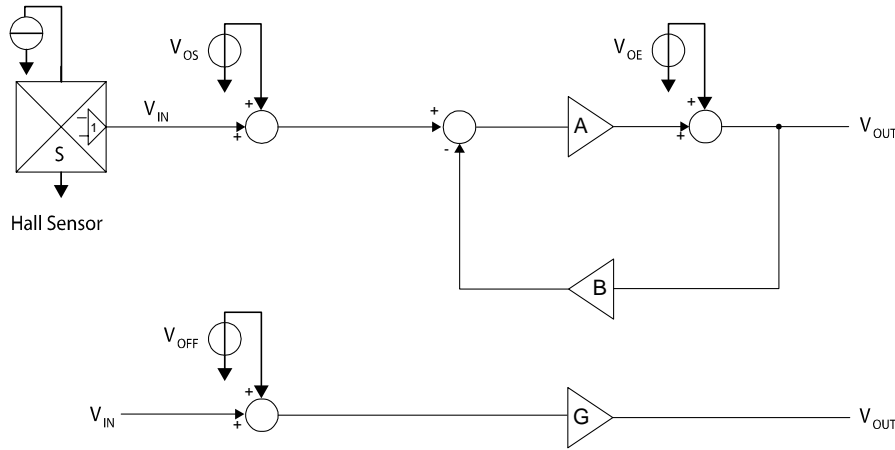


Fig. 5.15: Schematic of the amplifier. V_{OS} is the sensor offset and V_{OE} is the electronic offset. The schematic equivalent is an amplifier with a gain G and an equivalent input offset V_{OFF}

$$G = \frac{A_{FB}}{1 + A_{FB} \cdot B} \cong \frac{1}{B} \quad (5.29)$$

It is now possible to increase the gain A_{FB} without increasing the gain G of the electronics which is roughly fixed by the feedback gain B . The full scale is consequently fixed by the feedback gain B and no more by the gain A_{FB} :

$$FS = \pm \frac{V_{DD}}{2} = \pm G \cdot S \cdot B_{SAT} \cong \pm \frac{1}{B} \cdot S \cdot B_{SAT} \quad (5.30)$$

The final magnetic offset equivalent is equal to:

$$B_{OFF,FB} = \frac{1}{GS} \left(\frac{A_{FB}}{1 + A_{FB} \cdot B} V_{OS} + \frac{1}{1 + A_{FB} \cdot B} V_{OE} \right) = \frac{1}{S} \left(V_{OS} + \frac{V_{OE}}{A_{FB}} \right) \quad (5.31)$$

The equation (5.31) demonstrates that it is now possible to reduce the electronics' part of the offset by increasing the direct gain A_{FB} , without modifying the final electronic gain G , which itself is fixed by the feedback gain B (5.29). If the sensor offset V_{OS} is negligible compare to the electronics offset V_{OE} , we can write:

$$\frac{A_{FB}}{A} = \frac{B_{OFF}}{B_{OFF,FB}} \quad (5.32)$$

We choose a ratio A_{FB}/A of 10 to decrease the residual offset of electronics by one order of magnitude.

5.7.2 Modifications

Only a few modifications are required to implement the feedback loop inside our electronics. An additional differential input on the DDA is required to connect the feedback.

It is fundamental that the feedback loop does not introduce itself an offset. The feedback is composed by a ratiometric voltage divider and a modulator to obtain the same square wave signal as the sensors with spinning current (Fig. 5.16). For this, four voltage switches controlled by the same signals than switch boxes are used.

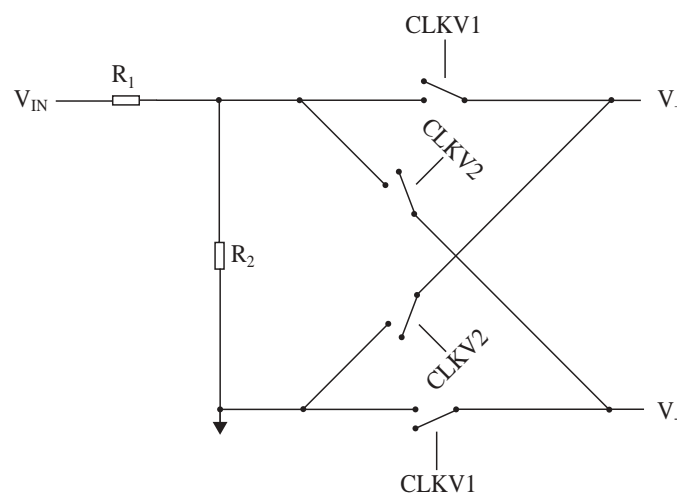


Fig. 5.16: Feedback loop. The feedback gain B is fixed by the resistors R_1 and R_2 . It is followed by a modulator controlled by the same signals as the switchboxes. V_+ and V_- are connected to a differential input of the DDA.

An additional amplification stage with a gain of 10 is added after the DDA. To avoid saturation of this amplifier due to the DC component of the offset, an RC high pass filter is therefore placed prior to this amplifier. It is composed of a 30 pF capacitor and a 220K Ω resistor.

To guarantee the stability of the feedback loop, a dominant pole is required. It is determined by the low-pass filter of the switch capacitors electronics of the sample and hold (§5.4.2).

5.7.3 Simulations

The microsystem is simulated with MATLAB SIMULINK using the model of the Fig. 5.17. A sensor residual offset is simulated by adding a DC voltage

source after the modulation of the Hall voltage. The electronics' offset is simulated by adding a voltage source and the output voltage of the S/H.

Limited bandwidth of the amplifiers and delays introduced by switch capacitors circuitry become sources of instability when a feedback loop is added. This dynamic behavior is introduced inside our model.

To ensure the stability of the loop, a dominant pole is placed after the S/H. As explained in §5.7.4, the cutoff frequency is not equal to the bandwidth of the microsystem due to rejection with the FB loop at higher frequencies. The initial microsystem contains a 100KHz 2nd order low pass filter. For stability reasons, this 2nd order filter is replaced by a 1st order one.

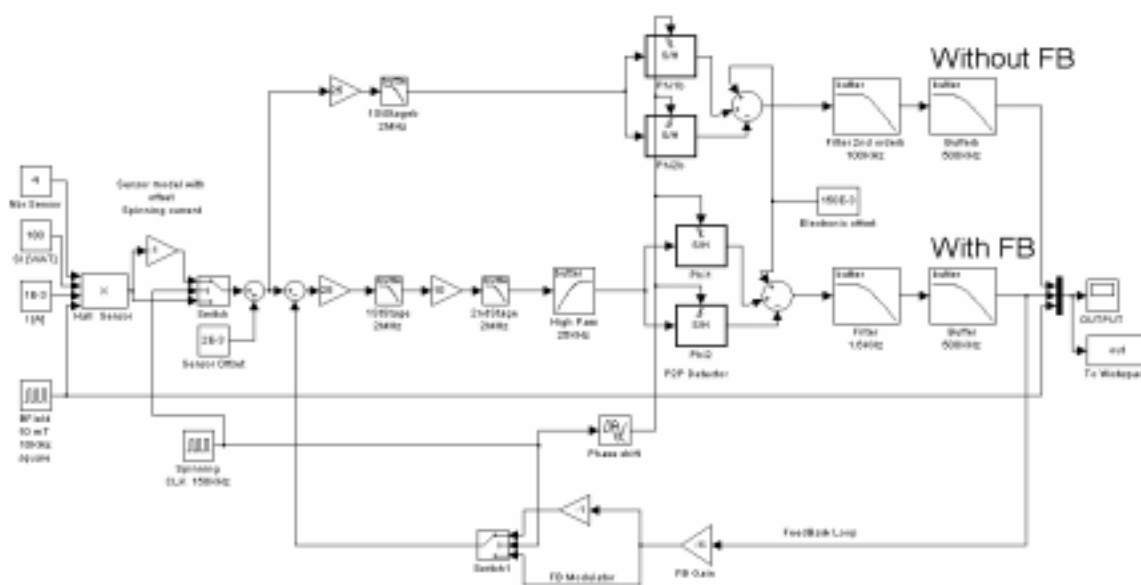


Fig. 5.17: *MatLab SIMULINK[®] model of the spinning current microsystem with and without the feedback loop. Two offset voltage sources are introduced before and after amplification to simulate the offset before and after amplification.*

As expected, stability is the main difficulty with the FB loop. A low pass filter with a cutoff frequency of 1.75KHz for a spinning current at 150KHz is obligatory if the direct gain A is increased by 10. However, the bandwidth of the system is not equal to the filter cutoff frequency, because of the feedback loop.

MATLAB SIMULINK[®] simulations confirm the efficiency of the feedback topology. The electronics offset is roughly divided by 10, the ratio of the direct gain with and without FB (Fig. 5.18). The frequency response is not too greatly deteriorated, compared to the initial microsystem with a 100KHz second order output filter.

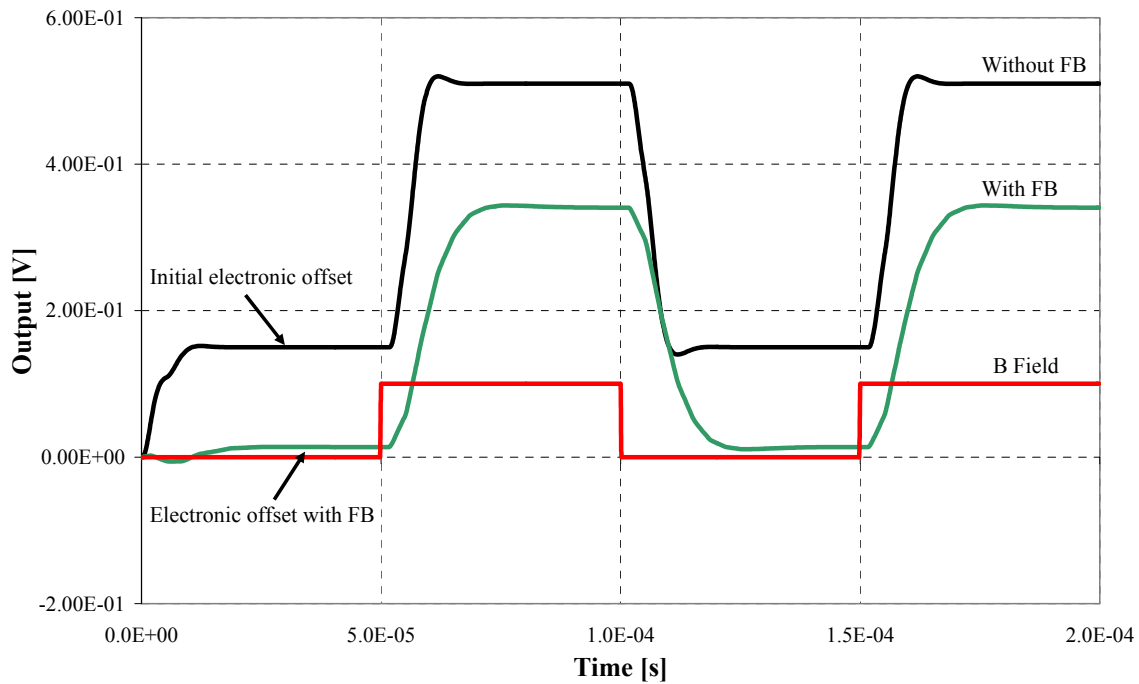


Fig. 5.18: *MATLAB SIMULINK® simulations of the microsystem with a 150 mV electronic offset. The microsystem's response is compared, with and without the FB loop, with an additional gain of 10. As expected, electronic offset at the output of the microsystem is roughly divided by a factor 10. The frequency response is not greatly deteriorated compared to the initial microsystem with a 100KHz second order output filter.*

5.7.4 Electronics dynamic behavior

To ensure stability, a dominant pole ω_0 is required inside the FB loop. An optimum frequency of 1.75KHz is found with SPICE simulations. Due to the closed loop, the cut off frequency ω_{FB} is rejected at higher frequency:

$$f_{FB} = f_c (1 + A \cdot B) = 1.75 \text{KHz} (1 + 500 \cdot 0.029) = 27 \text{KHz} \quad (5.33)$$

This value is much greater than the usual bandwidth of an angular position sensor (200'000 RPM).

This filter is introduced inside the SH which itself already allows filtering (see §5.4.2). This approach fixes the pole without an inaccurate RC constant. The time delay introduced by the switch capacitors is inversely proportional to the frequency of the spinning current. The cut off frequency is also inversely proportional and consequently the stability is guaranteed for a reasonable clock frequency.

The Fig. 5.19 shows the P-Spice simulated transient response of the microsystem for a sine and a square input.

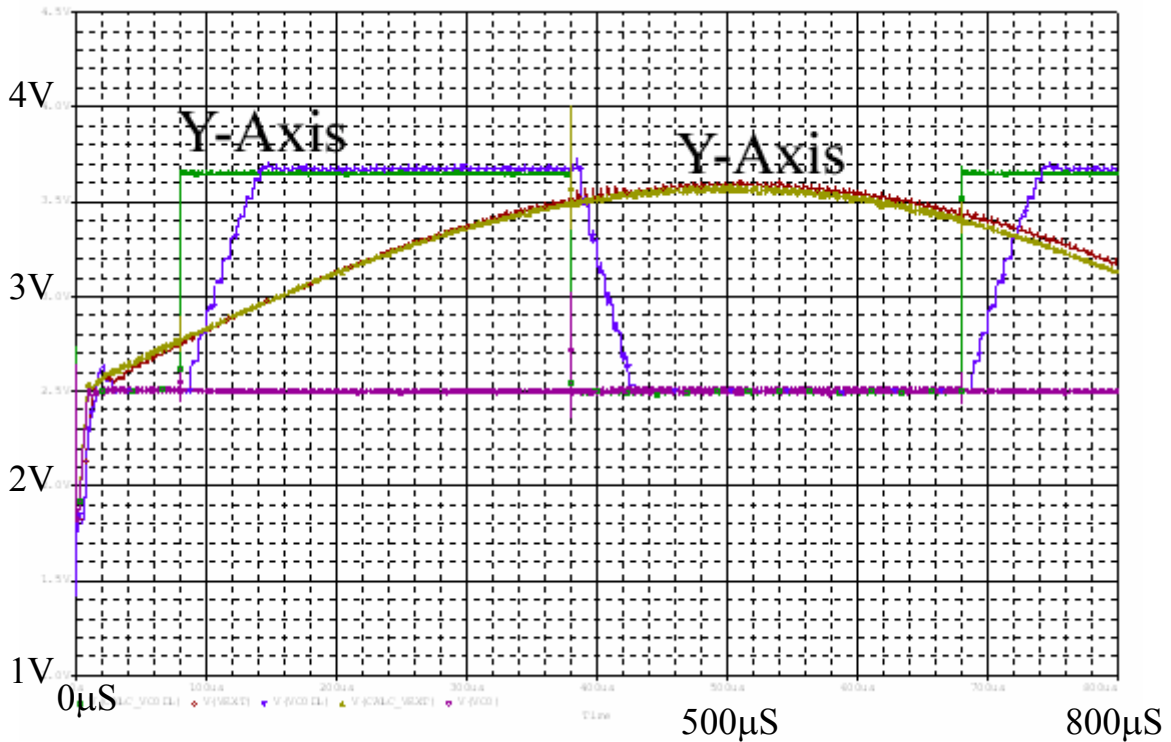


Fig. 5.19: P-Spice transient simulations of a two dimensional microsystem for a sine (X-axes) and a square (Y-axes) input. The slope of the square wave in close loop is caused by the slew rate of the SC filter.

The dynamic behavior is above all limited by the slew rate S_R due to loading of the 60pF C_3 capacitor filter. The current load is limited by the SC equivalent resistor (5.19) and the electronics' saturation at roughly half the 5V supply voltage V_{DD} .

$$S_R = f_s \frac{V_{DD} C_3}{2 C_1} \quad (5.34)$$

C_1 is the 4pF sampling capacitor, f_s the 165KHz sampling frequency.

A slew rate of 28mV/ μ s is calculated with Equ. (5.34). This corresponds well to the predictions of the Spice simulations (Fig. 5.19).

5.7.5 Measurements

A 1-dimensional microsystem using the new feedback configuration has been realized and tested (6 samples). As simulated in §5.7.3, it is designed with $A_{FB}/A=10$ to reach a residual offset from electronics at the microsystem output of about 1mV. To measure the electronics performances, the sensor connections are short circuited. We measure a standard deviation of the microsystem output equal to 15.3mV without the FB loop (Fig. 5.20). With the FB configuration, it is decreased by more than a factor 12 to reach 1.2mV (Fig. 5.20). The electronics' gain is reduced by 18% when FB is turned on. Consequently, the residual input offset is decreased by a factor 9.8 using the new FB principle. This is what was predicted with the additional gain of 10: the measurements confirm indeed the SIMULINK and Spice simulations.

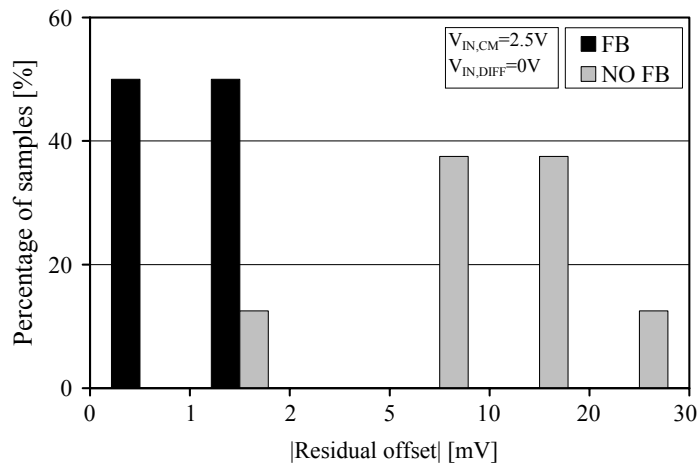


Fig. 5.20: Measurements of 6 chips residual offset at the output of the microsystem with and without feedback. The feedback strongly reduces residual offset. The result is comparable to a single OA offset (!).

The cross-sensitivity of the residual offset to other parameters is also measured with and without feedback (Fig. 5.21). We measure the residual offset with variations of the supply voltage and the spinning frequency. As expected, the cross-sensitivities are strongly reduced with the feedback configuration.

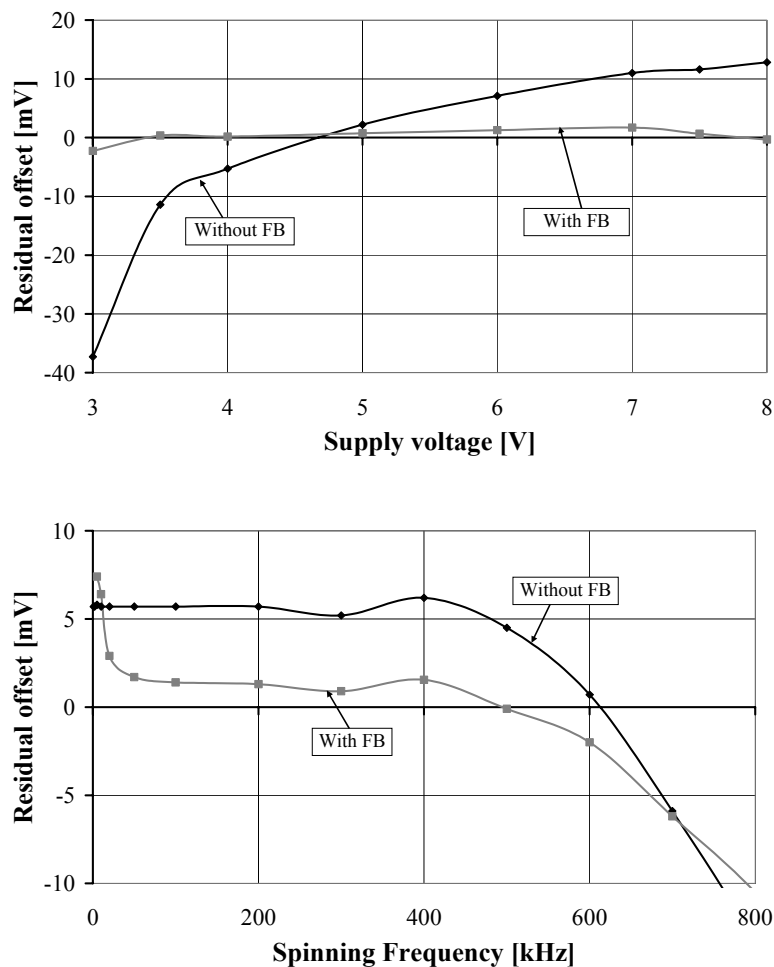


Fig. 5.21: Comparisons of measurements with and without the FB principle. The cross sensitivity of the residual offset to supply voltage and spinning frequency is reduced.

We also measure the linearity of the microsystem. Feedback is known to increase the linearity, because the gain is fixed by the feedback. The $1+AB$ increase of linearity is equal to 15. The measurements (Fig. 5.22) confirm that non-linearities are strongly reduced when the electronic circuits reach saturation. The difference between the theory and the measurements is due to the reduced direct gain A near the saturation. Note that only the non-linearities from the electronic circuit are reduced with the electronics' feedback. Only a magnetic feedback is able to decrease the sensor non-linearities.

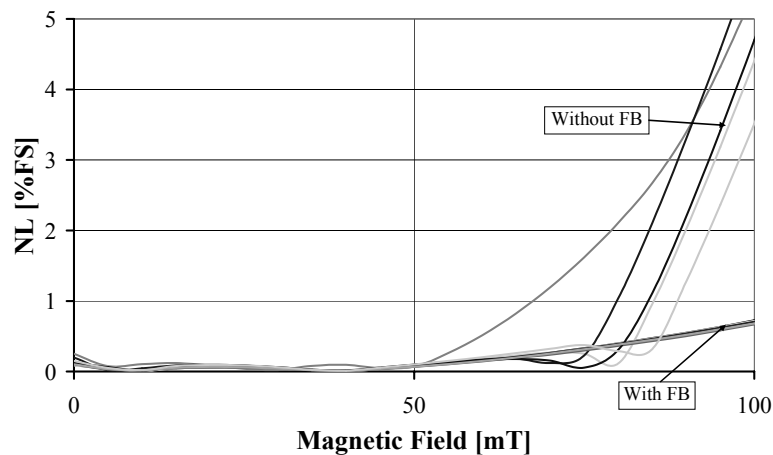


Fig. 5.22: Measurements of the non-linearity with and without feedback. The feedback increases the linearity near the saturation, due to the gain being fixed by the feedback resistor and not by the amplifiers.

5.8 4-Phases Spinning Current

Two-phases spinning current (where the current flows in two orthogonal directions) is unable to cancel all main sources of residual offset (see §4.4 for miniaturized Hall plates) [Steiner99] [Ruther02a]. The junction field effect (JFE) is amplified with CMOS vertical Hall sensors and miniaturized sensors, due to higher ratio between depletion length and sensor thickness. JFE is a main source of residual offset when combined with mechanical stresses [Ruther02b]: a 2-phases spinning current electronics' block is unable to suppress quadratic terms of residual offset with biasing current, while if we use a 4-phases spinning current, it is completely removed.

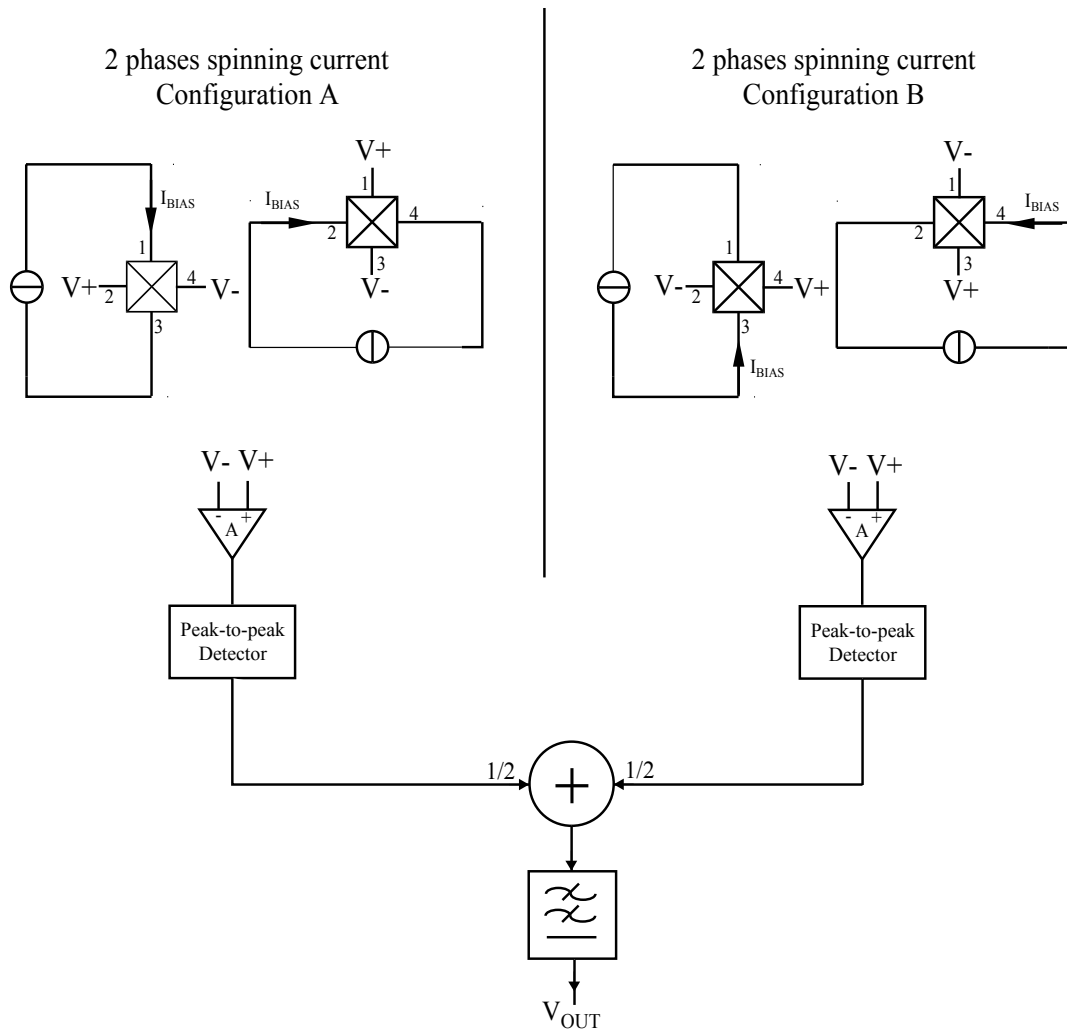


Fig. 5.23: Simplified block diagram of the 4-phases spinning current electronics. It is composed of two blocks of the 2-phases spinning current A and B, but using opposite current directions. The two results are averaged and the parasitic ripple filtered. It is accomplished with multiplexing of amplifiers and peak-to-peak detection. Filtering of the two multiplexed signals achieves the averaging. Only additional switches for modulation and novel clock signals are required to adapt the 2-phases electronics.

The 4-phases implemented principle is to measure twice the two-phases spinning currents by inverting the current directions (Fig. 5.23), i.e. the current flows in the 4 orthogonal directions. The sensitivities are equal, but the sign of the residual offset is changed (Fig. 5.24). After the peak-to peak detection, the two signals are averaged to cancel the residual offset. This is done by the low-pass filtering of the sample-and-hold which integrates the two results. Only additional modulation switches are required with adapted clock signals, without other modifications of the analog front-end.

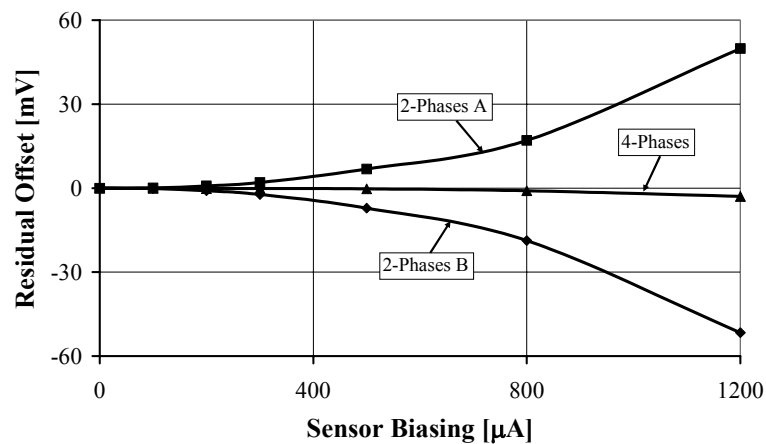


Fig. 5.24: Residual offset with the 2-phases and the 4-phases spinning current for a couple of CMOS vertical Hall sensors with the feedback. The 2-phases residual offset is opposite when the current direction is inverted [Ruther02b].

Even if a residual offset is still observed (Fig. 5.25) with this electronic circuit, the residual offset is substantially reduced for a low additional silicon surface. The 4-phases is particularly efficient if junction field effect is present inside the sensor. Junction field effect is particularly serious when Hall sensors are miniaturized (4.2.1). Pairs of CMOS vertical Hall sensors (§2.3.2) have an asymmetry due to junction field effect [Schurig03]. This asymmetry is not cancelled with 2-phases spinning current (Fig. 5.25a). Consequently, the distribution of residual offset is not centered to zero. 4-phases is able to suppress this asymmetry and the residual offset is consequently similar to single Hall sensors.

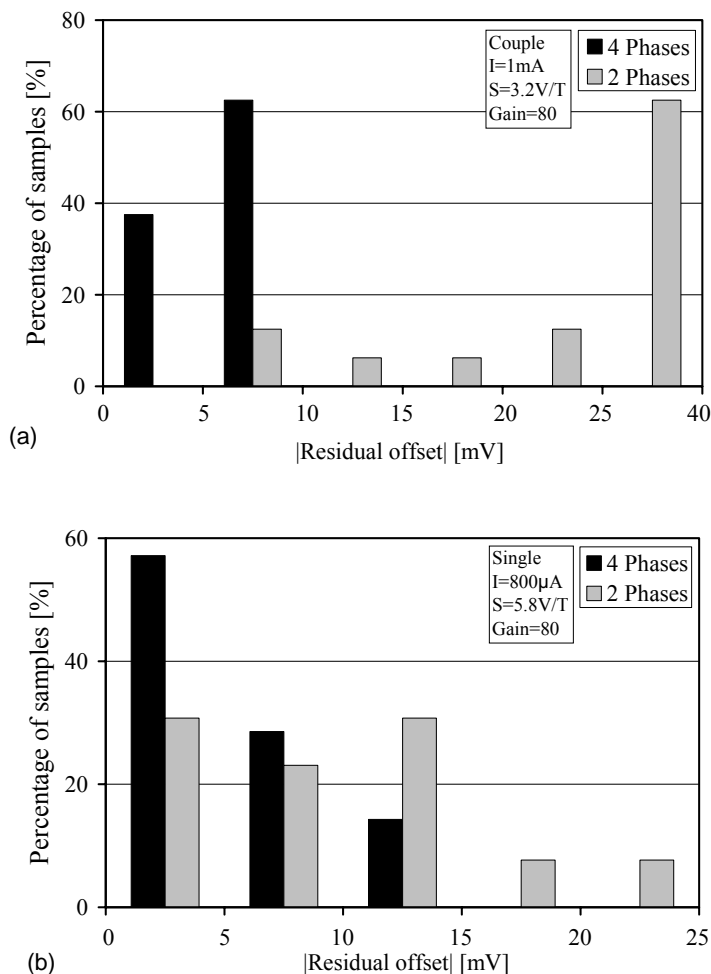


Fig. 5.25: Measurements of the residual offset of 12 chips for 2- and 4-phases spinning current methods with the feedback configuration. The first graph (a) is for a pair of CMOS vertical Hall sensors connected to the spinning current electronics. This sensor introduces a residual offset due to its asymmetry, which is not removed by the 2 phases configuration. The 2nd (b) is for a single vertical Hall sensor. For both sensors, the residual offset is noticeably reduced with 4-phases spinning current. Note that the residual offset and the magnetic equivalent residual offset are much smaller with a lower biasing current, as demonstrated in §4.4.

5.9 2D-Spinning Current

For our angular microsystem, two axes of sensitivity, and consequently two outputs are requested. It is also crucial to have a matching of the electronics' gain between the X and Y axes. One way to guarantee this fact is to use the same analog chain twice. For this reason, a temporal multiplexing of X and Y axes is used (Fig. 5.26); half of the cycle for both axes.

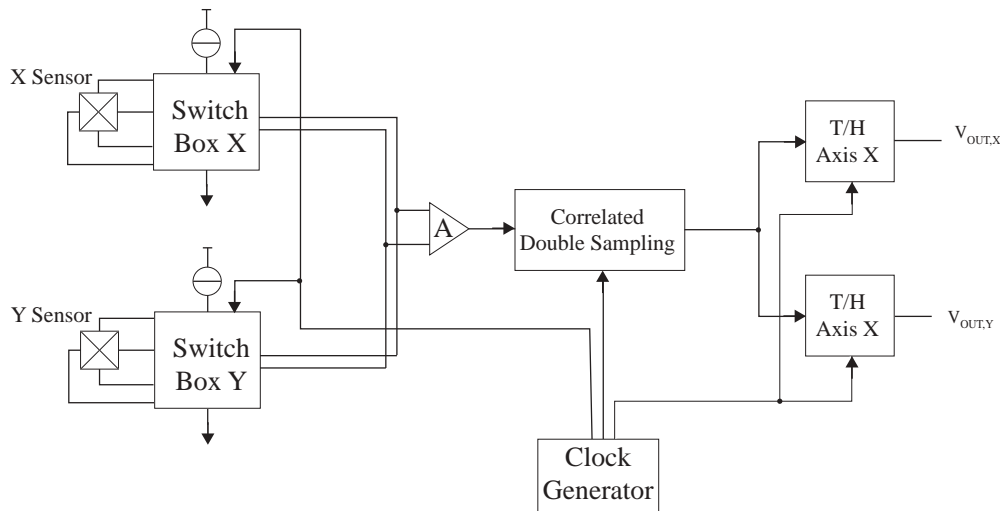


Fig. 5.26: Multiplexing of X and Y axes for a two dimensional microsystem. This ensures matching of the gain.

The microsystem we realize allows also the 4-phases spinning current and the feedback configuration for offset reduction of both electronics and sensors.

The clock generator is modified to consecutively select both axes with their respective switchboxes. That requires additional switch boxes for the new axes, a second sample and hold (to always have the two outputs valid), two output buffers and a switching between outputs for the feedback. The high pass filter, which is placed between the two amplification stages, is also modified in order to filter the DC component of both axes. As the offset is different for both axes, two "analog memories" are needed: an electronic switch between the two capacitors will be used (Fig. 5.27).

Clock signals change the capacitor only at the start of each the SC phases to avoid charge injection between the two spinning directions. If it is not the case, a residual offset appears prior to the amplification.

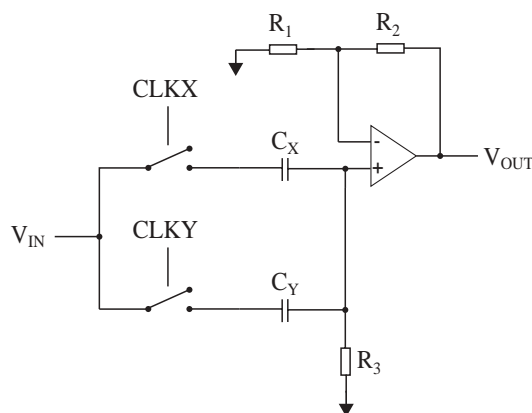


Fig. 5.27: The DC offset (from electronics and sensor) is stored with a capacitor. As the system is multiplexed for the two axes, the electronic circuit permutes between two capacitors when the axes change.

The demodulator output swings between X results and Y results. It is the reason why the ameliorated peak to peak detector presented in §5.4.1. is used only in one dimensional microsystems.

If the feedback spinning current is used, a multiplexer is required to switch between outputs.

5.10 Conclusion

We first develop an efficient analog two phases spinning current electronics' block (§5.1). The electronic sources of residual offset are clearly identified and understood (Table 1). They are mainly the switch capacitors circuits' nonidealities (§5.4.4). Other sources of minor influence are also explained, such as OA offset after demodulation, DDA imperfections (§5.3) and dynamic effects (§5.2). The residual offset of our microsystem does not depend on the spinning frequency. That's why dynamic effects (transitions spikes and settling time) are not a main source of residual offset in our microsystem.

A new principle that we have called feedback spinning current (§5.7) is implemented successfully to reduce the offset which appears after the amplification (peak-to-peak detector and output buffer). With a better system

approach and smaller modifications, we measured that the residual offset from the electronics is divided by an order of magnitude to reach a standard deviation of only 1.2mV. It is comparable to a single OA offset. Using this new principle, the electronics' residual offset can be further reduced, but we have had to compromise between the system's frequency response (§5.7.4) and its' residual offset.

CMOS vertical Hall sensors and miniaturized Hall plates are "degenerated"; they suffer from nonidealities due to junction field effect (§4.2.1). Two phases spinning current unfortunately is not efficient enough and too high a residual offset is present (§5.8) (Table 1). This is the reason why the microsystem is adapted to a 4-phases spinning current method. The total microsystem, i.e. from sensors and electronics, is once more greatly reduced.

Sources of noise in the microsystem are identified (Table 1). Only white noise is observable up to 1 Hz, even if the 1/f noise of buffer and SH is not suppressed by the spinning current method. The sources of white noise are mainly the sensors, the preamplifier and the undersampling in the SC circuits.

	<i>White Noise</i>	$\sigma(\text{Residual offset})$
<i>Sensor $R_S=6K\Omega$, $S=60mV/T$ 2-Phases spinning current</i>	<i>160nT/$\sqrt{\text{Hz}}$</i>	<i>1.2mT</i>
<i>Sensor $R_{\text{SENS}}=6K\Omega$, $S=60mV/T$ 4-Phases spinning current</i>	<i>160nT/$\sqrt{\text{Hz}}$</i>	<i>330μT</i>
<i>Modulator $R_{\text{ON}}=\frac{1}{2}R_{\text{SENS}}$</i>	<i>160nT/$\sqrt{\text{Hz}}$</i>	<i><1μT</i>
<i>Preamplifier (CMOS Vertical Hall)</i>	<i>400nT/$\sqrt{\text{Hz}}$</i>	<i>40μT</i>
<i>P2P detector ($B_{\text{SAT}}=830mT$)</i>	<i>PSD multiply by 7</i>	<i>4mT (!)</i>
<i>P2P with FB loop ($A_{\text{FB}}/A=10$)</i>	<i>PSD multiply by 7</i>	<i>1/10·4mT=400μT</i>

Table 1. Main sources of noise and residual offset for a 4 phases spinning current for a full scale of about 500mT using a vertical Hall sensor with 2V biasing.

To guarantee a matching of the amplification chain and also to reduce the surface of the electronics, the amplification chain of the X and Y axes is multiplexed (§5.9). The Hall signal are amplified successively for both axes and stored inside two sample and holds.

The “final” microsystem we develop, at the end of this work, for angular measurement is the combination of all the improvements. The new feedback configuration reduces efficiently the offset from electronics. The 4-phases spinning current reduces the sensors residual offset. The amplification of X and Y axes by the same analog chain guaranteed the matching of the two axes. The combination of all this techniques is the only way to reach 0.3% (0.1°) high accuracy angular measurements without calibrations (§6). Angular measurements is the topic of the next chapter. The “final” microsystem . Unfortunately, the chips are received too late to be included in the following chapter. This is the reason why we use a microsystem without the feedback configuration and the 4-phases spinning current. Consequently, the offset has to be calibrated.

5.11 References

- [Bakker99] A. Bakker, A.A. Bellekom, S. Middelhoek and J.H. Huijsing, Low-Offset Low-Noise 3.5mW CMOS Spinning-Current Hall Effect Sensor with Integrated Chopper Amplifier, 13th European Conference on Solid-State Transducers, 28C2, pp. 1045-1048, 1999.
- [Bilotti97] A. Bilotti, G. Monreal, and R. Vig, Monolithic Magnetic Hall Sensor Using Dynamic Quadrature Offset Cancellation , IEEE J. of SSC, vol. 32, no. 6, 1997.
- [Bilotti99] A. Bilotti, G. Montreal, Chopper-Stabilized amplifiers with a Track-and-Hold Signal Demodulator, IEEE Transactions on Circuits and Systems I, Volume: 46 Issue: 4 , pp. 490-495, 1999.
- [Daniil82] P. Daniil and E. Cohen, Low field Hall effect magnetometry, J. Appl. Phys., vol. 53, no. 11, pp. 8257-9, 1982.
- [Endo02] H. Endo, Residual Offset of Hall Devices under the Spinning Current Technique, LMIS3 internal report, 2002.
- [Enz87] C. Enz, E.A. Vittoz, F. Krummenacher, A CMOS Chopper Amplifier, IEEE Journal of Solid-State Circuits, Vol. SC-22. No. 3, pp. 335-342, 1987.
- [Enz96] C. C. Enz and G. C. Temse, Circuit Techniques for Reducing the Effects of Op-amp Imperfections: Autozeroing, Correlated Double

-
- Sampling, and Chopper Stabilization, Proc. IEEE, vol. 84, no. 11, pp. 1584-1614, 1996.
- [Fischer82] J. H. Fischer, Noise sources and calculation techniques for switched capacitor filters, IEEE Journal of Solid-State Circuits, Volume: 17 Issue: 4, pp. 742 -752, 1982.
- [Frounch01] J. Frounchi, M. Demierre, Z. Randjelovic and R. Popovic, Integrated Hall Sensor Array Microsystem, ISSCC2001 Conference, San Francisco, pp. 248-249, 2001.
- [Furrer01] B. Furrer, Rauschen und Sample and Hold, Mikroelektronik – Design & Beratung, Private document, 2001.
- [Hooge94] F.N. Hooge, 1/f Noise Sources, IEEE Transaction on Electron Devices, Vol. 41, No. 11, 1994.
- [Kansy80] R.J. Kansy, Response of a correlated double sampling circuit to 1/f noise [generated in CCD arrays], IEEE Journal of Solid-State Circuits, Vol. 15 Issue: 3 , pp. 373-375, 1980.
- [Matsui81] K. Matsui, S. Tanaka and T. Kobayashi. GaAs Hall Generator Application to a Current and Watt Meter, Proc. 1st sensor symp., ed. S. Kataoka, Institute of Electrical Engineers of Japan, Tokio, pp. 37-40, 1981.
- [Maupin80] J.T. Maupin and M.L. Geske, The Hall effect in silicon circuits, The Hall effect and its applications, ed: C.L. Chien and C.R. Westgate, New York London Plenum Press, pp 421-445, 1980.
- [Munter90] P.-J.-A- Munter, A low-offset spinning-current Hall plate, Sensors and Actuators, A21-A23, pp. 743-746, 1990.
- [Popovic96] R. S. Popovic, J. A. Flanagan, and P. A. Besse, The future of magnetic sensors, Sensor and Actuators A, vol. 56, no 1-2, pp. 39-55, 1996.
- [Port01] L. Portmann, Termis Hall Sensor test and operation, Esprit project 29'598, Technical report, EPFL, 2001.
- [Randjel00] Z. Randjelovic, Low-Power High Sensitivity Integrated Hall Magnetic Sensor Microsystems, Ph.D. Thesis, (EPFL No 2198), Hartung-Gorre (Konstanz, Germany), ISBN : 3-89649-617-4, 2000.
-

- [Razavi01] B. Razavi, Design of Analog CMOS Integrated Circuits, McGraw-Hill series in Electrical and Computer Engineering, ISBN0-07-238032-2, 2001.
- [Ruther02a] P. Ruther, U. Schiller, W. Buesser, R. Janke and O. Paul, Thermomagnetic Residual Offset in Integrated Hall Plates, to be published in Proc. IEEE Sensors conference, USA, 2002.
- [Ruther02b] P. Ruther, U. Schiller, W. Buesser, R. Janke and O. Paul, Influence of the Junction Field Effect on the Offset Voltage of Integrated Hall-Plates, European Conference on Solid-State Transducers, Prague, pp. 709-710, 2002.
- [Säckin87] E. Säcker, W. Guggenbühl, A versatile Building Block: The CMOS Differential Difference Amplifier, IEEE Journal of Solid-State, vol. SC-22. No. 2, 1987.
- [Schurig02] E. Schurig, M. Demierre, C. Schott and R. S. Popovic, A vertical Hall device in CMOS high-voltage technology, Sensors & Actuators A: Physical, Vol 97, pp. 47-53, 2002.
- [Schurig03] 0.2mT Residual Offset of CMOS Integrated Vertical Hall Sensors, E. Schurig, C. Schott, P.-A. Bessel, M. Demierre, R.S. Popovic, to be published in Sensors and Actuators, 2003.
- [Steiner98] R. Steiner, Ch. Mayer, A. Häberli, F.-P. Steiner and H. Baltes, Offset Reduction in Hall Devices by Continuous Spinning Current Method, Sensors and Actuators A (66), pp.167-172, 1998.
- [Steiner99] R. Steiner, C. Maier, M. Mayer, S. Bellekom and H. Baltes, Influence of Mechanical Stress on the Offset Voltage of Hall Devices Operated with Spinning Current Method, Journal of Microelectromechanical Systems, Vol. 8, No. 4, pp. 466-471, 1999.
- [Trontelj99] J. Trontelj, Optimization of Integrated Magnetic Sensor by Mixed Signal Processing, Proc. Of IMTC/99, vol. 1, pp. 299-302, 1999.
- [Vittoz85] E. A. Vittoz, Dynamic Analog Techniques, Design of MOS VLSI Circuits for Telecommunication, Y.P. Tsividis and P. Antognetti, Ed. Englewood Cliffs, Prentice-Hall, 1985.

6 Angular position sensors

The operation principle of the magnetic angular position sensor, which we shall consider here, consists in rotating a small diametrically-magnetized permanent magnet placed above a two-dimensional magnetic sensor microsystem (§2.4.2) (Fig. 6.1). Usually the magnet is made of a rare earth to increase the magnetic field. The sensor measures the X and Y components of the magnet field in the plane of the substrate. It transforms these components into electrical signals suitable to retrieve the angle information. This measurement principle, the sensor aligned with the rotation axis, is very robust to alignment tolerances and to the permanent magnet properties [Burger01].

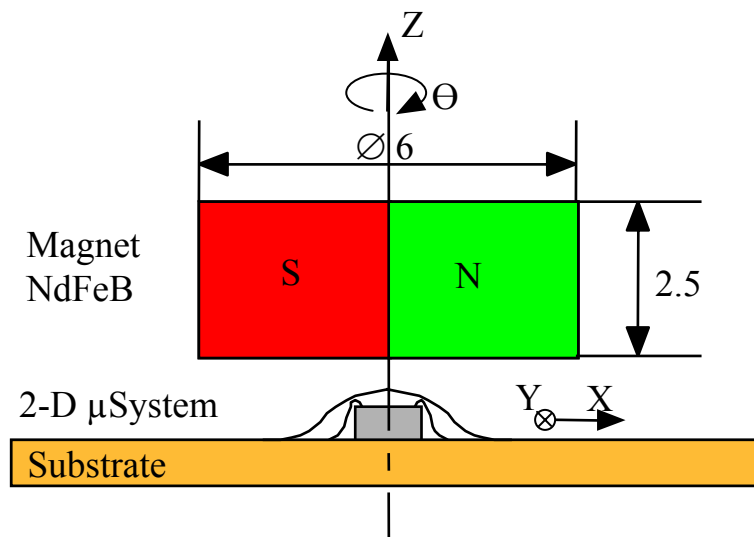


Fig. 6.1 Principle of the angular measurement. A permanent magnet (often rare earth) rotates around the Z axes. A 2-D magnetic microsystem measures the X and Y components of its magnetic field to obtain the sine and cosine electrical signals.

We previously explained how to build an efficient 1-Dimensional (1-D) Hall microsystem. In this chapter, two of them are orthogonally combined in order to obtain a 2-Dimensional (2-D) microsystem. The projections of the external magnetic field give the sine and cosine of the rotation angle θ . Thus, it is possible to calculate the angle over 360° without any discontinuity or dead angle (angles where the measurement or the rotation are impossible). The angle is

extracted from these two values using the four quadrant inverse tangent. The methods of calculation are explained in the §2.3.6.

The extracted angle, from the X- and the Y-axes, suffers from non-linearities. We found within this chapter their sources, their value and also their “signatures”. Their “signatures”, show on Lissajoux curves and graphs of the non-linearity, allow us their compensations in order to increase the sensor accuracy.

Based on the state of the art, two types of sensors, built in a CMOS well, are identified with our requirements of an accuracy of 3‰ without and 1‰ with calibration. The first one consists of two vertical Hall sensors [Popovic84] oriented orthogonally to each other in order to measure the X and Y components of the magnetic field. The second one uses Hall plates and an integrated magneto-concentrator [2SA-10]. We found the sources of inaccuracy of each sensor. Finally we compare the results to obtain the advantages and disadvantages of each solution.

6.1 Hall Sensors related non-linearities

The non-linearity (NL) of the angular measurement describes the deviation from the best linear fit. It is used to evaluate the accuracy of the angular sensor. Hall 1-D microsystems do not generate ideal output signals. In this application, they suffer mainly from sensor non-linearities, (residual) offset, offset drifts and sensitivity drift.

Noise doesn't generate NL. It is responsible for the limitation of the detectivity, often incorrectly called resolution. Usually the magnetic field for angular sensors is as high as 100mT. It is enough to obtain high signal to noise ratio and a detectivity of at least 0.1° with a careful design (see §6.4).

With the signal treatment, the 2-D microsystem is supposed to be equivalent to an orthonormal projective point [Drljaca02]. New sources of NL appear if it is not the case. The first one is the non orthogonality between the axes; it comes from a misalignment of the X and Y axes. The second one is a sensitivity mismatch, where the amplitude of the X and Y signals are not equal.

The two X and Y outputs of the angular microsystem are represented on a Lissajoux curve (Fig. 6.2) to clearly show the NL. Ideally, the curve is a circle c centered at $O(0,0)$. With the previously described imperfections, it is deformed and we obtain an ellipse c' . Offset, non-orthogonality and sensitivity mismatch related NL, which are the main NL sources, are studied in detail bellow.

After calculating the angle from the sine and cosine signals, the ideal output is linear.

The absolute non-linearity (ANL) is defined as the difference between the results and the best fit of the unitary slope. For an angular sensor, the results are equal to a 0° and 360° measurements. This is why the use of ANL is preferred to the usual non-linearity (NL) for the evaluation of the performances of the 360° absolute angular sensors.

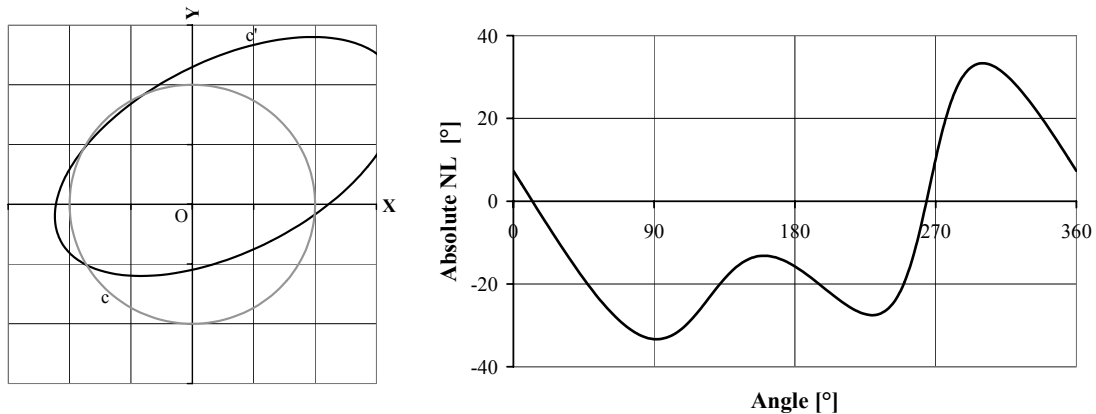


Fig. 6.2 Typical effects of the Hall elements' related absolute non-linearities: X and Y offsets, sensor non-linearity, sensitivity mismatch between axes and non-orthogonality between axes. The left part shows the Lissajoux curve, which is ideally a circle, and the right one the absolute non-linearity.

6.1.1 Offset

Offset is often the most problematic effect when using Hall sensors (§2.1.5), even if spinning current is used (§5). The offset is present on both X ($V_{\text{OFF},X}$) and Y ($V_{\text{OFF},Y}$) axes. It appears as a vector on the Lissajoux curve (Fig. 6.3) which displaces the center of the circle O to a new one O'.

The ANL caused by the offset is a fundamental function of the rotation angle (f-type), i.e. with a period of 360° (Fig. 6.3).

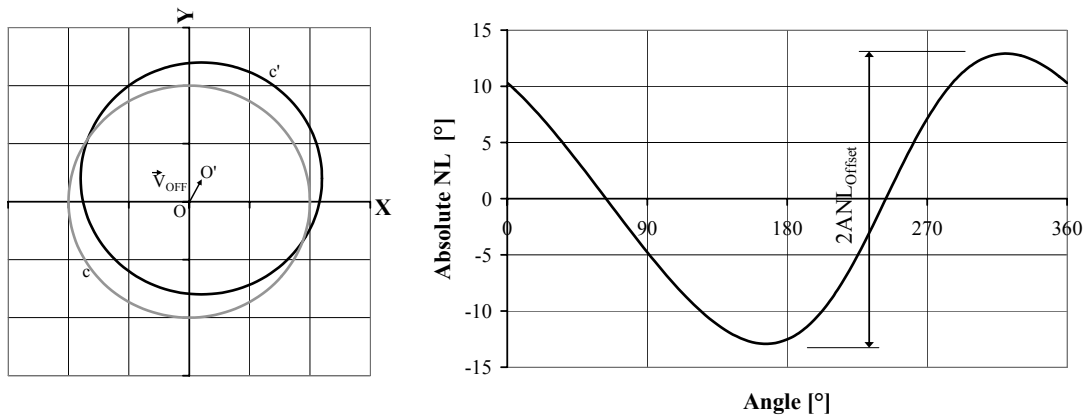


Fig. 6.3 X and Y axes offsets ($B_{off,x}/B=0.1; B_{off,y}/B=0.2$). The left figure presents the Lissajoux curve, where the circle is displaced by a vector composed of the X and Y offsets. The ANL is presented on the right figure. For small offset over amplitude ratio, it is a fundamental function of the angle (f-type) with a phase depending on the distribution of offsets between axes.

For a small offset over amplitude ratio this ANL can be approximated by a sine function with the following amplitude:

$$ANL_{Offset} [^\circ] \cong \left| \arctan\left(\frac{\sqrt{B_{off,x}^2 + B_{off,y}^2}}{B}\right) \right| \cong \frac{180}{\pi} \left(\frac{\sqrt{B_{off,x}^2 + B_{off,y}^2}}{B} \right) \quad (6.1)$$

Where B is the amplitude of the magnetic field at the position of the sensor and $B_{off,x}$ and $B_{off,y}$ the equivalent magnetic offset on the X and Y axes respectively.

The angular dependency of the ANL depends on the distribution of the offset between the axes. It is optimum when the offset vector $\vec{B}_{OFF} = \begin{pmatrix} B_{OFF,X} \\ B_{OFF,Y} \end{pmatrix}$ is

orthogonal to the angular direction vector $\begin{pmatrix} \cos\theta \\ \sin\theta \end{pmatrix}$, where θ is the angle to be measured. The angle of maximum error α_{off} is:

$$\tan(\alpha_{off}) = -\frac{B_{OFF,X}}{B_{OFF,Y}} \quad (6.2)$$

The ANL from offset, which is a function of the angle, is consequently equal to:

$$ANL_{Offset}(\theta)[^\circ] \cong \frac{180}{\pi} \left(\frac{\sqrt{B_{off,X}^2 + B_{off,Y}^2}}{B} \right) \cos(\theta - \alpha_{off}) \quad (6.3)$$

The easiest way to reduce ANL due to offset is naturally to increase the rotating magnetic field. The residual offset after the spinning current method [Bilotti97] [Frounchi01], measured in the §5.5, is typically 450μT. The ANL is 0.18° (0.5‰) using a 200mT magnetic field from the permanent magnet with a 450μT residual offset on both X- and Y-axis. The statistical approach of the ANL is given in the §6.3.

6.1.2 Sensitivity Mismatch

The angle is extracted using the four quadrant inverse tangent. Consequently the ratio of the two X and Y signals is indirectly calculated. In the ideal case, the two sensitivities are equal. This is the reason why this measurement principle is not sensitive to the amplitude of both signals in the ideal case, i.e. the sensitivities are equal.

Unfortunately this is not the case, because of a non-ideal matching between the sensors. That is the second main source of Hall elements induced NL, called the sensitivity mismatch between axes (SMIS). This miss-matching exists although the sensors are on the same chip (matching) and the electronic amplification is multiplexed (the same analog chain).

SMIS will stretch the circle of the Lissajoux figure in the X or Y directions to obtain an ellipse (Fig. 6.4). Consequently, a sine ANL with a period of 180° appears. This NL is null for angular directions parallel to the X and Y axes,

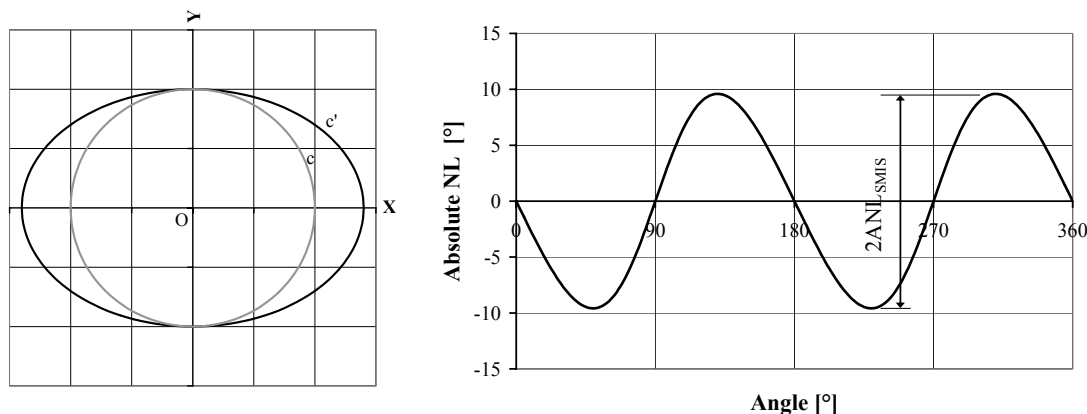


Fig. 6.4 Sensitivity mismatch between X and Y axes ($S_{MIS}=1.4$). The left figure shows the Lissajous curve, where the circle is stretched into an ellipse. The NL is presented in the figure on the right. It is a second harmonic function of the angle (2f-type).

The X over Y sensitivities ratio is defined as S_{MIS} . The ANL is a second harmonic function of the angle (2f-type) which is zero at $k \cdot 90^\circ$, with k an integer. It is optimal when the angle is a multiple of 45° . It is then equal to:

$$ANL_{SMIS} [^\circ] \cong |45^\circ - \arctan(S_{MIS})| \cong \frac{90}{\pi} |S_{MIS} - 1| \quad (6.4)$$

A calibration of the sensitivity at room temperature is able to suppress this error. After this operation, only the difference between axes of the sensitivity drift, i.e. a different cross sensitivity towards the temperature or other parameters, provokes still ANL. This effect is called the sensitivity drift mismatch. In this case the calibration becomes difficult or even impossible because of the unknown variations of the cross parameters (see §2.1.2).

With CMOS Hall angular sensors using IMC (see §2.4.4), the SMIS can reach several percent and even one percent provokes an ANL as high as 0.29° (0.8%). In the worst measured case of a thermal sensitivity drift mismatch of 100 ppm/°C; an ANL of only 0.28° (0.8%) for a temperature variation of 100°C is obtained.

6.1.3 Non-orthogonality

The third main source of Hall sensor related NL is the non-orthogonality of the X and Y sensors. One way to build a 2-D sensor is to orthogonally assemble two single-axis devices [Malco00]. However, in practice, the angle will deviate by several degrees from the desired orthogonality, due to industrial mounting

tolerances [KMZ52] when usual techniques are used for the alignment of hybrid devices.

In the case of integrated 2-Dimensionnal sensors, where the sensors are on the same chip, the orthogonality is guaranteed by the accuracy of the masks and of the process. However, a miss-alignment is still present. It is caused by imperfections of the CMOS process, such as the implantation angle, the gradient of the doping level inside the wafer and mask imperfections.

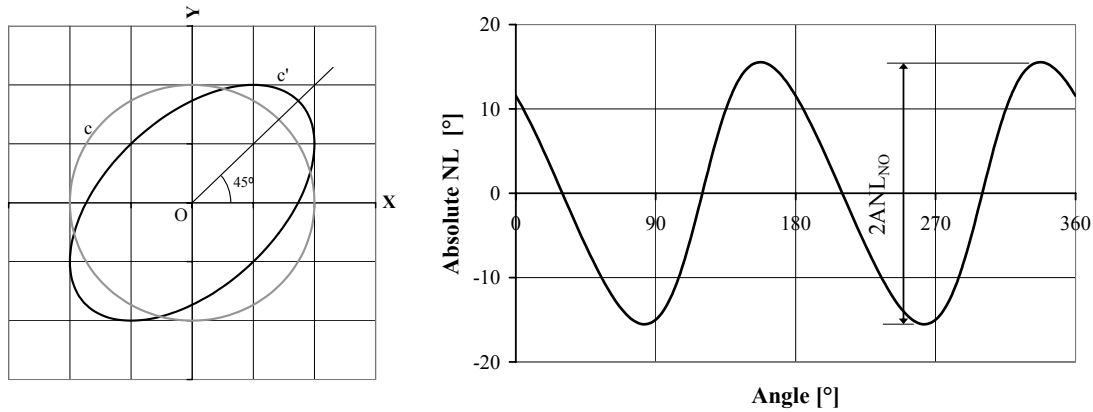


Fig. 6.5 Non-orthogonality between X and Y axes ($\alpha_{NO}=30^\circ$). The left figure shows the Lissajoux curve, where the circle is transformed into an ellipse oriented at 45° . The ANL is presented on the right figure. For small angles of non-orthogonality, it is a second harmonic periodic function of the angle (2-f type).

If we suppose that the angle between sensors deviates from the desired 90° by an angle α_{NO} , the ANL is, for small non-orthogonality angles, a cosine with a period of 180° (Fig. 6.5). The ANL is equal to:

$$ANL_{NO} \cong \frac{\alpha_{NO}}{2} \quad (6.5)$$

The ANL is optimum when the direction of the angular vector is aligned with the X and Y axis. It is null for $\theta=45^\circ+k\cdot 90^\circ$, k being an integer. Note that the phase shift allows to differentiate the ANL from the SMIS and from the non-orthogonality.

To compensate this non-orthogonality, the angle α_{NO} has to be measured. One way to do this is to rotate the magnetic field during one turn. If it is assumed that the X-axis is aligned, it is possible to correct the Y-axis measurement V_Y using the following equation [Philips]:

$$V_{Y,corrected} = V_Y \frac{1}{\cos \alpha_{NO}} - V_X \tan \alpha_{NO} \quad (6.6)$$

6.1.4 Magnetic sensor non-linearity

Hall sensors exhibit almost a linear response for magnetic fields up to and even beyond 1 Tesla. However the saturation of the electronics is responsible for NL. In the case of integrated magneto-concentrators, with the angular sensor based on the disk (§2.4.4), the saturation of the ferromagnetic material induces also a NL of the magnetic measurement (see §6.6.2). The NL is often an order 3 odd distortions and the Hall signal V_H can be approximated by a cubic response:

$$V_H = S(B + k_3 B^3) \quad (6.7)$$

With B the magnetic field, S the sensitivity and k_3 the order 3 parameter related to the cubic component of the sensitivity.

By calculating the signals $V_{H,X}$ and $V_{H,Y}$ on respectively the X- and Y-axes with a rotating magnetic field, we found:

$$V_{H,X} = SB(\cos(\theta) + k_3 B^2 \cos^3(\theta)) = SB \left[\left(1 + \frac{3k_3}{4}\right) \cos(\theta) + \frac{k_3 B^2}{4} \cos(3\theta) \right] \quad (6.8)$$

$$V_{H,Y} = SB(\sin(\theta) + k_3 B^2 \sin^3(\theta)) = SB \left[\left(1 + \frac{3k_3}{4}\right) \sin(\theta) - \frac{k_3 B^2}{4} \sin(3\theta) \right] \quad (6.9)$$

The Lissajoux curve, drawn from the two previous functions, is distorted and it is no more an ellipse (Fig. 6.6). For small angles, this ANL is a third harmonic (4f-type) of the angle with a phase shift of $k \cdot 90^\circ$, k being an integer. This ANL is equal to:

$$ANL_{NL} [^\circ] = \arctan \left(\frac{k_3 B^2}{4 + 3k_3 B^2} \right) \cong \frac{180}{\pi} \frac{k_3 B^2}{4 + 3k_3 B^2} \cong \frac{90}{2\pi} k_3 B^2 \quad (6.10)$$

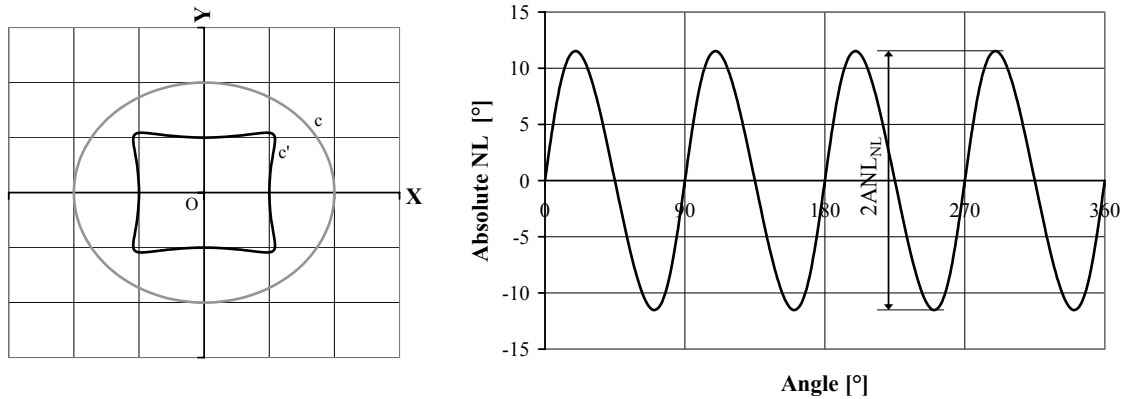


Fig. 6.6 The left figure shows the Lissajoux curve when the sensing part has a cubic NL ($k=-0.5; S=1$); the ideal circle is symmetrically twisted. The ANL is presented on the right figure. For small angles of non-orthogonality, it is a 4th harmonic (4f-type) periodic function of the angle.

6.2 Other sources of non-linearities

6.2.1 Mechanical alignment

As described before, the angular microsystem is based on a sensor and a rotating permanent magnet aligned with the rotation axes (Fig. 5.4). The sensing area is small compared with the typical magnet diameter of several millimeters, allowing the magnetic field to be considered as homogeneous. It is why the system can be considered as a "point like" sensor, which is favourable to the accuracy [Burger01]. The alignment between the sensor and the permanent magnet is a major source of non-linearity, although the principle is very robust to mechanical tolerances [Demierre98].

In the case of an off-center (a misalignment in the sensors' XY plane or an eccentricity of the magnet), the NL is equal to 0.05° (0.14‰) for a $D=50\mu\text{m}$ misalignment with an optimized $\varnothing 6\text{mm}$ NdFeB permanent magnet (Fig. 6.7). It reaches 0.13° (0.36‰) for $D=100\mu\text{m}$.

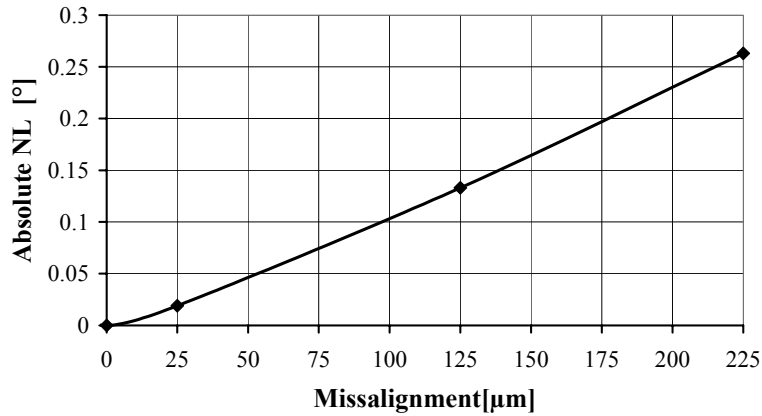


Fig. 6.7 Measured non-linearities resulting from off-centering for a distance of 8mm between the magnet ($\varnothing 6\text{mm}$) and the sensor surface.

For small misalignments, the ANL is approximately a fundamental function (f type) of the angle (Fig. 6.8), similar to the f-type ANL from sensor offsets. We can write:

$$ANL_D(\theta)[^\circ] \cong 0.1 \frac{D[\mu\text{m}]}{100} \sin(\theta + \alpha_D) \quad (6.11)$$

With α_D , the phase of the ANL, an angle which depends on the direction of the misalignment.

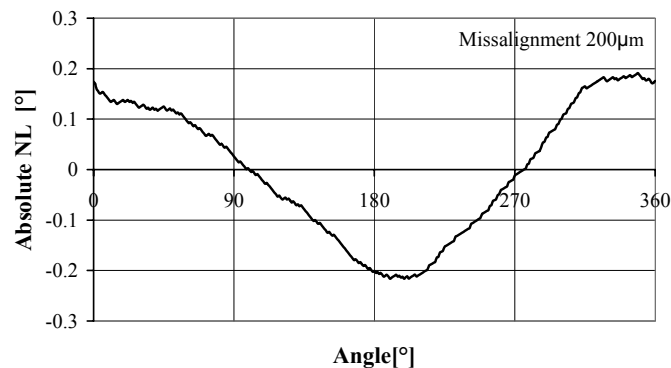


Fig. 6.8 Measurement of the ANL resulting from a 200μm misalignment of the X-axes. It is in first approximation a fundamental function of the angle (f-type).

The measurement is in first approximation independent on the distance Z between the sensor and the permanent magnet, because this parameter, which changes the amplitude of the Hall signals proportionally for both axes, is removed during angle extraction. On the other hand, the effects of noise and offset are inversely proportional to the amplitude of the magnetic field. The minimum distance, i.e. the maximum field, is given by the saturation of the electronics. The distance and the shape of the magnet are optimized in order to increase the homogeneity of the field in the XY plane to reduce the influence of mechanical tolerances.

The sensor tilt β_S is defined as the angle between the normal of the sensor and rotation axes plane. This tilt will modify the amplitude of the rotating field, because the field is projected on the sensor plane. The resulting ANL is equivalent to a sensitivity mismatch (see §6.1.2). The NL is equal to:

$$ANL_{TILT} [^\circ] \cong \frac{90}{\pi} (1 - \cos \beta_S) \quad (6.12)$$

A sensor tilt of 5° produces a 2f-type ANL of only 0.1° (0.3%).

The magnet tilt β_M , which represents a non-orthogonality between the magnet and the axis of rotation, has no influence on the angular measurement. It only reduces the amplitude of the rotating magnetic field projected in the sensor plane by a factor $\cos \beta_M$, i.e. the diameter of the circle on the Lissajoux curve.

6.2.2 Ferromagnetic materials

Ferromagnetic elements external to the sensor generate interferences if they are close to the permanent magnet or the Hall sensor. They are for instance, purposely placed to shield the angular sensor from external magnetic field. Two kinds of interference can occur with ferromagnetic materials, called "soft" and "hard" iron effects [Caruso99] [Lund83]. By avoiding ferromagnetic elements in our measurement setup, these two effects will be absent from the following sections (excepted for the permanent rotating magnet).

"Hard" iron effects are caused by the remanent field from magnetized objects. This field is superimposed on top of the rotating magnetic field: it is seen as a magnetic offset, i.e. a constant when the external field is suppressed. Consequently, the same NL as that seen with the offset is observed (part 6.1.1). If the rotating field from the magnet is large enough to modify its magnetization, the output of the system will depend on the history of the system (for instance, the hysteresis). Consequently, the offset source is non-deterministic and it can therefore not be compensated.

The magnetic field may be distorted by Ferromagnetic materials. This is called the "soft" iron effect (Fig. 6.9). If the material doesn't enter saturation, the Lissajoux curve is deformed into an ellipse and we will have a sensitivity mismatch and a non-orthogonality. Several sophisticated calibration schemes [Denne98] exist to calibrate the sensor, all based on a rotation of the external field. In the case of a field great enough for the material to enter the "soft" material in the NL region of the BH curve, i.e. the relative permeability is strongly reduced, a NL effect appears with a fourth harmonic of the magnetic field (see §6.1.4 for a similar effect).

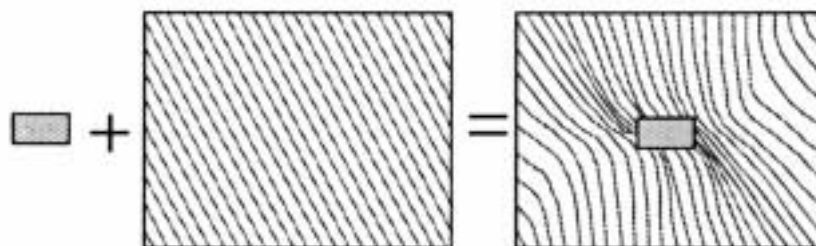


Fig. 6.9 "Soft" iron disturbances in uniform magnetic field (reprinted from [Caruso02]).

The calibration strategies for deterministic effects consists in extracting the X and Y equivalent offsets, the gain-mismatch and the non-orthogonality from an angular measurement in order to transform the ellipse of the Lissajoux curve into a circle. Note that "hard" iron effects often dominate over "soft" iron effects provided ferromagnetic materials near the sensor [Stork00]. In this case, only the offset has to be calibrated. For instance the equivalent offset is obtained by the bidirectional calibration, i.e. adding two measurements with a 180° rotation of the permanent magnet.

6.3 Statistical approach of the non-linearities

As example, we calculate the standard deviation resulting from the sensor offsets based on the Equ. (6.3). The offsets $B_{Off,X}$ and $B_{Off,Y}$, present on both axes, are supposed to be not correlated and to have the same variance $\sigma(B_{Off})$. Consequently α_{OFF} is a random angle. The average standard deviation of the ANL is equal to:

$$\begin{aligned}\sigma(ANL_{off}) &\cong \frac{180}{\pi} \left(\frac{\sigma(B_{off})}{B} \right) \sqrt{\frac{1}{2\pi} \int_0^{2\pi} [\cos^2(\theta - \alpha_{off})] d\alpha_{off}} \\ &\cong \frac{180}{\pi\sqrt{2}} \left(\frac{\sigma(B_{off})}{B} \right)\end{aligned}\quad (6.13)$$

The total non-linearity ANL is the sum of all the contributions of non-linearities, taking into account of the frequency and the phase shift of the signals. We calculate, without disturbing ferromagnetic pieces and using the approximations for small errors:

$$\begin{aligned}ANL[^\circ] &\cong \frac{180}{\pi} \left(\frac{B_{off,X}^2 + B_{off,Y}^2}{B} \right) \cos(\theta + \alpha_{off}) - \frac{90}{\pi} (S_{MIS} - 1) \sin(2\theta) \\ &\quad + \frac{\alpha_{NO}^\circ}{2} \cos(2\theta) + \frac{180}{\pi} \frac{k_3}{4 + 3k_3} \sin(4\theta) + 0.1 \frac{D}{100} \sin(\theta + \alpha_D) \\ &\quad \pm \frac{90}{\pi} (1 - \cos \beta_s) \sin(2\theta)\end{aligned}\quad (6.14)$$

The ANL can be decomposed in a determinist and a random part. The determinist part, such as the k_3 non-linearity parameter of the sensor, are equal to zero with an ideal design of the system.

The parameters $B_{off,X}$, $B_{off,Y}$, S_{MIS} , α_{NO} , D and β_s are random variables and contribute to the variance of the ANL . They have in most cases a Gaussian distribution. They are supposed to be uncorrelated. $B_{off,X}$ and $B_{off,Y}$ have the same $\sigma(B_{off})$ standard deviation. α_{off} and α_D are once more supposed to be fully random, because the two components of the offset and misalignment vectors are not correlated. The non-linearities of the sensor (parameter k_3) are supposed to be a constant. Consequently its standard deviation is zero. The standard deviation of the ANL , which is a function of the angle θ , is equal, with small standard deviations to:

$$\begin{aligned}\sigma^2(ANL(\theta)[^\circ]) &\cong \frac{180^2}{2\pi^2} \left(\frac{1}{B} \right)^2 \sigma^2(B_{off}) + \frac{1}{1000^2} \frac{1}{2} \sigma^2(D) \\ &\quad + \frac{90^2}{\pi^2} \sigma^2(S_{MIS}) \sin^2(2\theta) + \frac{1}{4} \sigma^2(\alpha_{NO}) \cos^2(2\theta)\end{aligned}\quad (6.15)$$

Without taking into account the phase, we can write that the ANL standard deviation is smaller or equal than:

$$\sigma(ANL[^\circ]) \leq \sqrt{\frac{180^2}{2\pi^2} \left(\frac{1}{B}\right)^2 \sigma^2(B_{off}) + \frac{1}{1000^2} \frac{1}{2} \sigma^2(D) + \frac{90^2}{\pi^2} \sigma^2(S_{MIS}) + \frac{1}{4} \sigma^2(\alpha_{NO})} \quad (6.16)$$

6.4 Angular noise

Based on the same calculation as for the standard deviation of the offset (§6.3), we calculate that the angular RMS noise, provoked by the magnetic equivalent noise of the sensor $B_{Noise,RMS}$ (§5.6), is:

$$\begin{aligned} \theta_{Noise,RMS} [^\circ] &\cong \frac{180}{\pi} \frac{B_{Noise,RMS}}{B} \sqrt{\frac{1}{2\pi} \int_0^{2\pi} [\cos^2(\theta - \alpha_{Noise})] d\alpha_{Noise}} \\ &\cong \frac{180}{\pi\sqrt{2}} \left(\frac{B_{Noise,RMS}}{B} \right) \end{aligned} \quad (6.17)$$

With a $0.9\mu\text{T}/\sqrt{\text{Hz}}$ white noise measured in the §5.6, a 10KHz bandwidth and a rotating magnetic field B of 100mT, we calculate that the RMS angular noise is only 0.04° . As expected, white noise is not the main problem of contactless potentiometer, when an efficient magnet is placed closed to the sensor. The contribution of $1/f$ noise is often more critical with low frequency measurements. Fortunately this type of noise is removed by the spinning current electronics (see §5.6.5).

6.5 Vertical Hall Sensors 2-D microsystem

As a first solution for the sensitive part of the Fig. 6.1, we propose a magnetic sensor based on CMOS compatible vertical Hall sensors (see §1.2.1).

6.5.1 Principle

The microsystem we realized contains a 2-Dimensional angular sensor based on four couples of 6-contact vertical Hall sensors [Schurig03], two for each orthogonal axis. The Hall sensors are orthogonally placed so as to be able to

measure the X and Y directions of the rotating magnetic field (Fig. 6.10). The orthogonality of the axes is mainly determined by the mask. The “Point-like” sensing area measures only $175 \times 240 \mu\text{m}^2$. The sensors are placed across a common symmetry point in order to reduce the sensitivity to mechanical tolerances. First order magnetic non-homogeneities disappear with the central symmetry of the sensor.

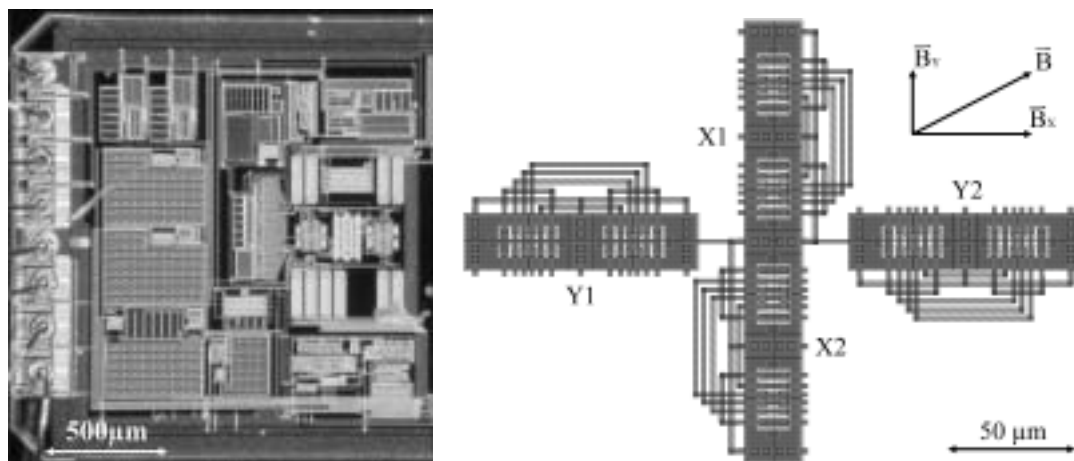


Fig. 6.10 CMOS microsystem containing the angular sensing element and a multiplexed 2-D spinning current electronics block. The figure on the right shows an optimized layout of a 2-dimensional Hall sensor, based on 4 vertical Hall sensor pair X1, Y1, X2 and Y2; two for each X and Y axis.

The Hall signals are amplified using the spinning current principle to greatly reduce the Hall sensors' offset (see §2.1.5 and §5). The tool for residual offset reduction (see §5.7 feedback spinning current) is not implemented with this design. Consequently a residual offset, incompatible with high accuracy angular measurements, is still present. Indeed, an offset calibration is required to reach high angular measurement accuracy (1‰ NL). Note that this microsystem, a 2-phases spinning current without the feedback topology, does not use all the improvements presented in the previous chapter. This is the reason why the residual offset is too large and has to be calibrated.

To guarantee the same gain on both axes and greatly reduce the size and the power consumption of the electronic circuit, a temporal multiplexing of axes X and Y is used (Fig. 6.11) (see §5.9). Consequently, the same analog chain is used twice. This is done via an adapted clock sequence for the spinning current switches. Firstly the two spinning phases of the X-axis sensors (X1 and X2) are measured and the output signal of the peak-to-peak detector (SC synchronous demodulator) is recorded with a sample and hold. During the next phase, the same operation is carried out for the Y-axis (sensors Y1 and Y2). These two

analog signals are connected to the outside through two buffers. The overall size of the microsystem without pads is only $1.5 \times 1.6 \text{ mm}^2$.

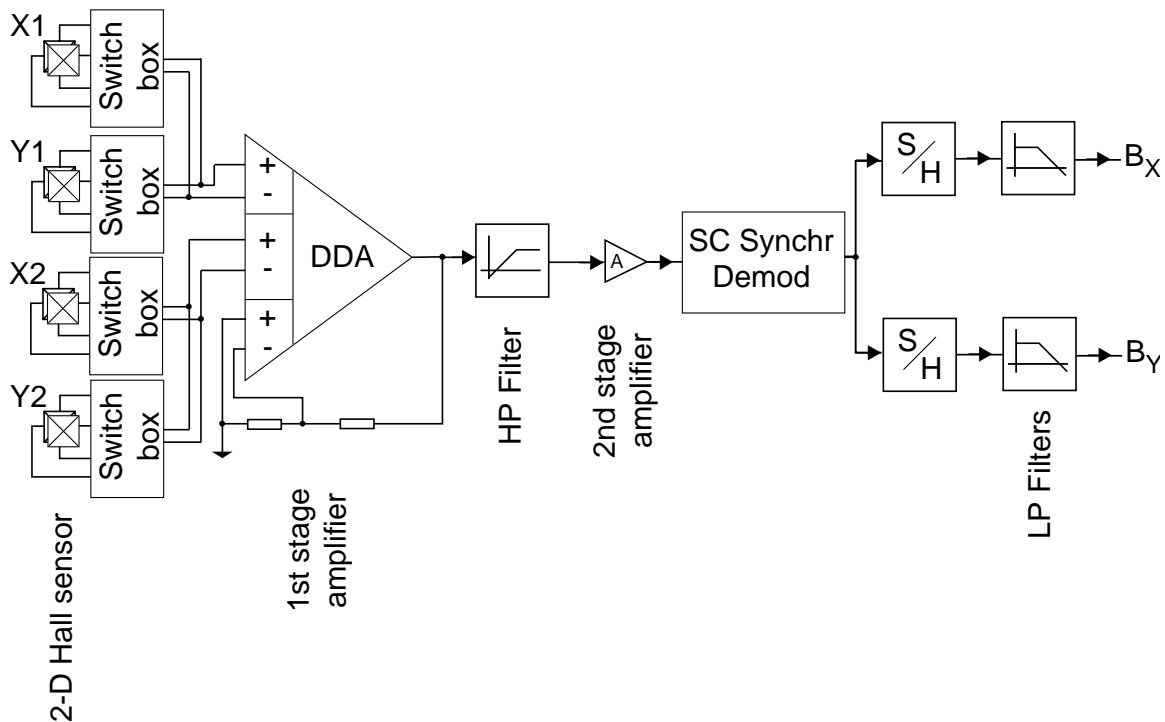


Fig. 6.11 Integrated electronic scheme. The 2-D Hall sensor contains 4 Vertical Hall sensor pairs X1, Y1, X2 and Y2; two for each direction X and Y respectively. Both axes are multiplexed with an adapted clock sequence for the spinning current switch boxes. The sample and hold are used for the demodulation.

6.5.2 Magnetic Measurements

A single vertical Hall sensor (§2.3) has a 175 mV/T sensitivity for a 5-volts biasing. Its input resistivity is about $6 \text{ k}\Omega$. The 2-D system has two main X- and Y-axes of sensitivity (Fig. 6.12). The electronics gain is equal to 100, resulting in a 17.5 V/T system sensitivity in the main directions. The cross sensitivities are far more than two orders of magnitude smaller.

This type of sensor presents the typical problems enumerated above, such as a residual offset after the spinning current method, misalignment between axes, gain-mismatch and non-linearities. They contribute in deteriorating the angular measurement.

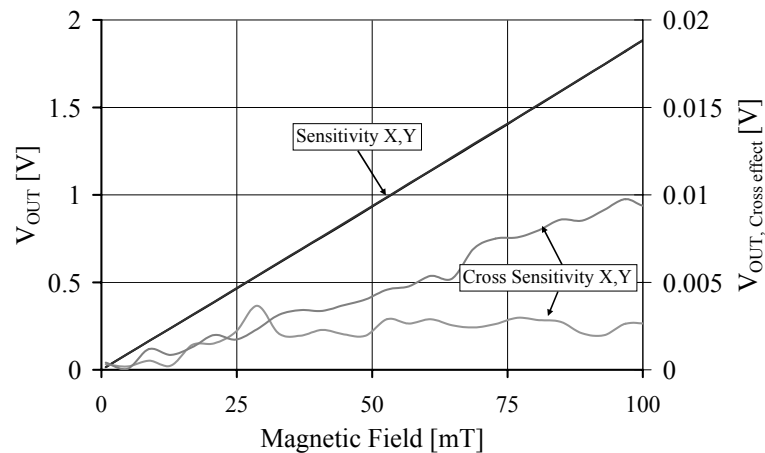


Fig. 6.12 Output signals of the microsystem for a field orthogonal (main signal) and parallel (cross sensitivity) to the sensor plane (biasing voltage 5V).

By rotating the external magnetic field from 0° to 90° , a non-orthogonality of about $\pm 0.4^\circ$ of the sensitivity directions X and Y appears.

Due to the small distance between the sensors of both axes, their sensitivity is almost matched. However the matching is not perfect. As explained before, the sensors' orientations are unfavorable to an accurate matching. A sensitivity mismatch of 0.3% is measured.

Magnetic NL (§6.1.4), appearing with the variations of the magnetic field, also contributes to the angular measurement distortions. The magnetic NL is about 0.5mT for a magnetic field of up to 80mT (Fig. 6.13). For larger fields, the NL is drastically increased to obtain 1mT for a 100mT external magnetic field. The

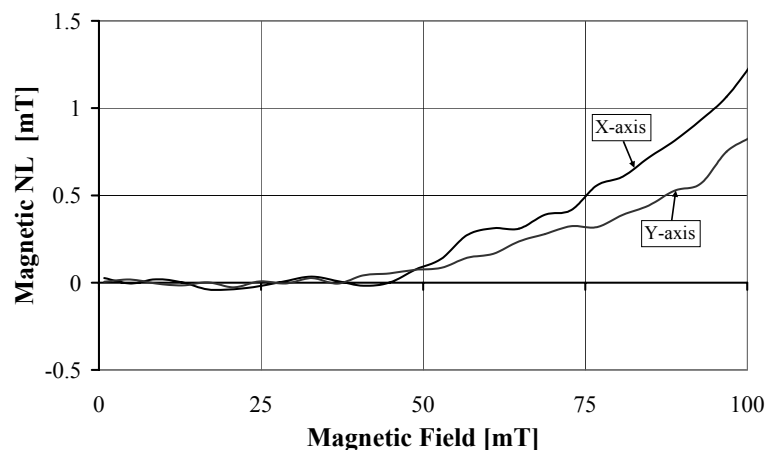


Fig. 6.13 Non-linearity of the magnetic measurements. A major NL appears with an external field superior to 50mT. Vertical Hall sensor NL due to junction field effect is suspected to be its source.

source of this non-linearity is not clearly identified. However, we suspect that the vertical Hall sensor itself is the source of this non-linearity, because of the large junction field effect which deteriorates also the Hall sensor linearity.

6.5.3 Angular measurements

Angular measurements are made by rotating the CMOS chip inside the homogeneous field created by Helmholtz coils. The coils are used to suppress the mechanical sources of NL (see 6.2.1). They are placed around the microsystem and their diameter is much greater than the site of the sensing area. An 80mT magnetic field is used, corresponding typically to a field used for contactless Hall potentiometers.

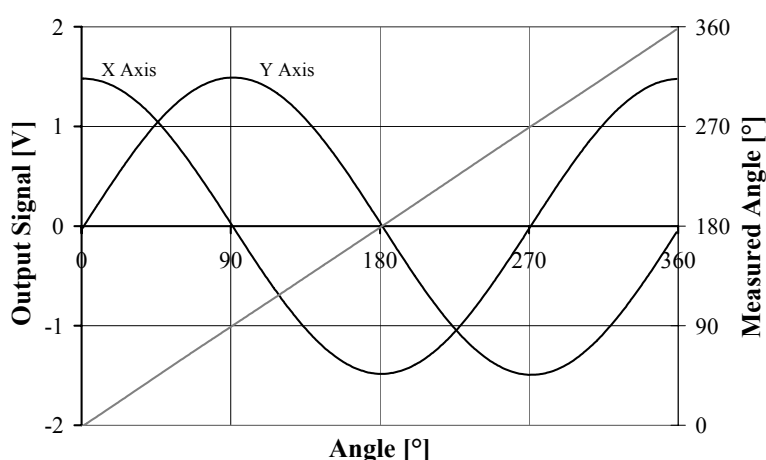


Fig. 6.14 Signals at the output of the microsystem rotating in an 80mT magnetic field. After a compensation of the offset, they correspond to the sine and cosine of the rotation angle. After the extraction of the angle, a linear response is obtained using the arctangent function.

The angle is extracted from the sine and cosine functions after the X and Y offset compensation (Fig. 6.14). This requires a four quadrant inverse tangent. In the laboratory setup, a 16-bits DAC card and a PC using LabView[®] (National Instruments[®] software) were used.

Measurements on four samples with a 360° rotation in an 80mT magnetic field (Fig. 6.15) showed that the ANL is 0.5° (0.14%). For every sample, an absolute non-linearity (ANL) of the second harmonic is observed; the main sources of ANL are gain-mismatch and a non-orthogonality of the sensor axes. For the various samples from the same run, a correlation of the results is observed. This is most certainly due to the matching between the chips because of the use of the same CMOS run.

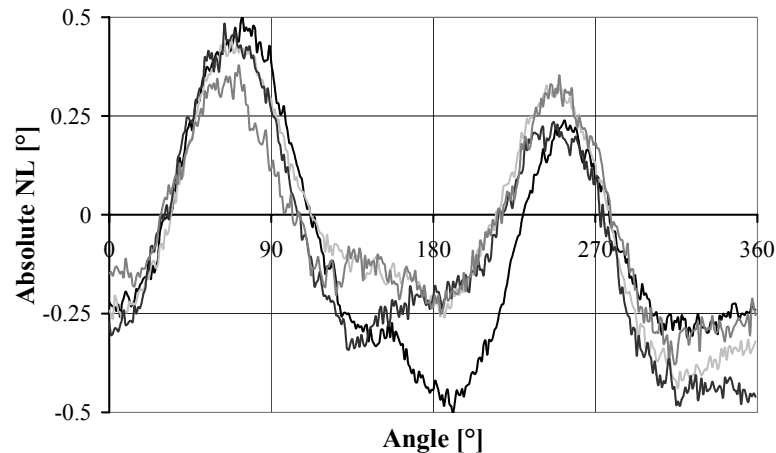


Fig. 6.15 Absolute non-linearity measured on 4 samples with a maximum of 0.5° (0.14%). A second harmonic ANL is clearly visible; this is mainly due to a gain-mismatch between axes and a non-orthogonality of the sensors.

Hysteresis, which is the difference between back-and-forth displacements, is another key parameter in angular sensors. Hysteresis, not measurable because of noise, is less than 0.05° (Fig. 6.16). This result was foreseeable, since our sensor contained no ferromagnetic parts and no "hard" ferromagnetic material inside the active area of the angular sensor.

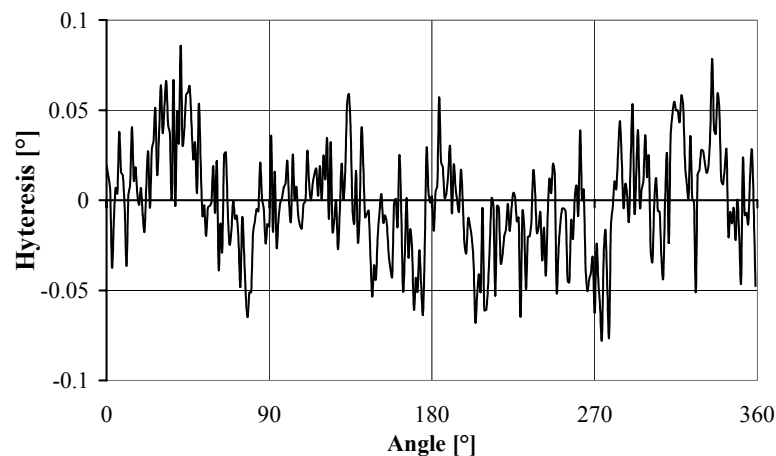


Fig. 6.16 Hysteresis. No hysteresis was observable due to lack of ferromagnetic materials inside the sensor.

6.5.4 Discussion

Axis misalignment and gain-mismatch are, as explained above, two of the main sources of absolute non-linearity (ANL) after the offset compensation. Based on the magnetic measurement, it is possible to calculate the non-linearity. The non-orthogonality is about $\pm 0.4^\circ$. Consequently, when the angle is extracted, a second harmonic ANL of 0.2° (0.56‰) with a phase of 0° or 90° appears. A gain-mismatch of about 0.3% is measured. This results in an angular ANL of less than 0.1° (0.28‰), which is equivalent to a $\pm 45^\circ$ phase second harmonic NL. The total second harmonic angular NL resulting from these two main effects (Fig. 6.17) is 0.22° (0.61‰).

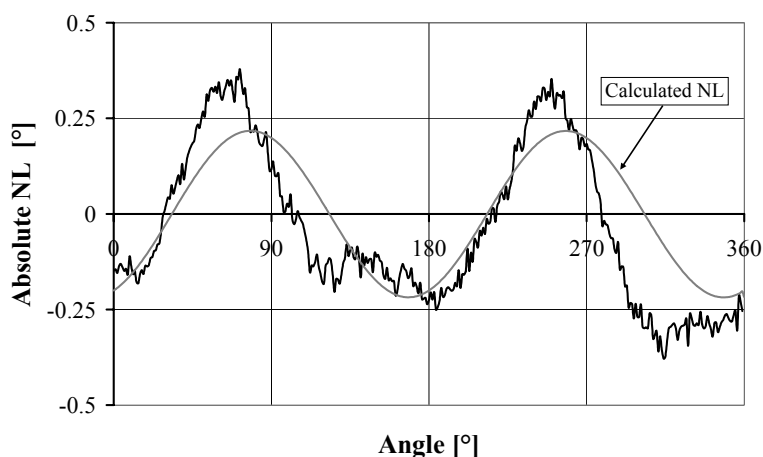


Fig. 6.17 Measured values compared to calculated angular NL resulting from the measured 0.3% gain-mismatch and 0.4° non-orthogonality of the sensors. There is a good correlation between magnetic and angular results.

When performing the angular measurement, the absolute non-linearity (ANL) is 0.35° (1‰). There is a good correlation between magnetic and angular results, even if other deteriorations of the angular measurement are present.

After a gain and phase compensation, using the previously measured magnetic values, the ANL is divided by a factor two to become 0.26° (0.7‰). The 4-f type ANL from magnetic NL (Fig. 6.13) also contributes to angular measurement inaccuracies. The equivalent magnetic NL is about 0.5mT for a magnetic field of up to 80mT, resulting in a 4th harmonic angular ANL of 0.1° . Other sources of NL, which are not yet well understood, generate an ANL of about 0.15° .

Using the gain-mismatch and non-orthogonality compensation to fit the parameters of the system, i.e. without using the results of the magnetic measurements, the reduction of the NL can be improved (Fig. 6.18). A residual

ANL of only 0.17° (0.5‰) is measured, mainly a 4th harmonic ANL due in part to the magnetic NL of the microsystem (see §6.1.4).

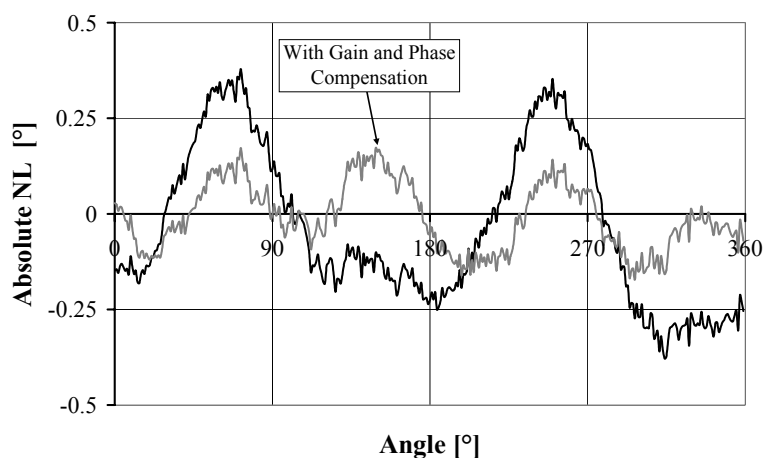


Fig. 6.18 NL before and after compensation of the gain-mismatch and the orthogonality of sensors. The residual ANL after compensation is more than halved to obtain 0.17° (0.5‰). It is a 4f-type coming from NL of the magnetic measurement.

6.6 2-D microsystem with integrated flux concentrators

It is a second microsystem for the sensing part of the Fig. 6.1. The previous Hall sensor uses a specific CMOS technology and as a result all the consequences related to its availability. This second solution asks for a more usual CMOS technology, but a post-processing to deposit a ferromagnetic disk is requested (see §2.3.4).

6.6.1 Principle

The sensor, shown in Fig. 6.19, consists of an integrated combination of a CMOS integrated circuit chip and a thin ferromagnetic disk [Popovic01]. The integrated chip is fabricated using a standard $0.8\mu\text{m}$ CMOS technology. It contains conventional NWell Hall elements. These are Hall plates sensitive in the direction Z , perpendicular to the chip's surface (see §2.1). The ferromagnetic disk (§2.4.4) is deposited using the Integrated Magneto-Concentrators (IMC) Technology [Popovic02] [Schott00]. It is a soft magnetic material with a high permeability (greater than 10^4), a low coercive field (less than 1mA/cm) and a saturation field greater than 0.5T . The Hall elements are positioned under the

periphery of the disk to measure the Z component of the fringe field. Two Hall elements are placed at the opposite sides of a ferromagnetic disk to obtain a push-pull measurement and to cancel the homogeneous external field.

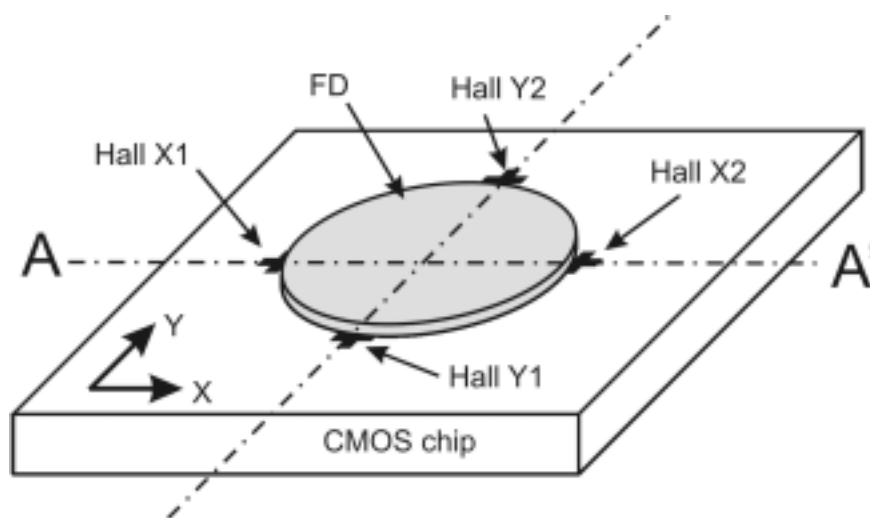


Fig. 6.19 A schematic view of the two-axes Hall angular position magnetic sensor using an Integrated magneto-concentrator (IMC). It is composed of 4 Hall plates and a ferromagnetic disk FD deposited at the surface of the CMOS chip.

If the sensor is exposed to a homogeneous magnetic field along the XY-plane the ferromagnetic disk will act as a magnetic flux concentrator. The consequence of this effect is that the magnetic field, originally parallel to the chip's surface, is locally converted into a perpendicular magnetic field and furthermore it will change following a cosine law along the ferromagnetic disk's edge. The vertical component of the field is strongest near the boundary of the disk. This is the place where we place the Hall elements. Furthermore, the vertical component of the field caused by the magnetic concentrator has different signs on the opposite ends of the disk. This gives us the opportunity to suppress the vertical component of the external field using two Hall elements for every measurement axis. Assuming a constant permeability of the disk and no saturation, the sensor output signals is the ideal sine and cosine signals for the angle extraction.

Numerical Model

The sensor's magnetic behavior is investigated using Flux 3D [Flux3D]. The three-dimensional simulation volume is composed of a sufficiently large air space, so that the field is quasi uniform at the outer surfaces. A ferromagnetic disk is placed in the middle of this volume. In the model, two different materials are present: the air with the unit relative permeability and an isotropic ferromagnetic material to model the ferromagnetic disk. This material was

modeled with an analytic saturation $B(H)$ curve with a bend adjustment provided by the Flux3D software. The relative permeability was set to $\mu_r=10^5$, the saturation magnetization to $B_{sat}=1\text{T}$, and the bend adjustment factor to $a=0.01$. This data was chosen according to the magnetic characteristics of the Vitrovac 6150F from Vacuumschmelze GmbH (Germany), the material used for the ferromagnetic disk. A diameter of $250\mu\text{m}$ and a thickness of $22\mu\text{m}$ were chosen for the simulations.

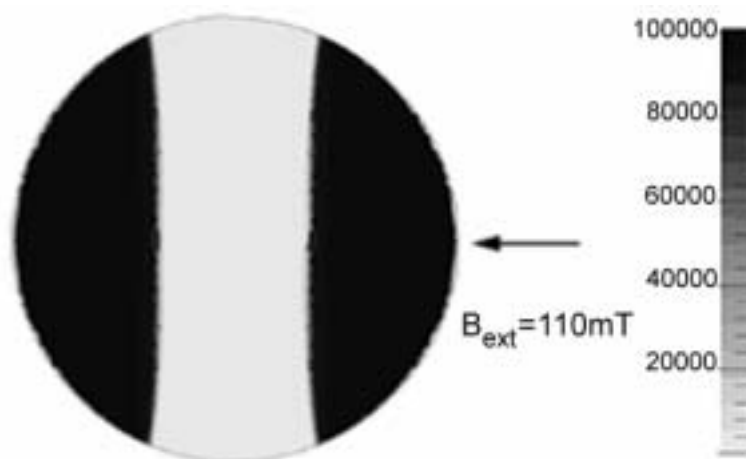


Fig. 6.20 Numerical solution for the saturation of the ferromagnetic $250\mu\text{m}$ disk distribution of the relative change in permeability, exposed to an external field of 110mT . The decrease in permeability shows the area where the saturation occurs, i.e. the flat of the BH curve.

To examine the effect of the saturation of the disk, we have to take into account that the external field is strong enough to partially saturate the disk. The distribution of values for the relative permeability will provide the location of saturation for the disk. The top view of the results obtained for an external field of 110mT is shown in Fig. 6.20. The disk concentrates the external field in this central area, where appears the saturation responsible for the non-linearity. After that, the saturation will rapidly spread throughout volume of the disk with the increase of the external field. This effect occurs after 60mT .

Analytical approach

A numerical model will give the complete insight into the problem including all the field components and distributions of the relative permeability. At the same time the 3D simulations need a lot of computer memory and processor time. It will be very useful to find a simple way to rapidly calculate the working linear range of the angular position sensor.

In order to estimate the value of the field for the increase of NL, a model of a disk-like magnetic concentrator with an oblate ellipsoid is used. The difference between geometry for very flat structures is small. We should take advantage of the fact that demagnetization factors exist only for ellipsoids in a closed analytical form [O'Handley00]. For a very flat oblate ellipsoid, with a magnetization parallel to the long axis, the demagnetization factor is defined as:

$$N \cong \frac{\pi}{4m} \left(1 - \frac{4}{\pi m}\right) \quad m \gg 1 \quad (6.18)$$

The parameter m is the ratio between the diameter and the thickness of the disk. If we assume that the factor μ is close to infinite, the external magnetic field induction at the onset of the saturation is given by:

$$B_{0sat} \approx NB_{sat} \quad (6.19)$$

Substituting this value in the equations (6.18) and (6.19) the value for the disk geometry, $B_{0sat}=62\text{mT}$ is obtained. This result is in very good concordance with the numerical results and shows the feasibility of equation (6.19) for rapid calculations.

6.6.2 Material related non-linearity

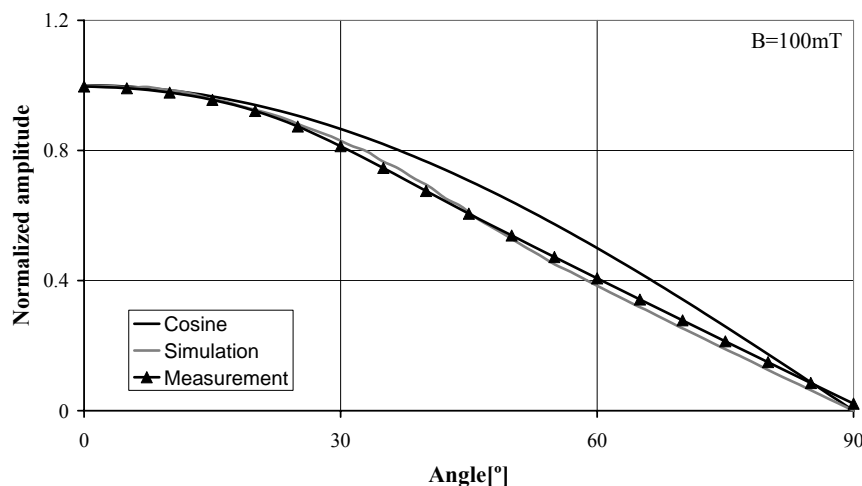


Fig. 6.21 Comparison of the obtained numerical data with measured results with a partially saturated ferromagnetic disk.

As explain before, the behavior of the ferromagnetic disk depends on the value of the external field because of the saturation of the material [DrIjaca02]. A two-

axis angular position sensor with a $250\mu\text{m}$ disk is exposed to a homogenous external magnetic field of 100mT , large enough to partially saturate the disk, which rotates around the sensor. Since the sensitivity of Hall elements is linear up to one Tesla, the non-linearities are due to the IMC saturation (Fig. 6.21).

The measured voltage compares well with the value of the field obtained from the numerical model (Fig. 6.21). The NL behavior is clearly shown by the large deviation of the output voltage from the ideal cosine law.

Using the developed numerical model, the NL is calculated as a function of the external field. The results obtained are shown in Fig. 6.22. The NL rapidly increases, with the rapid change of the relative permeability. This effect occurs after 60mT due to a partial saturation of the disk. The NL observed below 60mT are due to the limitation of the finite element modeling (intrinsic simulation error). With a large magnetic field, the angular non-linearity is about 1.5% (5°). The simulations show curiously that it is almost independent to the rotating magnetic field amplitude.

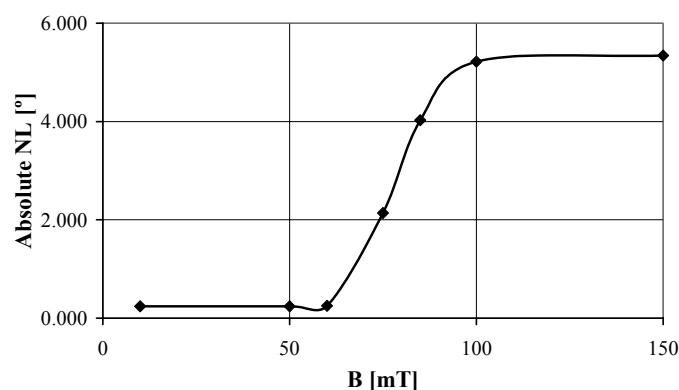


Fig. 6.22 Simulated NL due to the saturation of the $250\mu\text{m}$ ferromagnetic disk in an external magnetic field. NL is not visible before 60mT . Low field NL comes from intrinsic simulation error.

When the angle is extracted, it results an inaccuracy (Fig. 6.23), which is as expected a 4f-type ANL coming from the non-linearity of the magnetic measurement (§6.1.4).

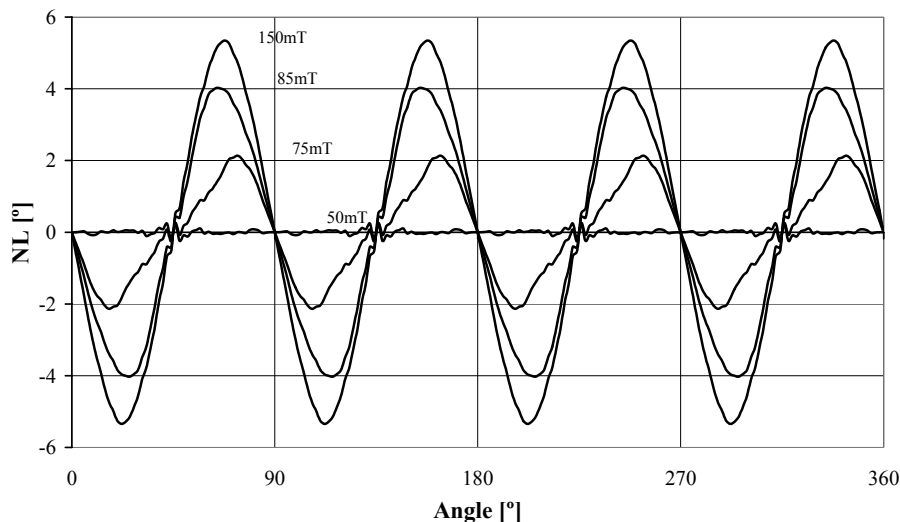


Fig. 6.23 Simulation with Flux-2D of the NL due to partial saturation of a 250µm ferromagnetic disk. Up to 50mT, no effects are observed. With a greater field, the NL is mainly a third harmonic (4f-type).

6.6.3 Misalignment related non-linearity

The ferromagnetic disk is placed on the top of the Hall elements using the IMC post-process. The alignment accuracy of the disk is limited by this photolithographic process. Etching of thick layers is the main constraint of the accuracy.

Using the data obtained from numerical simulations, it is possible to calculate ANL compared with the displacement of the disk in one of the four Hall element directions (Fig. 6.24). The angular NL increases with the higher misalignment.

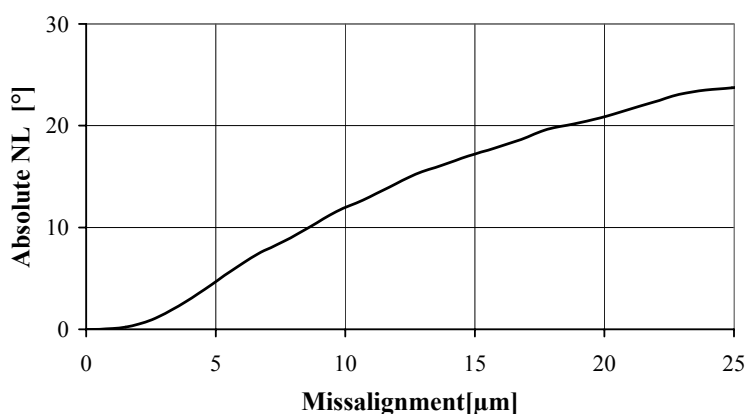


Fig. 6.24 Simulated angular NL versus misalignment of a 250µm ferromagnetic disk and integrated Hall elements.

With a misalignment of $10\mu\text{m}$ we obtain a huge value of 12° (3.3%) of angular ANL (!).

Luckily misalignment provokes mainly a NL due to the sensitivity mismatch between the two axes. This error of 3.3% for a displacement of $10\mu\text{m}$ can be corrected by a compensation of the amplitude of the two signals (Fig. 6.25). In this case the residual NL is only 0.54° (1.5‰), with a misalignment over radius ratio as high as 8%. This result is the main proof of the feasibility of this angular sensor, because it is compatible with the limitations of the IMC technology.

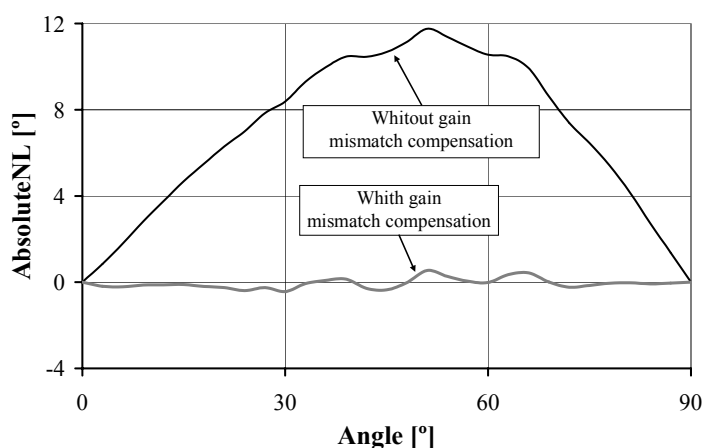


Fig. 6.25 Simulations of the angular NL versus the angle, for a $10\mu\text{m}$ misalignment, with and without gain compensation.

The effect of the misalignment is also a function of the sensors position under the magneto-concentrator. The sensors placed in the higher gain range are more subject to misalignment effects (Fig. 6.26). To compensate the effect of the misalignment NL, the best choice is to place the sensor below the disk, where the magnetic field vary linearly with the position of the concentrator: the variations are compensated by the "push-pull" measurement.

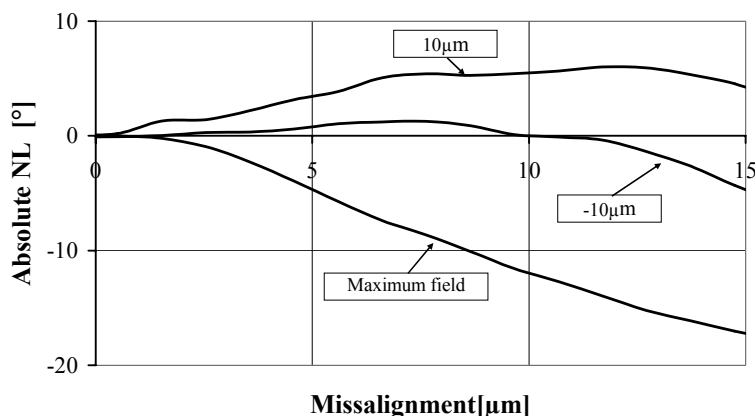


Fig. 6.26 Simulation of the misalignment NL for a punctual Hall sensor. The misalignment is also a function of the sensor's position under the ferromagnetic disk. The figure presents the NL for the best gain with the sensor $10\mu\text{m}$ under the disk and $10\mu\text{m}$ outside. The influence is strongly reduced in the case of the sensors being placed under the disk.

6.6.4 Measurements

The integrated 2-axis Hall microsystem 2SA-10 from Sentron [2SA-10] using a $200\mu\text{m}$ ferromagnetic disk and a spinning current electronics without the feedback configuration (§5.7) are measured. This microsystem allows the on chip programming of a residual offset, a gain-mismatch and non orthogonality, thanks to the AMS "zener zapping" cells. Unprogrammed sensors are used for the evaluations. The sensor packaging is SOIC-8.

Sensitivity measurements

For the magnetic measurements, a sweep of the magnetic field is used to measure the offset and the sensitivity of the system on both orthogonal axes, i.e. by rotating the sensor 90° in comparison with the magnetic field.

Fig. 6.27 presents the sensitivity drift for a temperature variation of the X and Y-axes. A sensitivity mismatch is observed at room temperature; it is typically 5% (4.9%, 0.5% and 7.1%). The alignment accuracy is limited. Sentron IMC's technology accuracy is less than $5\mu\text{m}$, but it is big enough to cause several percent of ANL as measured. The temperature sensitivity drift is roughly $700\text{ ppm}/^\circ\text{C}$. This drift is not relevant for angular measurements, because of the angular calculation. The sensitivity drift mismatch is a key parameter. It is defined as the difference of sensitivity drift between the X and Y axes after a sensitivity mismatch compensation. This is represented in the Fig. 6.27 by the

difference of slope between the measurements. For the majority of cases with the 2SA-10 microsystem, the sensitivity drift mismatch is typically less than $10\text{ppm}/^\circ\text{C}$, but in some cases it can reach $100\text{ppm}/^\circ\text{C}$. The resulting ANL on the angular measurement is typically $1\text{ppm}/^\circ\text{C}$ (max. $8\text{ppm}/^\circ\text{C}$); the angular error is typ. 0.02° for a temperature variation of 50°C .

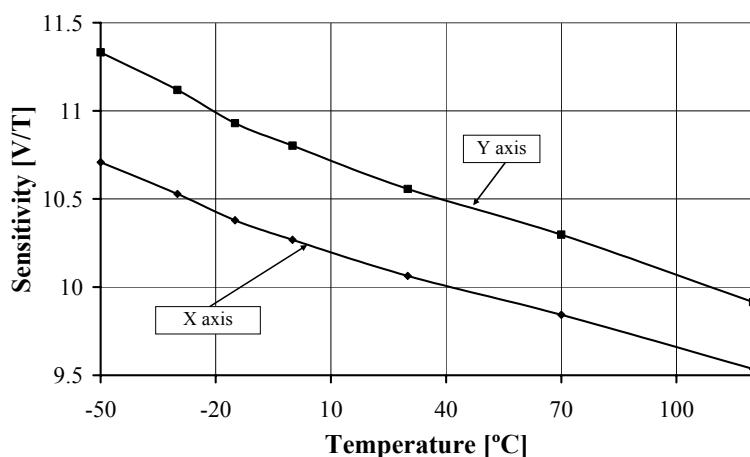


Fig. 6.27 Sensitivity temperature drifts for a 2SA-10 sensor in a SOIC-8 package. The initial sensitivity mismatch is provoked by misalignment of the IMC.

Offset measurements

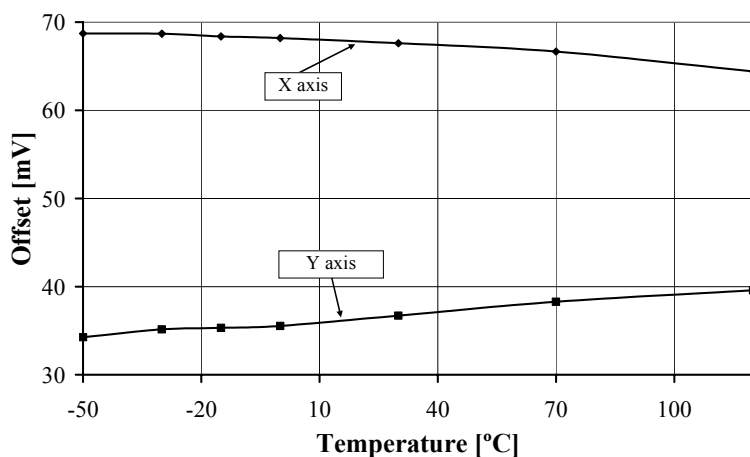


Fig. 6.28 Offset thermal drift for a 2SA-10 sensor in a SOIC-8 package. It is less than $\pm 50\mu\text{V}/^\circ\text{C}$. Note that this microsystem does not use the improvements presented in the chapter 5.

The 2SA-10 chip suffers from a large offset and offset drift (Fig. 6.28). The origin of this drift is the electronics imperfections (§5.5). The microsystem

allows a one point calibration of the residual offset with on-chip calibration table. The calibration of the offset is easily done during the chip tests, because it doesn't require any external rotating magnetic field. It is fully compatible with the usual test and calibration techniques of the microelectronic industry.

After calibration, the initial offset is irrelevant. However there is still an offset temperature drift (Fig. 6.28): this drift is $\pm 40\mu\text{V}/^\circ\text{C}$ ($\pm 4\mu\text{T}/^\circ\text{C}$). The resulting angular NL is as large as $10\text{ppm}/^\circ\text{C}$ (0.2° for 50°C temperature variation) for a 1V amplitude sine and cosine signals. This value is incompatible with our objective of 0.1% accuracy.

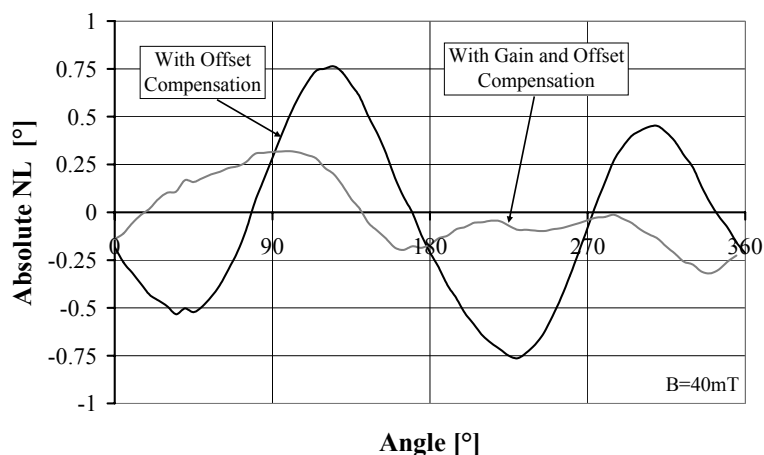
This commercial microsystem does not use the improvements to reduce the residual offset presented in this thesis (§5.7 and §5.8). This is the reason why the offset and its drift is too large. With the feedback configuration, the offset drift from electronics is theoretically reduced by one order of magnitude. The resulting angular NL is so only $1\text{ppm}/^\circ\text{C}$ (0.02° for 50°C temperature variation) for a 1V amplitude sine and cosine signals.

Angular measurements

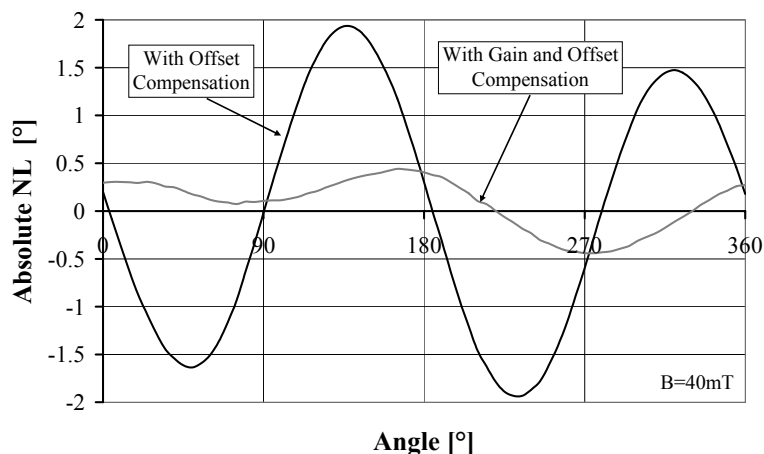
Angular measurements are made by rotating the CMOS chip in a homogeneous field created by Helmholtz coils. We used a 40mT magnetic field, for the measurements without any saturation of the ferromagnetic disk and a 80mT field to observe any NL induced by saturation.

After offset compensation, ANL up to 2° (0.6%) are measured (Fig. 6.29). The source of this NL is the sensitivity mismatch between axes. After compensation of the gain, it is decreased by more than a factor 5, to reach 0.31° (0.8%) and 0.44° (1.2%) on the two samples measured. The source of this gain-mismatch is, as predicted by the theory and the magnetic measurements, the misalignment between the IMC and the sensors (see §6.6.3).

The non-orthogonality between the sine and cosine signals is not measurable. Our theoretical approach also showed that it is not a key parameter. However, second order effects can certainly cause non-orthogonality, such as a combination of large X and Y misalignment of the IMC.



Sensor 1



Sensor 2

Fig. 6.29 Measurement of the NL of two identical angular microsystems with residual offset compensation and with additional sensitivity mismatch calibration.

We also studied the temperature behavior of angular measurements with temperatures from -50°C to 120°C . The Fig. 6.30 shows the results after a one point calibration of the offset and a sensitivity mismatch at a temperature of 30°C . The results clearly show the influence of the offset drift. Indeed, the ANL is almost a sine function coming only from the offsets. No other drifts, such as sensitivity mismatch drift, are observable with our measurements. This result demonstrate the importance of an efficient spinning current electronics (see §5.7), which is not implemented inside this 2-dimensionnal microsystem.

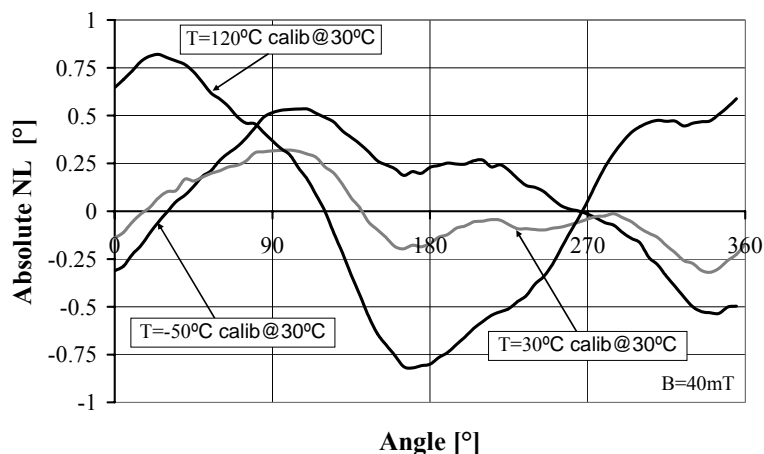


Fig. 6.30 Evolution of the ANL with the temperature after a one point calibration of the offset and sensitivity mismatch. The shape of the NL at extreme temperatures is typically due to an offset problem.

As previously explained, the NL behavior of the ferromagnetic disk, when the disk starts to saturate, is a main source of ANL during angular measurements with too high magnetic fields. Two angular measurements are presented in the Fig. 6.31; one with a 40mT magnetic field and another with 80mT magnetic field to partially saturate the disk. The typical 4f-type ANL (§6.1.4) appears when the field is increased. As expected, at a higher magnet field, the output signal is higher, and consequently the signal to noise ratio is increased.

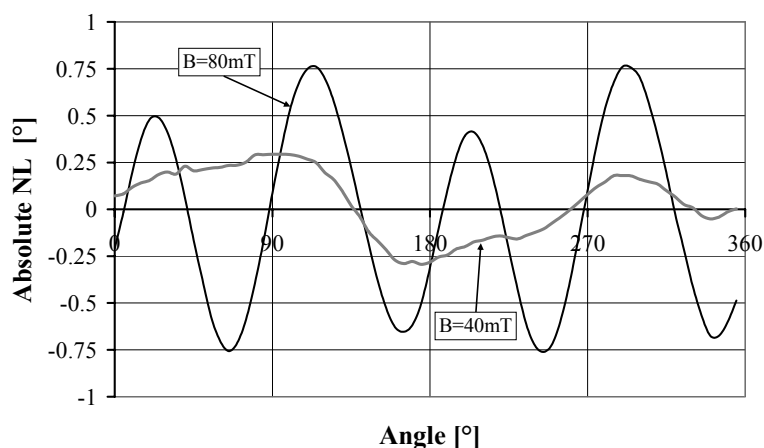


Fig. 6.31 NL caused by the saturation of the 200 μ m ferromagnetic ring by an 80mT magnetic field. A typical NL with a period of 90° appears.

6.6.5 Discussion

The measured sensitivity mismatch is typically 5%, because of missalignment of the integrated magneto-concentrator (§6.6.3). Therefore the resulting angular NL can be as high as 1.4° (3‰). This result corresponds to angular measurements where a sensitivity mismatch of 2% and 6% are observed. This sensitivity mismatch can be compensated through calibration. The calibration of the offset is easy to obtain during the chip tests, because it is a simple electrical field without a magnetic component. Unfortunately the calibration of the sensitivity mismatch requires external rotating magnetic fields. That is not compatible with the usual test and calibration techniques of the microelectronic industry [Trontelj01]. Note that the coils developed in the §3.2 are not useful for this calibration. The flat coil is able to calibrate the Hall sensor, but not the gain of the concentrator and consequently the misalignment of the sensor. To use a coil for the angular sensor calibration, the coil has to generate a field similar to the rotating field. The field has to be homogeneous on the surface of the concentrator (more than $\varnothing 100\mu\text{m}$).

This microsystem has a large residual offset after the spinning current method of several 10mV, because this commercial microsystem does not use the improvements presented in the §5.7. This is the reason why a calibration of offset is needed. After a one point offset calibration, there is still an offset drift equal to approximately $40\mu\text{V}/^\circ\text{C}$. Consequently, with a temperature variation of 90°C , the offset variation is 3.6mV (340 μT) on both axes. Due to the limitations of the magnetic field by the saturation of the disk, a 40mT magnetic field is used for the following evaluation. The NL resulting from this temperature variation is 0.7° (1.9‰). This result corresponds very well with the angular measurements (Fig. 6.30) where 0.68° and 0.82° are obtained at temperatures of 120°C after a one point offset calibration at 30°C . If a higher accuracy is desired, it is proposed to also calibrate the slope of the offset temperature drift as 1-D sensors from Sentron [1SA-1V] or better to increase the performances of the spinning current electronics using the feedback principle presented in the §5.7. With the feedback configuration presented in the §5.7, the drift is reduced by one order of magnitude. With a 40mT rotating magnetic field, the expected NL will be only 0.07° (0.19‰) for a temperature variation of 90°C (2.2ppm/ $^\circ\text{C}$).

Data from simulations were used to calculate the NL depending on the value of the external field. The results obtained showed a rapid change with a field around 60mT for a $200\mu\text{m}$ disk. An analytical approach provides results which correspond well with the measurements. The Equ. (6.19) gives the saturation value of a $200\mu\text{m}$ disk with a 74mT external field. This typical 4f-type ANL is visible at 80mT with the 2SA-10 microsystem.

Using the same finite element model, we were able to calculate the NL introduced by a misalignment of the ferromagnetic disc with the Hall elements on the silicon chip. Results showed 12° (3.3%) of error for a $10\mu\text{m}$ displacement. With the proposed gain-mismatch compensation we were able to reduce the angular error by more than a factor 20 down to less than 0.5° (1.4%). The repercussions of misalignment are reasonably low and easy to calibrate.

The measurements with Sentron 2SA-10 sensors, clearly confirm our analysis. Offset and sensitivity mismatch are clearly the problem of these sensors; they require an additional calibration to reach a 1‰ accuracy. With temperature variations, the problem comes mostly from a thermal offset drift. This results in a NL as high as 0.8° (2.3‰) for a temperature ranging from -50°C to 120°C (13ppm/°C). Note that the use of the feedback configuration for spinning current (§5.7) reduces the drift: with an additional gain of 10, this drift is reduced by one order of magnitude.

6.7 Comparison between the two sensing elements

Vertical Hall (VH) sensors require a specific high-voltage CMOS technology with a deep NWell. This specific technology has a cost approximately 20% higher than standard technology. For integrated magneto-concentrators (IMC), a simple post-processing is required to deposit the concentrators. The overcharge (cost ratio of the specific technology and of the CMOS chip) of this post processing is about 10-20%. In terms of production cost, these two solutions are virtually identical. The IMC technology is compatible with all microelectronic technologies where a standard Hall plate is feasible. It is a great advantage in terms of flexibility and adaptability for "in fashion" modern technologies. Note that high-voltage technologies will certainly not disappear because they are still required to control actuators such as motors.

Using VH and after an easy offset calibration, a NL of only 0.5° (1.4‰) is measured. This NL can be improved with a gain and phase calibration to reach 0.26° (0.7‰). With IMC, a NL of 2° (5.6‰) is obtained with the offset calibration. This relatively disappointing result is mainly due to the gain-mismatch of up to 5%. It is caused by the misalignment of the IMC and results in a calibration being required for the sensitivity mismatch. After this calibration, the NL reaches about 0.4° (1.1‰) which is 57% worse than a calibrated VH microsystem. Sensitivity mismatch is unfortunately much more difficult to calibrate than offset because it requires a sensitivity measurement on both axes, or a measurement of the amplitude of the signals with a rotating magnetic field. This is of course incompatible with typical microelectronics

installations for functionality tests, such as an industrial wafer prober; This calibration requests a non-ferro-magnetic chuck not to deform the magnetic field and a 2-axes coils or a rotating permanent magnet to generate the rotating magnetic field. The integrated coils of the §3 are useless for the calibration of angular sensors with disk. Indeed, the coil measures the sensitivity of the Hall sensor without the magneto-concentrator and not the gain of the magneto-concentrator; the variations of this gain is rightly responsible for the gain-mismatch between axes.

In terms of signal to noise ratio (SNR), IMC allows an external magnetic field amplification, depending of the diameter of the IMC disk; the larger the disk, the larger the SNR will be. Consequently, the detectivity can be greatly improved compared to the VH sensors, although Hall plates are actually a little less noisy than VH sensors. It allows increasing the distance between the magnet and the sensor or the decrease of the magnet strength.

Sensors using IMC are not well adapted for high magnetic fields ($>100\text{mT}$), because of the ferromagnetic material saturation which decrease the accuracy to 1.5% (§6.6.2). In this case, VH microsystems would certainly be a better solution. However non-linearities from the magnetic field measurement (§6.5.2) are supposed to limit the angular accuracy (§6.1.4) when a large field is applied.

6.8 Conclusion

Two types of angular microsystems were analyzed. The nonlinear behavior of the angular positions was investigated. The sources of absolute non-linearities (ANL) for the two types of angular sensors are clearly identified and well understood. Some of them are related to the 2-Dimensionnal measurement, such as non-orthogonality between the axes and the sensitivity mismatch. Offset, already present in a 1-Dimensionnal Hall sensor, is identified as the most problematic ANL source. The measurements demonstrate that an efficient spinning current electronics is requested (the improvements of the §5 are not applied). Even if the offset is calibrated at room temperature (one-point calibration), its drift is responsible for ANL thermal drift. Mechanical tolerances and the presence of ferromagnetic materials also limit the accuracy of the system.

The saturation of the IMC is a specific source of non-linearity for angular sensors using the ferromagnetic disk. The numerical model developed showed a rapid saturation of the disk for high external magnetic fields. It showed that the saturation depends on the characteristics of the material and the geometry of the

disk. The experimental results obtained showed a predictable behavior and verified the proposed finite element model.

This chapter presented the first absolute angular CMOS microsystems sensor using vertical Hall devices. They achieved 1‰ non-linearity after calibration. These are produced using high-voltage CMOS technology. A thermal drift of only a few ppm/°C is expected. The vertical Hall sensors are implemented with a deep diffusion layer. We demonstrated that these angular sensors exhibit exceptional results for a CMOS angular microsystem. With only a residual offset compensation, accuracy is much greater than that required for the majority of low-cost angular measurement applications. For the first time, a CMOS Hall microsystem for angular measurement reaches a 2‰ level of accuracy with offset compensation. With additional sensitivity mismatch and non-orthogonality compensation, the barrier of 1‰ is broken.

An angular sensor based on IMC is also studied in detail. This sensor doesn't require a specific CMOS technology, but a simple post-processing. It is compatible with almost all existing and future CMOS technologies. Although it doesn't reach the accuracy of VH angular sensors, it offers great advantages for low field measurements; the IMC amplifies the external field. The drawback of this angular sensor is the sensitivity mismatch. Without its calibration, the non-linearity is as high as 2° (0.6%). It is a factor four higher than VH sensors. However, this accuracy is reasonable for the majority of industrial applications.

6.9 References

- [Bilotti97] A. Bilotti, G. Monreal and R. Vig, Monolithic Magnetic Hall Sensor Using Dynamic Quadrature Offset Cancellation, IEEE Journal of Solid-State Circuits, vol. 32, No. 6, pp. 829-836, 1997.
- [Burger01] F. Burger, High Precision Miniaturized Magnetic Angular Encoder, Ph.D. Thesis, (EPFL No 2269), Hartung-Gorre (Konstanz, Germany), ISBN : 3-89649-629-8, 2001.
- [Caruso99] M.J. Caruso, L.S. Withanawasam, Vehicle Detection and Compass Application using AMR Magnetic Sensors, Sensors Expo Proceedings, May, 477-489, 1998.
- [Caruso02] M.J. Caruso, Application of Magnetic Sensors for Low Cost Compass Systems, Technical article, Honeywell, 2002.

-
- [Demierre98] M. Demierre, Dispositif de réglage de précision sans contact, Diploma thesis, EPFL, Lausanne, 1998.
- [Denne98] W. Denne, Magnetic Compass Deviation and Correction, Brown, Son and Ferguson, Scotland, 1998.
- [Drljaca02] P.M. Drljaca, M. Demierre, C. Schott, R.S. Popovic, Nonlinear Effects In Magnetic Angular Position Sensor With Integrated Flux Concentrator, Proc. 23rd Int. Conference On Microelectronics (MIEL 2002), Vol. 1, Nis, Yugoslavia, 12-15 May, 2002, pp. 223-226.
- [Flux3D] Flux 3D 3.2 reference manual, Cedrat Technologies, for details see www.cedrat.com.
- [Frounchi01] J. Frounchi, M. Demierre, Z. Randjelovic, and R. Popovic, Integrated Hall Sensor Array Microsystem, ISSCC-2001 Conference, San Francisco, 2001.
- [KMZ-52] KMZ52 Magnetic Field Sensor, product specification, Philips, 2000.
- [Lund83] C.A. Lund, Compasses in Small Craft, Brown, Son and Ferguson, Scotland, 39-62, 1983.
- [Malco00] P. Malcovati, F. Maloberti, An integrated Microsystem for 3-D Magnetic Field Measurements, IEEE Transactions on Instrumentation and Measurement, Vol. 49, No2, 2000.
- [O'Handley00] R.C. O'Handley, Modern magnetic materials, John Wiles & Sons, Inc. 2000, section 2.3.
- [Philips] Electronic Compass Design using KMZ51 and KMZ52, AN00022, Application note, Philips Semiconductors.
- [Popovic84] R.S. Popovic, The Vertical Hall-Effect Device, IEEE Electron Dev. Lett., EDL-5(9), 1984, pp. 357-358.
- [Popovic01] R.S. Popovic, C. Schott, P.M. Drljaca and R. Racz, "A new CMOS Hall angular position sensor", Technisches Messen, Vol. 6, pp. 286-291, 2001.
- [Popovic02] R.S. Popovic, C. Schott, Hall ASICs with integrated magnetic concentrators, Proceedings SENSORS EXPO & CONFERENCE, Boston, Ma, USA, September 23-26, 2002.

- [Schott00] C. Schott, R. Racz and R.S. Popovic, Sensor for the detection of the direction of a magnetic field, Sentron AG, US Patent, US2002/0021124A1.
- [Schurig03] E. Schurig, C. Schott, M. Demierre, P.-A. Besse and R.S. Popovic, CMOS Integrated Vertical Hall Sensor with Low Offset, to be published in *Sensors & Actuators*, 2003.
- [Stork00] T. Stork, Electronic Compass Design using KMZ51 and KMZ52, Application note AN00022, Philips, 2000.
- [Trontelj01] J. Trontelj, Functionality Test for Magnetic Angular Positioning Integrated Circuit, *Informacije MIDEM* 31(2001),4, Ljubljana, pp. 287-289, 2001.
- [1SA-1V] 1SA-1V Integrated Hall sensor, datasheet, Sentron, 2002.
- [2SA-10] 2SA-10 Integrated 2-axis Hall Sensor, preliminary datasheet, Sentron, 2002.

7 Conclusion and Outlook

7.1 A toolbox for Hall microsystems

In this thesis we have developed a toolbox to construct very accurate CMOS Hall microsystems; each so-called tool solves a limitation of Hall sensors. In addition to a careful sensor design, the relationships between the system components, i.e. sensors and electronics, are extensively used to improve the microsystem behavior.

The first tool is calibration coils (§3) for both Hall plates and vertical Hall sensors. Using Hall plates of usual size, the efficiency of the coil, i.e. the ratio of the magnetic field over the current, is poor. The efficiency is greatly increased when the coil is miniaturized to the limit of this technology. The efficiency is limited by the distance between the coil and the sensor and the size of the Hall sensor. We found the rules to optimize the coil performances. This allows us to reach an efficiency of respectively 390mT/A and 230mT/A for Hall plates and vertical Hall sensors. It corresponds to a magnetic field of about 1mT for a biasing current of only 3.6mA. For each coil, we propose a simplified analytical model which corresponds well with these measurements. Using an array of 4 coils, we achieve a total magnetic efficiency of 1600mT/A for Hall plates. With a bandwidth of 1Hz, which is sufficient for most applications, and a 3.6mA coil current, the SNR is 66dB. Gluing a ferromagnetic layer on the surface of the chip increases the coil efficiency by 40% to above 2000mT/A.

Miniaturized Hall plates (§3) are required for efficient coils. We create a sensor with a spatial resolution of about 2.5 μ m width. The miniaturization of this sensor is limited by the non-linear behavior of its internal resistors due to the junction field effect. The voltage related efficiency with a low biasing is 78% of the theoretical value using the best cross. It is reduced to merely 30% with 5V biasing. The larger junction field effect is also responsible for an increase in residual offset after the spinning current method.

We analyze the self-calibration of a Hall microsystem sensitivity based on the calibration coils. An in-situ coil, built with the metallic layers of the CMOS process, permits an accurate calibration of the sensitivity when biased with an accurate laboratory current source. With Hall plates we obtain an exceptional sensitivity drift of less than 30ppm/ $^{\circ}$ C (§3.14). This is more than one order of

magnitude smaller than the drift of an integrated current source and it is also smaller than the drift of a reference voltage bandgap. Note that this method not only reduces the thermal drifts, because all the sensor drifts are replaced by those of the coil. We propose for the first time a calibration scheme which is independent of the electronic references (§3.15). We call this reference a geometrical reference, because it depends only on the geometry of the coil and the distance from the sensor.

The second tool concerns the offset of Hall microsystems (§5). Offset is a major limitation of Hall sensors, however the spinning current method (§2.1.5) is well known to substantially reduce this offset. However a residual offset after the spinning current method is still observed. To achieve lower residual offset, we analyze the sources of residual offset inside our microsystem with an analog output. We find that it is composed of a residual offset from the sensor itself, but also by imperfections of the electronic circuits. We developed an enhanced microsystem, with a better systemic approach based on a feedback configuration (§5.7), to reduce the residual offset from electronics by one order of magnitude. Note that this technique can be used to reduce further the residual offset, but with a reduction of the dynamic performances. The 2-phases spinning current, where the current flows in two orthogonal directions, is not efficient enough against the offset from miniaturized “degenerated” Hall sensors, i.e. with a strong non-linear behavior. The residual offset of these Hall sensors is substantially decreased using the 4-phases spinning current (§5.8). This is clearly shown with a couple of vertical Hall sensors, where the residual offset is roughly decreased by a factor 5 for a 1mA biasing. The final results from the spinning current electronics render the offset calibration redundant for contactless potentiometers up to about 2‰ accuracy. If a greater accuracy is required, an offset calibration combined with other, more calibrations is obligatory.

7.2 Angular position sensors

In this thesis we have developed a very accurate CMOS Hall microsystem for angular position measurement. The principle chosen at the beginning of the thesis consists in placing a permanent magnet on a rotating shaft in front of a magnetic microsystem (§2.4.2). The magnetic field is measured, in two orthogonal directions parallel to the surface of the chip, in order to calculate the angle over 360° without any dead angle. We have studied within this thesis two corresponding microsystems based on the Hall effect: CMOS vertical Hall sensors (§2.3) placed orthogonally to each other and a combination of Hall plates and a ferromagnetic disk (§2.4.4).

We realized a CMOS angular microsystem using CMOS vertical Hall sensors. This microsystem does not use the feedback configuration to reduce the residual offset developed in §5.7 and the 4-phases spinning current in §5.8. This is why residual offset compensation is necessary to reach 0.3% accuracy. The Hall sensors are directly produced using the deep NWell occurring during a high voltage CMOS process, whereas electronics use the standard 5V core. No post- or pre-processing are required. With only a residual offset calibration after the spinning current method, an outstanding accuracy of 0.5° (1.4‰) is obtained. With additional gain-mismatch and non-orthogonality compensation the accuracy is improved to 0.17° (0.5‰).

We analyze a second kind of angular sensors, produced industrially by our industrial partner, in order to compare it with the previous ones. This microsystem is composed of two pairs of Hall plates placed orthogonally under the periphery of a ferromagnetic disk (§2.4.4) deposited using a post-processing of integrated magneto-concentrator. The Hall signals are amplified using a spinning current electronics without the feedback configuration presented above. With residual offset compensation, the accuracy of the angular measurement is only 2° (5.6‰); it is about a factor 4 larger than the previous sensor. Mechanical tolerances during the post-process create an inaccuracy in the concentrator magnetic gain. This results in a gain-mismatch between the axes which drastically decreases the performances of the sensor. However, using an additional gain-mismatch calibration, we can reach an accuracy of 0.4° (1.1‰). This gain calibration requires a relatively complicated calibration because of the external field which is required for sensitivity measurements. This is unfortunately incompatible with usual microelectronics installations for functionality tests, in contrast with the easy offset compensation. This calibration requests a modified wafer-prober, with 2-axes coils or a rotating permanent magnet to generate the rotating magnetic field and a non-ferromagnetic chuck not to deform the magnetic field.

Sensors using the ferromagnetic disk are better adapted for a lower magnetic field than vertical Hall sensors. The concentrator amplifies the external magnetic field, increasing the detectivity. However the maximum field is limited by the saturations of the concentrator material. This sensor has the enormous advantage of being compatible with all CMOS technologies as long as using Hall plates is still feasible. On the other hand, the microsystem using vertical Hall sensors does not require a post- or pre-processing, but a specific CMOS technology. The disappearance of this specific CMOS technology will lead to the death of the sensor. The accuracy of this sensor however is much better, even without any complicated calibration of the sensitivity. The range of the magnetic field of this vertical Hall sensor is only limited by its non-linearities, which are negligible at least up to 50mT (§6.5.2). As a result it is better suited to larger magnetic fields than the other sensor using the disk.

Sensitivity drift (§6.6.4) is not responsible for angular errors if the two X and Y axes are matched, because the ratio of the two signals is used; only the mismatch of the sensitivity between the two axes induces inaccuracies. An excellent matching of typically $10\text{ppm}/^\circ\text{C}$ of the two axes sensitivity, equivalent to an $0.8\text{ppm}/^\circ\text{C}$ angular drift, is measured for the angular sensor using an integrated magneto-concentrator. This demonstrates that matching is efficient enough without any calibration, even if low cost plastic packaging is used. However the coils can be used for the self-test of the angular microsystem or for production purposes (§2.2).

The offset and its drift are much more dominating effects (§6.6.4). When the feedback configuration for spinning current (§5.7) is not used, we measure an offset drift of $50\mu\text{V}/^\circ\text{C}$. With a 1V sine and cosine amplitude, we calculate a $10\text{ppm}/^\circ\text{C}$ angular drift. With the feedback spinning current (§5.7), the cross-effects are reduced (§5.7.5). With the last microsystem, we expect that the angular thermal drift from offset is only $1\text{ppm}/^\circ\text{C}$ (§6.6.4).

7.3 Outlook

The last engineering CMOS run, not measured within this thesis, based on CMOS vertical Hall sensors and using the thorough knowledge of residual offset (§5.5) acquired within this thesis (Fig. 7.1) will render the offset calibration for most applications pointless. This microsystem will reach an outstanding angular accuracy better than 0.3% (1°) without any calibration, pre- or post-processing for an optimized magnetic field. The first results obtained at the end of this thesis confirm the good behavior of this microsystem. A low residual offset of only a few millivolts, equivalent to the offset of a simple operational amplifier, is measured with the feedback spinning current (§5.7). We hope that a microsystem with such excellent performances will be commercialized soon.

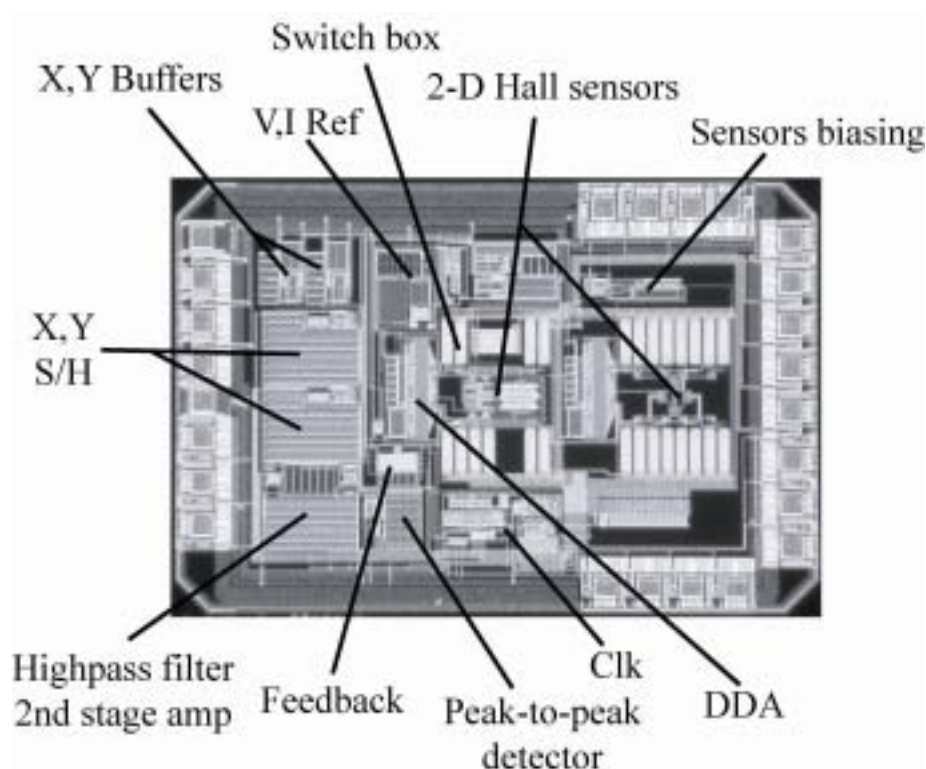


Fig. 7.1 Picture of the integrated Hall sensor microsystem for two dimensional magnetic measurements using CMOS vertical Hall sensors. It contains the spinning current electronics for a 2- or 4-phases spinning current with the new feedback topology. Two sensor banks of vertical Hall sensors can be connected to the electronics. The chip size is $2.75 \times 1.85 \text{mm}^2$.

The spatial resolution of our miniaturized CMOS Hall sensor (§4.1) is about $2.5 \mu\text{m}$. It permits high resolution mapping of a magnetic field, in order to, for

instance, analyze ferromagnetic materials or to measure micrometric magnetic dipoles, such as ferromagnetic and superparamagnetic microbeads. The CMOS process allows the multiplexing of an array of sensors. This small sensor, which can be considered as a pixel, can be combined into an array to obtain a magnetic camera. The application domain of such a camera is vast; for instance a position sensor similar for an optical coder based on the displacement of micrometric magnetic patterns. Another application of this magnetic camera is a magnetic tracking system of a magnetic dipole (permanent magnet) with 5 degrees-of-freedom. For instance the position of a magnetic bearing shaft can be measured for its regulation with a single CMOS microsystem and a magnet.

Another interesting emerging project is a fully integrated 3-dimensionnal magnetic probe, which is the combination of the 2-dimensionnal Hall sensor for measurements parallel to the surface of the chip and a Hall plate to measure the perpendicular magnetic field.

The coils developed within this thesis and the calibration scheme for the geometrical reference (§3.15) are a new way to drastically reduce sensitivity drifts for a Hall microsystem. A further step is the integration of the whole microsystem onto the same CMOS chip to obtain a “driftless” magnetic sensor. What's more the sensitivity meter based on this reference coil is an excellent candidate for the study of stresses in silicon by measuring variations of the current related sensitivity due to the piezo-Hall effect (§2.1.3). This has the huge advantage of compatibility with a standard wafer prober. Because no external magnetic sources are required (in-situ CMOS coil), stress measurements can easily be obtained at a larger scale.

Acknowledgments

First of all I would like to thank Prof. R.S. Popovic, head of our laboratory of microsystems, who has continually shared his great knowledge of microsystems. Since the first lecture I had with him, he has communicated his enthusiasm for integrated sensors. I also thank Dr. Pierre-André Besse for all its contributions about my so-called “octopus projet”. A special thanks to Dr. Beat Furrer for the sharing of his vast knowledge of integrated circuits and for his availability for fascinating discussions. I am also very grateful to Dr. Pavel Kejik who helps me IC design and rescues me from insolvable layout mistakes. I also thank my colleagues who have helped me during this work: Dr. Frederic Burger for his contributions about angular sensors, Predrag Drljaca and Franck Vincent for their fruitful work on magnetoconcentrators, Enrico Schurig for the optimization of my first CMOS vertical Hall sensors, Dr. Javad Frounchi and Dr. Zoran Randjelovic for the electronics. I also cannot forget Yves Pilloud and the ACORT team for their uninterrupted assistance, without whom my work would have been infeasible.

I have to thank Dr. Christian Schott from my industrial partner Sentron AG. Even if he spent all his time with his company, he leads my project from an industrial point of view. I hope that the fruit of my thesis will appear soon inside commercial sensors.

Many thank to Svend Hoyer, Pierre Lamon, Pierre-Yves Lampo, Mathias Link, Christiano Niclass and Sergio Pesenti who were “my” students. It was a great pleasure to transmit my flame for the design of microsystems. I also thank Niall McCullough who has considerably improved my writing of my thesis.

This work has been made possible by the financial support of the European project Surface and the Swiss program TopNano21.

Let's also have a big hand for all my colleagues. They were always available for technical discussions or more often to have fun during the breaks. I would like to thank in particular Vincent Schlageter with whom I share my office.

But my utmost gratitude goes directly to my family and all my friends who have always supported me. No words are great enough to express my thanks to my parents, my brother and my wife Marilyne.

Curriculum Vitae

Personal data

Michel Demierre

Born 1974 in Lausanne, Switzerland

Married

Swiss

michel@techt.ch

Professional and teaching activities

2000-2003 Research assistant at the Institute of Microelectronics and Microsystems, Swiss Federal Institute of Technology in Lausanne (EPFL). Teaching activities (laboratories, supervision of student projects and diploma works).

1998-2000 Research assistant at the Institute of Microelectronics and Microsystems, EPFL.

Formation

2000-2003 Ph.D thesis at the Institute of Microelectronics and Microsystems, EPFL.

1998-2003 Day release: low-voltage analog CMOS IC design, contactless measurement of size and movements, writing of reports.

1998 Swiss license of explosive use, deliver by the office fédéral de la formation professionnelle et de la technologie.

1993-1998 Swiss Federal Institute of Technology in Lausanne (EPFL), section microtechnology, orientation integrated products.

1990–1993 Baccalauréat type C (Mathématique-Science), Prize Dr Pierre May, Gymnase cantonal de la Cité.

Hobby

Caving Member of the Groupe Spéléo Lausanne committee, of the specialist explosives and the regional rescue teams of the Spéléo Secours Suisse. Underground photography.

Publications about microsystems

M. Demierre, E. Schurig, C. Schott, P.-A. Besse, Contactless 360° Absolute Angular CMOS Microsystem based on Vertical Hall Sensors, *Sensors & Actuators A*, in press.

M. Demierre, P. M. Drljaca, P.-A. Besse and R. S. Popovic, Self-calibration of CMOS Hall microsystems, *Sensors & Actuators A*, in press.

G. Boero, M. Demierre, P.-A. Besse and R.S. Popovic, Micro-Hall devices: performance, technologies and applications, *Sensors & Actuators A*, Vol 106, pp. 314-320, 2003.

E. Schurig, M. Demierre, C. Schott and R. S. Popovic, A vertical Hall device in CMOS high-voltage technology, *Sensors & Actuators A*, Vol 97, pp. 47-53, 2002.

M. Demierre, S. Pesenti, J. Frounchi, P.-A. Besse and R. S. Popovic, Reference magnetic actuator for self-calibration of a very small Hall sensor array, *Sensors & Actuators A*, Vol 97, pp. 39-46, 2002.

M. Demierre, S. Pesenti, and R. S. Popovic, Self calibration of a CMOS twin Hall microsystem using an integrated coil, *Proc. 16th Eurosensors Conference*, Prague, Czech Republic, pp. 573-574, 2002.

P.-A. Besse, G. Boero, M. Demierre, V. Pott, R. S. Popovic, Detection of a single magnetic microbead using a miniaturized silicon Hall sensor, *Applied Physics Letters*, Vol. 80, No. 22, pp. 4199-4201, 2002.

P. M. Drljaca, M. Demierre, C. Schott, R. S. Popovic, Nonlinear Effects In Magnetic Angular Position Sensor With Integrated Flux Concentrator, *Proc. 23rd Int. Conference On Microelectronics (MIEL 2002)*, Vol. 1, Nis, Yugoslavia, 12-15, pp. 223-226, 2002.

M. Demierre, S. Pesenti, J. Frounchi, R.S. Popovic, Reference Magnetic Actuator for self calibration of a Very Small Hall Sensor Array, *Transducers'01*, München, 2001.

J. Frounchi, M. Demierre, Z. Randjelovic, and R. Popovic, Integrated Hall Sensor Array Microsystem, *ISSCC2001 Conference*, San Francisco, 2001.

F. Burger, M. Demierre, A. Drapp, P.A. Besse and R.S. Popovic: Three branches Vertical Hall Device for the Accurate Control of Brushless Micromotors, *Proc. Transducers'99*, Sendai, Japan, pp. 84-87, 1999.

L. Guérin, M. Bossel, M. Demierre, S. Calmes, P. Renaud, Simple and low-cost fabrication of embedded micro-channels by using a new thick-film Photoplastic, Proc. Transducers 97, Chicago, USA, Vol. 2, pp.1419-1422, 1997.

Other publications

M. Demierre, Les leds blanches , Le Trou, bulletin du Groupe Spéléo Lausanne, No.65, pp. 78-86, 2003.

M. Demierre and V. Ballenegger, Le Réseau du Folliu, Le Trou, bulletin du Groupe Spéléo Lausanne, No.65, pp. 67-75, 2003.

M. Demierre, Les leds blanches: la nouvelle lumière spéléologique?, Spelunca, Fédération Française de Spéléologie, No. 89, pp.12-16, 2003.

M. and J. Demierre, Monoxyde de carbone et minage en spéléologie, report for the specialist explosives of caving, 26 pages, 2002.

M. Demierre and J. Perrin, Baume de la Joux de Bière, Le Trou, bulletin du Groupe Spéléo Lausanne, No.60, pp. 3-6, 1996.